

THE MORPHOLOGY OF RADIATION DAMAGE IN COPPER  
IRRADIATED WITH NEUTRONS AT  
ELEVATED TEMPERATURES

A Thesis presented to the  
Department of Physics, University of Natal,  
Durban.

in partial fulfilment of the requirements for  
the degree of Doctor of Philosophy.

by

KELVIN      RICHARD      KEMM

January, 1977.

### ACKNOWLEDGEMENTS

I wish to express my sincere thanks and appreciation to the following persons who have contributed to this project in various ways.

Dr. D.R. Spalding, my supervisor, for his companionship and his help and encouragement during the project.

Dr. P.J. Jackson, for his interest and many helpful discussions throughout the project.

Mr. E.E. Higginson for his interest in the project as a whole and his craftsmanship in constructing the necessary apparatus, particularly the High Temperature Irradiation Rig.

Dr. R.M. Mayer of the Atomic Energy Board for a number of helpful discussions.

Special thanks are due to Messrs. H. Niebuhr, T. Evans and T. Duncan and the rest of the staff of the SAFARI 1 reactor at Pelindaba for their friendliness and valuable assistance in the irradiation of the specimens.

I would also like to express my gratitude to all my colleagues in the Physics Department for making my stay in the department such an enjoyable one.

My thanks are also due to my wife, Diana, for her constant encouragement and assistance in many tasks associated with the production of this thesis, and also to Mrs. E. Serfontein for typing the manuscript.

Finally, thanks are due to the Atomic Energy Board for financial assistance.

## PREFACE

This thesis describes an investigation of the damage morphology found in high purity copper crystals which were irradiated with fast neutrons at elevated temperatures. These irradiations were carried out in the SAFARI I reactor in Pretoria.

Transmission electron microscopy was the main method of examination used by the author and all electron microscopy results in this thesis are the work of the author.

Many of the radiation damage features studied were very large in size, and thus to complement the electron microscopy results etch pit techniques were used which provide a macroscopic view of the damage morphology. This etch pit work was carried out in Pietermaritzburg by Dr. P.J. Jackson and Messrs. P.N. Nathanson and K. Black. The results of these researchers are referenced throughout this work.

To produce the irradiated crystals which were examined in this work it was necessary to design and build a High Temperature Irradiation Rig to carry out irradiations to a high degree of precision. The author was involved in the design of some of the mechanical components of this rig and was totally responsible for the design and construction of the electrical system of the rig. The mechanical construction of this rig was carried out by Mr. E.E. Higginson in the Physics Workshop in Durban. The author was responsible for the commissioning and testing of the rig in the SAFARI I reactor and also operated the rig during all of the irradiation runs carried out over a period of two years.

The crystal growing apparatus described in Chapter 5 was initially constructed by Mr. S. Baines but was greatly modified and improved by the author.

A new JEOL Jem 100C electron microscope was used in the course of this work and this microscope was commissioned and calibrated by the author before the commencement of the present investigation.

The crystallographic notation used in this thesis is as follows:

$(1\bar{1}1)$  indicates a crystallographic plane.

$\{111\}$  indicates a set of crystallographic planes.

$\langle 1\bar{1}1 \rangle$  indicates a crystallographic direction.

$[111]$  indicates a set of crystallographic directions.

## SUMMARY

This thesis is an investigation of the radiation damage morphology of high purity copper crystals irradiated with fast neutrons at temperatures in the range of 250°C to 400°C. At these high temperatures neutron damage is found to accumulate into large 3-dimensional rafts up to 100  $\mu\text{m}$  in size, and the well known homogeneous distribution of black dot damage which is characteristic of irradiations at lower temperatures is not observed.

The characteristics and composition of the rafts of damage at different temperatures in the range 250°C to 400°C have been compared and found to differ to a large extent. It has also been shown that the background areas between rafts contain a rather low density of damage at all temperatures studied.

It is therefore concluded that many of the interstitial atoms formed during irradiation migrate over large distances through the crystal lattice to precipitate at the sites of the dislocations forming the large rafts, and so denuded inter-raft areas are left behind. It is proposed that these large rafts originate from grown-in dislocations present in the crystals before irradiation.

## CONTENTS

Page

### CHAPTER ONE

#### THE IMPORTANCE OF RADIATION DAMAGE STUDIES 1

#### 1.1 Introduction 2

### CHAPTER TWO

#### RADIATION DAMAGE IN CRYSTALLINE SOLIDS: A REVIEW OF FUNDAMENTALS 4

#### 2.1 Summary 5

#### 2.2 The nature of the radiation damage process 5

##### 2.2.1 Introduction 5

##### 2.2.2 Displacement damage 6

##### 2.2.3 Crystal lattice effects 8

##### 2.2.4 Point defects and diffusion 11

#### 2.3 Interactions of point defects 16

##### 2.3.1 Nucleation of point defect clusters 16

##### 2.3.2 Interaction of point defects with dislocations 23

##### 2.3.3 Increase in dislocation density induced by radiation 28

##### 2.3.4 Impurity effects 29

##### 2.3.5 Effect of irradiation temperature on point defect trapping 32

##### 2.3.6 Relation between irradiation temperature and flux 36

#### 2.4 Fast neutron irradiation 37

CHAPTER THREEREVIEW OF PREVIOUS EXPERIMENTAL RESULTS

<u>3.1</u>	Introduction	39
<u>3.2</u>	The damage morphology at different temperatures	41
3.2.1	Irradiations at low temperatures	41
3.2.2	Irradiations at ambient temperatures	43
3.2.3	Irradiations at high temperatures	53
<u>3.3</u>	Conclusions	59

CHAPTER FOUR

TRANSMISSION ELECTRON MICROSCOPY OF RADIATION  
- INDUCED DEFECTS

<u>4.1</u>	Introduction	62
<u>4.2</u>	Diffraction contrast in the electron microscope	62
4.2.1	Introduction	66
4.2.2	Summary of diffraction contrast theory	66
<u>4.3</u>	The appearance of defects in the final image	73
4.3.1	Small strain centres	73
4.3.1.1	Introduction	73
4.3.1.2	Black-white images	74
4.3.1.3	Edge loops	75
4.3.1.4	Non-edge loops	78
4.3.1.5	Small voids	78
4.3.1.6	Stacking fault tetrahedra	78

	Page
<u>CHAPTER FOUR CONTINUED</u>	
4.3.2 Large dislocation loops	79
4.3.2.1 Contrast properties	79
<u>4.4</u> The experimental determination of the vacancy or interstitial character of loops	80
4.4.1 Determination of the nature of the loops	80
4.4.2 Determination of the sense of inclination of a loop	81
<u>4.5</u> Summary	84

## CHAPTER FIVE

<u>EXPERIMENTAL PROCEDURE</u>	85
<u>5.1</u> Introduction	86
<u>5.2</u> The specimens used	86
<u>5.3</u> Crystal growing system	86
5.3.1 Introduction	86
5.3.2 Crystal growing apparatus	88
5.3.3 Crystal mould assembly	90
5.3.4 The seed crystal	92
<u>5.4</u> Irradiations	93
<u>5.5</u> Specimen preparation	94
5.5.1 Introduction	94
5.5.2 Crystals used for etch pit studies	94
5.5.3 Crystals used in mechanical testing	96
5.5.4 Electron microscopy specimens	96
<u>5.6</u> Electron microscopy	97

CHAPTER SIX

	<u>THE HIGH TEMPERATURE IRRADIATION RIG</u>	98
<u>6.1</u>	Introduction	99
<u>6.2</u>	Design criteria of the high temperature irradiation rig (H.T.R.)	99
<u>6.3</u>	Construction of the H.T.R.	101
<u>6.4</u>	H.T.R. Instrumentation	107
<u>6.5</u>	Performance of the H.T.R.	112
<u>6.6</u>	Handling and loading procedures of the H.T.R.	116

CHAPTER SEVEN

	<u>MORPHOLOGY OF HIGH TEMPERATURE RADIATION DAMAGE</u>	121
<u>7.1</u>	Introduction	122
<u>7.2</u>	Qualitative survey of present results	122
<u>7.3</u>	Proposed shape of the prism of radiation damage	125
<u>7.4</u>	Alignment of comet-shaped rafts	127
<u>7.5</u>	Details of the general damage morphology	128
7.5.1	Specimens irradiated at 250°C	128
7.5.2	Specimens irradiated at 300°C	130
7.5.3	Specimens irradiated at 350°C	131
7.5.4	Specimens irradiated at 400°C	133
<u>7.6</u>	Comparison of electron microscope data and etch pit data	135

CHAPTER EIGHTTHE ANALYSIS OF THE COMPONENTS OF THE DAMAGE

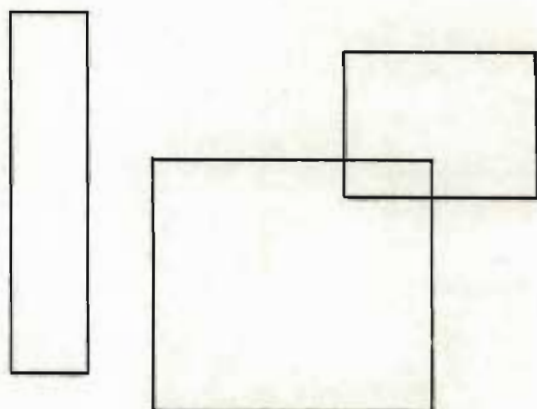
		141
<u>8.1</u>	Introduction	142
<u>8.2</u>	The association of damage and dislocations	142
<u>8.3</u>	Rafts of damage contain all possible Burgers vectors	142
<u>8.4</u>	The character of large loops	143
<u>8.5</u>	Small loops	145
<u>8.6</u>	Dislocation dipoles	150
<u>8.7</u>	Different doses for irradiations at 250°C	151

CHAPTER NINEDISCUSSION

		154
<u>9.1</u>	Introduction	155
<u>9.2</u>	Migration of damage	155
<u>9.3</u>	Discussion of possible mechanism of raft formation	160
<u>9.4</u>	Relation of the proposed formation mechanism to the observed damage morphology	169

CHAPTER TENFUTURE WORK

		173
<u>10.1</u>	Summary of future work	174
	References	176



CHAPTER ONE

THE IMPORTANCE OF RADIATION DAMAGE STUDIES

1.1 Introduction

## 1.1 INTRODUCTION

Studies of the effects of nuclear radiations on solids have applications throughout fission and fusion reactor technology as well as space technology. In space environments, the effects of Van Allen and solar-wind irradiations on solar cells and metal-oxide semiconductor devices have received extensive investigation.

Deficiencies in understanding the changes induced by radiation in materials used in reactors have led to costly modifications in design and operational procedures. Lack of complete knowledge of these complex processes in engineering materials requires periodic retrieval of samples from present light-water reactors for materials testing. There is also the possibility that the deterioration of the containing vessel may make it necessary to shut down the reactor and thus shorten its useful life. The thermal reactors now in service could operate much more efficiently and at lower cost if the designers did not have to make allowances for radiation damage effects. These deficiencies in materials knowledge have been estimated to have cost the United States \$480 million in 1974 with an increase to over \$1 billion in 1982 (Report of the A.P.S. : Problems Relating to Energy Technologies (1975)).

The radiation-effects research done in the past has been of great value in the design of the power reactors now in operation. However, a considerably enhanced effort in this research will be required to provide the insight and information necessary for the solution of problems in the present light-water reactors and even more for the design of future fission and fusion reactors, because these will operate at temperatures and with particle fluxes far above those of present day reactors. The most important radiation effects to components of light-water reactors are the results of fast neutron damage

to structural materials. The fast-neutron fluxes to be expected in a typical fast breeder reactor are about  $10^{16}$  fast neutrons. $\text{cm}^{-2} \cdot \text{s}^{-1}$  compared to fluxes of a few times  $10^{13}$  in thermal reactors.

As a result of these considerations the study of fast neutron radiation damage in materials at high temperatures is of great importance.

## CHAPTER TWO

### RADIATION DAMAGE IN CRYSTALLINE SOLIDS:

#### A REVIEW OF FUNDAMENTALS

- 2.1 Summary
- 2.2 The nature of the radiation damage process
  - 2.2.1 Introduction
  - 2.2.2 Displacement damage
  - 2.2.3 Crystal lattice effects
  - 2.2.4 Point defects and diffusion
- 2.3 Interactions of point defects
  - 2.3.1 Nucleation of point defect clusters
  - 2.3.2 Interaction of point defects with dislocations
  - 2.3.3 Increase in dislocation density induced by radiation
  - 2.3.4 Impurity effects
  - 2.3.5 Effect of irradiation temperature on point defect trapping
  - 2.3.6 Relation between irradiation temperature and flux
- 2.4 Fast neutron irradiation

## 2.1 SUMMARY

In this chapter the fundamental processes in radiation damage, and the diffusion of the resulting point defects are discussed briefly. The geometry of some crystal lattice defects produced during irradiation is described.

## 2.2 THE FUNDAMENTAL PROCESS IN RADIATION DAMAGE

### 2.2.1 Introduction

When solids are bombarded with energetic particles they may be damaged in three ways:

Firstly, in an electrically insulating solid the atoms may be ionized.

Secondly, atoms may be displaced from their normal lattice positions when struck by a bombarding particle or, in a secondary collision, by a moving displaced atom.

Thirdly, foreign atoms may be introduced into a solid when it is bombarded with ions of a different species which are then retained in the solid, or alternatively, nuclear transmutations may occur in target nuclei struck by incident particles. Neutron irradiation of materials containing the isotope  $^{10}\text{B}$  is an example since it leads to the accumulation of helium and lithium as a result of the fission transmutation  $^{10}\text{B} (n, \alpha) ^7\text{Li}$ . Other examples are:  $^{58}\text{Fe} (n, \gamma) ^{59}\text{Fe}$ ,  $^{238}\text{U} (n, f)$ .

In this thesis we shall be concerned with radiation damage in pure copper bombarded with fast neutrons, where only displacement

damage is important. We now consider this process in more detail.

### 2.2.2 Displacement damage

Consider an elastic collision in which kinetic energy  $E_t$  is transferred from an incident particle (mass  $m$ , kinetic energy  $E_k$ ) to an atom in the solid (mass  $M$ ) which we shall refer to as the primary recoil atom.

Considering classical calculations in centre of mass coordinates we get:

$$E_t = \frac{4 mM}{(m + M)^2} E_k \sin^2 \frac{\theta}{2} \quad (2.1)$$

where  $\theta$  is the angle through which the incident particle is deflected. The relativistic formulation of (2.1) is not relevant in this case.

Unless  $E_t$  exceeds a threshold  $E_D$  (typically 15-50 eV in a solid) the primary recoil atom is not displaced permanently from its position in the lattice.  $E_D$  depends on the type of solid, and the crystallographic direction of displacement.

If  $E_t > E_D$  then the target atom will be displaced forming an interstitial atom and leaving behind a vacancy. If a second critical energy  $E_C$  (1 to 30 KeV) is exceeded by  $E_t$  then a cascade of displaced atoms  $N(E_t)$  is formed instead of a single displaced atom (Figure 2.1).

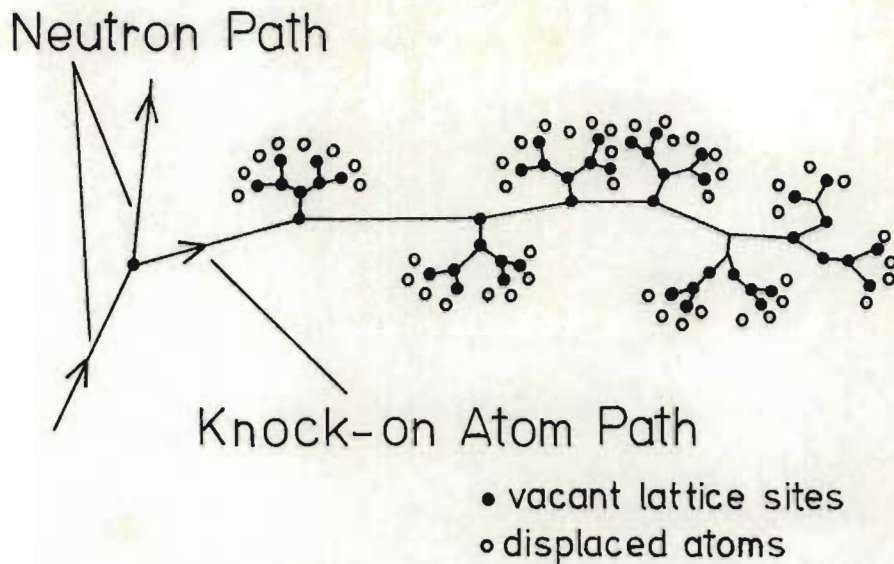


FIG (2.1) The Collision Cascade

An expression for  $N(E_t)$  has been derived by Kinchin and Pease (1955) assuming that the collisions are elastic impacts between hard spheres. They found that  $N(E_t)$  is simply proportional to  $E_t$ , i.e.

$$N(E_t) = \frac{\bar{E}_t}{2 E_D} \quad (2.2)$$

where  $\bar{E}_t$  is the average transmitted energy. It was also assumed by Kinchin and Pease that inelastic losses by electron excitation occur only above some specific energy (which is  $\sim A$  KeV where  $A$  is the mass

number). This model forms the basis of many later calculations.

An improved version of the Kinchin and Pease model, known as the 'Half-Nelson' model has been presented by Nelson, Etherington and Smith (1971). This model takes account of deviations from hard-sphere behaviour, recombination within the cascade, and incorporates a more realistic approach to inelastic losses and the effects of crystal structure such as channelling and focusing (to be described below).

### 2.2.3 Crystal lattice effects

Much of the early radiation damage work carried out neglected any effects due to the lattice structure. Two phenomena of importance are focusing and channelling.

Close packed rows of atoms, such as the  $\langle 110 \rangle$  row in the F.C.C. lattice, are able to transfer momentum out of displacement cascades very efficiently by focusing. A focused collision sequence (first analysed by Silsbee (1957)) is shown in Figure 2.2. In this sequence each atom in a close packed row strikes its neighbour thus transporting energy along the row. Between 10 and 15 atoms in a row undergo collisions, the number depending on the incident energy (Thompson (1969)). Focusing occurs only at low incident energies up to a few hundred eV, and a critical focusing energy  $E^{hkl}$  exists below which focusing occurs in the  $hkl$  direction. Thompson (1969) tabulates figures which show that  $E^{hkl}$  varies from  $\sim 10$  eV for light elements to  $\sim 10^3$  eV for heavy elements, and thus focused collision sequences exert their greatest influence on cascades in heavy elements. Gibson *et al.*, (1960) calculate  $E^{110}$  for copper to be 67 eV. Most damage caused by focusing occurs when a focused collision sequence is defocused at an existing lattice defect.

It has been shown by means of computer simulations (Gibson *et al.*, (1960)) that focused collision sequences also occur along  $\langle 100 \rangle$  rows in the F.C.C. lattice at energies above the limit for simple focusing. The clue to this mechanism, called assisted focusing, lies in the ring of atoms formed by neighbouring rows which are seen to recoil outwards as the sequence passes through (Figure 2.2).

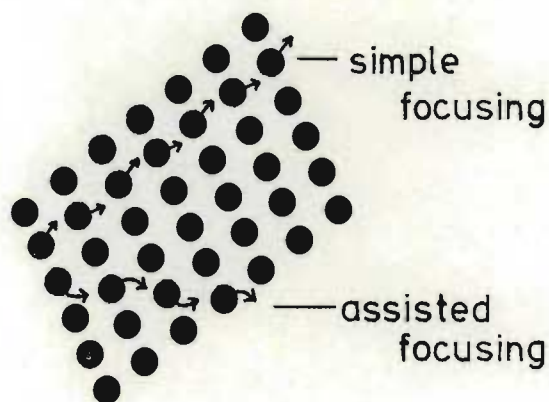


FIG (2.2) Focused Sequences

Matter can also be transported along rows of atoms by means of a replacement collision sequence in which each atom replaces its neighbour in the focusing line. The importance of the replacement sequence is that it moves every atom forward by one place, leaving a vacant site at one end and forming an interstitial at its terminus. A replacement collision sequence is also referred to as a 'dynamic crowdion'.

Channelling occurs when a particle (usually a large particle such as an ion or primary knock-on atom) is projected into the 'channel' between rows of atoms (Figure 2.3). The motion of a channelled atom is

very stable since it undergoes glancing collisions which constrain it to remain in the channel, where it is less likely to undergo displacement collisions. Also it slows down gradually giving its energy to many thousands of secondaries, none of which receives enough to be displaced. In addition damage is spread over a large volume of the crystal due to the long range of channelled atoms. Robinson and Oen (1963) show that channelled 5 KeV Cu ions in copper can travel up to 500 Å in the  $\langle 110 \rangle$  channel.

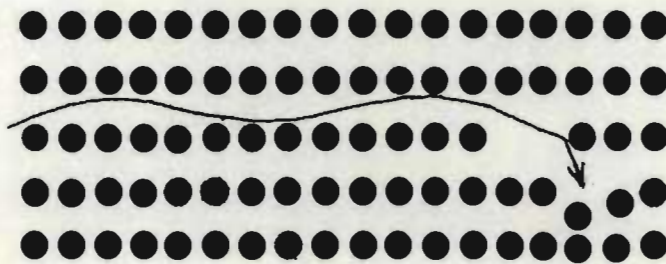


Figure (2.3)

Schematic representation of a channelled trajectory showing dechannelling at a lattice defect.

For each channel one can define a critical channelling energy  $E_{ch}$  below which channelling is unlikely to occur. Thompson (1969) gives as an order of magnitude  $E_{ch} \sim 300$  eV for copper. The rate of damage due to channelling is dose dependent since as time passes the channels become blocked resulting in a reduction in channelling.

From low temperature damage experiments and from computer simulations Robinson (1973) has shown that in the case of neutron irradiation both blocking and dechannelling play a very small role.

#### 2.2.4 Point defects and diffusion

As explained above, if a particle incident on a solid displaces the primary knock-on atom and transfers sufficient energy to it, it will produce secondary, tertiary and further groups of displacements. In the limit of this effect, the cascade produced may be considered to produce complete disarrangement of a lattice volume which Brinkman (1954) defined as a displacement spike (Figure 2.1).

This volume around a collision cascade has been modified in concept in recent times due to concepts such as focusing and channelling and is now called a 'depleted zone'. This term arises due to the fact that these zones contain a relative excess of vacancies - the local vacancy concentration at the centre of a cascade may be as high as 10%.

There are two other 'spike' phenomena which are of importance. After a collision cascade subsides there is a local heating effect known as a thermal spike. Also, in light elements, moving atoms lose considerable amounts of their kinetic energy to the electrons of the solid, resulting in a cylindrical volume of excited electrons along the track of the moving atom. Seitz and Koehler (1965) called these energetic electrons an ionization spike.

The next problem is to follow the events occurring after the collision cascade has taken place, leaving behind its debris of lattice defects. These defects are primarily vacancies and interstitials. To experimentally study the sequence of events at this point it is necessary first to prevent thermal migration of the point defects and thus a method used is to maintain the specimen at a low temperature during irradiation, and then to allow it to progressively warm up after irradiation while studying the point defect motion by various methods.

As a criterion to decide the irradiation temperature ( $T$ ) one requires, so that no jumps are made by any point defect during the irradiation  $t$ , we consider the jump rate given by Thompson (1969):

$$\text{Jump rate} = \nu \exp (- U_m/kT) \quad (2.3)$$

where  $U_m$  is the migration energy of the point defect.

$\nu$  is the oscillation frequency of the defect, and

$k$  is Boltzman's constant =  $0,86 \times 10^{-4} \text{ eV} \cdot ^\circ\text{C}^{-1}$

Then the average time per jump is:

$$t^* = 1/(\nu \exp (- U_m/kT)) \quad (2.4)$$

We must have  $t \ll t^*$  and thus we write (2.4) as:

$$T \ll \frac{U_m}{k \log \nu t} \quad (2.5)$$

If we consider a lowest possible activation energy for interstitials in copper of  $U_m^i \sim 0,1 \text{ eV}$  and  $t = 10^6 \text{ s}$  and  $\nu = 10^{13} \text{ s}^{-1}$  we get that  $T \ll 20^\circ\text{K}$ .

After an irradiation carried out at a temperature defined by (2.5) a much used method of examination is to progressively raise the temperature of the specimen and to measure the recovery of its electrical resistivity as a function of temperature. This is an index of the presence of point defects. A schematic curve showing the annealing stages for the isochronal annealing of resistivity in a copper specimen is shown in Figure 2.4. This curve is very simplified and the complete

picture is considerably more complex than this - for example exhaustive studies have shown that Stage I actually contains five substages, designated Ia  $\rightarrow$  Ie.

Low temperature experiments such as these are the means by which the formation and migration energies of point defects are determined. In metals interstitials have a higher formation energy than do vacancies, but require less energy for migration. Thus in a progressive warm-up interstitials will migrate first. In copper interstitials are mobile at temperatures  $> \sim 50^\circ\text{K}$  (Corbett, Smith and Walker (1959a,b)) and vacancies become mobile at temperatures in the order of  $300^\circ\text{K}$  (Thompson (1969)).

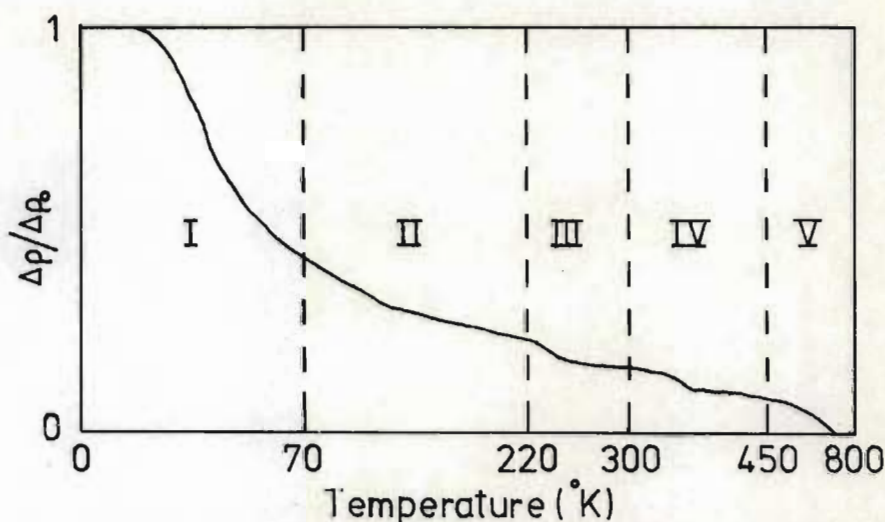


Figure (2.4) Schematic curve for the isochronal annealing of resistivity in copper (From HOLMES (1964)).

The migration energies of point defects are a function of temperature (Table 2.1) and there is currently still disagreement as to precise values. Additional complicating factors are that more complex defects such as divacancies, trivacancies and other groupings exist and the measured activation energy is an effective energy for all the vacancy

TABLE 2.1  
MIGRATION AND FORMATION ENERGIES OF POINT DEFECTS  
(IN COPPER)

from Bourassa and Lengler (1976)  
Walker (1962)  
Thompson (1969)

Vacancy formation energy	1,27 ± 0,05	
Divacancy formation energy	2,39	
Interstitial formation energy	3,9 ± 0,5	Dumb-bell
	4,7 ± 0,1	Crowdion
Vacancy migration energy	0,74 ± 0,08	~ 0°C Stage III
Vacancy migration energy	0,05 → 0,12	< 70°C Stage I
Interstitial migration energy	0,05	Dumb-bell
Interstitial migration energy	0,25	Crowdion

defects migrating in any stage. Bourassa and Lengler (1976) discuss two relatively high temperature recovery stages in copper, one at around 0°C and the other above 200°C. These authors state that single vacancies migrate in the first recovery stage (~0°C) and that they form divacancies and higher vacancy clusters. They conclude that these vacancies partially disappear at sinks and partially from stable clusters but that all of these clusters anneal above 200°C. Thus when considering the radiation damage resulting in a specimen at temperatures above cryogenic temperatures it is important to consider point defect migration, and thus diffusion is briefly treated below.

Neglecting any crystal lattice effects, the diffusion of point defects through a solid is governed by Fick's Laws of Diffusion. The first equation (2.6) merely expresses the fact that diffusion is a random-walk process, in which a net flux from regions of high concentration to regions of lower concentration occurs simply because there are more point defects in the region of high concentration. Thus the flux  $\phi$  is proportional to the gradient of the concentration C.

$$\vec{\phi} = - D \nabla C \quad (2.6)$$

where D is the diffusion coefficient.

The second equation (2.7) shows that the rate of change of the concentration of point defects is given by:

$$\frac{\partial C}{\partial t} = - D \nabla^2 C \quad (2.7)$$

Lattice effects however do play a part in diffusion and the earliest experimental evidence of the acceleration of diffusion by lattice imperfections (termed short-circuit diffusion) came from direct comparisons of diffusion in single crystals and polycrystals (e.g.

Hevesy and Obrutsheva (1925) in lead). Matano (1934), studying diffusion in copper, found that at a temperature of 500°C the diffusion coefficient of an annealed sample was about one quarter of that of a non-annealed sample, whereas at a much lower temperature the two samples had nearly the same value.

The term 'radiation-enhanced diffusion' is used for ordinary diffusion mechanisms which are enhanced by higher-than-equilibrium concentrations of point defects. Recently another type of migration has been studied called 'radiation-induced diffusion' (Urban and Seeger (1974)) in which vacancies and interstitials carry out an athermal radiation-induced long range migration during irradiation.

If during migration two unlike point defects meet then annihilation will usually result. If they are alike they may tend to aggregate and clusters of point defects may form. Point defects may also be attracted to defects that were present before irradiation, such as dislocations. They may also escape to the surface of the crystal.

## 2.3 INTERACTIONS OF POINT DEFECTS

### 2.3.1 Nucleation of point defect clusters

An appreciable amount of direct recombination of the vacancies and interstitial atoms occurs during the dispersal of each collision cascade. Beeler (1966) and Doran (1970) have carried out computer simulated anneals of cascades in  $\alpha$ -Fe and Doran estimates that between 50% and 80% of point defects recombine, the precise value depending on temperature. The model used in these calculations however did not allow for the enhanced spread of interstitial atoms due to lattice effects such as focusing and channelling.

Foreman (1974) has shown that vacancy-interstitial recombination is almost temperature independent within the actual collision cascade itself. Some small variation with temperature arises due to the temperature dependence of the number of sites from which an interstitial atom can annihilate a vacancy by a single jump, and vice versa. The amount of recombination depends on the size, shape and density of the cascade as well as on the efficiency of transport of interstitials away from the site of the cascade. Foreman (1974) shows that recombination approaches 100% for very dense cascades but never reaches 100% since the effect of dynamic crowdions becomes a dominant factor in allowing interstitial atoms to escape from very dense cascades.

The point defects themselves can form various configurations such as the divacancy, trivacancy, the dumbbell or  $\langle 100 \rangle$  type interstitial and the crowdion or  $\langle 110 \rangle$  type interstitial (Figure 2.5) and under thermally induced or radiation induced diffusion can migrate together to form larger clusters of point defects such as the 'black dot' defects observed in irradiated materials in the electron microscope. These black dot defects are small clusters of point defects which appear as unresolved black dots in the electron microscope. Most of these black dots are in fact small dislocation loops, too small to be resolved as loops (Section 4.3).

Point defect clusters may be nucleated in a number of ways. Firstly there are the pre-existing lattice defects which can act as nuclei on which point defects can condense. Alternatively the nuclei might be formed in the spike region at the site of a collision cascade. Thus the density of this type of cluster nucleus should be a function of the fluence of irradiating particle. In addition there is homogeneous nucleation in which clusters form as a result of two or more point defects

meeting during their migration and forming a nucleus for further condensation. This process should be a function of the irradiation temperature.

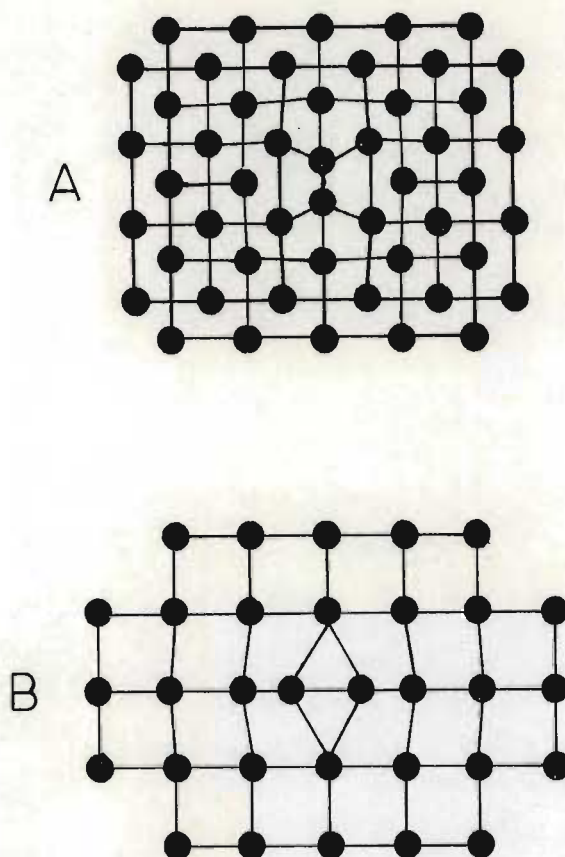


Figure 2.5(A) The  $\langle 100 \rangle$  dumb-bell interstitial Configuration.

(B) The  $\langle 110 \rangle$  Crowdion interstitial Configuration.

A migrating point defect meeting a point defect of the other kind will in most cases result in annihilation and thus mutual recombination will be a function of defect mobility and thus of irradiation temperature. The growth of any cluster is therefore the

outcome of a competition between recombination, and the migration of a particular point defect type to a growing cluster. A cluster can also shrink by the same process - that is if the defect type arriving at the cluster causes recombination within the cluster itself.

Also, the surrounding strain field of a cluster changes as it changes size. It is quite possible that once a certain concentration of clusters is reached it will be impossible for new ones to nucleate due to the long range attractive forces from their larger neighbours and from other crystal defects. This possible maximum number of clusters will depend on the mobility of the point defects themselves and hence on irradiation temperature.

When a small number  $n$  of point defects (e.g. vacancies) group together they will form a spherical void of volume approximately  $n\Omega$  where  $\Omega$  is the atomic volume. Thompson (1969) shows that this is favourable for a small  $n$  and that the formation energy of such a small sphere is:

$$U_f^{\text{sphere}} = (6 \sqrt{\pi n \Omega})^{2/3} \gamma \quad (2.8)$$

where  $\gamma$  is the surface energy per unit area.

If for a large  $n$  the vacancies formed a disc shape as in Figure 2.6A then again a sphere has a lower formation energy since the disc has a larger surface area. But if the disc shaped void collapses in its central region to reunite the exposed surfaces (Figure 2.6B) it releases a large amount of surface energy and results in a dislocation loop being formed. In this process the surface energy has been converted to strain energy.

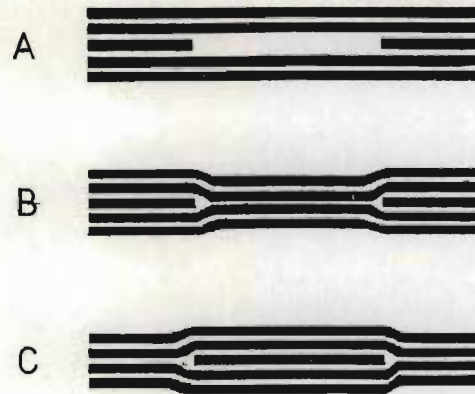


Figure (2.6)

- (A) Disc shaped void
- (B) Vacancy loop
- (C) Interstitial loop

The formation energy of a loop is (Thompson (1969)):

$$U_f^{\text{loop}} \sim 2\sqrt{n\pi} \Omega^{1/3} \mu b^2 \quad (2.9)$$

where  $\mu$  is the shear modulus of elasticity and  $b$  is the Burgers vector which gives  $\mu b^2$  as the formation energy per unit length of dislocation line.

Comparing the loop with the sphere gives:

$$\frac{U_f^{\text{loop}}}{U_f^{\text{sphere}}} = \frac{\mu b^2}{\gamma} \cdot \frac{2\pi^{1/6}}{6^{2/3} n^{1/6} \Omega^{1/3}} \quad (2.10)$$

showing that when the sphere reaches a critical size (i.e. large enough  $n$ ) then collapse to a loop becomes energetically favourable.

Spherical clusters of interstitials cannot form since this would require an excessively large strain energy in the surrounding matrix. However a plate of atoms (Figure 2.6C) may condense to form an interstitial loop which has the same appearance as a vacancy loop in the electron microscope.

When a sphere of vacancies collapses to a loop the opposite sides of the loop need not join together in a perfecting stacking sequence. The loop will then enclose an area of stacking fault, and a faulted loop results. In an F.C.C. lattice this fault can be removed by shearing in the  $\{111\}$  plane by a vector  $\frac{1}{6}a \langle 11\bar{2} \rangle$ . The reaction is:

$$\frac{1}{3}a \langle 111 \rangle + \frac{1}{6}a \langle 11\bar{2} \rangle \rightarrow \frac{1}{2}a \langle 110 \rangle$$

Similarly in the case of an interstitial loop which is faulted the fault can be removed by sweeping the extra plate of atoms by two partial dislocations of the type  $\frac{1}{6}a \{121\}$ , one above and one below the plate. This reaction is:

$$\frac{1}{3}a \langle 111 \rangle + \frac{1}{6}a \langle 2\bar{1}\bar{1} \rangle + \frac{1}{6}a \langle \bar{1}2\bar{1} \rangle \rightarrow \frac{1}{2}a \langle 110 \rangle$$

A group of vacancies can also form a stacking fault tetrahedron (S.F.T.) in which the vacancies are converted into planes of stacking fault on the four  $\{111\}$  planes with their edges along the six  $\{110\}$  axes. It is likely that an S.F.T. may grow in tetrahedral form from a very small size by a mechanism involving jog lines on the faces of the tetrahedron (Silcox and Hirsch(1959a)) but one can consider the growth to proceed from a triangular sessile loop of vacancies on a  $\{111\}$  plane. This

loop has its sides along  $\langle 110 \rangle$  directions and collapses to form a stacking fault enclosed by a loop of  $\vec{b} = \frac{1}{3}\mathbf{a} \langle 111 \rangle$ . The loop throws off a partial dislocation of the type  $\frac{1}{6}\mathbf{a} \langle 121 \rangle$  onto each of the upright faces of the tetrahedron, leaving a dislocation of the type  $\frac{1}{6}\mathbf{a} \langle 110 \rangle$  on the base according to:

$$\frac{1}{3}\mathbf{a} \langle 111 \rangle \rightarrow \frac{1}{6}\mathbf{a} \langle 101 \rangle + \frac{1}{6}\mathbf{a} \langle 121 \rangle$$

The partials eventually meet one another and form dislocations of the same type,  $\frac{1}{6}\mathbf{a} \langle 110 \rangle$

i.e. 
$$\frac{1}{6}\mathbf{a} \langle 121 \rangle + \frac{1}{6}\mathbf{a} \langle \bar{1}\bar{1}\bar{2} \rangle \rightarrow \frac{1}{6}\mathbf{a} \langle 01\bar{1} \rangle$$

and thus the whole tetrahedron is constructed of  $\frac{1}{6}\mathbf{a} \langle 110 \rangle$  type dislocations.

There is good evidence that the  $\frac{a}{3} \langle 111 \rangle$  dislocations bounding small Frank loops in copper and silver undergo dissociation into  $\frac{a}{2} \langle 112 \rangle$  Shockley partials and  $\frac{a}{6} \langle 110 \rangle$  stair rod dislocations (Haussermann (1972), Wilson (1971), Jenkins (1974)). A stacking fault tetrahedron then forms by the Silcox-Hirsch mechanism (Silcox and Hirsch(1959a)).

If a small sphere of vacancies continues to grow as a sphere and does not collapse to a loop, a void is formed. This has been found to occur if helium or hydrogen gas present in the solid, migrates to the vacancy group. This gas (produced for example in  $(n, \alpha)$  reactions) then stabilizes the void against collapse to a loop. Various void shapes can occur and in F.C.C. metals they are often bounded by  $\{100\}$  and  $\{111\}$  planes (Norris (1971)).

### 2.3.2 Interaction of point defects with dislocations

A point defect in a crystal lattice distorts the lattice in its immediate vicinity producing a stress field. An interstitial atom causes its neighbouring atoms to be pushed outwards, while the neighbouring atoms to a vacancy fall inwards. Heald (1974) shows these misfits to be:

$$\frac{\Delta V_I}{\Omega} = 1,10 \quad (2.11)$$

$$\frac{\Delta V_V}{\Omega} = -0,45$$

where  $V_I$  = volume occupied by an interstitial

$V_V$  = volume occupied by a vacancy

and  $\Omega$  = atomic volume.

The distortions of the crystal lattice around a point defect and around dislocations cause an interaction between their respective stress fields. Thus the point defect will experience a force which attracts it to the region where it can relieve the most stress. As a result atmospheres of point defects may collect around dislocations.

There is an intimate relation between the climb of dislocations and the generation or absorption of point defects. The formation or disappearance of a vacancy on the edge of a straight dislocation requires the creation of a pair of jogs while the absorption of a vacancy at a jog merely moves the jog by one lattice spacing and does not alter the energy of the jog. The climb of an edge dislocation by one lattice spacing corresponds to the generation or absorption of an entire

line of point defects. It is usually assumed that the growth sites of dislocations are jogs where point defects may be most easily created or destroyed (Mott (1951), Weertman (1955,1957), Lothe (1960), Thomson and Balluffi (1962a,b), Friedel (1964), Seidman and Balluffi (1967)). Climb is caused by the diffusion of point defects into or out of the jogs as they propagate along the dislocation and thus the rate at which jogs absorb or emit point defects as well as the number of jogs present then determines the dislocation climb rate. The detailed configurations and energies of jogs are largely unknown but Seeger (1955a,b) pointed out that in metals of low stacking fault energy, such as silver, the energy of a jog would be high and that the activation energy for dislocation climb would be much higher than in a metal of high stacking fault energy such as aluminium.

The determination of point defect diffusion fluxes to or from the jogs poses problems, and in addition, diffusion may occur either through the bulk or along the dislocation core which acts as a fast diffusion pipe ((Turnbull and Hoffman (1954), Love and Shewman (1963), Love (1964))). Differences in the climb rate may be anticipated depending on how fast the defects diffuse along the dislocation cores. However, it is not known whether the fast diffusing defects are primarily vacancies or interstitials or a combination of both. The highest possible climb rate is achieved when the kinetic processes at the dislocation core are fast enough to maintain the point defects which diffuse to or from the dislocation, at near their equilibrium concentration in the vicinity of the entire core length. The climb rate is then controlled by the rate of diffusion of defects through the lattice to or from the dislocation and is thus diffusion limited. Achievement of this condition is aided by a high jog density and/or fast diffusion of the point defects along the core. At other times, the rate of production and destruction of point defects controls the climb rate which is then production limited.

Hirsch (1962) has studied more complex dissociated jogs in which the dislocations dissociate to form, for example, a sessile extended jog or a glissile extended jog. The most striking result of Hirsch's analysis concerns the effect of an applied stress on the mobility of a jog. In general, a given applied stress will move the dislocation in a definite direction but if the jog is sessile it will be joined to the new line of the dislocation by a row of vacancies or in the case of a long jog, by a dipole (Figure 8.9) formed by two edge dislocations of opposite sign. The jog is referred to as a vacancy producing jog or an interstitial producing jog.

A pure screw dislocation cannot climb but becomes a spiral when point defects condense onto it. By receiving interstitial atoms or giving off vacancies, a right-handed screw dislocation becomes a left-handed helix (and conversely) (Frank (1957)). If segment AB of the helix in Figure (2.7) glides towards the helix then a procession of dislocation loops is formed.

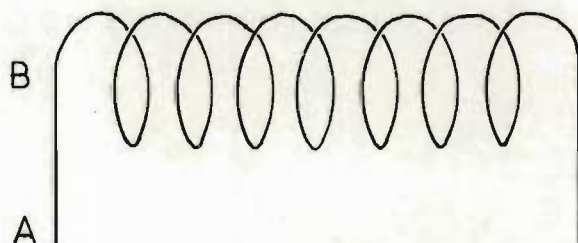


Figure (2.7) A dislocation helix

From Nabarro (1967)

It is clear that large numbers of point defects diffusing to dislocations will result in an increase of dislocation density i.e. an increase in the length of dislocation line within the sample. This is particularly important in the case of radiation damage where there

is a continuous production of large numbers of point defects far in excess of the thermal equilibrium concentration.

An important asymmetry in the interactions between point defects and dislocations is that of the two types of point defect, interstitials are preferentially attracted to dislocations. It has been observed that in aluminium (Risbet (1974)) and magnesium (Levy (1974)) voids nucleate preferentially in the vicinity of dislocations with an edge component. In addition this observation is corroborated by the fact that there is good correlation between void number and dislocation density (Levy (1974), Norris (1972)). Furthermore electron irradiation experiments (Norris (1971)) indicate that the growth rate of an individual void depends on its distance from a dislocation.

The dislocation-point defect interaction is stronger in the case of self interstitials because of their much larger associated misfit strains, and thus dislocations are poor vacancy sinks and would rather expel vacancies than receive them. The fact that voids appear near dislocations is good evidence that edge dislocations do act as biased sinks absorbing interstitials preferentially to vacancies and furthermore implies the existence of a vacancy concentration peak in the vicinity of the dislocation.

Considering dislocation loops, the rate equations which define the rate of growth of vacancy and interstitial loops during irradiation are (Eyre and English (1974)):

$$\begin{aligned} \frac{dr_L}{dt} \frac{1}{V.L} &= \frac{1}{b} \left[ D_v C_v - Z_i D_i C_i - D_s \exp \left( \frac{(F_{el} + \gamma_{sf})}{kT} \right) b^2 \right] \\ \frac{dr_L}{dt} \frac{1}{I.L} &= \frac{1}{b} \left[ Z_i D_i C_i - D_v C_v + D_s \exp - \left( \frac{(F_{el} + \gamma_{sf})}{kT} \right) b^2 \right] \end{aligned} \quad (2.12)$$

where  $C_v$  and  $C_i$  are the vacancy and interstitial point defect concentrations.

$D_v$  and  $D_i$  are the diffusivities of the vacancies and interstitials.

$Z_i$  is the parameter representing the preferred attraction of the loops for interstitials and it is suggested from current theory that this value is 1.08 (Bullough *et al.*, (1975))

$D_s$  is the vacancy self diffusion coefficient.

$\gamma_{sf}$  is the stacking fault energy of faulted loops.

$F_{el}$  is the elastic self energy of the loops.

The balance between the fluxes of interstitials and vacancies arriving at the loops is indicated by the first two terms in the square brackets while the third term represents the thermal emission of vacancies from the loops.

When the production rate of single interstitials and vacancies is identical, (2.12) show two important points in regard to the growth or shrinkage of loops. These are that the preferential attraction of loops for interstitials as indicated by  $Z_i$  results in an excess of interstitials arriving at the loops, and also that the thermal emission of vacancies from the loops results in the shrinkage of vacancy loops and in the growth of interstitial loops.

One may conclude that interstitial loops, once formed, are inherently stable and that they have a natural tendency to growth, while even if the nucleation conditions are satisfied for vacancy loops they have a natural tendency to shrink.

It has also been shown (Heald and Speight (1975)) that the dislocation preference for the capture of interstitials is a function of

the irradiation temperature, increasing to a maximum at  $\frac{T}{T_m} \sim 0,3$  ( $T_m$  = melting temperature in  $^{\circ}\text{K}$ ) and then gradually decreasing.

### 2.3.3 Increase in dislocation density induced by radiation

It has been observed by means of electron microscopy that in neutron irradiated metals the dislocation density increases with fluence ((Risbet (1974), Packan (1971), Levy (1974)). On annealing an irradiated metal containing black dot damage the first observable result is usually the formation of resolvable dislocation loops. Both interstitial and vacancy loops are observed in neutron irradiated metals, and in the case of interstitial loops the rate of loop growth increases as a function of temperature; and loop nucleation is influenced by impurities (Section 2.3.4). As a function of irradiation time the interstitial loops grow and interact to form a dislocation network. This interstitial agglomeration is probably the main cause of the increase in dislocation density with irradiation.

As has been shown in the preceding section, vacancy loops are not expected to grow during irradiation, but large vacancy loops have been observed in a number of neutron irradiated metals (Risbet (1974), Levy (1974), Glowinski *et al.*, (1973), Brimall *et al.*, (1971), Evans (1973), Kelly and Blake (1973), Hulett *et al.*, (1968), Risbet and Levy (1975)). Since vacancy loops are biased sinks absorbing interstitials preferentially their presence seems to be a contradiction. However the analysis of neutron irradiated aluminium and aluminium alloys has shown that these large loops are not due to vacancy clustering as a result of migration but are formed by a dipole mechanism involving dislocation climb (Risbet and Levy (1975)). Two different mechanisms producing large vacancy loops have been detected by these authors and these are illustrated in Figure 2.8.

The first mechanism occurs when an edge dislocation absorbing interstitials is pinned during the climb process creating a vacancy dipole, the interaction of the opposite segments of the dipole leading to the formation of a vacancy loop (Figure 2.8A).

The second mechanism (Figure 2.8B) involves the interaction of a climbing edge dislocation with an interstitial loop which itself may or may not be growing. Both the interstitial loop involved and the dislocation must have the same Burgers vector.

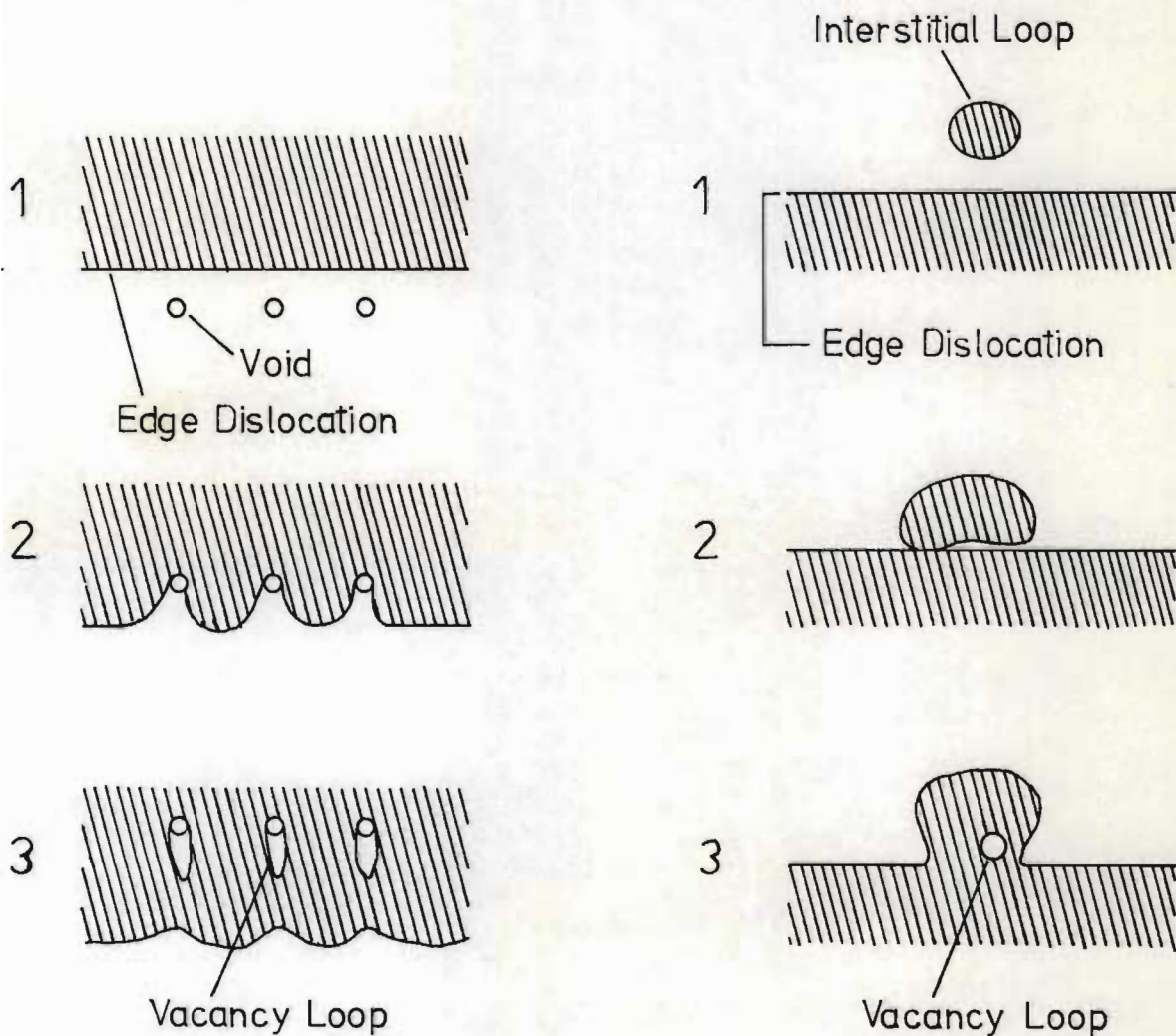
#### 2.3.4 Impurity effects

Irradiations at low temperatures have indicated the impurities have two main effects on the clustering and survival of defects during irradiation.

Firstly there is evidence that interstitials interact directly with impurities. This affects their mobility and the scale on which interstitial loops are nucleated. Shimomura (1969) found that in electron irradiated gold the number of visible loops increased by more than an order of magnitude on going from 99,9999% to 99,999% pure metal (Figure 2.9).

Secondly, there is evidence that impurities may influence vacancy survival in the displacement cascades (English *et al.*, (1975)). These results show that in a pure metal, such as copper, there is a much greater defect yield and efficiency of vacancy survival than in a complex alloy such as stainless steel. In the case of swelling as a result of void formation the general rule is that the purer the metal the greater the swelling.

Formation of Large Vacancy Loops



Mechanism (A)

The debris mechanism for vacancy loop formation

Mechanism (B)

A climbing edge dislocation interacting with an interstitial loop of the same Burgers vector.

(after RISBET and LEVY (1975))

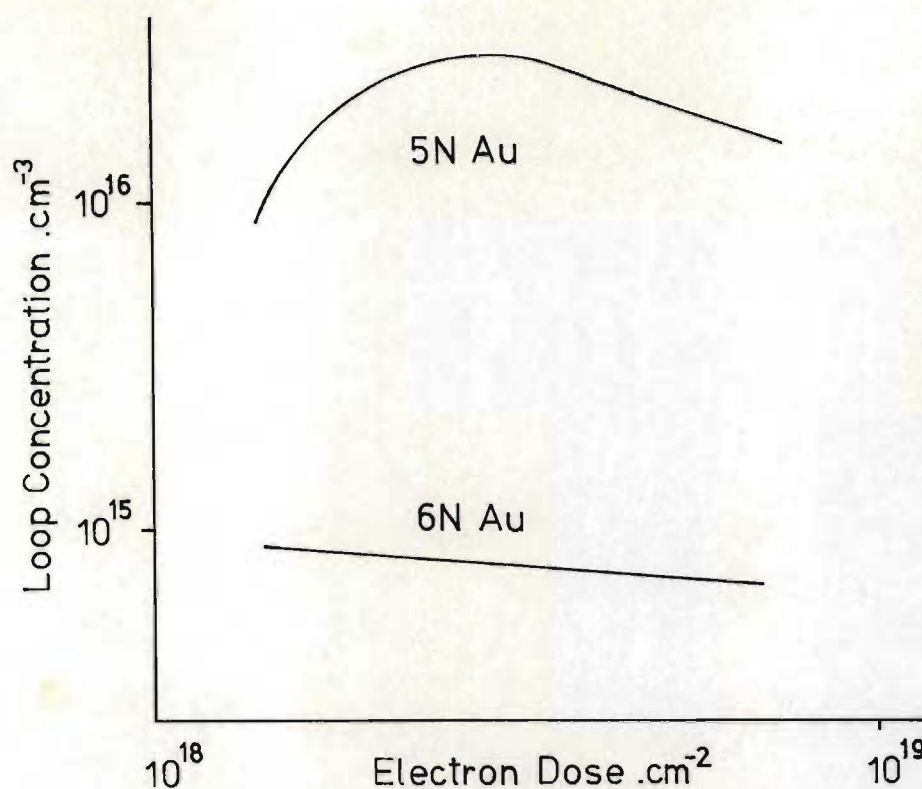


Figure (2.9) The number of loops nucleated as a function of specimen purity - results of SHIMOMURA (1969)

Some experiments in copper (Labbe and Poirier (1973), Wolfenden (1972)) and in aluminium (Risbet (1974)) suggest that it is the type of impurity which must be considered rather than the total quantity. More specifically it can be argued that the strain fields associated with solute atoms are responsible for defocusing focused collision sequences thus depositing interstitials closer to the cascade centres and thus increasing their probability of recombination with vacancies.

### 2.3.5 Effect of irradiation temperature on point defect trapping

It is important to determine whether irradiation at a low temperature followed by an anneal at a higher temperature  $T$  produces the same result as an irradiation at temperature  $T$ . Any process that is favoured by a high ambient concentration of defects, such as point defect clustering, will operate more efficiently in the sample which is first irradiated at the low temperature and then warmed up, because this process enables a large concentration of point defects to become mobile suddenly.

It will now be shown (Thompson (1969)) that the process of point defect trapping is also different in the two cases. Consider an irradiation at a temperature high enough for the interstitials to be mobile. The crystal is assumed infinite with an initial concentration  $C_{st}$  of saturable trapping sites. Clustering of point defects will be neglected.

As the irradiation proceeds the concentration of trapped interstitials  $C_{sti}$  will increase and the number of free trapping sites will decrease to  $(C_{st} - C_{sti})$ . In this model, either the interstitial is trapped or it suffers annihilation by a vacancy and thus for each trapped interstitial there is one vacancy left, i.e.:

$$C_v = C_{sti} \quad (2.13)$$

As the concentration  $C_d$  of vacancy-interstitial pairs increases by  $dC_d$ , during irradiation, the interstitials have the choice of migrating to  $C_v$  vacancies or  $(C_{st} - C_{sti})$  unfilled traps. Assuming that the vacancy and trap are surrounded by strain fields of equal attraction it follows that the proportion of interstitials migrating

to traps is:

$$\left( \frac{C_{st} - C_{sti}}{C_{st} - C_{sti} + C_v} \right) \quad (2.14)$$

From (2.13) this is:

$$\left( 1 - \frac{C_{sti}}{C_{st}} \right) \quad (2.15)$$

and thus the increase in trapped interstitials  $dC_{sti}$  is:

$$dC_{sti} = \left( 1 - \frac{C_{sti}}{C_{st}} \right) dC_d \quad (2.16)$$

and the increase in free vacancies  $dC_v$  is:

$$dC_v = \left( 1 - \frac{C_v}{C_{st}} \right) dC_d \quad (2.17)$$

Integrating (2.16) and (2.17) over the infinite crystal we get:

$$C_{sti} = C_{st} \left[ 1 - \exp \left( \frac{-C_d}{C_{st}} \right) \right] \quad (2.18)$$

and

$$C_v = C_{st} \left[ 1 - \exp \left( \frac{-C_d}{C_{st}} \right) \right]$$

Thus the trap concentration governs the saturation process, but for a more realistic model we must take into account that interstitials can condense onto dislocations, causing climb, and the number of such trapping sites is, to a first approximation, unsaturable.

These unsaturable traps (concentration  $C_{ut}$ ) are unaffected by

the concentration  $C_{uti}$  of interstitials that have passed to them. Also the constant concentration of sinks represented by the crystal boundary can be lumped together with  $C_{ut}$ . As  $C_d$  increases by  $dC_d$  in a crystal containing only unsaturable traps the concentration of vacancies is always equal to the concentration of interstitials that have migrated to the traps, e.g.:

$$C_v = C_{uti} \quad (2.19)$$

Using similar arguments to those above:

$$dC_{uti} = \frac{C_{ut} dC_d}{(C_{uti} + C_{ut})} \quad (2.20)$$

which on integration gives:

$$\frac{C_{uti}^2}{2C_{ut}} + C_{uti} = C_d$$

and solving this quadratic in  $C_{uti}$  gives:

$$C_{uti} = \left[ \sqrt{1 + \frac{2C_d}{C_{ut}}} - 1 \right] C_{ut} \quad (2.21)$$

and

$$C_v = \left[ \sqrt{1 + \frac{2C_d}{C_{ut}}} - 1 \right] C_{ut}$$

Thus the presence of unsaturable traps will not produce saturation in the defect concentration but simply a slowing down of damage production rate as a function of dose. This is intuitively reasonable, for as  $C_v$  increases there is an increasing tendency for interstitials to annihilate vacancies rather than to become trapped.

In a crystal containing both saturable and unsaturable traps

Thompson (1969) shows that the defect concentration increases according to:

$$C_{uti} = \left[ \left( \frac{1 + 2C_{ut} C_d}{(C_{ut} + C_{st})^2} \right)^{\frac{1}{2}} - 1 \right] (C_{ut} + C_{st}) \quad (2.22)$$

$$C_{sti} = C_{st} \left[ 1 - \exp \left( \frac{-C_{uti}}{C_{ut}} \right) \right]$$

and

$$C_v = C_{uti} + C_{sti}$$

Following Thompson's argument further and considering an infinite crystal with saturable traps only we consider an irradiation at a low temperature followed by an anneal at a higher temperature. The starting condition (ignoring any grown-in vacancy concentration) would be a concentration  $C_d$  of interstitials confronted with the choice between  $C_d$  vacancies and  $C_{st}$  saturable traps. When the concentration  $C_i$  of interstitials falls by  $dC_i$  the choice facing the migrating interstitials is between  $(C_{st} - C_{sti})$  unfilled traps and  $C_v$  vacancies and thus the concentration going to traps is:

$$dC_{sti} = \frac{-(C_{st} - C_{sti})}{(C_{st} - C_{sti} + C_v)} dC_i \quad (2.23)$$

but the total number of interstitials trapped and remaining free equals the number of vacancies, i.e.

$$C_v = C_i + C_{sti} \quad (2.24)$$

then it follows that:

$$\int_0^{C_{sti}} \frac{dC_{sti}}{C_{st} - C_{sti}} = \int_0^{C_i} \frac{dC_i}{C_{st} + C_i}$$

which gives:

$$C_{sti} = \frac{C_d C_{st}}{C_{st} + C_d} \quad (2.25)$$

and

$$C_v = \frac{C_d C_{st}}{C_{st} + C_d}$$

The ratio of (2.18) to (2.25) is:

$$\left(1 + \frac{C_{st}}{C_d}\right) \left[1 - \exp\left(\frac{-C_d}{C_{st}}\right)\right] \quad (2.26)$$

For the case of either small  $C_d$  or large  $C_d$  this ratio tends to unity but is greater than one for all intermediate values of  $C_d$ . Thus in the case of a low temperature irradiation followed by an anneal to a higher temperature the concentrations  $C_{sti}$  and  $C_v$  are larger than in the case of irradiation at a higher temperature. It is thus clear that to study high temperature irradiation effects irradiations must be carried out at the temperature of interest and that simulated conditions involving annealing do not produce the same effects.

#### 2.3.6 Relation between irradiation temperature and flux

The rate of production of defects is proportional to the radiation flux  $\phi$  while the rate of removal of defects is proportional to

$$\exp\left(\frac{-U_m}{kT}\right)$$

where  $U_m$  is the migration energy of the defect concerned (From (2.3)). If in different irradiations using the same incident particles with similar energies the ratio between these two rates is the same then damage should accumulate in the same form. Thus as shown by Thompson (1969),

for irradiations to produce the same effect at temperatures  $T_1$  and  $T_2$  and with specimens receiving the same total dose  $\phi_1 t_1 = \phi_2 t_2$  we require:

$$\phi_1 \exp\left(-\frac{U_m}{kT_1}\right) = \phi_2 \exp\left(-\frac{U_m}{kT_2}\right)$$

or

$$T_1 = \left[ \frac{1}{T_2} - \frac{k}{U_m} \log \frac{\phi_1}{\phi_2} \right]^{-1} \quad (2.27)$$

Thus irradiations involving the same particles and energies should be equivalent for temperatures  $T_1$  and  $T_2$  satisfying (2.27). It must be noted that (2.27) can only be applied where only one defect type with a single value of  $U_m$  is migrating during irradiation. In practice this condition is not met. However (2.27) can be used as a first approximation to relate the irradiation effect observed in a materials testing reactor to the expected effect in a reactor under design.

## 2.4 FAST NEUTRON IRRADIATION

The effects described in this chapter may arise from defects produced by any type of nuclear irradiation. In nuclear reactors however, neutrons produce the vast majority of displaced atoms in metals, and only in insulators can the ionizing radiations compete. We now briefly consider fast neutrons since this thesis is concerned with the study of a metal irradiated with radiation from a nuclear reactor.

Neutrons with energies above 100 eV are generally able to produce damage by direct collision. The resulting energy spectrum of the primary recoil atoms is wide, extending up to  $10^5$  eV or more. Since thermal neutrons have insufficient energy to displace atoms in direct

collision, their contribution to the damage must be through nuclear reactions. An investigation of the possibilities shows that  $(n,\gamma)$  reactions predominate. Also, a nucleus may absorb a thermal neutron and become excited after which it will decay, emitting a number of energetic  $\gamma$ -rays. The recoil energy which is of the order of 100 eV is then transmitted to the entire atom so that typically between one and three vacancy-interstitial pairs are produced.

The mean free path between collisions in the case of fast neutrons is of the order of a few centimetres and thus the damage is uniformly produced, even in large samples.

### CHAPTER THREE

#### REVIEW OF PREVIOUS EXPERIMENTAL RESULTS

- 3.1 Introduction
- 3.2 The damage morphology at different temperatures
  - 3.2.1 Irradiations at low temperatures
  - 3.2.2 Irradiations at ambient temperatures
  - 3.2.3 Irradiations at high temperatures
- 3.3 Conclusions

### 3.1 INTRODUCTION

In this chapter we consider experimental studies which are relevant to the present investigation. These have been carried out by bombarding metals with:

1. neutrons (mainly of fission energies)
2. electrons (usually between 200 KeV and 1 MeV)
3. ions (including heavy fission fragments, deuterons, protons, etc.)

Metals of F.C.C. structure which have been extensively studied include copper, aluminium, silver, platinum and nickel, while of the metals of B.C.C. structure molybdenum and various stainless steels have been extensively examined. A large range of particle fluences has been used ranging from short irradiation times to those times which produce the large fluences which are expected to occur in the cores of Fast Breeder Reactors and Fusion Reactors of the future. Fluences up to  $6 \times 10^{22}$  f.n.  $\text{cm}^{-2}$  have been used in some experiments.

The damage structures which are observed in irradiated materials are a direct result of point defect mobility which in turn is a function of temperature, and thus it is appropriate to relate irradiation and examination temperatures to the ranges over which the principal annealing stages occur. (Figure 2.4).

These can be divided into three basic ranges:

1. Temperatures at which the vacancies and interstitials are immobile, i.e.  $T < \text{Stage } I_E$ .
2. Temperatures at which the interstitials but not the vacancies are mobile, i.e.  $\text{Stage } I_E < T < \text{Stage III}$ .
3. Temperatures at which interstitials and vacancies are possibly both mobile, i.e.  $T > \text{Stage III}$ .

Table 3.1 shows the approximate temperatures at which the annealing stages occur for pure copper.

Radiation damage has historically been studied in three main temperature ranges:

1. The cryogenic range below  $0^{\circ}\text{C}$ .
2. The ambient reactor temperature range between approximately  $0^{\circ}\text{C}$  and  $100^{\circ}\text{C}$ .
3. The high temperature range above about  $100^{\circ}\text{C}$ .

To carry out experiments in the first temperature range one needs a sophisticated cooling rig (e.g. Isebeck (1972)) since all measurements have to be carried out at the low temperature, and thus electron microscopy cannot be used since specimens would have to be warmed to room temperature for study. The second temperature range, which was the first to be investigated in any depth, is essentially the working range of a normal fission nuclear reactor and the extremities of this range are easily reached experimentally without very sophisticated irradiation rigs. For the third temperature range one needs a heating rig. In many instances post-irradiation anneals have been included in the experimental process to assist in the identification of radiation damage morphologies and structures.

### 3.2 THE DAMAGE MORPHOLOGY AT DIFFERENT TEMPERATURES

#### 3.2.1 Irradiations at low temperatures

Irradiation experiments in the cryogenic range are primarily concerned with understanding the fundamental damage processes which occur during irradiation. At these low temperatures damage events and processes can be 'frozen in time' and thus particular point defect reactions can be studied. The basic idea of low temperature irradiation

TABLE 3.1THE APPROXIMATE TEMPERATURES OF THE RECOVERY  
STAGES IN PURE COPPER

(Stages as shown in Figure 2.4)

from Schilling, Burger, Isebeck and Wenzl  
(1970)

Aspeling (1976)

---

Recovery Stage	Temperature °K
I	0 - 55
II	55 - 220
III	220 - 340
IV	340 - 450
V	450 →

---

experiments is that under suitable experimental conditions it is possible to generate independent vacancies and interstitials and then by a carefully controlled warming-up procedure one can determine the motion of these defects and the reactions between them.

Studies of the fundamental nature and properties of point defects in metals began in the 1940s as a result of an increasing interest in the mechanism of self-diffusion, the generation of point defects during plastic deformation, and then latterly, the defect morphology produced by radiation. The early work of Corbett, Smith and Walker (1959a,b) was of fundamental importance when they demonstrated by the low-temperature electron irradiation of copper that an elementary intrinsic point defect, presumably a self-interstitial, is capable of migrating freely at about 50°K. Further low temperature results will not be reviewed in the present work and for a comprehensive study of experimental results obtained by means of electrical resistivity measurements reference can be made to Schilling *et al.*, (1970).

A study was made by Scheidler *et al.*, (1966) of the defect density and size as a function of irradiation temperature in the range of 4°K to 378°K. These results are discussed in Section 3.2.2.

### 3.2.2 Irradiations at ambient temperatures

In the first paper on neutron radiation damage in copper, Silcox and Hirsch (1959a) were able to identify point defect clusters with diameters larger than 200 Å as perfect dislocation loops with Burgers vector  $\vec{b} = \frac{1}{2} \langle 110 \rangle$ . Further irradiations were carried out by Greenfield and Wilsdorf (1960, 1961) and then in a series of papers by Makin, Whapham and Minter (1961, 1962) and Makin and Manthorpe (1963) which followed, the density and size distribution of the small visible defect clusters in neutron irradiated copper were studied for radiation

doses between  $6 \times 10^{17}$  and  $4 \times 10^{18}$  fast neutrons.cm<sup>-2</sup> ( $E > 1$  MeV). These authors obtained a size distribution function using micrographs taken under kinematical imaging conditions which showed that the smallest defects were in the majority and that the number steadily decreased with increasing defect diameter  $d$ . This distribution function (3.1) was confirmed by Scheidler, Makin, Minter and Schilling (1966) and by Rühle (1967a,b, 1968).

The distribution function is of the form:

$$P(d) = P(o) \exp \left( \frac{-d}{d_o} \right) \quad (3.1)$$

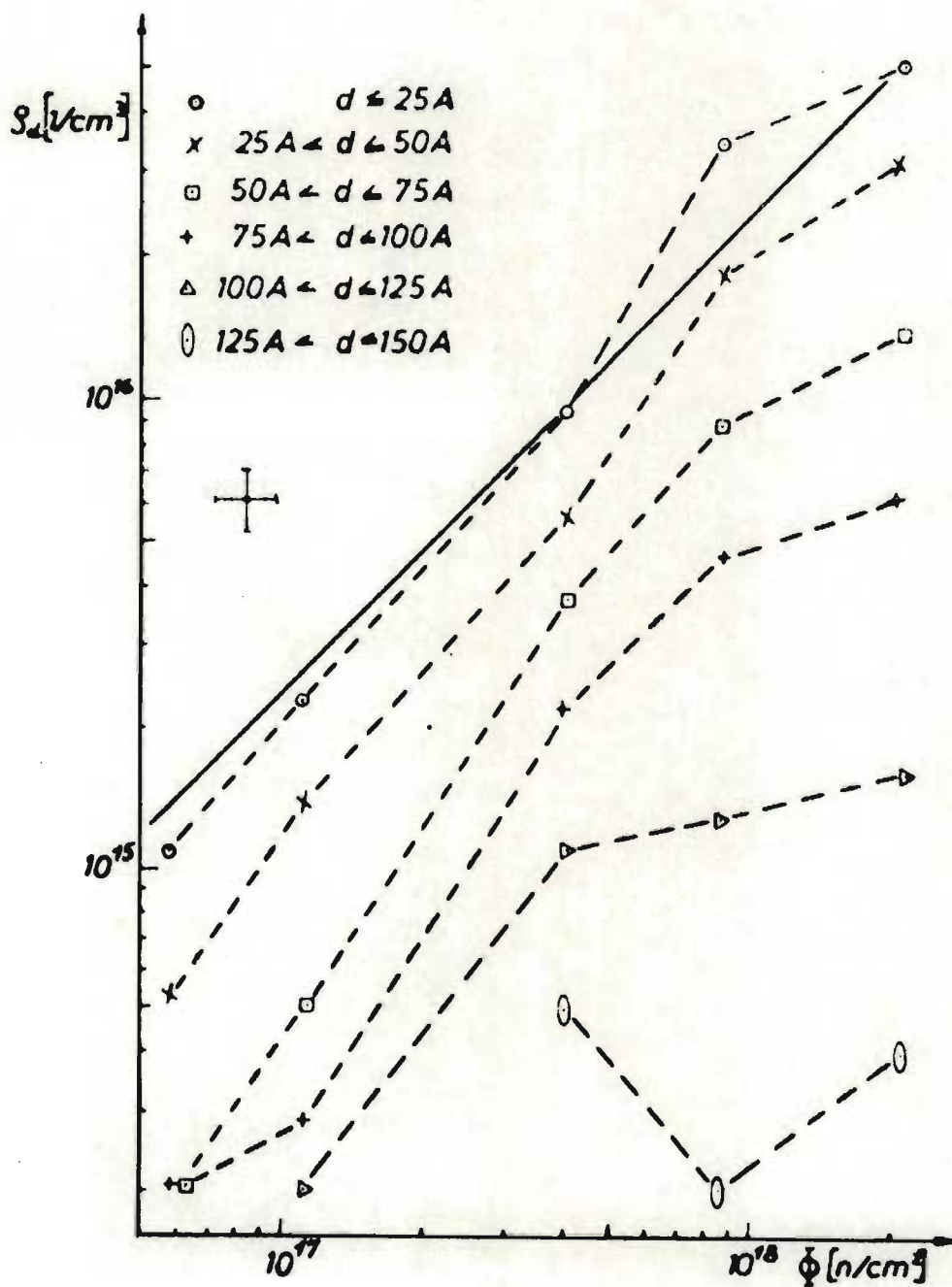
where the parameters  $P(o)$  and  $d_o$  allow for a simple characterization of  $P(d)$ . Both of these groups obtained significantly different values for  $P(o)$  and  $d_o$  although they both agree that  $d_o$ , which is in the order of 25-50 Å, decreases with decreasing irradiation temperature.

For a number of years there was uncertainty as to the specific nature of the small lattice defects and hence the unspecific name 'black dot' damage was used (Pashley and Presland (1961)) until it was determined that the defects were mainly small dislocation loops. The word 'small' means as compared to the extinction length in this context. According to Makin, Whapham and Minter (1962) these small ( $d < 50$  Å) defect clusters obey a relationship between  $\rho_d$ , the volume density, and the radiation dose  $\phi$  which is fairly linear. The doses used were up to  $\phi = 4 \times 10^{18}$  f.n.cm<sup>-2</sup> and it was found that for the larger defects the dose dependence was weaker than linear. Rühle (1967a,b) collected similar data over a large dose range and confirmed these findings. Rühle's results (Figure 3.1) show clearly the linear dose dependence of the small defect clusters and the tendency for saturation for the larger clusters. Rühle's irradiation temperature was 80°C.

Figure 3.1

(From Rühle (1967) )

Loop density per size interval,  $\rho_d$ , in neutron-irradiated copper as a function of the irradiation dose  $\phi$  ( $T_{\text{irr}} = 80^\circ\text{C}$ ). The slope of the full line in the double logarithmic plot represents proportionality between  $\rho_d$  and  $\phi$ . The indicated error marks correspond to a  $\pm 20\%$  uncertainty of both  $\phi$  and  $\rho_d$ .



Scheidler *et al.*, (1966) carried out experiments on the neutron irradiation of copper in the temperature range of 4°K to 378°K. The evidence that they gained from the neutron irradiated bulk copper showed a homogeneous distribution of radiation damage over the temperature range examined. It was also clearly shown that the size of the larger loops increased rapidly with dose. The irradiation temperatures that Scheidler *et al.*, used were above and below the point at which interstitials become mobile but below the point at which vacancies are appreciably mobile. Scheidler *et al.*'s., results show the homogeneous distribution of black dot damage which is a typical result of these sorts of irradiation experiment. Their results clearly indicated that the defect clusters in specimens irradiated at 4°K were smaller than those in specimens irradiated at 293°K, the most obvious difference being the absence of large loops in the specimen irradiated at 4°K.

The results of Scheidler *et al.*, are reproduced in Figures 3.2 and 3.3 in which the density of clusters  $n$  is plotted as a function of their size. In the graphs,  $\log_{10} n$  is plotted against mean diameter  $d$ . Their relationships are linear to within the experimental scatter of the results and thus the authors indicate that their results can be represented by:

$$n = k e^{-bd}$$

where  $k$  and  $b$  are constant.

These authors point out that the comparison of the two lines in Figure 3.3 indicates clearly the effect of the 4°K irradiation as compared to the 293°K irradiation. The density of the 0-25 Å diameter clusters is approximately 2,5 times greater at the low temperature whereas the density of clusters larger than 75-100 Å is reduced at this temperature. However on assuming that all the clusters were

FIG(3.2)

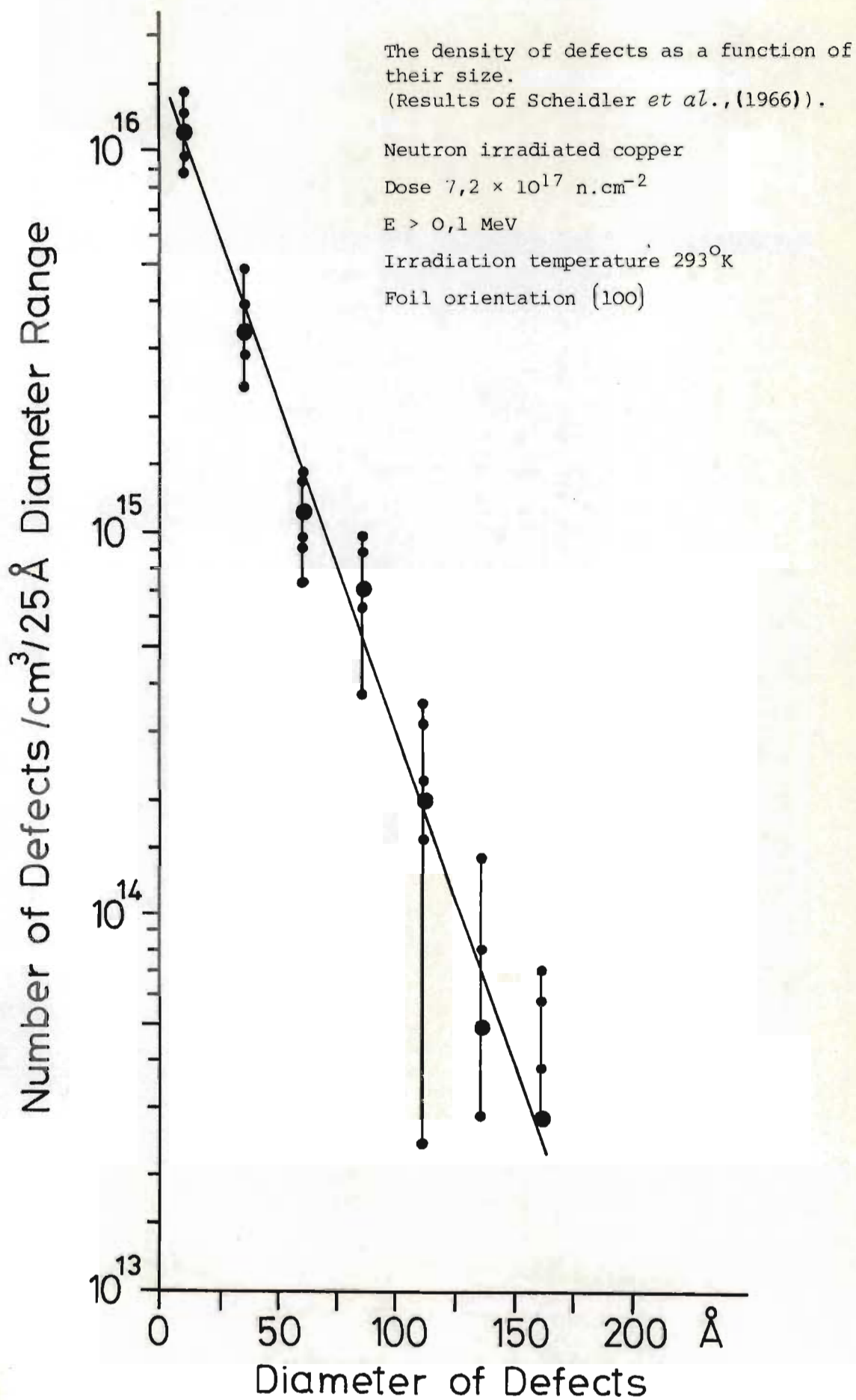
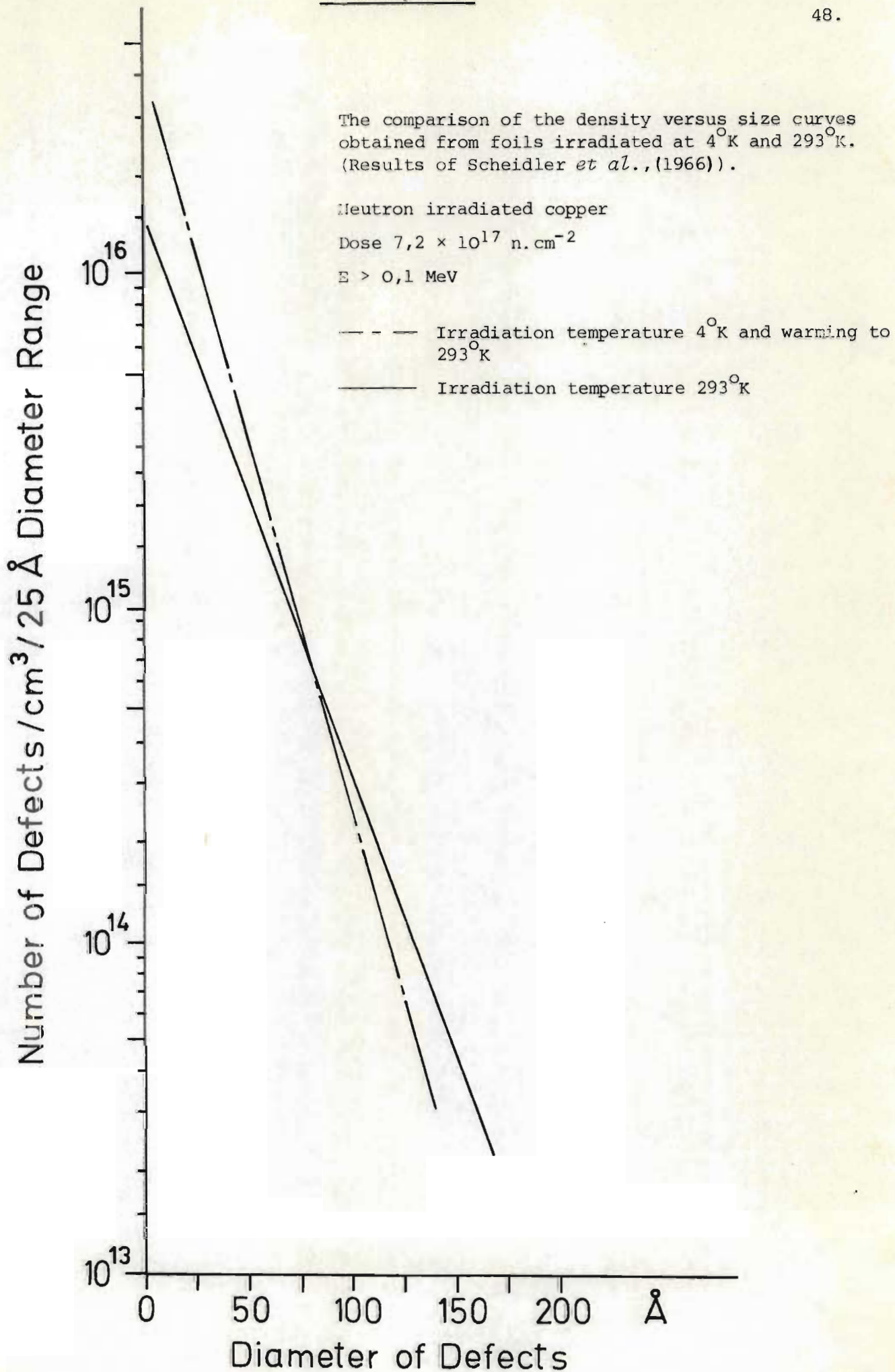


FIG (3.3)



circular loops they state that the total loop area was approximately constant and thus was independent of the temperature of irradiation.

A further effect mentioned by Scheidler *et al.*, (1966) was the degree of interaction between the point defect clusters and dislocations initially present in the specimen. They state that at both 4°K and 77°K there was very little evidence of the defects clustering around dislocations but in both the 293°K and 378°K irradiations the dislocations were decorated with a number of point defect clusters.

All the examinations of Scheidler *et al.*, were carried out in an electron microscope at ambient temperatures and the 4°K and 293°K irradiations were carried out in the T.T.M. facility of the F.R.M. reactor at Munich while the 77°K and 378°K irradiations were carried out in the B.E.P.O. reactor at Harwell. At F.R.M. the flux was  $10^{13}$  f.n.  $\text{cm}^{-2} \text{s}^{-1}$  ( $E > 0,1 \text{ MeV}$ ) while at B.E.P.O. the flux was  $\sim 5 \times 10^{11}$  f.n.  $\text{cm}^{-2} \text{s}^{-1}$ .

In the initial stages of the examination of neutron irradiated copper in this temperature range there was considerable confusion as to the vacancy or interstitial nature of the damage since different workers published apparently conflicting results. Using annealing experiments Makin *et al.*, (1961, 1962) and Makin and Manthorpe (1963) concluded that the small defects of diameter  $d < 50 \text{ \AA}$  were presumably of vacancy type and that the larger ones of  $d > 50 \text{ \AA}$  were interstitial in character. Makin and Manthorpe (1963) stated that the results of Barnes and Mazey (1960) from  $\alpha$ -particle irradiated copper, and the loop analysis of Mazey, Barnes and Howie (1962) supported their conclusions.

In 1964 Essman and Wilkens concluded that the lattice defects giving rise to black dots under kinematical imaging conditions and producing black-white lobes under dynamical imaging conditions are small

Frank dislocation loops. It then followed that Rühle, Wilkens and Essmann (1965) and Rühle (1967a,b) extended the theory of diffraction contrast for small strain centres as published mainly by Ashby and Brown (1963a,b) and made an extensive theoretical study of the diffraction contrast from small Frank dislocation loops which was later extended by McIntyre and Brown (1966a,b).

As a result of these calculations Diepers and Diehl (1966, 1967a,b) and Rühle (1967a,b) were able to develop the stereo-technique (described in Section 4.3.1) designed to differentiate between the vacancy or interstitial character of these small loops in the 50 Å size range. As a result of this technique the Stuttgart group concluded that the black dots were due to Frank-type dislocation loops with  $\vec{b}$  parallel to  $\langle 111 \rangle$  - directions and that only about 5% of the loops had  $\frac{1}{2} \langle 110 \rangle$  type Burgers vectors. Rühle (1967a,b) and Rühle and Wilkens (1967) using the stereo-technique concluded that the small Frank loops in neutron irradiated copper were mainly of vacancy type. However McIntyre (1967) obtained results in direct contrast to Rühle's and he obtained only interstitial loops, while Crump III (1968) agreed with Rühle's findings (Table 3.2). Further confusion arose when Bourret and Dautreppe (1967) irradiated copper specimens under different atmospheres and obtained either only vacancy loops or only interstitial loops. The vacancy loops were obtained after irradiation in an oxidising atmosphere while interstitial loops were obtained after irradiation in an atmosphere of pure helium gas.

As a result of these publications Rühle, Häussermann, Huber and Wilkens (1968) irradiated two batches of copper specimens, one in liquid helium and the other in an oxidising atmosphere. Their results showed that all loops with a diameter less than approximately 75 to 100 Å were mainly vacancy while those loops with diameters greater than this were interstitial. This result was found in both the specimens

irradiated in the oxidising atmosphere and those irradiated in helium and thus this indicated that the initial cluster formation is not very sensitive to the surrounding atmosphere during irradiation, or to the irradiation temperature in this temperature range. In addition it was found by these workers that vacancy loops were found in that size range which obeys a linear dose dependence of their volume density.

The Stuttgart group proposed as an explanation of the conflicting experimental results that different researchers had inadvertently selected out different size groups of defects to study and thus had arrived at apparently opposing conclusions.

However in 1970 Rühle, Häussermann and Rapp irradiated copper specimens in the F.R.M. reactor at Munich and in the 'Herald' reactor at Aldermaston and obtained a majority of vacancy defects. But the irradiation in the 'Herald' reactor was repeated under identical conditions by Ipohorski and Brown (1970) who obtained opposite results. Ipohorski and Brown carried out three irradiations, in water, helium, and air respectively and in each case found 92% of the defects to be interstitial. The irradiation of copper in air in the SAFARI 1 reactor carried out by Kemm (1973) produced results similar to those of Ipohorski and Brown. The diameters of defects examined in this work were mainly of the order of  $50 \text{ \AA}$ .

The extent of the disagreement which arose regarding the nature of the small loops can be appreciated from the summary of published results presented in Table 3.2.

There is now general agreement however that the loop populations are mixed with regard to their vacancy or interstitial nature and in addition it is now established that the loops at the small end of the

TABLE 3.2

## THE CHARACTER OF SMALL LOOPS AS DETERMINED BY DIFFERENT RESEARCHERS

Worker	Reactor	Atmosphere	Total dose (n.cm <sup>-2</sup> )	Temperature (K)	% vacancy	% interstitial
Rühle (1967b)	Munich Research Reactor	Not known	$6 \times 10^{16} - 10^{18}$ (E > 0,1 Mev)	350	97	3
McIntyre (1967)	'Herald' Aldermaston	Water	$3,10^{17}$ (E > 1 Mev)	340	14	86
Bourret & Dautreppe (1967)	Not reported	Helium containing O <sub>2</sub>	$6,4.10^{17}$ (E > 1 Mev)	340	100	0
-do-	-do-	Pure helium	-do-	340	0	100
Rühle <i>et al.</i> , F.R. Munchen (1970)		Not reported	$4.10^{17}$ (E > 0,1 Mev)	250	89	11
-do-	-do-	-do-	$6.5,10^{17}$ (E > 0,1 Mev)	4,2	87	13
Rühle <i>et al.</i> , (1970)	'Herald' Aldermaston	Water	$4.10^{17}$ (E > 0,1 Mev)	300	74	26
Ipohorski & Brown (1970)	'Herald' Aldermaston	Water	$5.10^{17}$ (E > 1 Mev)	300	8	92
-do-	-do-	Helium	-do-	300	8	92
-do- (1970)	-do-	Air	-do-	300	8	92
Kemm (1973)	'Safari I' Pelindaba	Air	$0,5.10^{18}$ (E > 0,1 Mev)	330	10	90

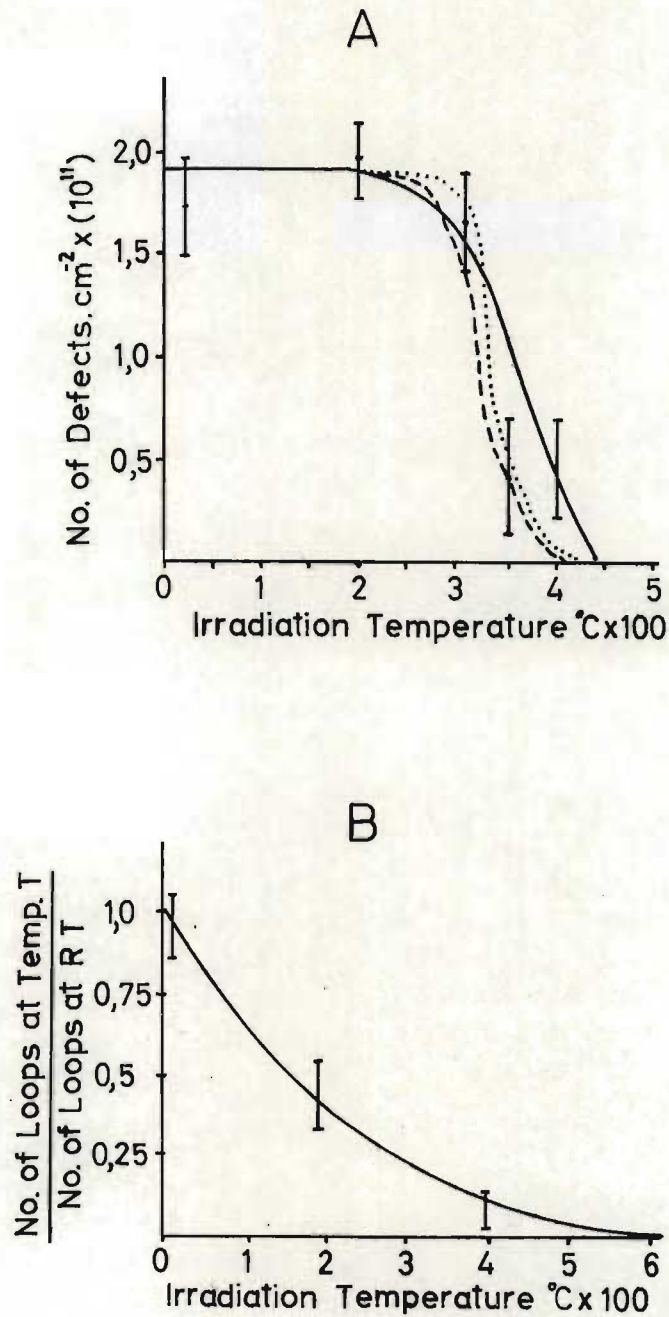
size spectrum are mainly vacancy and that the larger ones are interstitial.

### 3.2.3 Irradiations at high temperatures

Very little quantitative radiation damage work has been carried out in high temperature ranges (i.e. irradiation temperatures above 200°C) but from the information that does exist, which includes electron irradiation experiments carried out in High Voltage Electron Microscopes, it is commonly observed that as irradiation temperature is increased interstitial loops are homogeneously nucleated on a coarser scale, and in addition as the temperature of irradiation is increased, for a given dose, the interstitial loops become larger and continue to grow until they eventually intersect one another to form a homogeneous dislocation network. Electron irradiation experiments carried out in H.V.E.M.s show that the dislocation network becomes progressively more tangled as the total dose is increased. Either a homogeneous or heterogeneous nucleation mechanism in which  $\ln N_L \propto \frac{1}{T}$  ( $N_L$  = number of loops) is consistent with this behaviour. Further work carried out has indicated that for F.C.C. metals the loops retain their faulted configuration until they intersect another loop or some other defect which then serves to nucleate the necessary shockley partials for unfaulting to occur.

Considering the vacancy loops, work on the self-ion irradiation of copper (English, Eyre and Summers) (Figure 3.4) has shown that the concentration of vacancy loops falls off very rapidly as a function of temperature above irradiation temperatures of 200°C. The solid line in Figure 3.4A is the experimentally measured result while the two broken lines are theoretical curves based on a simple model in which the variation in vacancy loop concentration with irradiation temperature

Graphs showing the variation in loop concentration  
with irradiation temperature.



- A. Copper irradiated with 30 KeV  $\text{Cu}^+$  ions to a dose of  $1,0 \times 10^{12}$  ions.  $\text{cm}^{-2}$ .
- B. Molybdenum irradiated with 6,0 KeV  $\text{Mo}^+$  ions to a dose of  $0,74 \times 10^{12}$  ions.  $\text{cm}^{-2}$ .

From Eyre and English (1974)

is arrived at by considering the competition between the loop shrinkage rate due to thermal vacancy emission, and the loop generation rate from collision cascades. The good correlation between these curves shows that the theoretical assumptions made were reasonable and also lends support to the assumption that loop generation due to cascade collapse is athermal over the temperature range studied.

The work of English, Eyre and Summers also indicates that in a low stacking fault energy metal such as copper the difference in shrinkage rate between perfect and faulted loops is small, but that as the stacking fault energy is increased this difference will become larger.

Their results on the vacancy loop concentration of self-ion irradiated molybdenum (Figure 3.4B) are very different to those of copper, and the behaviour of molybdenum cannot be explained by the same simple model which was successfully applied to the copper results. In the case of neutron irradiation experiments (Eyre, Maher and Bartlett (1971), Bentley, Eyre and Loretto (1974) and Bentley (1974)) the decrease in vacancy loop number in molybdenum was accompanied by the formation of a high concentration of small voids at irradiation temperatures of  $330^{\circ}\text{C}$  and above. Thus the vacancies are not simply lost by recombination or migration to the crystal surfaces and these workers have therefore concluded that in molybdenum loop nucleation becomes more difficult in cascades as the irradiation temperature is increased. It is suggested that the vacancies diffuse away from the cascades and are thus available for void formation if the required nuclei exist. This apparent difference in behaviour between copper and molybdenum is not understood but the efficiency of vacancy loop nucleation in the cascades could be inhibited as stacking fault energy is increased, particularly at higher temperatures.

Isolated stacking fault tetrahedra have been observed in copper specimens proton irradiated at a temperature of  $450^{\circ}\text{C}$  (Muncie, English and Eyre) and Kemm and Spalding (1974) observed S.F.T. in copper irradiated with fast neutrons in an atmosphere of air at a temperature of approximately  $250^{\circ}\text{C}$ . It has also been shown that as irradiation temperature is raised an increasing proportion of the surviving loops are perfect with  $\vec{b} = a/2 \langle 110 \rangle$  (Muncie, English and Eyre; English, Eyre and Summers).

In 1968 Jackson observed a large scale (10-100  $\mu\text{m}$ ) inhomogeneous clustering of radiation damage into large rafts in copper irradiated with fast neutrons to a dose of  $5 \times 10^{17} \text{f.n.cm}^{-2}$  at a temperature of approximately  $250^{\circ}\text{C}$ . This irradiation was carried out in air. In the same year Hulett *et al.*, (1968) published results on similar irradiations but their temperatures were not accurately known and were estimated to be  $\sim 400^{\circ}\text{C} \pm 50^{\circ}\text{C}$ . Their fast neutron ( $E > 1 \text{ MeV}$ ) doses were  $1 \times 10^{18} \text{f.n.cm}^{-2}$  and the irradiations were carried out in a helium atmosphere. There are marked differences in the work of Jackson and Hulett *et al.* Hulett *et al.*, noted loose rafts of defect up to 100  $\mu\text{m}$  in diameter which were described by the authors as 'regions containing a high concentration of defects', while Jackson noted very dense defect rafts of very specific macroscopic shape. Some of these rafts were triangular in shape while others had a long 'comet' shape reaching lengths of 100  $\mu\text{m}$ . A further effect observed by both of these workers was that the background area between rafts contained considerably less damage than expected.

Larson and Young (1972) irradiated pure copper specimens in a helium atmosphere to a total fluence of  $10^{18} \text{f.n.cm}^{-2}$  ( $E > 0,6 \text{ MeV}$ ) in the temperature range of  $200^{\circ}\text{C}$  to  $400^{\circ}\text{C}$ . Much of their analysis work was carried out by means of anomalous X-ray transmission studies

from which they produced a graph of anomalous X-ray transmission as a function of irradiation temperature (Figure 3.5). Their total irradiation doses actually varied from  $0,5 \times 10^{18}$  f.n.  $\text{cm}^{-2}$  to  $0,72 \times 10^{18}$  f.n.  $\text{cm}^{-2}$  for their various sets of specimens but in Figure 3.5 their results were all scaled to a constant dose of  $1 \times 10^{18}$  f.n.  $\text{cm}^{-2}$ . They found no indication of a significant change in the defect character for temperatures from  $43^{\circ}\text{C}$  to  $160^{\circ}\text{C}$  but at about  $200^{\circ}\text{C}$  the effective X-ray absorption coefficients increased sharply such that at  $300^{\circ}\text{C}$  they were 20 to 40 times larger than at the lower temperatures (Figure 3.5). At an irradiation temperature of  $400^{\circ}\text{C}$  these figures fell rapidly to a point at which they could no longer detect any damage by this method.

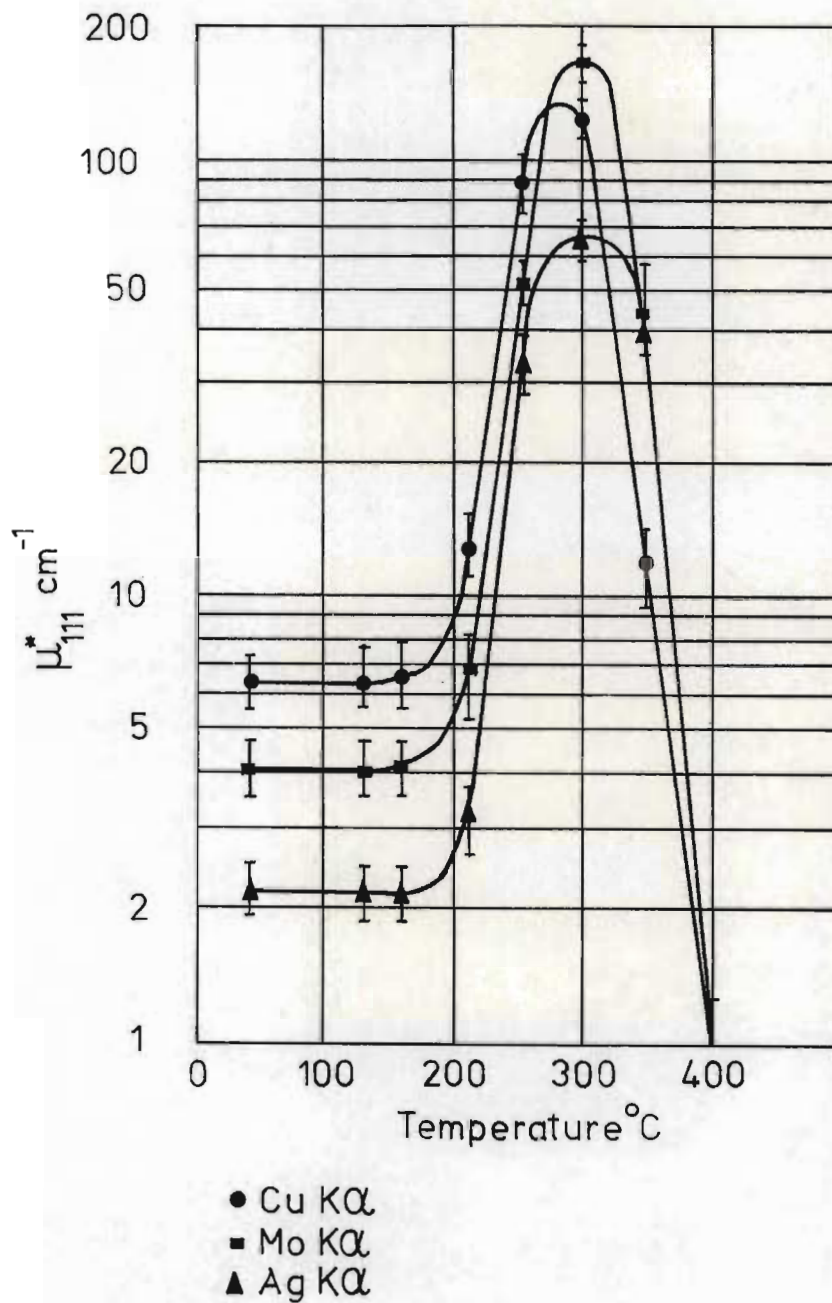
Both Hulett *et al.*, and Jackson noted that it appeared that the larger defect regions tended to be associated with grown-in dislocations. As discussed above, Scheidler *et al.*, (1966) observed that radiation damage accumulated near grown-in dislocations in copper irradiated at  $378^{\circ}\text{K}$ . However the micrographs of Scheidler *et al.*, do not look like either those of Jackson or Hulett *et al.*, and do not exhibit a marked clustering of damage into rafts.

Both Jackson and Hulett *et al.*, found that this damage annealed out in the temperature range of  $500^{\circ}\text{C}$  to  $800^{\circ}\text{C}$  which is well above the temperature necessary (i.e.  $400^{\circ}\text{C} \pm$ ) for the removal of radiation damage formed in specimens irradiated at temperatures below  $100^{\circ}\text{C}$ .

Larson and Young (1972) attempted to produce similar defect rafts in aluminium but were unable to detect any by means of X-ray methods.

Further work on these large defect rafts has been carried out by

Graph of integrated anomalous X-ray transmission intensities tabulated in terms of effective absorption coefficient  $\mu^*$  vs irradiation temperature for copper specimens irradiated with fast neutrons. All irradiations were scaled to a constant dose of  $1 \times 10^{18}$  f.n.  $\text{cm}^{-2}$ . (From results of Larson and Young (1972)).



Kemm (1973) and Jackson, Kemm and Spalding (1974), and the earlier results of Jackson (1968) were confirmed.

### 3.3 CONCLUSIONS

A large amount of radiation damage work has now been carried out at ambient temperatures and relatively little at high temperatures.

The ambient temperature work (Section 3.2.2) has shown that vacancy loops are found in that size range which obeys a linear dose dependence of their volume density and thus it was concluded that vacancy loops are nucleated by the primary damage events such as displacement cascades. These vacancy loops then have a tendency to shrink as the irradiation proceeds. Scheidler *et al.*, (1966) (Section 3.2.2) pointed out that the larger black dots observed in irradiated metals increase rapidly in size with dose which suggested that they were interstitial loops growing by absorbing interstitials - this was later proven to be true. Scheidler *et al.* also pointed out that the temperature of irradiation should have an effect on the size distribution and density of cluster formation, since in the heterogeneous theory of nucleation the critical nucleus size is expected to be smaller at low temperatures, and in the homogeneous theory the mobility of interstitial atoms is essential for these clusters to form at all.

These observations are explained by the fact that during irradiation at very low temperatures the interstitials are not very mobile and thus a large number of small defect clusters are formed, while at higher irradiation temperatures the interstitials are more mobile and their steady state concentration is lower and thus a smaller number of larger defects are formed. This explanation is consistent with the decoration

of dislocations at higher temperatures ( $T > 300^{\circ}\text{K}$ ) and not at low temperatures (Section 3.2.2) since the mean free path for diffusion of interstitials is much greater at the higher temperatures and thus more interstitials pass into the influence of the strain field of the dislocations.

At higher temperatures it has generally been observed that interstitial loops grow rapidly as a function of irradiation temperature and dose until they intersect to form a dislocation network. Vacancy loops shrink and disappear as a function of irradiation temperature and dose and are not generally observed except in the case of those large vacancy loops formed by climb-mechanisms (Figure 2.8). Very large fast neutron fluences together with elevated temperatures (up to  $\sim 800^{\circ}\text{C}$ ) can produce voids of varying shape and size. Voids are of great technological importance and a large amount of applied research has been carried out in the field in addition to fundamental research (for details see the review articles by Norris (1972a,b)).

In general, radiation damage has been observed to form homogeneously, but in contrast a few researchers (Section 3.2.3) have observed large inhomogeneous rafts of damage. As a result of these observations a High Temperature Irradiation Rig (described in Chapter 6) was built at the University of Natal to carry out high temperature irradiations under accurately controlled conditions in the SAFARI 1 reactor in Pretoria. Specimens from these irradiations are examined in this thesis.

## CHAPTER FOUR

### TRANSMISSION ELECTRON MICROSCOPY OF RADIATION - INDUCED DEFECTS

- 4.1 Introduction
- 4.2 Diffraction contrast in the electron microscope
  - 4.2.1 Introduction
  - 4.2.2 Summary of diffraction contrast theory
- 4.3 The appearance of defects in the final image
  - 4.3.1 Small strain centres
    - 4.3.1.1 Introduction
    - 4.3.1.2 Black-white images
    - 4.3.1.3 Edge loops
    - 4.3.1.4 Non-edge loops
    - 4.3.1.5 Small voids
    - 4.3.1.6 Stacking fault tetrahedra
  - 4.3.2 Large dislocation loops
    - 4.3.2.1 Contrast properties
- 4.4 The experimental determination of the vacancy or interstitial character of loops
  - 4.4.1 Determination of the nature of loops
  - 4.4.2 Determination of the sense of inclination of a loop
- 4.5 Summary

#### 4.1 INTRODUCTION

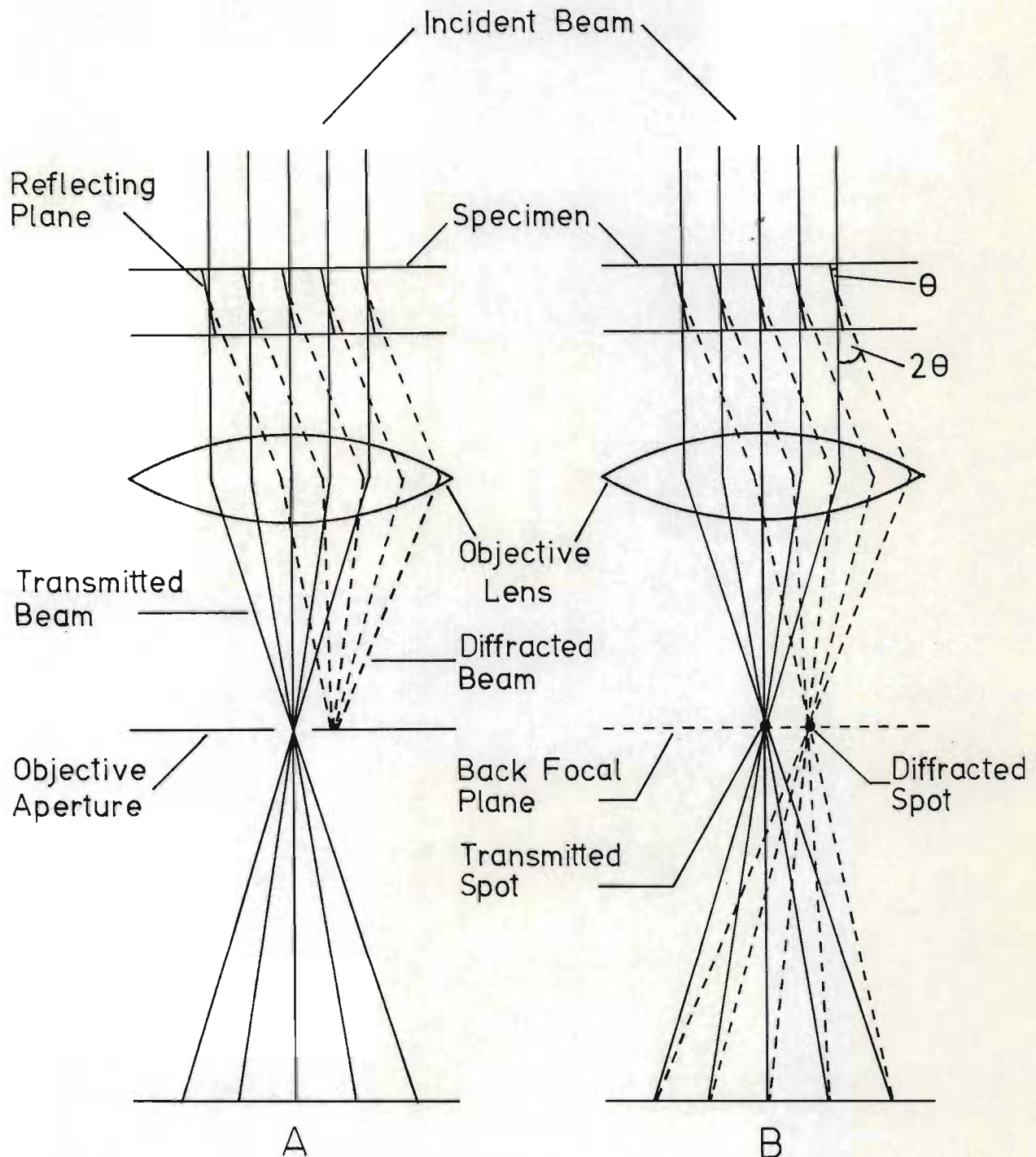
Defects in crystalline solids are studied by means of diffraction contrast (Section 4.2.1) . Hirsch *et al.*, (1965) obtained a large measure of success in the 1960's in the application of diffraction contrast theory to simple crystal defects such as dislocations and extended stacking faults. Success was also obtained in the treatment of more complicated defects such as dislocation loops and stacking fault tetrahedra as long as the dimensions of the defect were comparable with, or greater than, the extinction length  $\xi_g$ . The extinction length (Figure 4.3) is the distance over which the diffracted beam intensity rises from zero to a maximum and back to zero as a result of the beating effect between the transmitted and scattered beams (Section 4.2.2) . The terms 'large' and 'small' when used in reference to defect sizes are generally used relative to the extinction length.

The study of small defects, as found in irradiated materials, has resulted in the formulation of theoretical and experimental methods (described in this chapter) of examination of these defects and thus the basic tools for the study of both large and small defects are now available.

#### 4.2 DIFFRACTION CONTRAST IN THE ELECTRON MICROSCOPE

##### 4.2.1 Introduction

The illuminating beam of electrons in an electron microscope is almost parallel as it travels down to the specimen (Figure 4.1). On striking the specimen surface some of the electrons will be reflected or back scattered, while others will be scattered away from their incident trajectories. When an electron is scattered by a solid, either

Objective Lens Geometry

The relationship between the specimen reflecting planes and incident illumination for a Bright Field image. The objective aperture allows only the transmitted spot to form an image.

The formation of a focused diffraction pattern in the back focal plane of the objective lens.  $\theta$  is the Bragg angle.

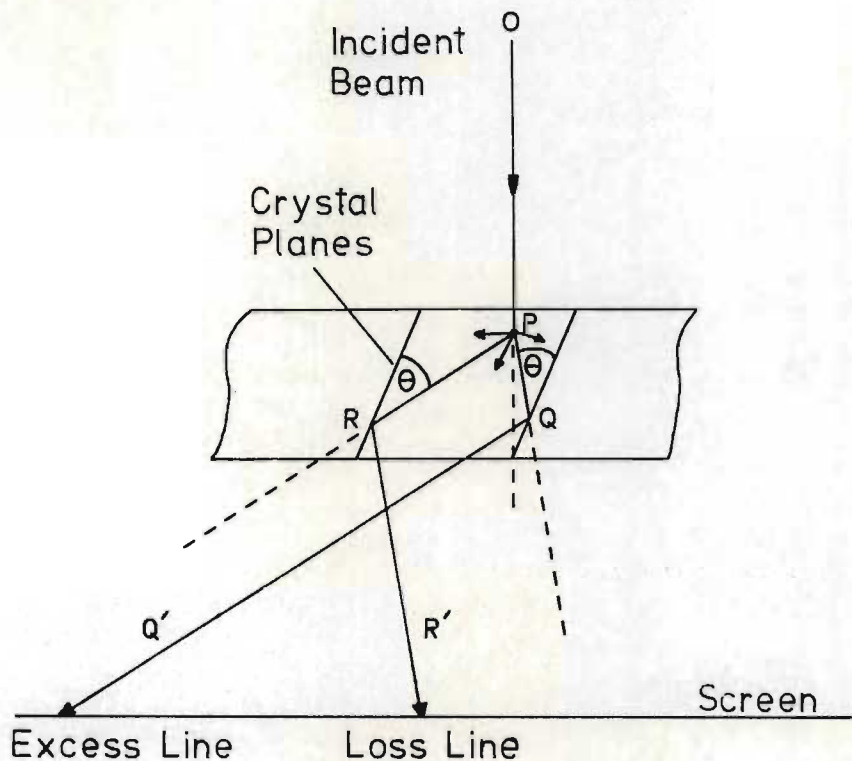
at the surface or within the solid, it may or may not lose energy. If the fast electron is scattered by the crystal and there is a negligible transfer of energy but a considerable momentum exchange between the lattice and the fast electron, the incident electron is said to be Bragg reflected or diffracted.

In a crystalline solid, this scattering causes the incident beam to be split into a direct beam and a number of Bragg diffracted beams which travel at very small angles to the direct beam; typically 1 or 2 degrees; these angles being determined by the electron energy and the type of lattice and lattice spacing. One or more of these elastically diffracted beams plus the direct beam is then focussed by the objective lens to form a transmission diffraction pattern in its back focal plane (Figure 4.1B), which is characteristic of the crystalline structure of the solid.

When the scattering of the fast incident electron is inelastic, the crystal is excited into an allowed excitation state appropriate to the energy transfer between the fast electron and the solid. The crystal then returns to its ground state by emitting radiation. The presence of inelastically scattered electrons is most noticeable in the electron diffraction pattern. When the crystal is thicker than about  $2000 \text{ \AA}$  the spots in the diffraction pattern become more diffuse as a result of small-angle inelastic scattering through larger angles. Kikuchi lines (Figure 4.2) may also be observed as a result of the subsequent Bragg reflection of these inelastically scattered electrons.

In the theory of elastic diffraction contrast from lattice defects, it is assumed that the electron microscope is focussed on the electron exit surface of the specimen. The contrast calculations are

## Formation of Kikuchi Lines



(from Hirsch *et al.*, (1965))

Kikuchi lines (Kikuchi (1928)) arise from the subsequent Bragg reflection of inelastically scattered electrons. Some electrons are inelastically scattered at P. Those that reach the reflecting planes at R and Q are Bragg reflected into  $RR'$  and  $QQ'$ . Because PQ is nearer the forward direction (i.e. more nearly along OP) than PR the intensity of the electrons scattered into  $QQ'$  is greater than that of  $RR'$ . The line of less intensity occurs nearer the origin of the diffraction pattern and is called the loss line while its associated bright line is called the excess line.

thus performed by calculating the lateral intensity distribution of the direct or of the diffracted beams at the exit surface.

Diffraction contrast images are produced by placing an aperture in the back focal plane of the objective lens which lets through either the direct beam only, when the 'Bright Field' image is produced (Figure 4.1A) or a diffracted beam only whereupon a 'Dark Field' image results.

#### 4.2.2 Summary of diffraction contrast theory

There are two mathematically different but physically equivalent formulations of the differential equations for diffraction contrast calculations. These are:

1. The plane wave equations.
2. The Bloch wave formulations.

Howie and Whelan (1961) derived the Plane wave equations and Takagi (1962) produced a more rigorous treatment. In this treatment the direct and diffracted beams are described by plane waves. A scattering between these plane waves is then used to describe the propagation of electrons inside the crystalline foil containing lattice defects.

In the Bloch wave formulations due to Howie (1963) and Wilkens (1964) and modified by Wilkens (1966) the propagation of electrons in the crystal is basically expressed in terms of Bloch waves of the undisturbed lattice. Lattice perturbations then cause a local scattering between the Bloch waves involved. This scattering is proportional to the derivative ( $Z'$ ) of that part of the displacement field which is in

in the direction of the electron beam. In the two beam case the  $Z$  direction is the direction of the bisector of the direct and diffracted beam directions. The advantages of this formulation are: that the resulting differential equations are solved only in the disturbed lattice regions, and that in special cases a comparatively simple first order perturbation solution can be obtained.

A detailed formulation of the dynamical theory for the case of several diffracted beams is presented by Howie (1970) and Goringe (1971). This multi-beam case is important for accelerating voltages  $> 300$  KV when two-beam conditions may be difficult to obtain for metallic specimens.

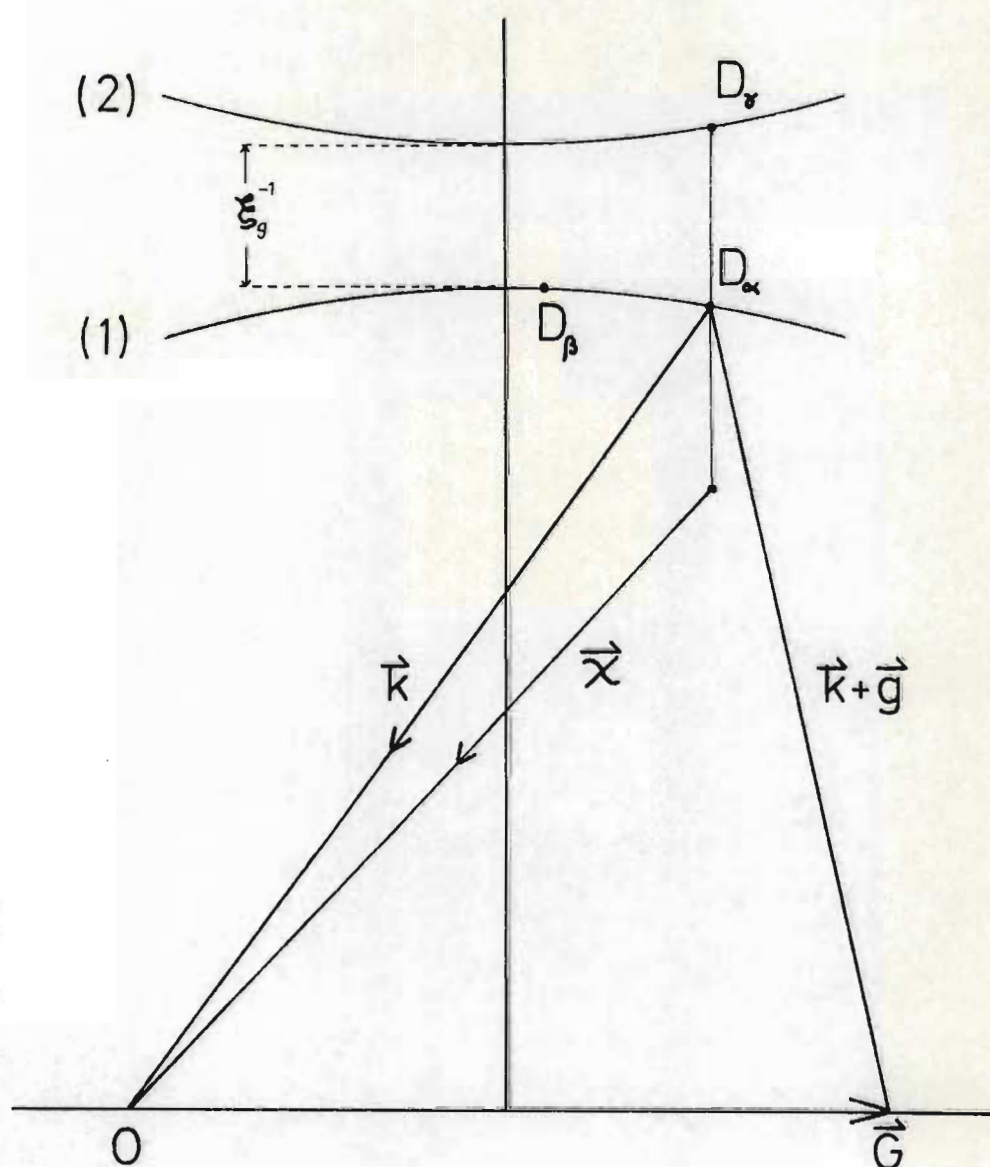
In the case of the two-beam approximation it is assumed that a single Bragg reflection is strongly excited so that only two wave amplitudes are of importance. On using the dynamical theory to consider this situation one finds that the resulting dispersion equation can be conveniently represented by a dispersion surface (Figure 4.3).

We now briefly consider the dispersion surface and how it is used, for example, to distinguish between the 'interband' or 'intraband' scattering of a Bloch wave traversing a crystal.

It is the wave-like nature of the electron which is directly responsible for electron diffraction effects. Thus we shall consider the solution of Schrödinger's equation in a periodic potential (i.e. periodic lattice).

Considering that the electron has energy  $eE$ , and moves in a potential  $V(\vec{r})$  we look for the steady state solution of the wave equation.

FIG (4.3)  
The Dispersion Surface



Representation of a dispersion surface consisting of bands (1) and (2). Each point  $D$  on a band is associated with wave vectors  $\vec{k}$  and  $\vec{k} + \vec{g}$ .  $\xi_g$  is the extinction length.

Starting with Schrödinger's wave equation:

$$\nabla^2 \psi(\vec{r}) + (8\pi^2 \frac{me}{h^2}) (E + V(\vec{r})) \psi(\vec{r}) = 0 \quad (4.1)$$

we follow the argument of Hirsch *et al.*, (1965):

When the electron moves in a vacuum we get  $V(\vec{r}) = 0$ , and a solution of the equation is given by:

$$\psi(\vec{r}) = \exp(2\pi i \vec{\chi} \cdot \vec{r}) \quad (4.2)$$

Provided that  $|\vec{\chi}| = \chi$  is chosen such that:

$$\frac{h^2 \chi^2}{2m} = eE \quad (4.3)$$

where  $\vec{\chi}$  is the wave vector.

Now considering the electron to be inside a crystal, where it is affected by the crystal lattice potential, we take the most general form of the crystal potential  $V(\vec{r})$ :

$$V(\vec{r}) = \frac{h^2}{2me} \sum_{\vec{g}} U_{\vec{g}} \exp(2\pi i \vec{g} \cdot \vec{r}) \quad (4.4)$$

where the  $U_{\vec{g}}$  are constants. Hirsch *et al.*, (1965) then show that for a real potential energy, and considering (4.4) together with (4.1) we get a set of equations satisfied by the wave amplitudes:

$$\{K^2 - (\vec{k} + \vec{g})^2\} c_{\vec{g}}(\vec{k}) + \sum_{\vec{h} \neq 0} U_{\vec{h}} c_{\vec{g}-\vec{h}}(\vec{k}) = 0 \quad (4.5)$$

where

$$K^2 = \frac{2 meE}{h^2} + U_0 = \chi^2 + U_0 \quad (4.6)$$

and  $K$  is the magnitude of the electron wave vector in the crystal, after correction for the wavelength change due to the mean crystal potential  $U_0$ .

If the Bloch wave consisted of  $N$  plane waves then (4.5) would consist of  $N$  equations each of  $N$  terms; thus we make the two beam approximation which reduces this number to two, which then reduce to:

$$(k - K) (|k + g| - K) = \frac{U_{-g} U_g}{4K^2} = \frac{|U_g|^2}{4K^2} \quad (4.7)$$

Thus we have (4.3) for the electron in vacuo and (4.7) for the electron in a crystal. These two equations relate the wave vector to the energy, and are called dispersion equations. They generally restrict the wave vector to lie on a surface called the dispersion surface, which for low energy electrons in crystals are the familiar Fermi surfaces. The dispersion surface corresponding to (4.7) is shown in Figure 4.3. The surface consists of two bands (1) and (2), and each point  $D$  on a band is associated with wave vectors  $\vec{k}$  and  $\vec{k} + \vec{g}$  down to the points  $O$  and  $G$  in the reciprocal lattice. Thus with each point  $D$  on a band there is associated a Bloch wave.

As a Bloch wave traverses a crystal it may be scattered. If, when scattered, its representative point stays on the same branch of the dispersion surface (e.g. its representative point moves from  $D_\alpha$  to  $D_\beta$  in Figure 4.3) then it is said to have been 'intraband' scattered. If on the other hand, its representative point moves to the other branch (e.g.  $D_\alpha$  to  $D_\gamma$  in Figure 4.3) then it is said to have been 'interband' scattered.

This difference between interband and intraband scattering gives rise, for example, to the black-white oscillation with depth from the

foil surface of small point defect clusters when imaged under dynamical two beam conditions with  $S = 0$ . (For full treatment see Hirsch *et al.*, (1965), Chapter 10)

For calculations of the contrast of the distorted lattice, the 'column approximation' introduced by Hirsch, Howie and Whelan (1960), has been applied with great success. By the use of the column approximation the partial differential equations, as derived from the Schrödinger equation, are reduced to ordinary differential equations. The column approximation assumes that due to the smallness of  $2\theta$  i.e. the scattering angle of the electrons where  $\theta$  is the Bragg angle (Figure 4.1) the intensity at a given point on the micrograph is determined solely by the varying diffraction conditions in a very narrow column parallel to the electron beam. The validity of the column approximation is related to the lateral distribution on the dispersion surface of Bloch waves excited as a result of scattering by the defect in question. The column approximation is valid when all of the scattered waves are closely concentrated in the neighbourhood of the unscattered waves. Empirically there is no doubt that the dynamical theory with the column approximation is very successful in high energy electron diffraction.

In general, well-defined contrast images are obtained only under two-beam conditions. The reflection at the lattice planes is described by the diffraction vector  $\vec{g}$ , which is perpendicular to the planes and has length  $1/d$  where  $d$  is the lattice spacing. Under two-beam conditions the electron beam propagates through the crystal in the form of two Bloch waves with slightly differing wave vectors  $\vec{k}$ . The reciprocal of the difference between these wave vectors,  $\frac{1}{\Delta|\vec{k}|}$  is a parameter characteristic of the substance and of the reflecting planes under consideration, and is called the extinction length  $\xi_g$ . The

extinction length is important for describing diffraction phenomena; but only if the primary beam satisfies the Bragg condition exactly does

$$\Delta |\vec{k}|^{-1} = \xi_g \text{ hold exactly.}$$

Deviations from the Bragg condition are measured by the 'excitation error'  $\vec{S} = g \cdot \Delta\theta$  (Figure 4.4) where  $\Delta\theta$  is the deviation angle of the primary beam from the Bragg angle  $\theta$ .

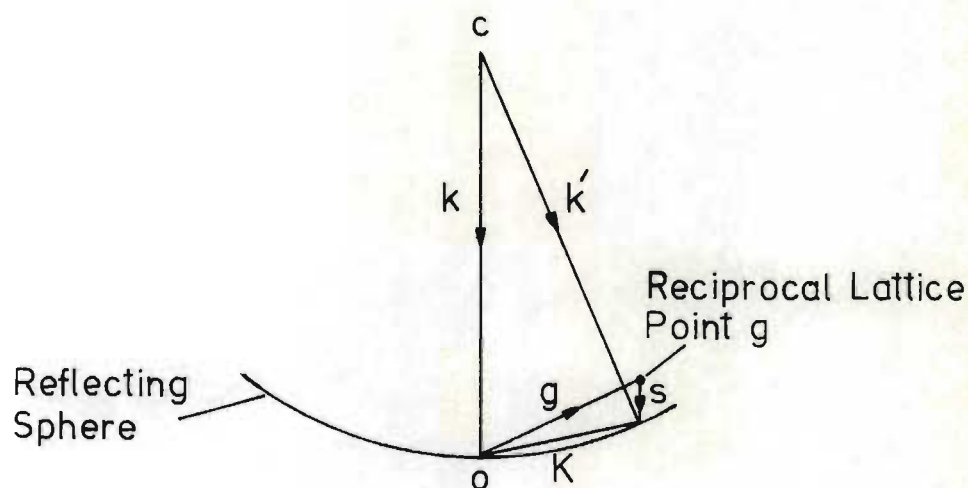


Figure 4.4 The Excitation Error  $\vec{S}$ .

For  $\vec{S} \neq 0$  the 'effective extinction length':

$$(\xi_g)_{\text{eff}} = \xi_g (1 + (\vec{S} \cdot \vec{\xi}_g)^2)^{-1/2}$$

has to be used, which can be written as:

$$\xi_g^W = \xi_g (1 + w^2)^{-1/2}$$

where

$$W = |\vec{S}| \cdot \xi_g = |\vec{g}| \cdot \Delta\theta \cdot \xi_g$$

is called the 'normalized excitation error'.

When  $W \sim 0$ , under two-beam conditions the diffraction contrast images produced are called 'dynamical images'. When  $W > 1$  or under many beam conditions, the images produced are called 'kinematical images'. The contrast is most sensitive to weak lattice strains under dynamical image conditions, and thus in the case of point defect clusters it is best to use dynamical conditions when information regarding the clusters symmetry and sign of lattice strains is wanted.

When information concerning the volume density and size distribution of the clusters is needed, then kinematical conditions should be used since under these conditions the contrast is more constricted to the 'physical size' of the defect.

#### 4.3 THE APPEARANCE OF DEFECTS IN THE FINAL IMAGE

##### 4.3.1 Small strain centres

##### 4.3.1.1 Introduction

Small damage (relative to  $\xi_g$ ) observed in the electron microscope usually appears as black dots (first observed by Makin *et al.*, 1960). These black dots can consist of small Frank dislocation loops, stacking fault tetrahedra, voids and fission fragment tracks.

#### 4.3.1.2 Black-white images

When imaged under kinematical diffraction conditions ( $W_g > 1$ ) 'black dot' damage appears simply as black dots, but Essmann and Wilkens (1964) noticed that when imaged under dynamical diffraction conditions ( $W_g \sim 0$ ) those defects lying close to either foil surface (within about  $1,5 \xi_g$ ) display a characteristic contrast image which appears as an extended dot, consisting of a black lobe and a white lobe. Those defects lying further than about  $1,5 \xi_g$  from either foil surface exhibit only 'black-dot' contrast for both  $W_g \sim 0$  and  $W_g > 0$  conditions.

A direction is given to the black-white defects by defining a vector  $\vec{\ell}$  which prints from the black part to the white part, when considering positive prints. A distinction is made between the direction and sense of  $\vec{\ell}$ , the former being the direction, irrespective of sign, relative to the diffraction vector  $\vec{g}$ ; and the latter being simply the sign of  $\vec{\ell}$ .

The dynamic contrast calculations of Ashby and Brown (1963a) showed that in the case of strain centres with spherical symmetry, the direction of  $\vec{\ell}$  is always parallel or anti-parallel to  $\vec{g}$ . However in the case of neutron irradiated copper Essmann and Wilkens found that the black-white contrast of the defect clusters which they observed had  $\vec{\ell}$  vectors which were nearly always parallel to a  $\langle 111 \rangle$  direction or to the projection of a  $\langle 111 \rangle$  direction onto the image plane. They thus made the assumption that the main displacement field of the defect clusters had a preferential direction and that the black dots were Frank sessile dislocation loops with Burgers vectors parallel to  $\langle 111 \rangle$ .

It has since been confirmed that for the case of edge loops

the direction of  $\vec{\ell}$  is very approximately independent of the direction of  $\vec{g}$  and is parallel or anti-parallel to the Burgers vector  $\vec{b}$  or to its projection onto the image plane. But significant deviations from this direction are expected for large angles between  $\vec{b}$  and  $\vec{g}$  (e.g. Eyre (1972)) and so the determination of the Burgers vector from the orientation of  $\vec{\ell}$  is now considered to be invalid.

#### 4.3.1.3 Edge loops

The general Burgers vector for a loop can be given as:

$$\vec{b} = \vec{b}_E + \vec{b}_S$$

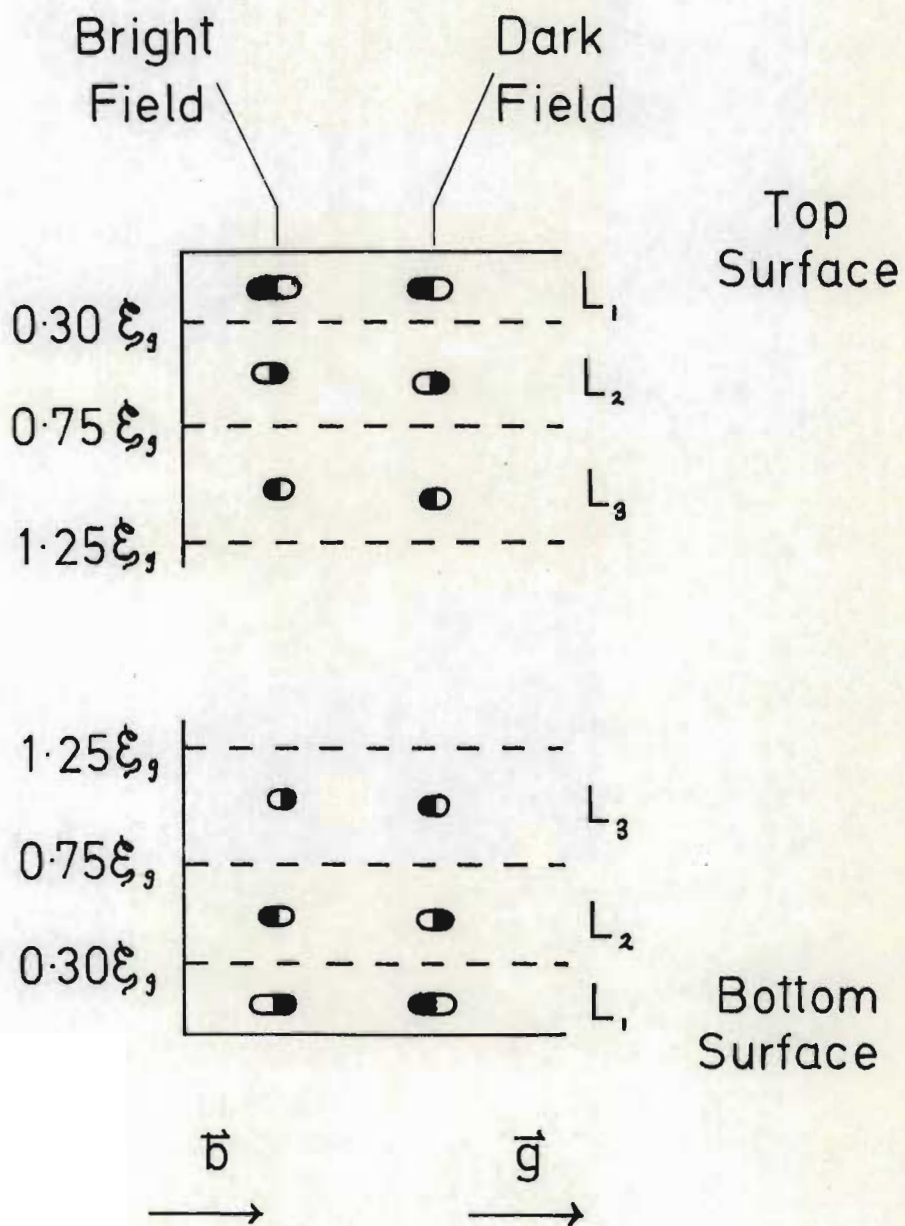
where  $\vec{b}_E$  is the edge component and  $\vec{b}_S$  is the shear component. For  $\vec{b}_S \neq 0$  the Burgers vector is not perpendicular to the loop plane and thus we will initially consider a pure edge loop where  $\vec{b}_S = 0$ .

The assumptions made by Essmann and Wilkens regarding the black-white contrast were verified theoretically by Rühle, Wilkens and Essmann (1965), McIntyre and Brown (1966a,b) and Rühle (1967a,b). These calculations predicted that the sign of  $\vec{\ell}$  would depend on the distance of the loop centre from the nearest foil surface, and on the vacancy or interstitial nature of the loops. Thus for a given loop type the sign of the product  $(\vec{g} \cdot \vec{\ell})$  oscillates with depth. This oscillation with depth divides the surface regions of the foil into quite well defined layers,  $L_1, L_2, L_3 \dots$  etc. in which the black-white contrast oscillates in sign for a given loop type (Figure 4.5). In the odd-numbered layers the interband and intraband scattering processes are in phase, while in the even-numbered layers they are in anti-phase.

For Frank loops with radii less than  $0,2 \xi_g (1 + W^2)^{-1/2}$  (where

FIG (4.5)

Depth Oscillations of Black-White  
Contrast of Vacancy Loops



$\vec{T}$  is opposite for  
 Interstitial Loops

$\xi_g (1 + W^2)^{-\frac{1}{2}}$  is the effective extinction length, Page 72) the dimensions of the layers are given by:

$$\begin{aligned} 0 &\leq L_1 \leq 0,3 \xi_g (1 + W^2)^{-\frac{1}{2}} \\ 0,4 \xi_g (1 + W^2)^{-\frac{1}{2}} &\leq L_2 \leq 0,75 \xi_g (1 + W^2)^{-\frac{1}{2}} \\ 0,82 \xi_g (1 + W^2)^{-\frac{1}{2}} &\leq L_3 \leq 1,2 \xi_g (1 + W^2)^{-\frac{1}{2}} \end{aligned}$$

The radii of the loops, to a slight extent, determine these layer dimensions and for radii larger than about  $0,2 \xi_g (1 + W^2)^{-\frac{1}{2}}$ ,  $L_1$  and  $L_3$  are extended by less than  $0,05 \xi_g (1 + W^2)^{-\frac{1}{2}}$ , while  $L_2$  becomes slightly narrower. It is interesting to note that for dislocation loops, the 'normalized misfit parameter' (McIntyre and Brown (1966a)) is:

$$\vec{P} = \Delta V \cdot \frac{\vec{g}}{\xi_g^2} \pi$$

where  $\Delta V$  which is the volume misfit of the defect, is always much less than 1. This indicates that depth oscillations are always expected in the case of dislocation loops since depth oscillations occur for  $P \ll 1$  but not for  $P \gg 1$ .

A black-white contrast is not observed for defects which lie in the narrow transition regions between layers.

All the above holds true for Bright Field imaging. However on changing from Bright Field to Dark Field, the black-white contrast in the layers adjacent to the top surface is unchanged, while the black and white parts of the contrast are interchanged in the layers adjacent to the bottom foil surface.

The application of the above summarized results enables

experimental determinations to be made of the nature of small loops by using the well known stereo technique developed by Diepers and Diehl (1966), Diepers (1967a,b) and Rühle (1967a).

#### 4.3.1.4 Non-edge loops

In Section (4.3.1.3) pure edge loops were considered, and since in F.C.C. metals most point defect agglomerates are of this type, it is justified to use this analysis. In B.C.C. metals though, theory causes one to expect a large shear component of the loop Burgers vector. If one of these loops is oriented, with respect to  $\vec{g}$ , such that  $|\vec{g} \cdot \vec{b}_s| \leq |\vec{g} \cdot \vec{b}_E|$  then the above properties of the black-white contrast can be safely used; but if  $|\vec{g} \cdot \vec{b}_E| < |\vec{g} \cdot \vec{b}_s|$  then different properties of the black-white contrast can arise.

#### 4.3.1.5 Small voids

In the case of a large void it is assumed that the vicinity of the void is strain-free. In the case of a small void there is an associated spherically symmetric strain field and the contrast properties are exactly the same as those for small Frank loops, except that  $\vec{\ell}$  is always parallel or anti-parallel to  $\vec{g}$ .

#### 4.3.1.6 Stacking fault tetrahedra

Quenching, or irradiation with fission fragments or other massive particles, or in some instances neutrons, may cause stacking fault tetrahedra. A stacking fault tetrahedron's associated strain field is much less than the strain field associated with a Frank loop consisting of the same number of atomic defects, and as a result a small tetrahedron's black-white contrast is weak (Brown (1964), Chick (1966)). Due to their small strain field, the diffraction contrast of stacking fault tetrahedra

resembles more closely their geometrical shape than does the contrast of small Frank loops, and tetrahedra of less than  $50 \text{ \AA}$  have been identified on micrographs by their characteristic shape alone.

Black-white contrast with a 'line of no contrast' perpendicular to  $\vec{g}$  has to date been observed only for  $\langle 100 \rangle$  foil-orientations with a  $\vec{g} = \{220\}$  operating diffraction vector. This characteristic 'line of no contrast' has been explained by Brown (1964) by considering the symmetry property of the strain field of a tetrahedron.

#### 4.3.2 Large dislocation loops

##### 4.3.2.1 Contrast properties

The geometrical shape of a loop is directly resolvable if it has a diameter greater than about  $0,5 \xi_g$ .

From the contrast calculations for single, straight dislocations in an elastically isotropic medium, produced by Hirsch, Howie and Whelan (1960), and Howie and Whelan (1961, 1962) it is known that for kinematic diffraction conditions ( $W \gg 1$ ) the dislocation image (i.e. intensity minimum) lies to that side of the dislocation core position where the lattice rotations introduced by the local curvature of the reflecting planes, due to the defect, tend to minimise the deviation from the Bragg angle. Due to the fact that loops are usually viewed under two-beam dynamical conditions, the magnitude of the image shift is dependent on the magnitude of the excitation error  $W_g$  and on the depth of the object (Howie and Whelan (1962)). Maher and Eyre (1971) showed that there is a critical value of the excitation error, say  $W_g^*$ , such that for all  $W_g > W_g^*$  the displacement of the image relative to the dislocation core is depth independent, and is determined by the local lattice curvature only.

This image shift property of dislocations enables one to differentiate between vacancy and interstitial loops and this method for loops with Burgers vectors  $\vec{b}$  perpendicular to the loop habit planes, is described in Section 4.4.

If  $\vec{b}$  contains a shear component parallel to the loop plane; application of this method may lead to errors. If  $\vec{b}$  has a shear component, the direction, irrespective of sign of  $\vec{b}$ , must also be known. Maher and Eyre (1971) give details, and faulted loops are treated by Mazey and Barnes (1968).

#### 4.4 THE EXPERIMENTAL DETERMINATION OF THE VACANCY OR INTERSTITIAL CHARACTER OF LOOPS

##### 4.4.1 Determination of the nature of the loops

Due to the shifting of the dislocation image for  $W_g \neq 0$  the projected loop position (intensity minimum) is either wholly inside or wholly outside the true dislocation core position. This is determined by the sense of rotation of the reflecting plans around the dislocation core. On changing the diffraction conditions from  $+\vec{g}$  to  $-\vec{g}$  with fixed sign of  $W_g$ , or by keeping  $\vec{g}$  fixed and changing the sign of  $W_g$  the intensity minimum of the image shifts from one side of the dislocation core to the other i.e. producing 'inside' to 'outside' contrast or vice versa. These image shifts are described in terms of the well known inequalities for dislocation loops:

$$\begin{aligned} \text{outside contrast implies } (\vec{g} \cdot \vec{b}) S_g &> 0 \\ \text{and inside contrast implies } (\vec{g} \cdot \vec{b}) S_g &< 0 \end{aligned}$$

For the case of loops in the size range 100 Å to 500 Å in

diameter  $W_g$  must be  $> \sim 0,6$  for the inside/outside contrast effect to be independent of depth in the foil. In addition for high-order reflections (e.g.  $\{310\}$ ,  $\{222\}$ ,  $\{321\}$ )  $W_g > 0,6$  must be used for some of the  $\pm \vec{g}$  pairs because these give the best cases of inside/outside contrast.

The nature of the loop can be determined from the sense of the Burgers vector, i.e. whether the defect has a 'centre of compression' or a 'centre of dilation'. This can be determined from the inequalities above.

However two possible senses of inclination of a dislocation loop are possible as shown in Figure 4.6. Since it can be seen from Figure 4.6 that opposite results can be obtained for a given sign of  $(\vec{g} \cdot \vec{b})$  it follows that for a loop characterisation the sense of inclination of the loop must also be known.

A number of methods of loop analysis have been proposed (Mazey *et al.*, (1962), Maher and Eyre (1971), Groves and Kelly (1961, 1962), Bell and Thomas (1966), Edmonds and Williamson (1964), Kelly and Blake (1973)). For perfect edge loops all these methods work but it has been shown by Maher and Eyre (1971) that loops with a shear component, only show contrast equivalent to a perfect edge loop until the shear component reaches a certain value. The important points of dislocation loop analysis are treated in detail by Edington (1975).

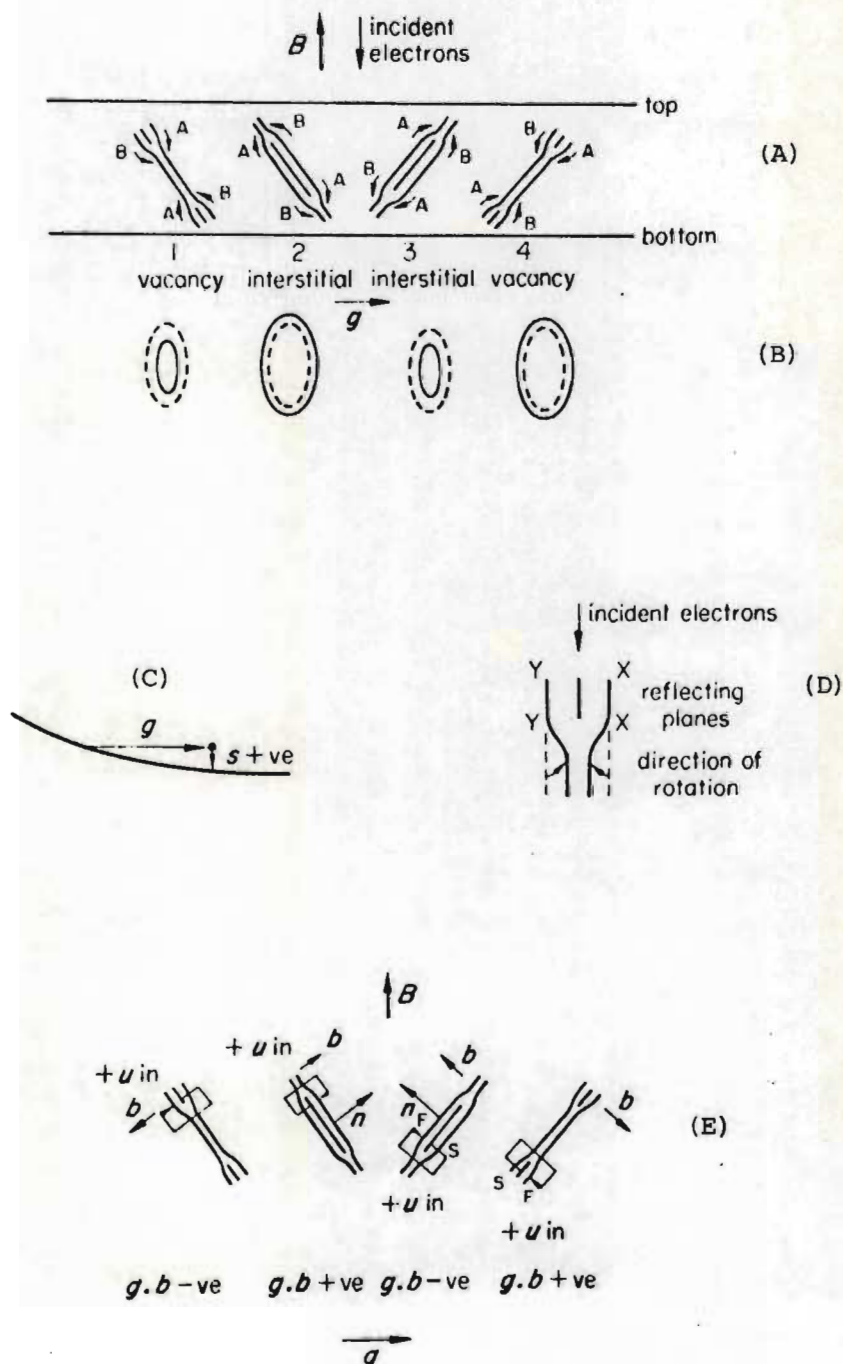
#### 4.4.2 Determination of the sense of inclination of a loop

The determination of the sense of inclination of a loop relative to the electron beam direction can be carried out in a number of ways - the most important of which are summarized below.

Figure 4.6

Inside and outside contrast for the two possible orientations of vacancy and interstitial loops. (from Edington (1975)).

- (A) The four possible configurations of inclined vacancy or interstitial loops.  
 (B) The position of the image (heavy line) relative to the core (dashed line).  
 (C)  $s$  positive for the operative reflection.  
 (D) The rotation of the reflecting planes at an edge dislocation.  
 (E) The direction of  $b$  for each loop, the upward drawn plane normal  $n$ , and the sign of  $g \cdot b$  are shown in each case.



- A. For large loops ( $> 500 \text{ \AA}$ ) the simplest method is to tilt the specimen through a large angle ( $\sim 30^\circ$ ) and note the change in shape of the projected loop image. From a knowledge of the sense of the tilt the inclination of the loop can be determined.  
For loops with diameters smaller than about  $500 \text{ \AA}$  the following methods can be used:
- B. If a loop which is elliptical in projection is tilted through some angle, say  $20^\circ$  or  $30^\circ$ , the major axis of the loop will rotate either clockwise or anticlockwise. By knowing the sense of the tilt and determining the sense of rotation of the major axis of the loop from the micrographs, the loop inclination can be determined.
- C. The dislocation loop may be tilted to the edge-on configuration and the habit plane evaluated from its trace.
- D. Method B. may be extended to a trace analysis by imaging the dislocation loop at two or more nearly exact orientations and then assigning a major axis to the image. This major axis vector is then assigned a crystallographic direction which is then assumed to lie in the plane normal to the electron beam direction  $\vec{B}$  and the loop plane. A graphical solution is then obtained by normalizing the families of all possible loop normals  $\vec{n}$ , for each  $\vec{B}$  considered, to a convenient orientation; and their intersections are therefore solutions to equations of the form  $\vec{t} \cdot \vec{n} = 0$  where  $\vec{t}$  is the estimated trace of the loop's minor axis in the foil.

## 4.5

SUMMARY

The diffraction contrast images of the various fundamental crystallographic defects is now well understood and in addition the theory to explain these fundamental diffraction contrast images has been formulated. Furthermore, procedures now exist to determine the vacancy or interstitial nature of large and small dislocation loops and thus the basic tools are available for use in attempting to explain the more complex radiation damage morphologies which are observed in neutron irradiated metals.

## CHAPTER FIVE

### EXPERIMENTAL PROCEDURE

- 5.1 Introduction
- 5.2 The specimens used
- 5.3 Crystal growing system
  - 5.3.1 Introduction
  - 5.3.2 Crystal growing apparatus
  - 5.3.3 Crystal mould assembly
  - 5.3.4 The seed crystal
- 5.4 Irradiations
- 5.5 Specimen preparation
  - 5.5.1 Introduction
  - 5.5.2 Crystals used for etch pit studies
  - 5.5.3 Crystals used in mechanical testing
  - 5.5.4 Electron microscopy specimens
- 5.6 Electron microscopy

## 5.1 INTRODUCTION

In the course of this work single crystals of pure copper were grown and then irradiated with fast neutrons at elevated temperatures. These specimens were then examined using various experimental techniques, the primary technique in the case of this thesis being electron microscopy.

## 5.2 THE SPECIMENS USED

The specimens used in the present study were seeded single crystals of pure copper 12 cm in length and of square cross-section ( $3 \times 3$  mm). They were grown under vacuum in split graphite moulds (Figure 5.1) by means of a modified Bridgman technique. The copper used was 99.999% pure metal obtained from the American Smelting and Refining Company (analysis shown in Table 5.1).

Each crystal was cut into two equal lengths by means of a spark erosion cutter after which one half was used to determine the pre-irradiation dislocation density and mechanical properties while the other half was irradiated.

## 5.3 CRYSTAL GROWING SYSTEM

### 5.3.1 Introduction

In the Bridgman technique the copper is placed in a suitable crystal mould made of graphite (Figure 5.1) with the axis of the desired crystals vertical. The mould is surrounded by a suitable heat source and is under vacuum. The heat source is arranged in such a way so as to produce a temperature gradient up the length of the crystal




Figure 5.1

The two halves of the graphite crystal mould containing a seed crystal and a set of grown crystals.

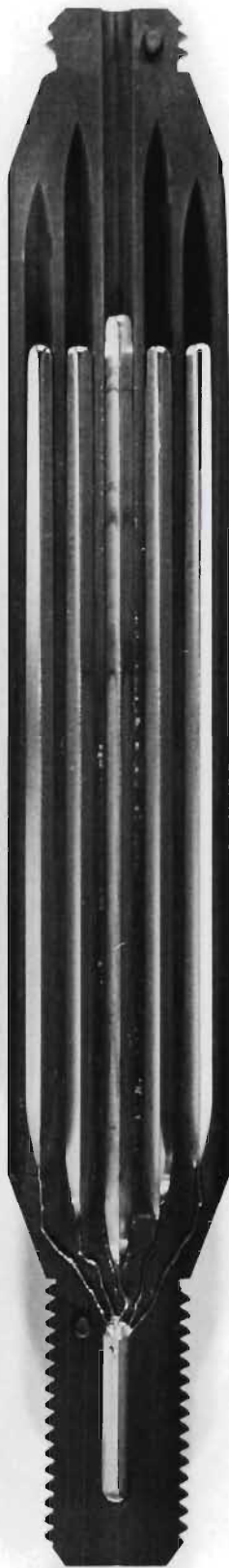
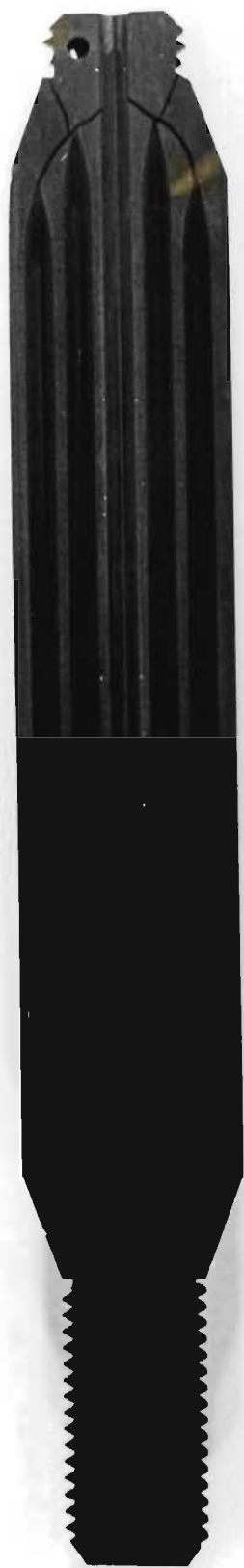


TABLE 5.1IMPURITY CONTENT OF 99,999% PURITY COPPER (SPECTROGRAPHIC ANALYSIS)SUPPLIED BY THE AMERICAN SMELTING AND REFINING COMPANY.

Fe	<	0,7 ppm.
Sb	<	1 ppm.
Pb	<	1 ppm.
Sn	<	1 ppm.
Ni	<	1 ppm.
Bi	<	0,1 ppm.
Ag	<	0,3 ppm.
As	<	2 ppm.
Cr	<	0,5 ppm.
Si	<	0,1 ppm.
Te	<	2 ppm.
Se	<	1 ppm.
S	<	1 ppm.

mould. This temperature gradient is then caused to move up the length of the mould at a suitable rate and thus there is progressive freezing of the set of crystals from the bottom to the top.

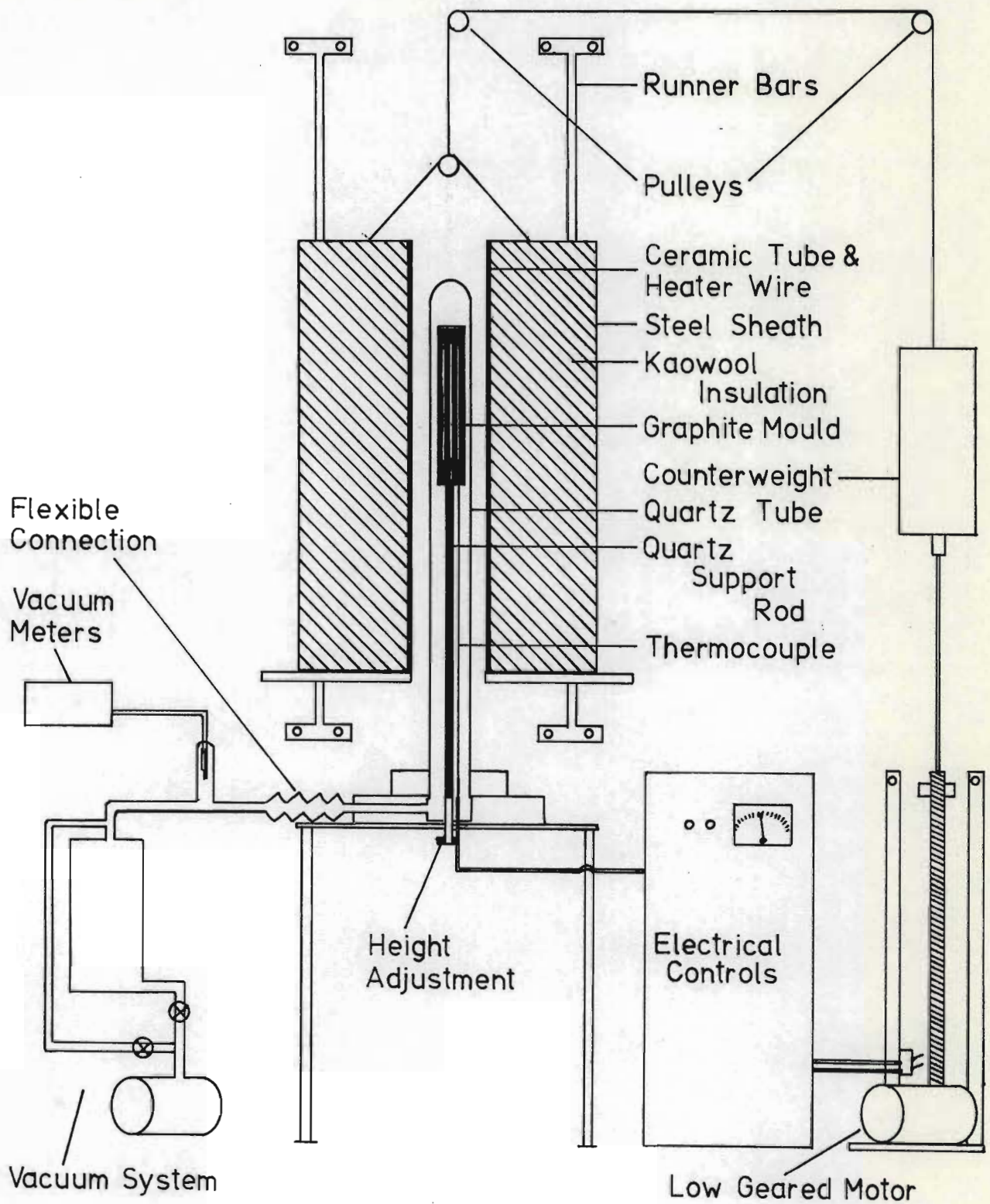
In the case of this work the method used was to keep the crystal mould fixed in the vacuum and to slowly drive the furnace upwards.

### 5.3.2 Crystal growing apparatus

The crystal growing apparatus (Figure 5.2) consists of a quartz tube sealed at one end and connected to a vacuum system at the other end. Into this quartz tube is fitted a graphite crystal mould which stands on a quartz support rod, the height of which can be adjusted from outside the vacuum through a vacuum tight seal. A stainless steel sheathed thermocouple is fitted into the base of the graphite mould and the electrical leads of the thermocouple lead out through a vacuum tight glass-to-metal seal to the thermocouple meter. A flexible vacuum coupling connects the quartz tube assembly to the vacuum system so as to minimise mechanical vibrations from the pumps.

The heat is supplied to the crystal mould by means of a resistive heater which was constructed by winding nichrome resistance wire around the outside of a ceramic inner tube whose diameter is about 1 cm greater than that of the quartz tube (Figure 5.2). The resistance wire is secured to the ceramic tube by means of a ceramic cement (Coarse Macle 3/8S from Vereeniging Refractories Ltd.). This wire is not uniformly wound but is wound to provide a temperature gradient as close to the ideal as is possible. The ceramic tube and heater wire assembly was then mounted firmly into an outer steel sheath and the space between the ceramic tube and outer sheath packed with thermally insulating kaowool (Figure 5.2).

# Crystal Furnace Arrangement



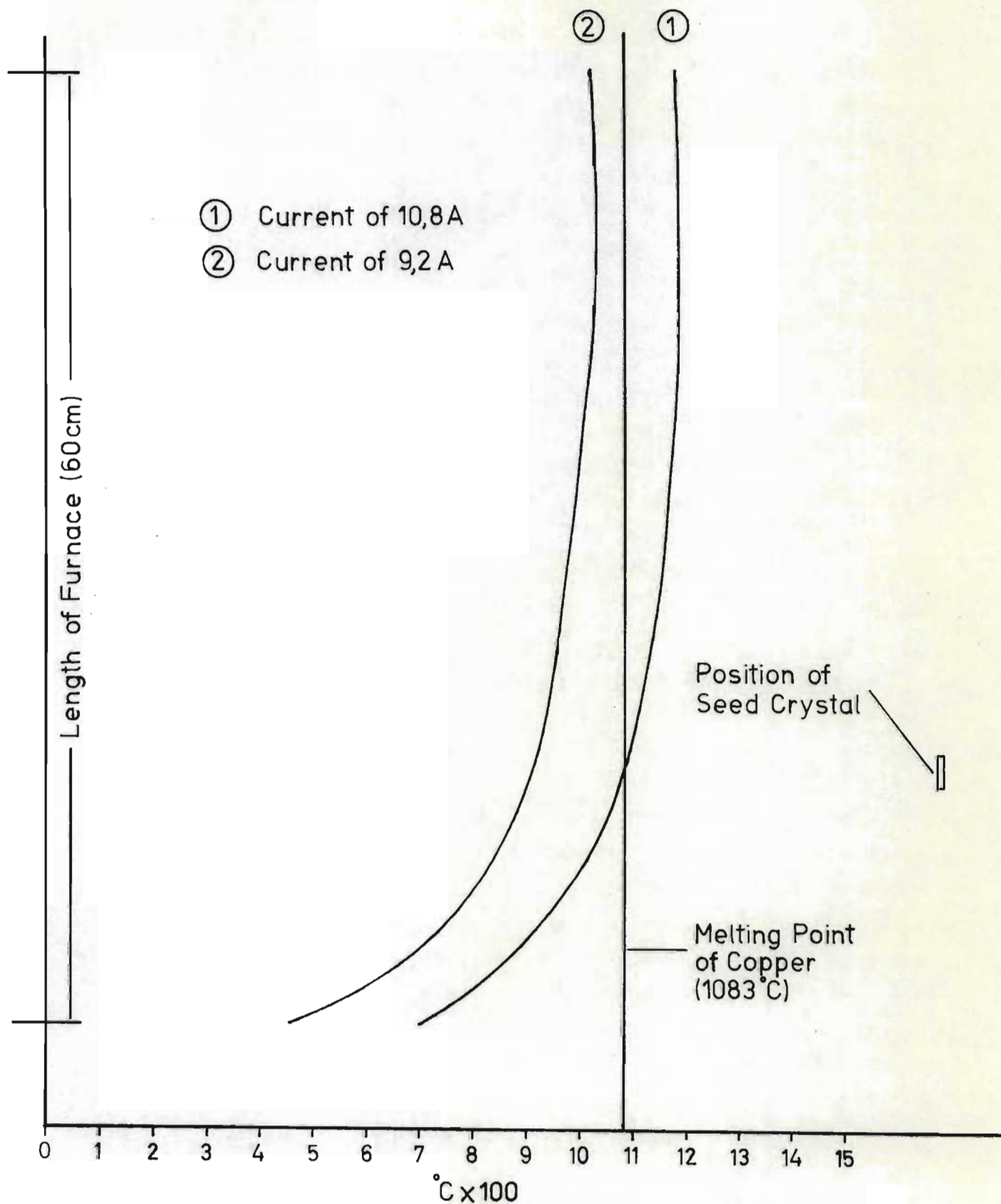
At this point the temperature profile of the ceramic tube and heater wire assembly on its own was known from experimental measurement, and thus it was possible to vary the density of packing of the kaowool up the length of the tube and so effect fine adjustments to the temperature profile of the furnace. It was found that a good profile could be achieved in this way (Figure 5.3). The furnace draws its heating current directly from the laboratory's mains supply via control circuitry, and the current used under full load is 10,8 A.

The completed furnace assembly is mounted onto a platform which is attached to the laboratory wall for rigidity. A steel cable is connected to the platform and runs over two fixed pulleys (Figure 5.2) to a counterweight which in turn is attached to a very low geared variable speed motor which can drive the furnace upwards at a speed of between  $1,5 \text{ cm.hr}^{-1}$  and  $12 \text{ cm.hr}^{-1}$  which results in a total crystal growing time of 32 hours to 4 hours. The variable speed motor assembly is supplied with two microswitches which first switch the furnace current down to 2A and then switch off the variable speed motor itself at the end of a crystal growing run. The reason why the furnace current is switched down to 2A and not switched off is that it was found that if the nichrome heating wire was allowed to cool to room temperature it became brittle and broke, but the 2A current running permanently when the furnace is not in use ensures that the nichrome wire is always warm and thus does not break.

The current to the furnace can be varied thus making it possible to anneal crystals under vacuum for any desired length of time.

### 5.3.3 Crystal mould assembly

Part of the graphite crystal mould containing a set of crystals

Temperature Profile of Crystal Furnace

and their seed is shown in (Figure 5.1). In addition to the two mould halves shown in (Figure 5.1) there is a screw-on cap which fits over the seed end and serves to hold the two mould halves firmly together, and also a screw-on reservoir which screws on at the top end and serves as the receptacle into which the high purity copper chunks are placed before melting. This reservoir is provided with a graphite lid which rests loosely on the top to prevent copper vapour from escaping and coating the inside of the quartz tube during melting, but which is loose enough to allow all gas to escape from the mould during the evacuation procedure. A thermocouple fits into the lower screw-on cap with its hot junction at a position approximately two thirds of the way up the seed chamber, and thus it is possible to detect when the top third of the seed has melted.

The crystals shown in (Figure 5.1) are of 3 mm square cross section as is also the seed which is 2,3 cm in length and which is joined to the crystals by thin copper strands which can easily be cut after the completion of crystal growth.

#### 5.3.4 The seed crystal

When a seed crystal is cut from a large crystal it is essential to ensure that the seed fits the crystal mould sufficiently well to prevent copper liquid from running down between the seed and the sides of the mould where it can freeze rapidly, resulting in the nucleation of unwanted crystal orientations. This problem is only encountered once when initiating the production of a series of crystals with the same orientation, since after the first set has been grown one of these crystals can be cut up to produce new seeds which fit the mould

perfectly since the seed compartment has the same cross section as the grown crystals.

Before a set of crystals is grown the inside of the graphite mould is coated with a thin layer of amorphous carbon to ensure that a very smooth inner surface is achieved which is free from any small, sharp irregularities which could cause different crystal orientations to be nucleated during freezing. This coating is deposited on the mould halves by gently passing an oxy-acetelene torch over them.

#### 5.4 IRRADIATIONS

A High Temperature Irradiation Rig (H.T.R.) was designed and built at the University of Natal for the purpose of carrying out accurately controlled fast neutron irradiations of the copper specimens. The design and construction of this rig is explained in detail in Chapter 6. All irradiations undertaken in the course of this work were carried out using this rig and the SAFARI 1 reactor at Pelindaba.

The copper crystals were all carried to Pretoria by the author to ensure that they suffered no rough handling in transit which could possibly have resulted in their initial dislocation densities being altered before irradiation.

After irradiation the rig was pressurized with one atmosphere of helium gas and stored underwater in the reactor pool for about one month to allow the radioactivity of the crystals and their container to decay to a level which is safe to handle. The specimens, still in their protective specimen block (Figure 6.7B) were then transported by air to Durban in airtight containers filled with vermiculite to cushion the specimen block against any mechanical shocks that the

container might receive.

For this work a total of five irradiations were carried out (Table 5.2).

## 5.5 SPECIMEN PREPARATION

### 5.5.1 Introduction

The irradiated specimens were studied by means of three experimental techniques:

1. Etch pit techniques.
2. Mechanical testing.
3. Electron microscopy.

Investigations using techniques 1. and 2. were carried out in Pietermaritzburg by Dr. P.J. Jackson and Messrs. P. Nathanson and K. Black, and are not dealt with to any depth in this thesis.

### 5.5.2 Crystals used for etch pit studies

The crystals used for etch pit studies were transported by hand to Pietermaritzburg. The orientations of the {111} atomic planes of these crystals were determined by means of Laue Back-Reflection X-ray methods after which {111} planes were exposed using a spark erosion cutter. These planes were then electro-chemically polished until they were extremely flat and then chemically etched in similar fashion to that employed by Mitchell *et al* (1967).

The etched {111} planes showing the dislocation structure of the irradiated crystals were then examined by means of optical microscopy.

TABLE 5.2  
IRRADIATIONS PERFORMED

Irradiation run	Temperature °C	Dose f.n. cm <sup>-2</sup>
1	250	$1,24 \times 10^{17}$
2	300	$2,92 \times 10^{17}$
3	350	$2,79 \times 10^{17}$
4	400	$2,59 \times 10^{17}$
5	250	$2,47 \times 10^{17}$

### 5.5.3 Crystals used in mechanical testing

By means of Laue Back-Reflection X-ray methods the orientation of the slip planes and tensile axes of the copper crystals were determined. These crystals were then examined by means of a sensitive tensile testing machine interfaced with a mini-computer - this apparatus is described fully in Nathanson (1975).

### 5.5.4 Electron microscopy specimens

A Rigaku Denki 1 KW X-ray generator equipped with a high speed polaroid camera was employed together with Laue Back-Reflection techniques to determine the orientation of the  $\{111\}$  planes of the copper crystals. Slices of copper 0,5 mm thick with  $\{111\}$  faces were then sectioned from the bulk crystals using a spark erosion cutter after which the spark cutter was used to cut 3 mm diameter discs from these slices.

A Bainbridge unithin electropolishing apparatus was then used with an electrolyte consisting of 25% orthophosphoric acid, 50% deionized water and 25% ethanol to produce dish-shaped indentations on the two sides of the copper discs.

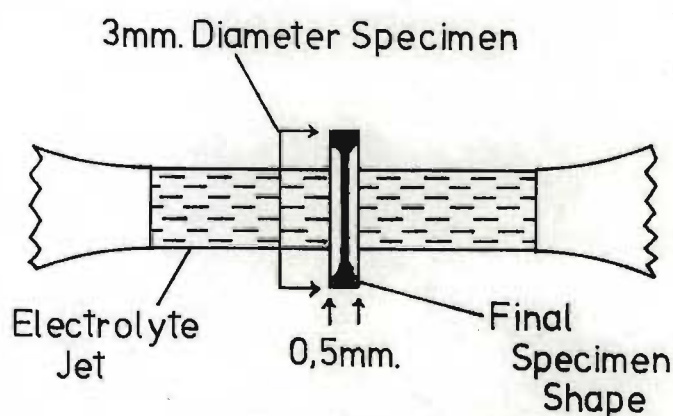


Figure (5.4) Schematic representation of a specimen being polished in the Unithin jet-polisher.

The unithin apparatus was operated at a potential of 30 V which produced a polishing current of about 200 mA. The polarity of the electrodes was changed every two seconds and the total 'dishing' time was calculated to almost penetrate the discs (leaving about 40  $\mu\text{m}$  of metal). As a result of polishing away more than 0,4 mm of metal and since the specimens were polished from both sides (Figure 5.4) all spark erosion damaged was removed (Hazzledine (1963)).

The 'dished' discs were then suspended by means of platinum tipped tweezers in an electropolishing bath operated at a stabilized voltage of 1 V. The electrolyte consisted of a mixture of 50% orthophosphoric acid and 50% deionized water maintained at a temperature of 34°C which resulted in an optimum polishing current of 15 mA. The specimen was kept under constant observation by means of a telescope until perforation occurred, at which point it was removed from the polishing bath and washed thoroughly in a sequence of four washing baths:

1. 10% orthophosphoric acid and deionized water,
2. deionized water,
3. 1% polyethylene glycol 400 and deionized water,
4. deionized water.

The specimens were then stored in ethyl alcohol.

## 5.6 ELECTRON MICROSCOPY

All of the electron microscopy was carried out using a JEOL Jem 100C electron microscope operated at an accelerating voltage of 100 KV and fitted with a goniometer stage capable of  $\pm 60^\circ$  tilt. A double tilting specimen holder was used which enabled a maximum tilt of  $\pm 45^\circ$  to be performed about the other axis.

The micro-structures encountered in the irradiated specimens were characterised in terms of general damage morphology and the geometry of structural components of the damage (e.g. defect shape, dislocation appearance and the nature of dislocation loops etc.).

## CHAPTER SIX

### THE HIGH TEMPERATURE IRRADIATION RIG

- 6.1 Introduction
- 6.2 Design criteria of the High Temperature Irradiation Rig (H.T.R.)
- 6.3 Construction of the H.T.R.
- 6.4 H.T.R. Instrumentation
- 6.5 Performance of the H.T.R.
- 6.6 Handling and loading procedures of the H.T.R.

## 6.1 INTRODUCTION

The High Temperature Irradiation Rig (H.T.R.) was designed and constructed to irradiate single crystals of high purity copper to a total integrated fluence of fast neutrons ( $E > 0,1$  MeV) of  $10^{17}$  to  $10^{18}$  f.n.  $\text{cm}^{-2}$  at temperatures in the range of  $100^{\circ}\text{C}$  to  $450^{\circ}\text{C}$ . The irradiation times required to achieve these fluences in the H.T.R. utilizing the SAFARAI I reactor (type O.R.R.) are between ten and two hundred hours, with the reactor operating power at 20 MW. The reactor's neutron spectrum was not modified in any way e.g. by filtering out thermal neutrons.

## 6.2 DESIGN CRITERIA OF THE HIGH TEMPERATURE IRRADIATION RIG

To obtain the required fast neutron fluence it was necessary to place the front end of the rig as close to the reactor face as possible. Thus the gamma-heating was quite severe (2 watts per gram at full power) and thus it was necessary to design the H.T.R. such that sufficient heat is lost to the reactor pool water to allow the lower required temperatures to be reached but that heat loss is not so great as to prevent the highest required temperatures from being attained. Furthermore, to attain the upper temperatures, a heater had to be built into the front end of the rig and the associated temperature control circuits had to be provided.

It is necessary to know the irradiation temperature as accurately as possible and thus thermocouples were provided for temperature measurement. The thermocouples were interconnected, by means of the control circuits, with the specimen heater assembly so that a stable temperature could be maintained throughout the irradiation run. It was required to keep the specimen temperature constant to within  $\pm 2^{\circ}\text{C}$ .

The control circuits had to adjust the output of the heater to allow for fluctuations in the gamma-heating produced by variations in the reactor itself, and also to allow for varying heat losses from the outside of the rig casing to the reactor pool water. Thus it can be appreciated that the lowest possible operating temperature of the rig is that temperature which is determined by the combined effects of the gamma-heating and the efficiency of thermal conduction through the components of the rig itself. The highest operating temperature obtainable is determined by the fact that the heater assembly is embedded in an aluminium block (Figure 6.7A) and aluminium has a melting point of  $660,1^{\circ}\text{C}$ .

For experimental control it is necessary to ensure that all of the irradiations of the copper crystals are carried out under a helium atmosphere and thus it was necessary to design the H.T.R. with vacuum pumping facilities so that the air could be removed from the rig and helium gas admitted to the desired pressure. The helium gas is used for two purposes, firstly as an inert atmosphere for the crystals during and after irradiation and secondly, by varying the gas pressure the helium can be used as a heat exchange gas which is an additional temperature control mechanism.

After an irradiation run, provision had to be made for the rig, containing a pressure of one atmosphere of helium, to rest in a storage position under the surface of the reactor pool for a period of some weeks until the radioactivity of the specimens had decayed to a level safe to handle.

During the course of construction of the rig great care had to be taken to ensure that no impurities which could give rise to nuclides

with long half lives were trapped in any of the metal joints. Thus very stringent conditions of cleanliness were necessary during the welding and machining of the components and in addition all welds had to be perfectly sealed so that no impurities could penetrate them and be trapped at a later date after the completion of welding. The integrity of welds was checked by means of X-rays and by dia-penetrant tests to make quite certain that they were completely sealed and dirt free. In addition, wherever possible, parts were machined out of solid blocks of material rather than constructed by means of joining.

The only materials permitted to come into contact with the reactor pool water are B51S grade aluminium and 316 grade stainless steel. Thus the rig was constructed of these materials, all of which were obtained from the Atomic Energy Board's bonded store; each piece of material being individually numbered with an identity number which was re-engraved onto the finished component.

Before construction of the rig could commence it was necessary to produce a report to prove to the reactor safety committee that a serious or dangerous malfunction would not occur during an irradiation run. The design report had to show that the reactor and its operating personnel could be in no danger as a result of the operation of the H.T.R.

### 6.3 CONSTRUCTION OF THE H.T.R.

During an irradiation run the rig is mounted onto a bracket which is bolted to one of the stub pipes on the side of the SAFARI I reactor vessel, while the rig's instrumentation is situated on the instrument gallery (Figures 6.1, 6.2, 6.3, 6.4). The rig consists of

FIG (6.1)

The H.T.R. and Control Panel in Position

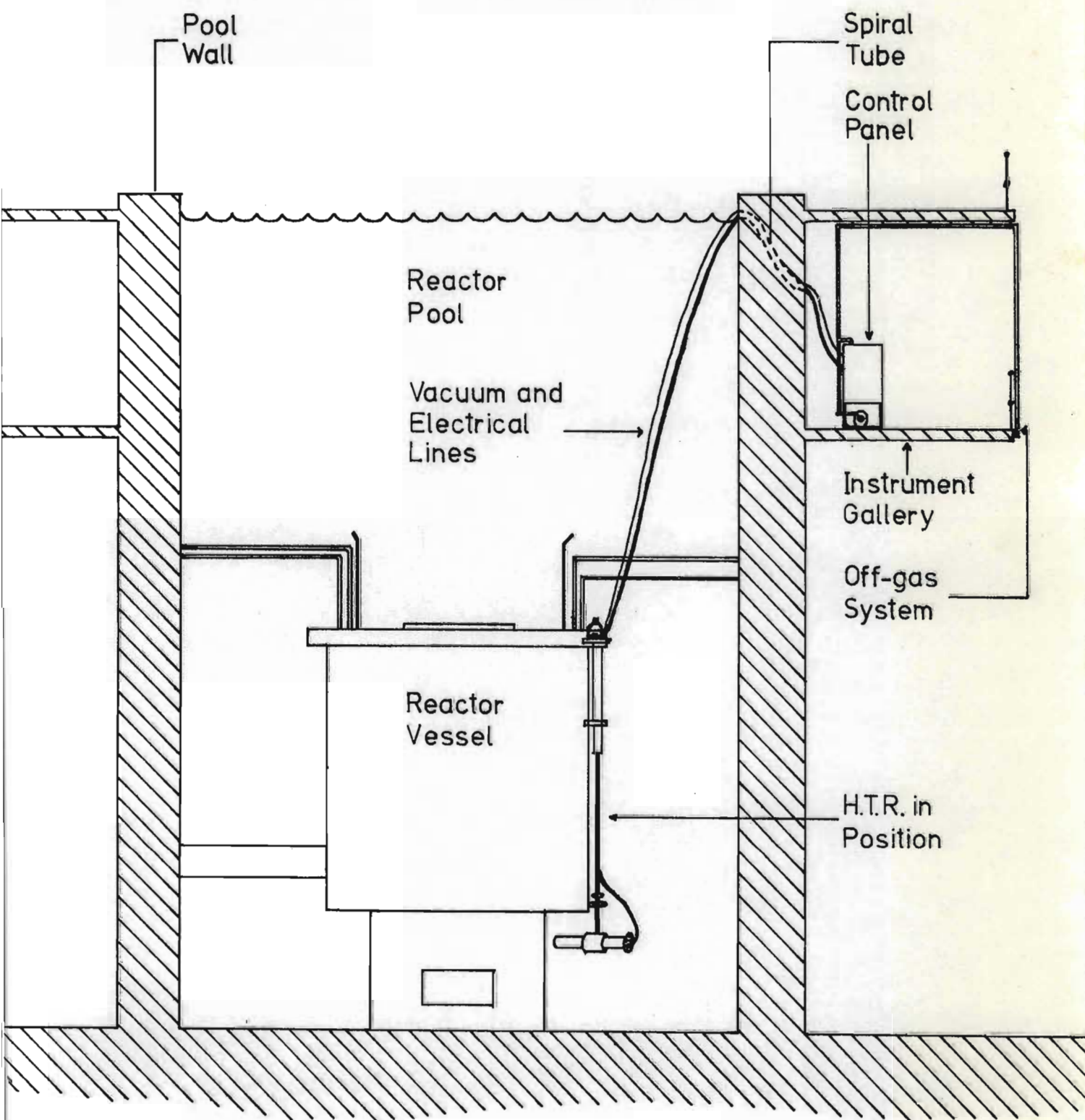


Figure 6.2

The H.T.R. in position on the SAFARI I reactor.

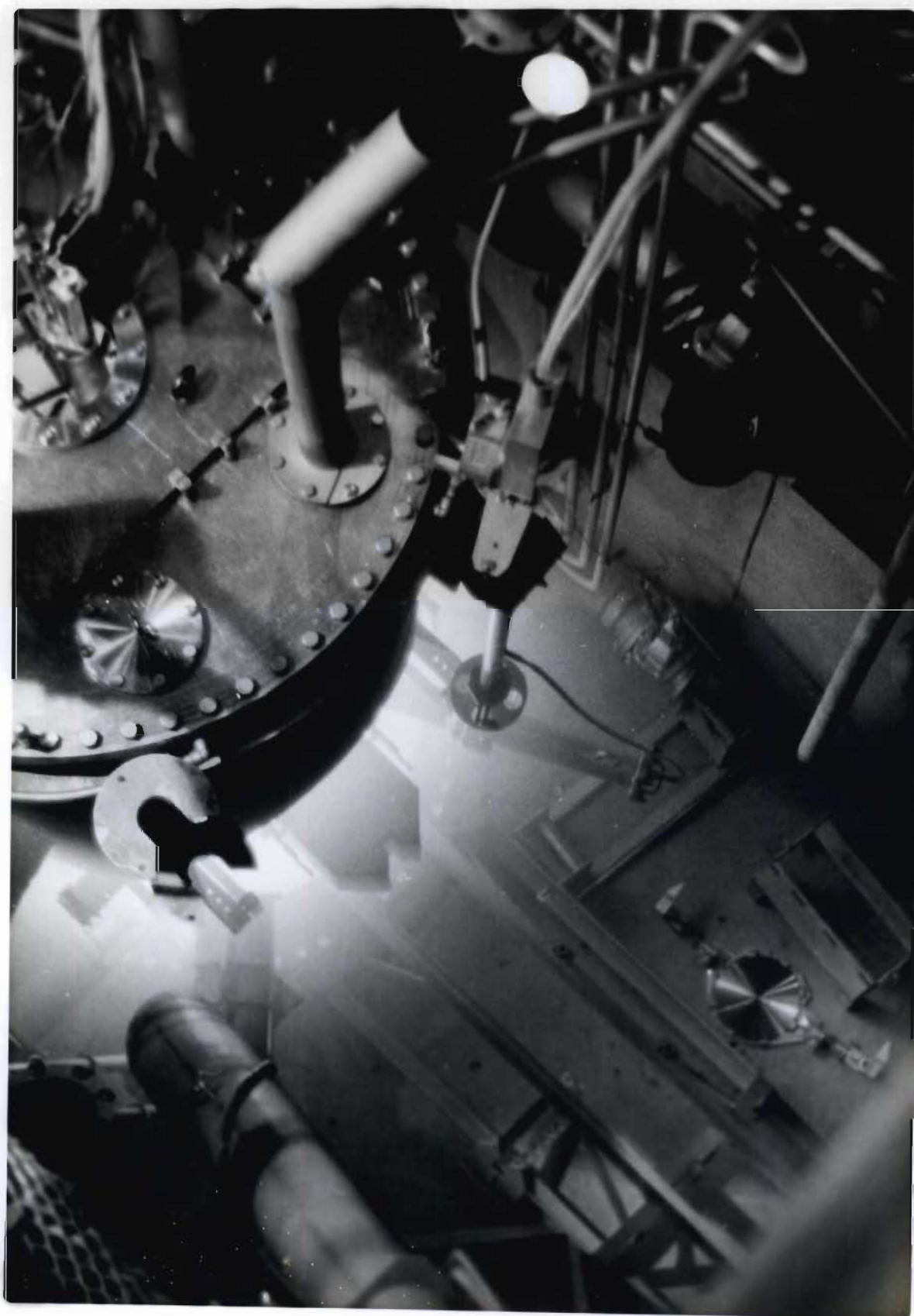
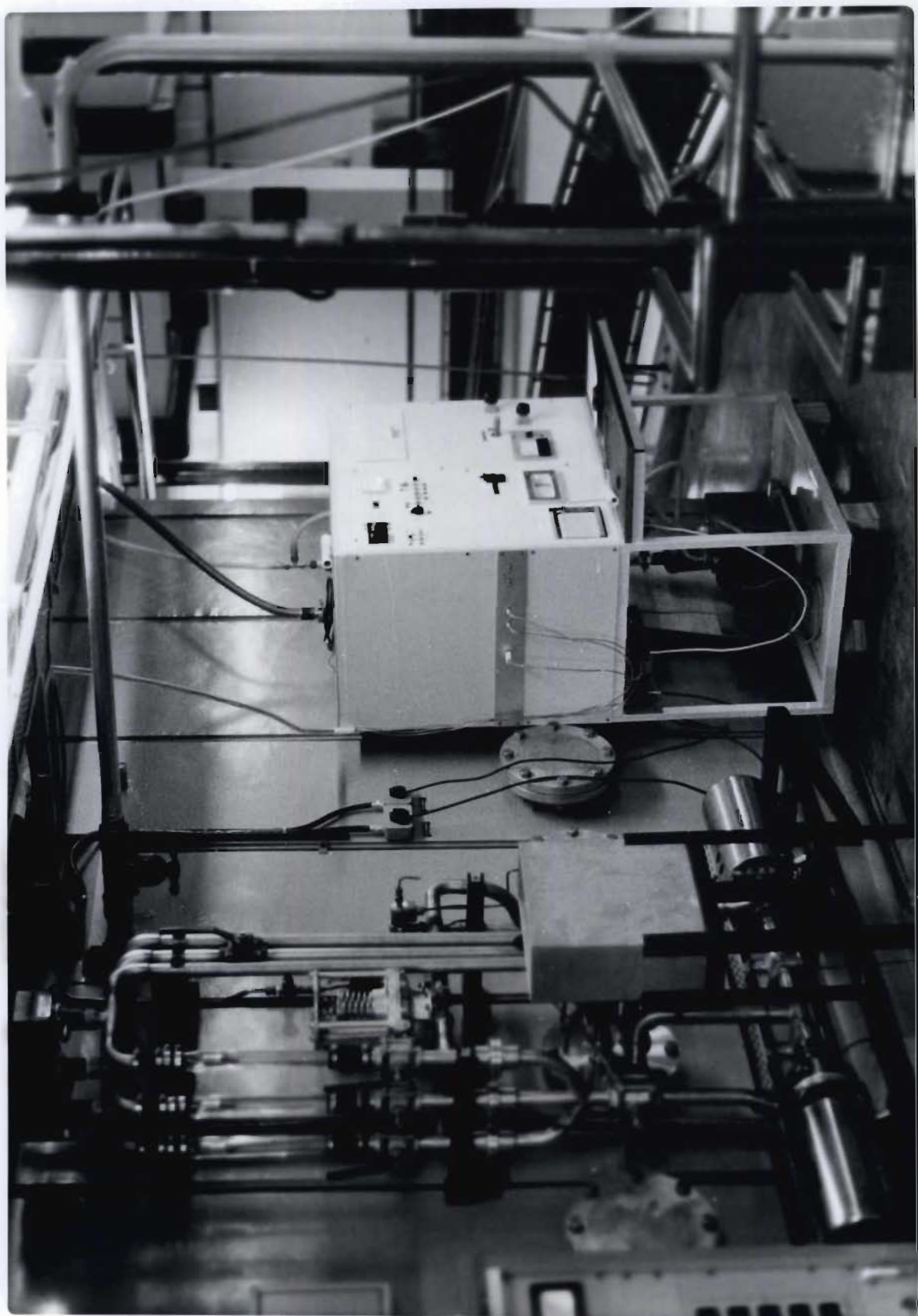
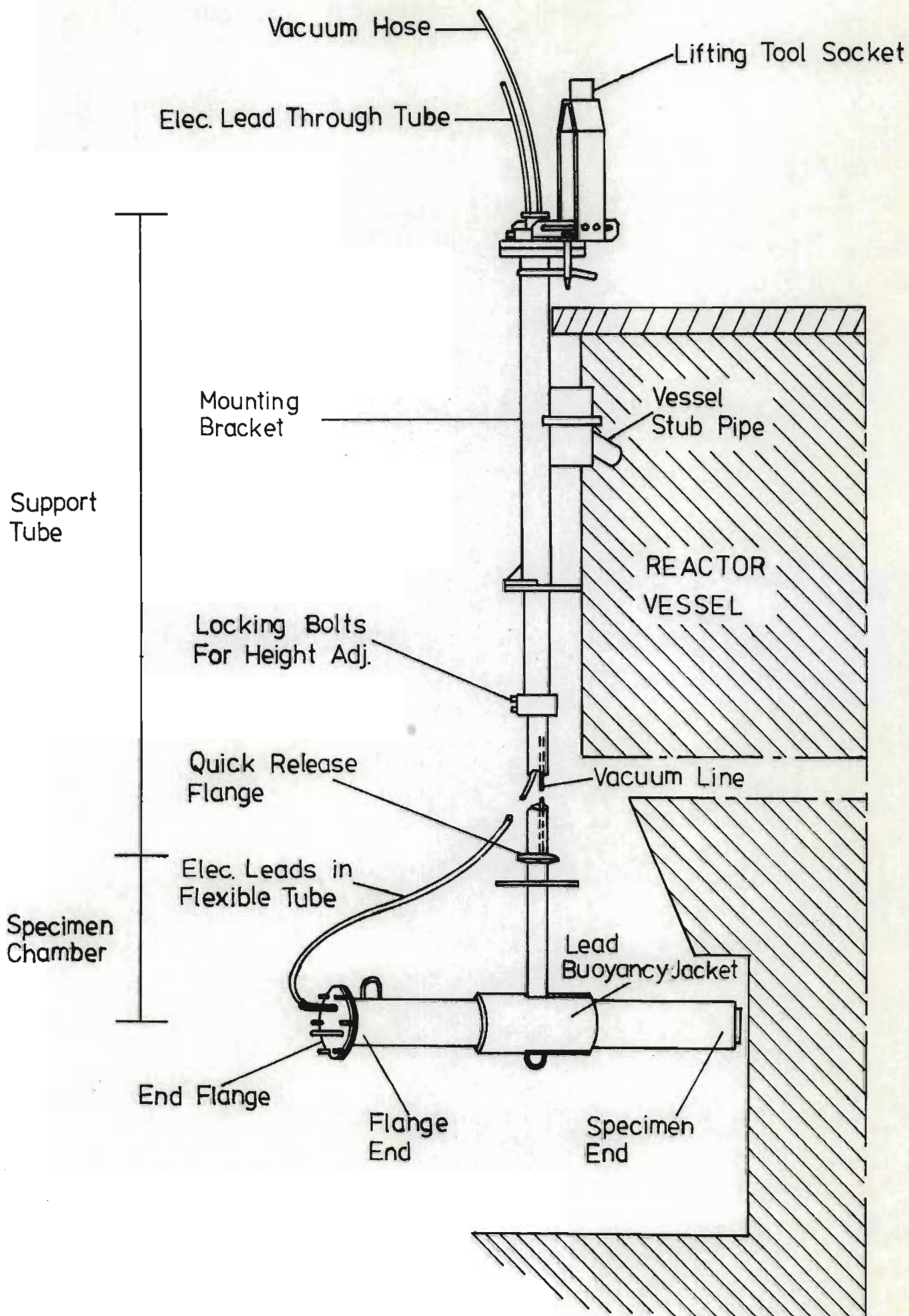


Figure 6.3

The H.T.R. control panel in position on the instrument gallery.



FIG(6.4) H.T.R.



two main sections (Figure 6.4):

1. The support tube assembly.
2. The specimen chamber assembly.

These two sections can be rapidly disconnected from one another by means of a quick release vacuum coupling (Figure 6.4).

The support tube assembly consists of an aluminium tube 6,3 cm in diameter to which is attached the male half of the mounting bracket. This 6,3 cm diameter tube can slide up and down in the male half of the mounting bracket to allow the specimen end of the rig to be accurately centred in the neutron flux. This centering is done only once at which stage the support tube is clamped firmly into the correct height position. Inside the support tube are two tubes which are the vacuum line and the protective covering for the electrical leads (Figure 6.4). The former is a 2,5 cm diameter aluminium tube which is welded into position to be vacuum tight. The latter is a plastic tube of 2 cm diameter which extends out of the bottom end of the support tube and terminates at the end flange (Figure 6.4). The area inside the support tube around the vacuum and electrical leads fills with water via milled slots when the rig is submerged, which assists in reducing the buoyancy of the rig and so simplifies the underwater handling operations. The vacuum and electrical lines both pass out of the top of the support tube in the form of plastic pipes (Figures 6.2 and 6.4) and pass to the surface of the reactor pool where they pass through one of the spiral pipes in the reactor pool wall and so along to the instrumentation on the instrument gallery (Figure 6.1).

The specimen chamber assembly consists of the chamber itself and the specimen mount which fits inside the chamber (Figure 6.5A).

The main part of the chamber is a 12,7 cm diameter aluminium pipe which is 112 cm long. The specimen end of this pipe (Figure 6.6A) is cut off at an angle of about  $45^{\circ}$  so that the specimen end is parallel to the outer wall of the reactor vessel. This is necessary since the rig fits into position on the reactor vessel at an angle as can be seen in (Figure 6.2) - this is done so that the specimens can be positioned approximately in line with the fuel elements. The other end of the chamber projects out into the pool and is referred to as the flange end because it is sealed off by means of a vacuum tight end flange which is retained in place by six stainless steel swing bolts (Figure 6.6B).

The specimen mount (Figure 6.5B) is inserted into the chamber via the flange end opening. The rear end of the specimen mount has built into it the female part of a custom made pyrophyllite/stainless steel/aluminium plug which connects the electrical leads to a short length of electrical cable which in turn connects to a custom made glass to metal seal which is housed in a vacuum tight seal in the end flange (Figure 6.5A). The specimen mount consists of an aluminium tube fitted with three guide flanges. The specimen end guide flange is aluminium and is angled so as to fit flush with the inside of the front end of the chamber (Figure 6.5A). This flange contains a recess which houses the heater block and specimen block as shown in (Figure 6.7A). The heater and thermocouple leads pass backwards along the inside of the specimen mount insulated from one another and from the mount walls by means of hollow ceramic sheaths. These leads terminate at the custom made plug built into the rear guide flange which is also made of aluminium. Attached to the rear guide flange is a spring-loaded handling hook (Figure 6.5A,B) which presses against the inside of the end flange and so keeps the front guide flange in firm thermal contact with the front end of the chamber. The centre guide flange (Figure 6.5B) is made of cadmium which to some degree reduces the amount of damage

Figure 6.5

A.

Diagram of specimen chamber assembly.

B.

Specimen mount showing the cadmium shield in the centre and electrical plug on the right.

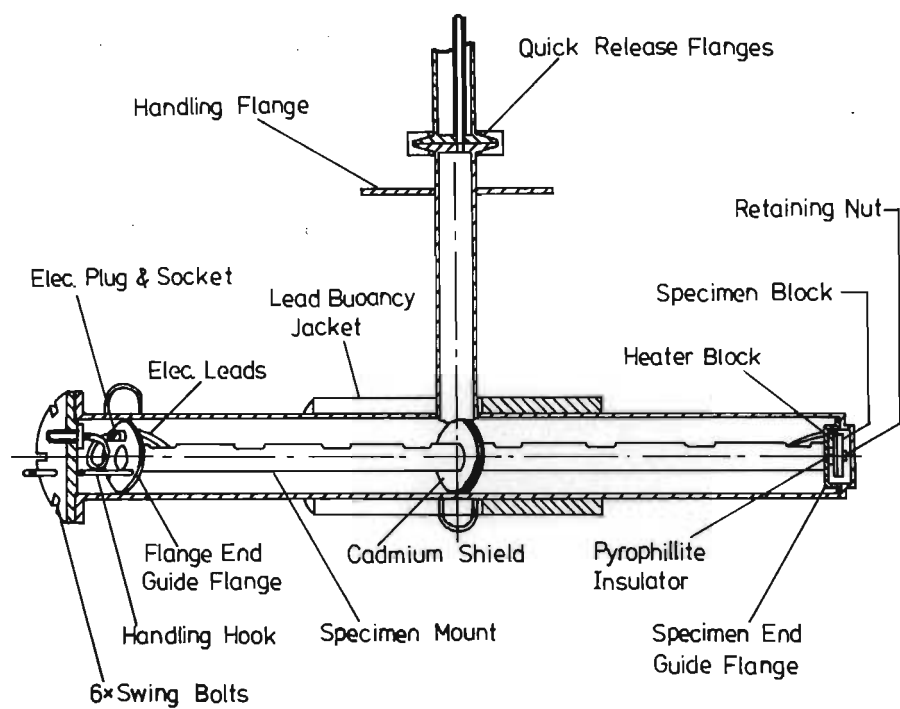


Figure 6.6

A.

The specimen-end weld showing the  
specimen block recess.

B.

The end flange showing the swing bolts  
and electrical leads.

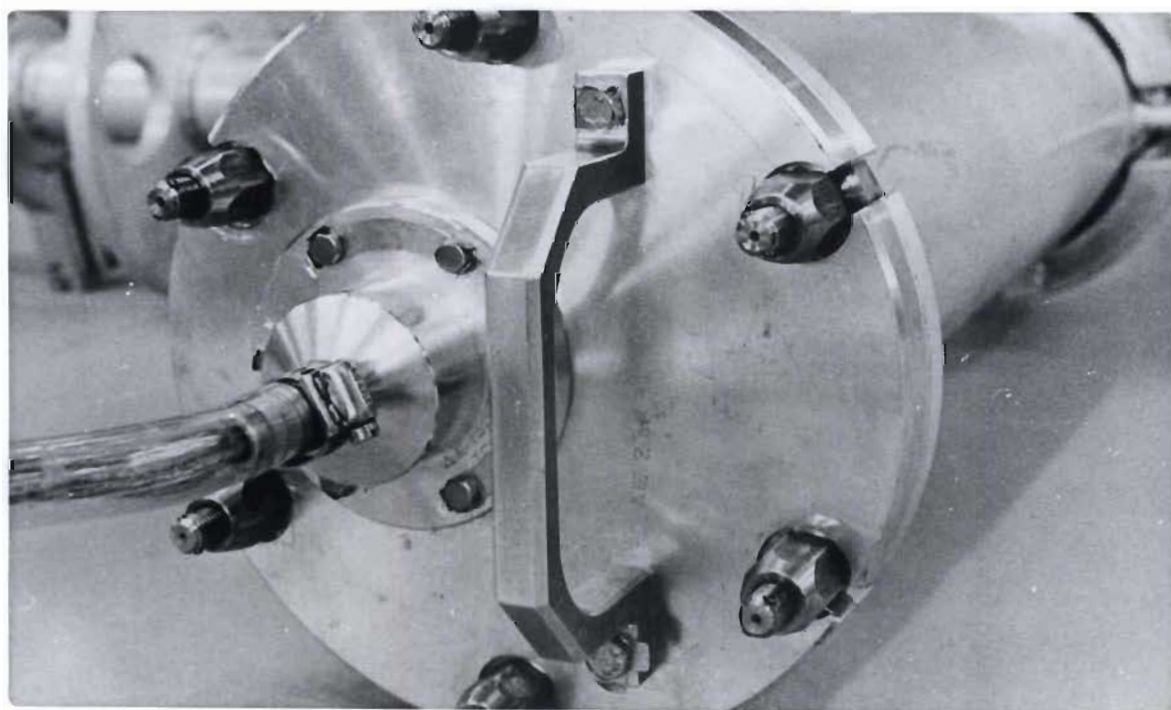
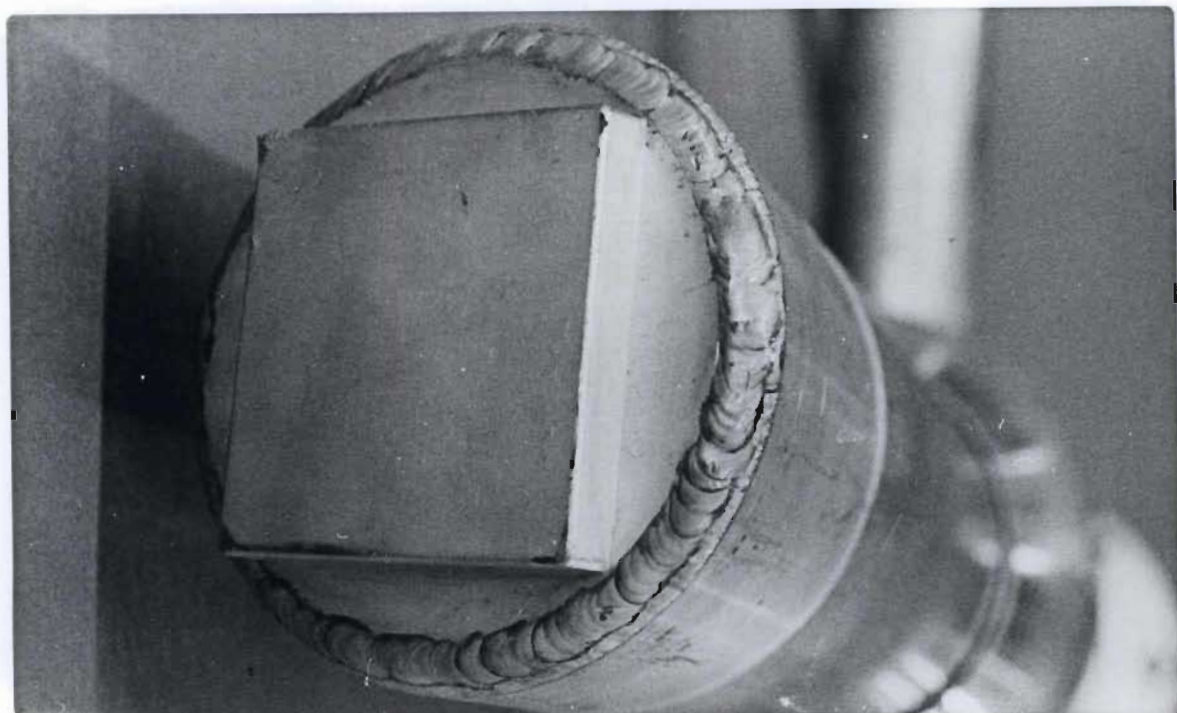


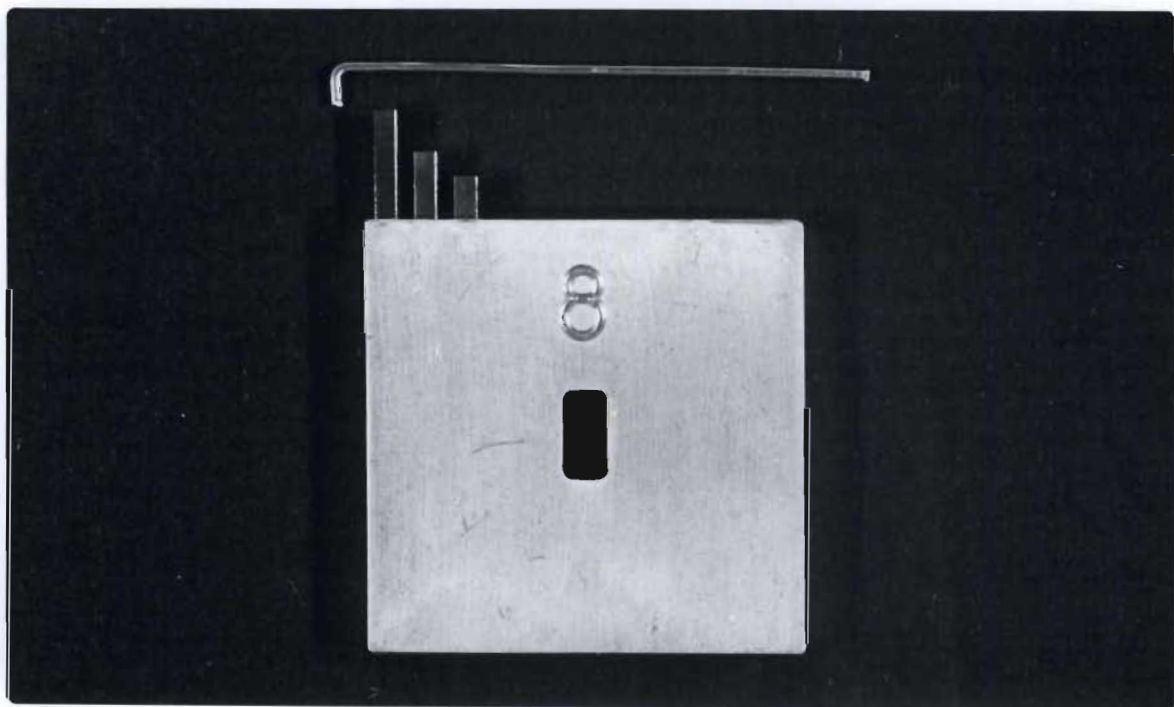
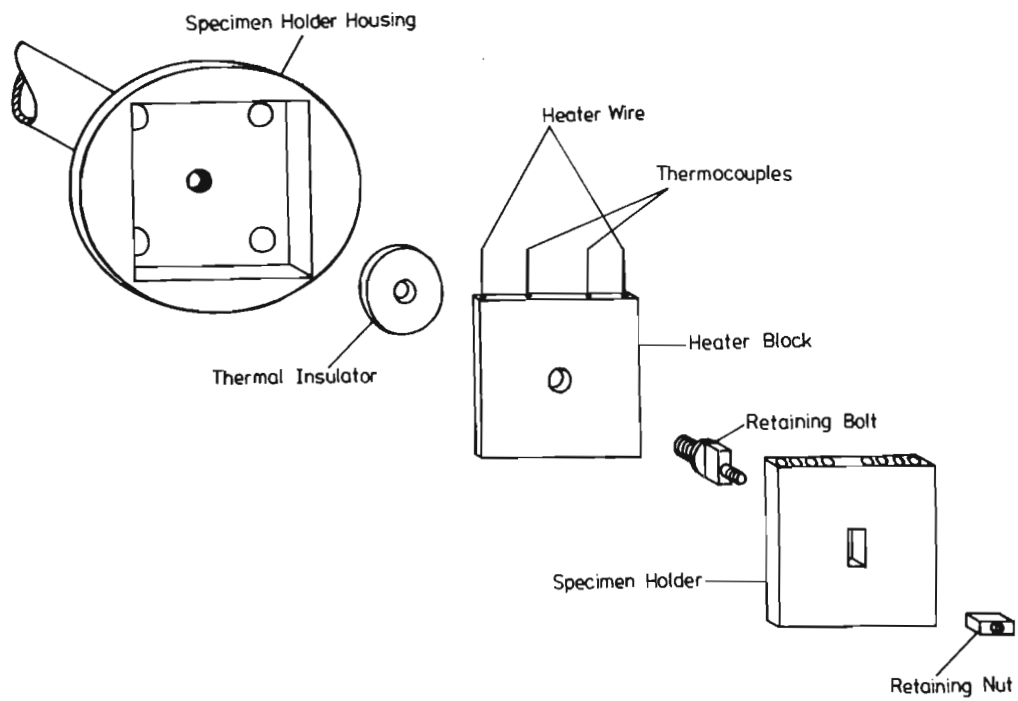
Figure 6.7

A.

Diagram of the specimen block and  
heater assembly.

B.

A specimen block showing three crystals  
and their aluminium locking wire.



caused to the custom made plug and glass to metal seal by the fast neutrons.

The specimen mount cannot be positioned incorrectly in the outer chamber since the angle of the front end and of the front guide flange ensures that the correct orientation is obtained easily, even when using remote handling tools in a radiation hot cell.

Details of the specimen block and heater block assembly are shown in (Figure 6.7). The heater block is made of stainless steel sheathed nichrome resistance wire which is wound into a spiral and housed in an aluminium casing. The hot junctions of two stainless steel sheathed chromal alumel thermocouples are also embedded in the heater casing. The heater is attached to the specimen mount by means of a short stainless steel retaining bolt, but is to a large degree thermally insulated from the mount by means of a pyrophyllite washer, the thickness of which is calculated to allow a predetermined amount of heat to flow through it. The pyrophyllite washer used was 5,6 cm in diameter and 0,5 cm thick.

The specimen holder is an aluminium block 6 cm square and 0,6 cm thick and is designed to take eight crystals of 5 cm in length in eight 0,5 cm diameter blind holes drilled down its length (Figure 6.7B). The 3 mm square cross section crystals are retained loosely in these blind holes by means of an aluminium wire threaded across the open ends of the holes. The specimen block is held firmly against the heater by means of a stainless steel retaining nut (Figure 6.7A). This nut is locked into place by a half turn and the operation can be easily carried out by mechanical arms in a radiation hot cell.

## 6.4

H.T.R. INSTRUMENTATION

The instrumentation of the rig falls into three categories:

1. Temperature monitoring and control.
2. Vacuum measurement and control.
3. Comprehensive safety and warning circuits provided to ensure the safety of the H.T.R., the reactor, and reactor personnel, in the event of any failures of the rig's construction or of its circuitry.

A block diagram of the instrumentation of the rig is shown in Figure 6.8.

The temperature control circuitry consists basically of a 100 watt heater of 110 V, 50 Hz, thermocouples and a control unit. This control unit consists of two distinct sections which are an Ether 1290B measuring unit and an Ether BHS/10 control unit.

The temperature which is desired is set manually on the measuring unit, then as the variation in electrical potential from the measuring thermocouple (the other thermocouple is a spare in case of thermocouple failure) is fed into the measuring unit a potentiometer circuit provides a signal to the control unit. The control unit consists primarily of two thyristors which operate by chopping out increasingly larger portions of the sine wave of the A.C. heating current as the actual measured temperature approaches the set temperature. If the actual temperature exceeds the set temperature the heating current is switched off altogether and thus the heater cannot overheat and damage the rig. By means of this system a constant set temperature can be maintained irrespective of the ambient temperature external to the rig.

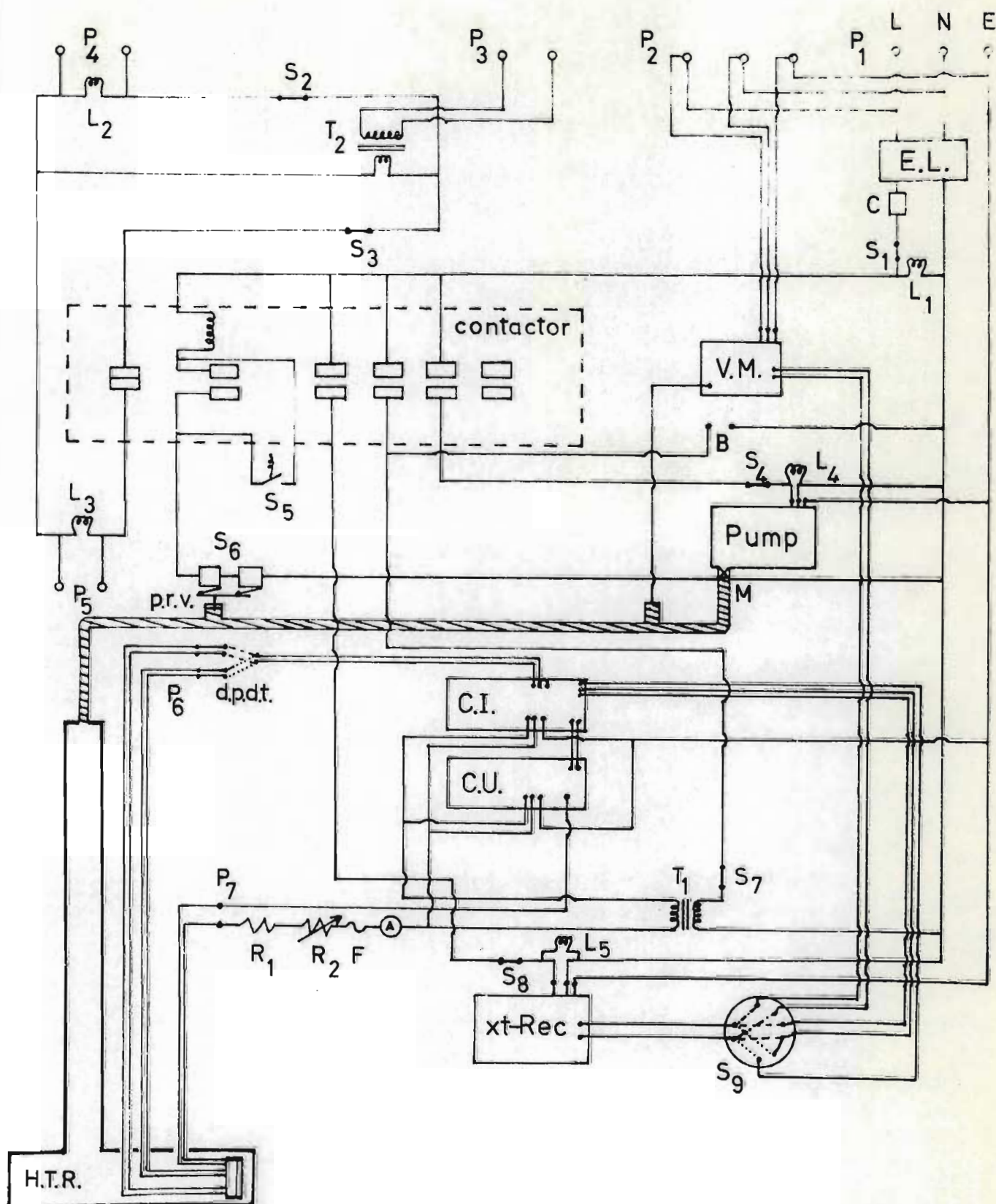
Figure 6.8Electrical circuit of the H.T.R.

(legend to diagram)

P <sub>1</sub>	Two possible power inputs
P <sub>2</sub>	
P <sub>3</sub>	Independent power input to emergency warning circuit
P <sub>4</sub>	Output from emergency warning lights to the reactor control room
P <sub>5</sub>	
P <sub>6</sub>	Plugs from control panel to the H.T.R.
P <sub>7</sub>	
S <sub>1</sub>	Main power switch
S <sub>2</sub>	Switches used to set the warning system
S <sub>3</sub>	
S <sub>4</sub>	Switch to pumping system
S <sub>5</sub>	Spring loaded switch which has to be manually operated to start the system
S <sub>6</sub>	Two microswitches which switch the system off in the event of the pressure in the H.T.R. rising above some preset value
S <sub>7</sub>	Heater switch
S <sub>8</sub>	Strip chart recorder switch
S <sub>9</sub>	Multiple switch to monitor either the temperature (either end of the potentiometer scale) or the pressure
T <sub>1</sub>	Transformer to produce 110 V for the heater
T <sub>2</sub>	Transformer to produce 6 V for the warning system
R <sub>1</sub> , R <sub>2</sub>	Resistors (set once during construction)
C.I	Control indication
C.U.	Control unit

V.M.	Vacuum meter
E.L.	Earth leakage device
P.R.V.	Pressure release valve
D.P.D.T.	Double pole double throw switch to change from one thermocouple to the other
F	Fuse to heater
A	Ammeter
M	Electrical switch in vacuum line
B	Spare plug switched by the contactor
C	15 amp circuit breaker
L <sub>1</sub> , L <sub>2</sub> ,	
L <sub>3</sub> , L <sub>4</sub> ,	Indicator lights
L <sub>5</sub>	

Figure 6.8  
Electrical circuit of the H.T.R.



If the measuring thermocouple breaks and goes open circuit the heating current is automatically switched off. The temperature of the specimen block can be read off at any instant from the measuring unit and in addition a continuous and permanent record of temperature is kept by means of a Hewlett Packard model 680 M 12 cm x-t recorder.

The vacuum system consists of a two stage rotary pump and vacuum measuring facilities. Due to the high level of radiation a vacuum gauge could not be placed anywhere near the specimens themselves and thus the measuring gauge was placed in a position in the vacuum line above the reactor pool surface. However before the rig was commissioned, a second gauge was placed at the site of the specimens and the readings produced by the two gauges were checked against one another during a simulated experimental run carried out in a large tank of water. It was found that even at the lowest pressures at which the rig operates ( $10^{-3}$  torr  $\pm$ ) the gas in the rig was not sufficiently rarified to cause much difference in the readings of the two vacuum gauges. At all pressures tested they agreed to within a few percent. Facilities are provided to fill the rig with a suitable gas if any particular specimen environment is required.

Also in the vacuum line is a custom made pressure release valve. In the event of the pressure in the rig rising above a preset value (usually set at atmospheric pressure plus 35 kPa) the pressure release valve opens and triggers two microswitches which cause the entire rig to shut down and an alarm to ring in the reactor control room. In addition the exhaust gas which would come out of the pressure release valve is vented into the reactor off-gas system which is a system which takes potentially radioactive gasses through a radiation monitor and safely out of the building. The pressure release valve

also has a ball valve associated with it, which activates the same triggers in the event of liquid (e.g. water) being forced back along the vacuum line. The normal exhaust gas from the rotary pumps is also fed back into the off-gas system.

In addition to the safety features already mentioned the rig has a circuit breaker in the heater circuit to allow for possible short circuits and also one on the mains input to the rig. There is also an earth leakage device in the mains input circuit. In the event of any of these safety devices being activated or there being a power failure in the building the rig automatically shuts itself down totally and rings an alarm in the reactor control room. If this happens the rig cannot restart itself - if for example a power failure is rectified - it is necessary for the H.T.R. to be manually restarted. This is a safety feature which requires that an operator check all the functions before restarting the rig or before aborting the run if this is found to be necessary.

#### 6.5 PERFORMANCE OF THE H.T.R.

As mentioned earlier in this chapter a helium gas atmosphere is put into the rig prior to a run for two reasons. Firstly an inert atmosphere is needed so that no chemical changes occur in the specimen crystals during irradiation, and secondly by altering the helium pressure in the rig a large degree of temperature control can be exercised since the amount of heat lost from the specimens by means of conduction and convection through the helium atmosphere is a function of pressure.

With the rig's heater switched off and the rig in its storage position in the reactor pool out of the radiation flux, the specimen

block stabilized at a temperature of  $30^{\circ}\text{C}$  which is the ambient temperature of the reactor pool water. When the rig was placed in its position on the reactor in the radiation flux with the reactor running at 20 MW power, the heating due to the gamma-radiation alone was found to raise the specimen block to a temperature of  $110^{\circ}\text{C}$  when the rig contained an initial pressure of one atmosphere of helium. When the helium pressure was reduced to 10 torr the gamma-heating raised the temperature of the specimen block to  $180^{\circ}\text{C}$ . Figure 6.9 shows the increase in temperature (due to  $\gamma$ -heating) and pressure for the first seven minutes after the rig is placed in the radiation flux with the rig containing an initial pressure of six torr of helium. This initial rapid pressure rise stabilizes after about 10 minutes. Thus it was found that the specimen temperature could be altered by as much as  $100^{\circ}\text{C}$  by means of the helium gas pressure alone.

The rig, containing one torr of helium and with the heater switched on, takes only two minutes to heat the specimen block to a temperature of  $400^{\circ}\text{C}$  after it is placed into the radiation flux. On taking the rig out of the radiation flux at the end of a run the heater is first switched off, then the rig is immediately removed from its position on the reactor (this operation is carried out in under half a minute). The temperature then falls to  $30^{\circ}\text{C}$  from  $400^{\circ}\text{C}$  in about 35 minutes. The initial fall in temperature is very rapid and thus no annealing of the specimens takes place.

During a run of 72 hours duration the specimen temperature does not vary from the set temperature by more than  $1^{\circ}\text{C}$ . This is due to the fact that the reactor pool water provides a very large, constant temperature, heat sink and that the thyristor controlled heating current is very stable. Before the rig was commissioned the temperature of the specimens at the specimen site was checked against the measuring

FIG (6.9)

The increase in temperature and pressure in the H.T.R. for the first seven minutes after the rig was placed in the radiation flux.

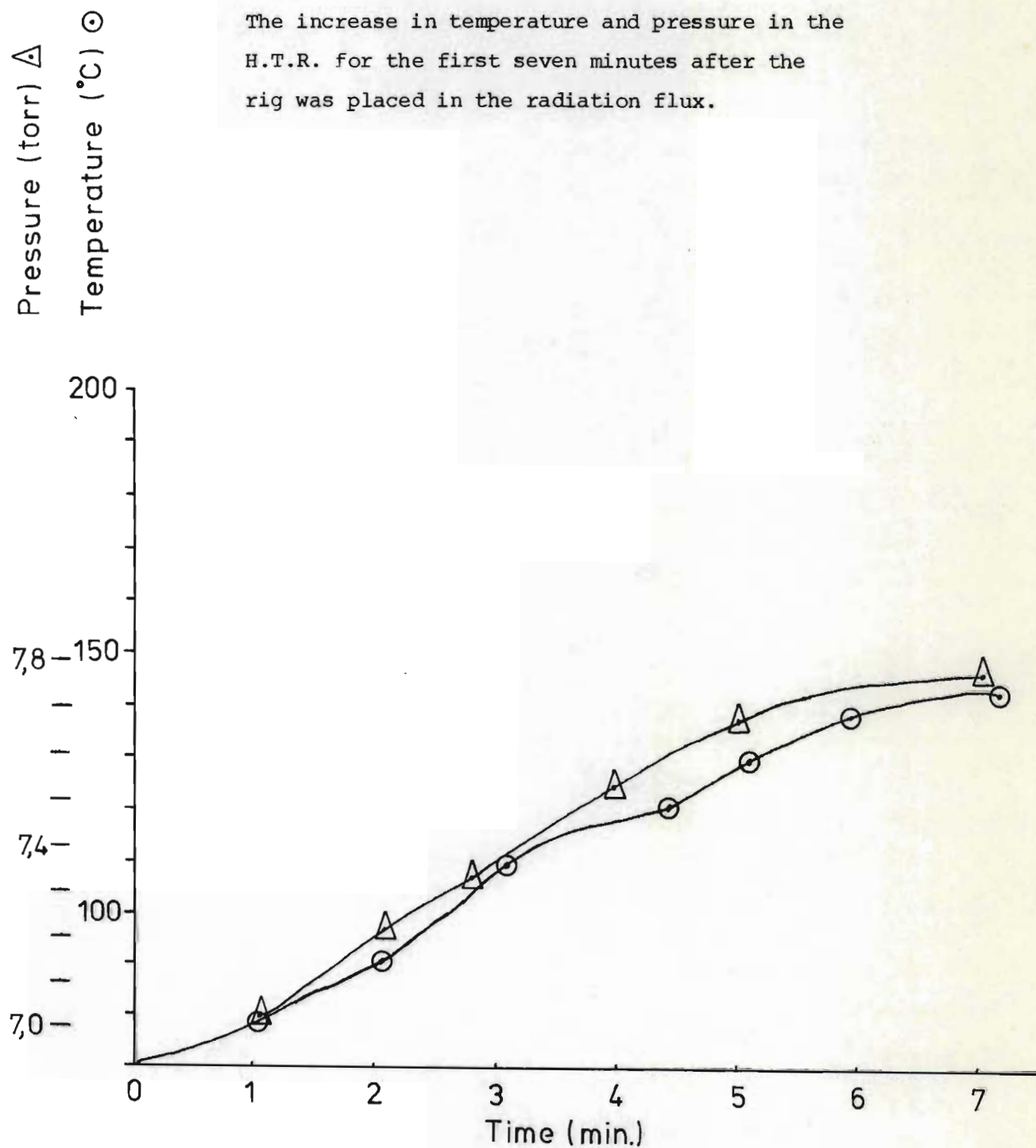


TABLE 6.1  
H.T.R. PERFORMANCE SPECIFICATIONS

Specimen temperature with H.T.R. in storage position,  
no heater.

30°C

Specimen temperature due to  $\gamma$ -heating alone.

110°C\* with 1 atm  
of He gas, 180°C  
with 10 torr of He gas

[ \*Minimum specimen temperature with standard thermal  
insulator (Figure 6.7A). ]

Maximum specimen temperature (determined by the  
fact that the specimen block is Al - melting  
point of Al = 660,1°C).

500°C ±

Range of temperature control from altering He gas  
pressure.

100°C ±

Variation in temperature over 72 hr. run.

< 1°C

Time required to heat from 30°C to 400°C  
(Pressure = 1 torr He).

2 min ±

Time required to cool from 400°C to 30°C  
(Pressure = 1 Atm He).

35 min ±

Fast neutron flux through specimen container  
(E > 0,1 Mev).

$1,5 \times 10^{12}$  f.n. cm<sup>-2</sup> s<sup>-1</sup>

unit's indication during a simulated experiment in a test bed, and was found to compare exactly.

The fast neutron flux (of neutron energies greater than 0,1 MeV) passing through the actual specimen block itself was measured and found to be  $1,5 \times 10^{12}$  f.n.  $\text{cm}^{-2} \text{ s}^{-1}$  (Figure 6.10). This was measured by manufacturing a special specimen block in which was placed magnesium, aluminium and sulphur flux monitors.

#### 6.6 HANDLING AND LOADING PROCEDURES OF THE H.T.R.

The handling and loading procedure is shown diagrammatically in (Figure 6.11). The copper specimens are loaded into the specimen block (Figure 6.7B) in Durban after which the loaded block is transported to the reactor at Pelindaba.

The specimen chamber of the rig (Figure 6.5A) is at this stage in the radiation hot cell where the flange end is sealed by means of a blanking flange. The blank end flange is then removed and the specimen mount (Figure 6.5B) is withdrawn by means of remotely controlled mechanical arms. The specimen mount is then clamped into a special securing bracket in the hot cell and the specimen block is locked into place on the specimen mount by means of its easy-action retaining nut (Figure 6.7A). Great care is exercised so as not to bump or drop the specimen block during loading since this could alter the pre-irradiation dislocation density of the crystals.

The specimen mount now containing the specimens, is then replaced in the specimen chamber, the blank end flange is replaced, and the whole specimen chamber is placed in a 600 Kg lead transportation container which is then transported by crane to the reactor and immersed

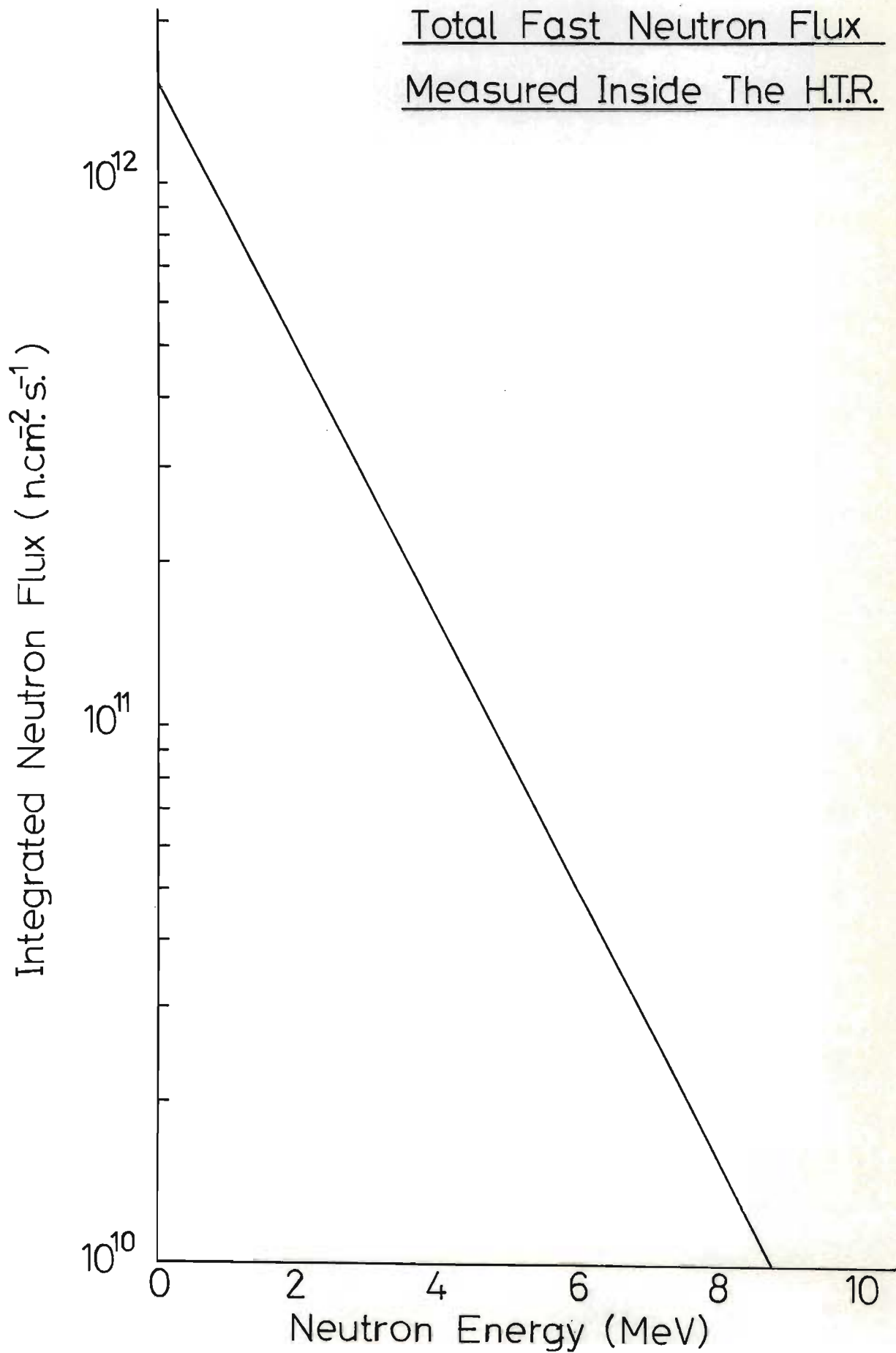
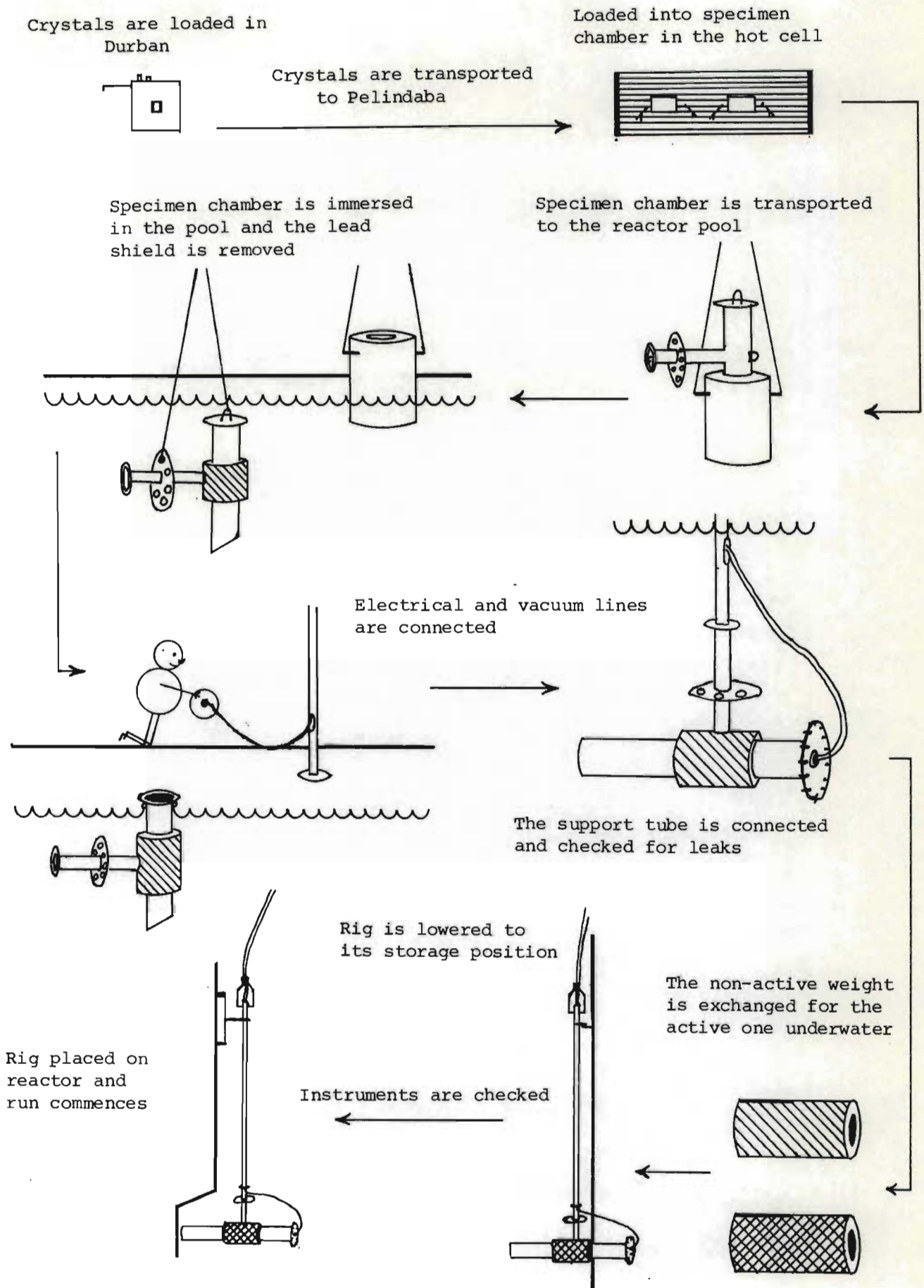


Figure 6.11  
H.T.R. Loading procedure.



in the reactor pool. The specimen chamber is then removed from the lead shield underwater and the shield is removed from the pool. The specimen chamber is then lifted until the end flange is just above water level whereupon the support tube, which has been lifted from its storage position underwater, is suspended above the specimen chamber while the blank end flange is removed and the electrical connections to the heater and thermocouples are made (Figure 6.12). The end flange containing the electrical lead-throughs is then clamped into place and the vacuum seals are checked by pressurizing the rig with two atmospheres of helium and lowering it under the water and checking for bubbles. The support tube is then joined to the specimen chamber and the vacuum seals checked again, after which the entire rig is lowered underwater.

At this point in the procedure the stainless steel encased lead buoyancy weight on the specimen chamber (Figures 6.4, 6.5A) is removed using handling tools and replaced by an identical weight which is radioactive and which is used while the rig is being irradiated. The radioactive buoyancy weight stays underwater permanently. The rig is now lowered to its underwater storage position on the wall of the reactor pool.

The rig is then evacuated after which helium is allowed into it to atmospheric pressure. This purging is done three times after which there is effectively an atmosphere of pure helium in the rig. The rig's heaters are now switched on and the rig attains its set temperature in a few minutes. The H.T.R. is then placed into its position on the reactor side - this operation takes under half a minute to execute.

On removing the rig from the reactor at the end of the

Figure 6.12

The electrical connections between the support  
tube and the specimen chamber are made.



experiment the heater is switched off before removal from the flux, and the rig is then rapidly moved to its storage position and pressurized with one atmosphere of helium. The rig is left in its storage position for some weeks until the radioactivity of the specimens has decayed to a level safe to handle.

CHAPTER SEVENMORPHOLOGY OF HIGH TEMPERATURE RADIATION DAMAGE

- 7.1 Introduction
- 7.2 Qualitative survey of present results
- 7.3 Proposed shape of the prism of radiation damage
- 7.4 Alignment of comet-shaped rafts
- 7.5 Details of the general damage morphology
  - 7.5.1 Specimens irradiated at 250°C
  - 7.5.2 Specimens irradiated at 300°C
  - 7.5.3 Specimens irradiated at 350°C
  - 7.5.4 Specimens irradiated at 400°C
- 7.6 Comparison of electron microscope data and etch pit data

## 7.1 INTRODUCTION

In this chapter the qualitative experimental results are presented. The rather complex damage morphology observed in the specimens irradiated at different temperatures is briefly compared in Section 7.2. The qualitative aspects of the radiation damage at each irradiation temperature are then discussed in detail in Section 7.5. (Note: All electron microscope foils examined had foil normals parallel to  $\langle 111 \rangle$ ).

## 7.2. QUALITATIVE SURVEY OF PRESENT RESULTS

A total of five sets of copper crystals were irradiated in the H.T.R. Four of these sets were irradiated at different temperatures in a helium atmosphere to similar total neutron doses (Table 7.1). Two irradiations were carried out at a temperature of  $250^{\circ}\text{C}$  where one set of crystals was irradiated to half the dose of the other set (Table 7.1). Some of the copper crystals of each batch (which were all grown from the same crystal seed) were sent to Pietermaritzburg to be examined by means of an etch pit technique. The etch pit results obtained can therefore be directly compared to the electron microscopy results. The etch pit work was carried out in Pietermaritzburg by K.E. Black and P. Nathanson.

The morphology of the radiation damage varied to a great extent as a function of temperature. Furthermore the damage in all specimens was characterised by its inhomogeneity over the small areas viewed in the electron microscope. Over the larger areas examined by etch pitting  $\{111\}$  planes, the distribution of the different components of the radiation damage was more even but it could not be described as

TABLE 7.1  
IRRADIATION PARAMETERS OF COPPER CRYSTALS IRRADIATED  
IN THE H.T.R.

Irradiation Temperature °C	Dose (E > 0,1 MeV) f.n. cm <sup>-2</sup>	Pre-irradiation dislocation density (cm <sup>-2</sup> )	Irradiation Atmosphere
250	$1,24 \times 10^{17}$	$2,4 \times 10^6$	1 atm He
250	$2,47 \times 10^{17}$	Not measured	"
300	$2,92 \times 10^{17}$	$7,1 \times 10^6$	"
350	$2,79 \times 10^{17}$	$9,7 \times 10^6$	"
400	$2,59 \times 10^{17}$	$11,4 \times 10^6$	"

homogeneous. A comparison between a typical etch pit photograph and a typical electron micrograph for each irradiation temperature is shown in Figures 7.1 to 7.4.

For an irradiation temperature of  $250^{\circ}\text{C}$  the damage was found to be collected into large, dense, well defined aggregates of small defects (Figure 7.1). These dense accumulations of damage were observed to vary in shape from small and almost circular shapes to triangular or 'fan' shapes and also long linear or 'comet' shapes. The long 'comet' shaped agglomerations of damage were found to vary considerably in length and examples as long as  $100\text{ }\mu\text{m}$  are observed.

The rafts observed in the specimens irradiated at  $250^{\circ}\text{C}$  are in general extremely dense and consist of dislocation line segments, small resolvable loops and black dot damage. Another striking feature of the damage morphology is the marked absence of radiation damage in the areas between rafts - a few dislocations and black dots are seen in these areas.

The specimens irradiated at  $300^{\circ}\text{C}$  contain a large amount of damage but no large rafts of damage are seen. The damage in these specimens consists of dislocation tangles, loops and black dot damage distributed essentially homogeneously over the whole volume of the specimen (Figure 7.2). Many of the tangles appear as tight knots of damage about  $1\text{ }\mu\text{m}$  in size, and there are no large damage-free regions like those in the specimens irradiated at  $250^{\circ}\text{C}$ .

Rafts of radiation damage similar to those observed in the  $250^{\circ}\text{C}$  irradiation are also observed in the  $350^{\circ}\text{C}$  irradiation (Figure 7.3)

Figure 7.1

Typical appearance of damage after an irradiation at a temperature of 250°C.

A

Electron micrograph with zone axis =  $\langle 111 \rangle$   
and  $\vec{g} = \langle 02\bar{2} \rangle$

B

An etched (111) plane.

In comparing the micrographs in Figures 7.1 to 7.4 it must be remembered that the magnifications used in the two different techniques are very different. Thus caution must be exercised in making direct comparisons. The comparisons are discussed in §7.6.

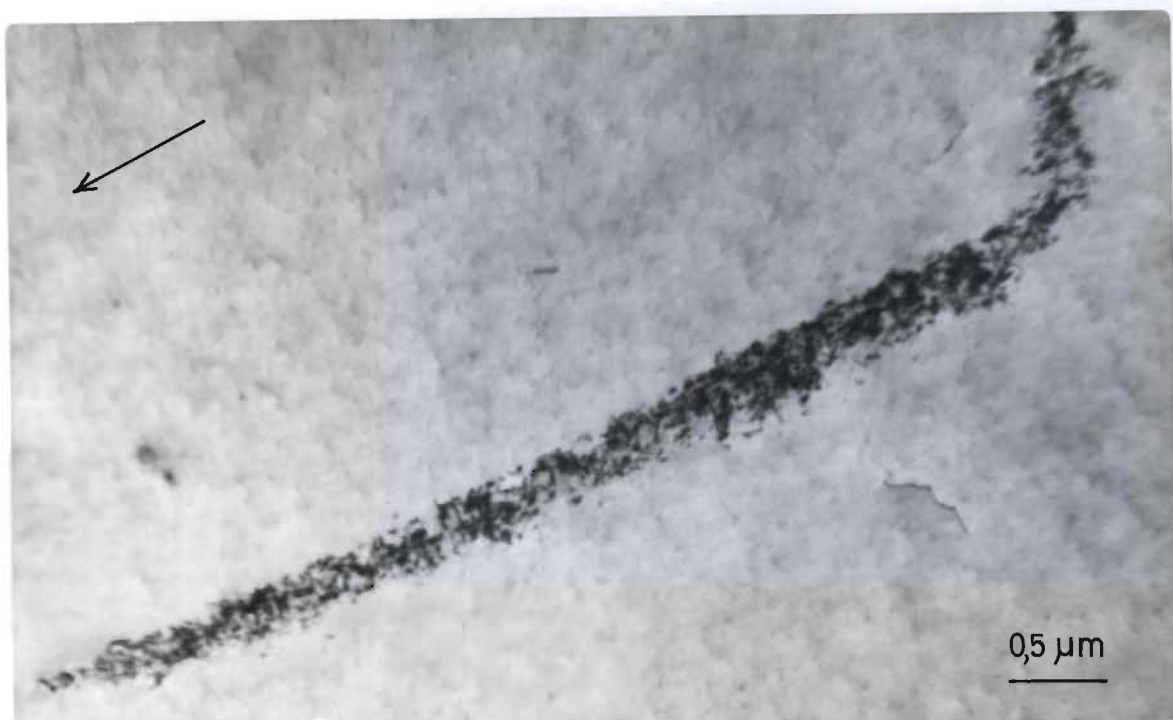


Figure 7.2

Typical appearance of damage after an irradiation at a temperature of 300°C.

A

Electron micrograph with zone axis =  $\langle 211 \rangle$  and  
 $\vec{g} = \langle 1\bar{1}\bar{1} \rangle$

B

An etched  $\langle 111 \rangle$  plane

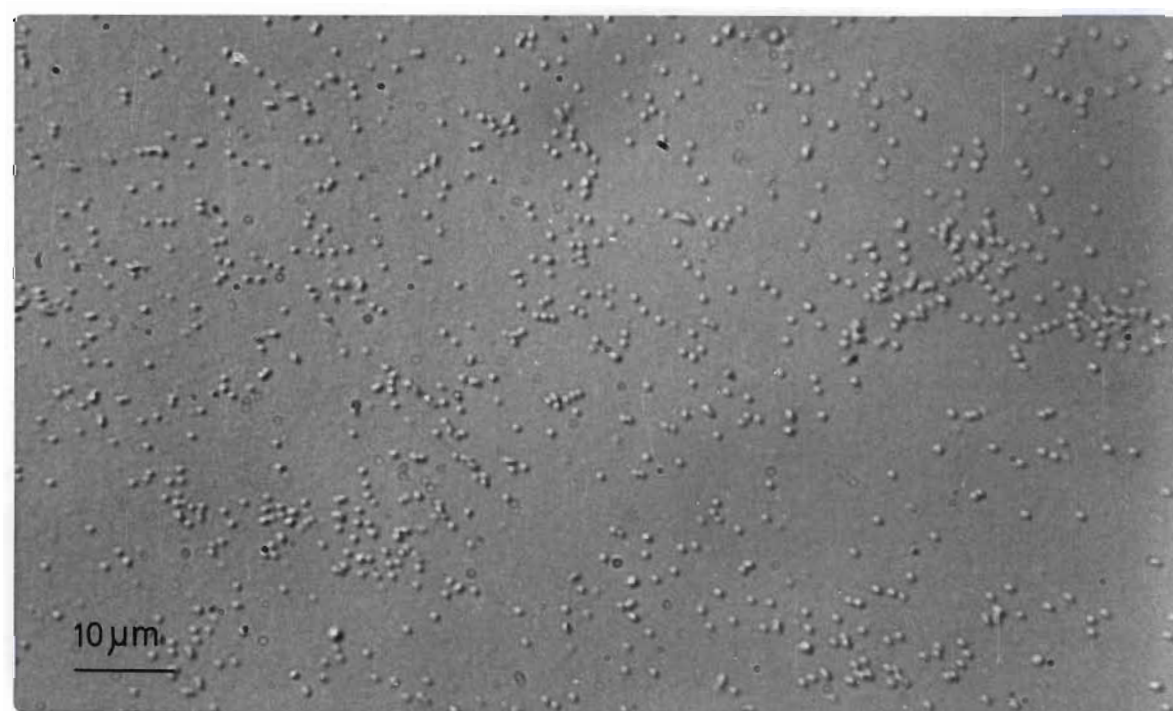
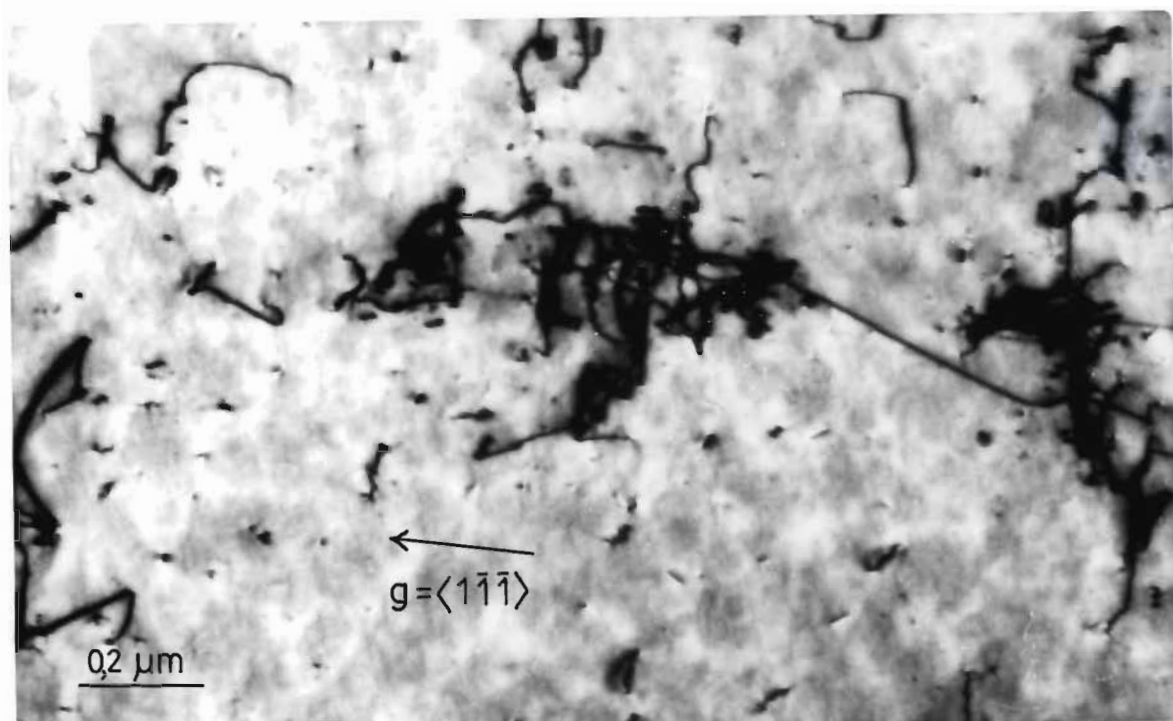


Figure 7.3

Typical appearance of damage after an irradiation  
at a temperature of  $350^{\circ}\text{C}$ .

A.

Electron micrograph with

Zone axis =  $\langle 211 \rangle$  and  $\vec{g} = \langle 1\bar{1}\bar{1} \rangle$

B.

An etched  $(111)$  plane



Figure 7.4

Typical appearance of damage after an irradiation  
at a temperature of 400°C.

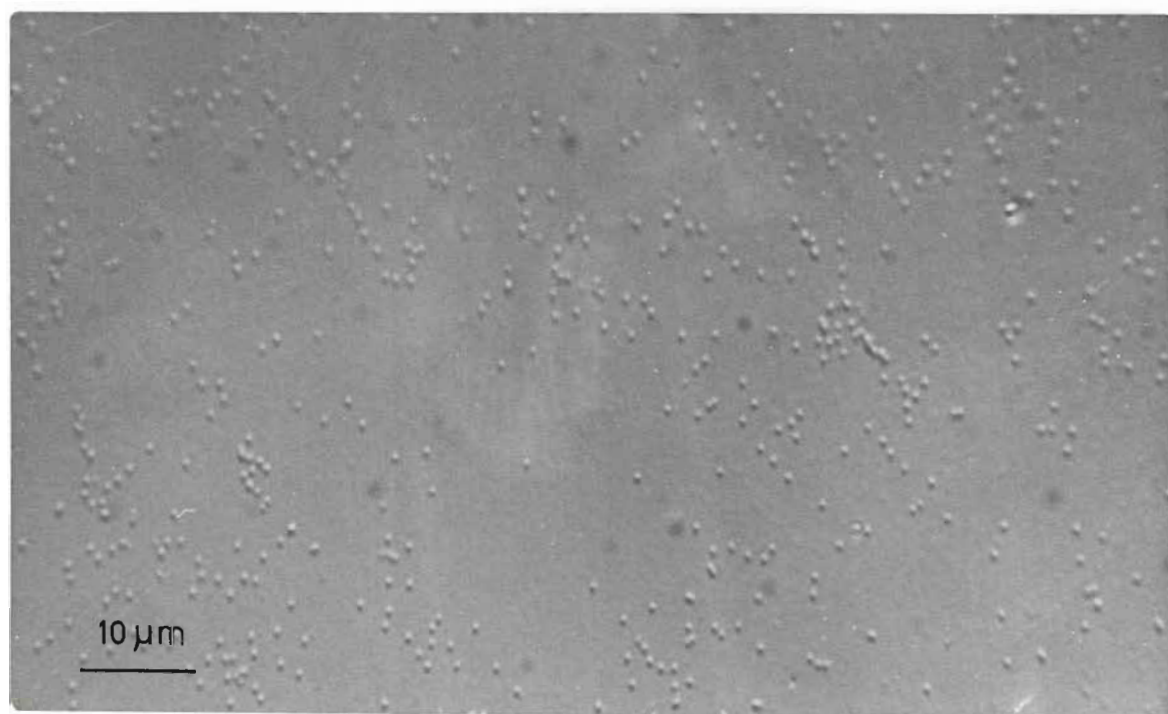
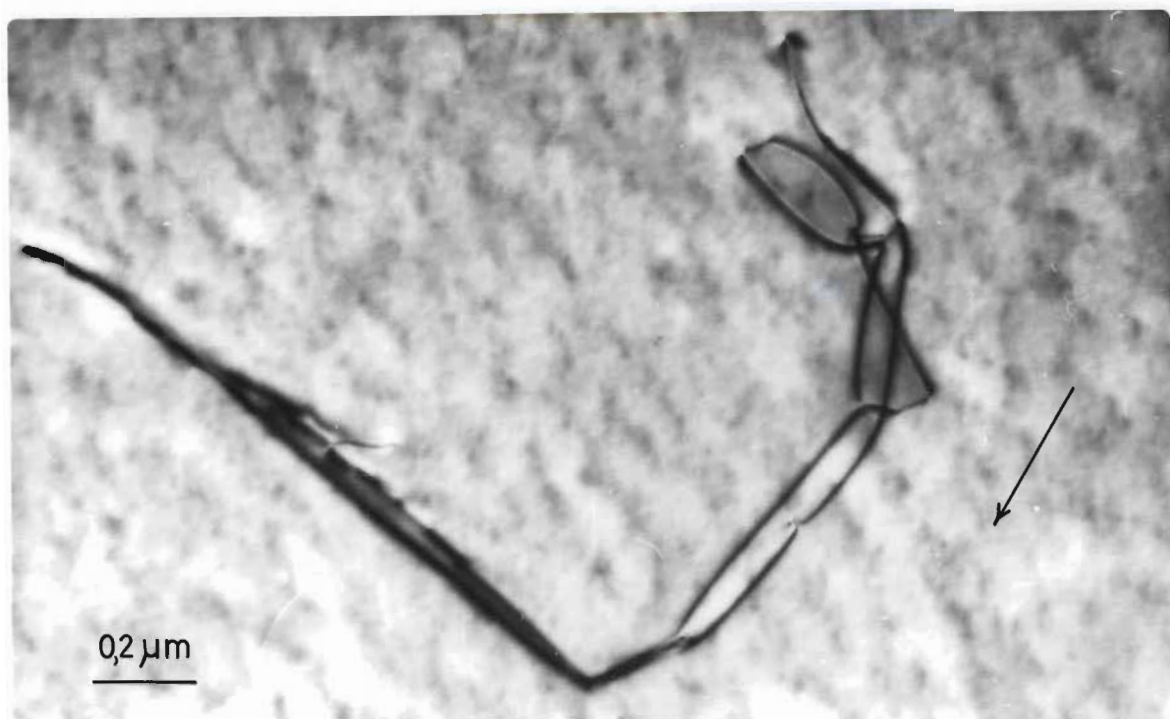
A.

Electron micrograph with

Zone axis =  $\langle 111 \rangle$  and  $\vec{g} = \langle \bar{2}20 \rangle$

B.

An etched (111) plane



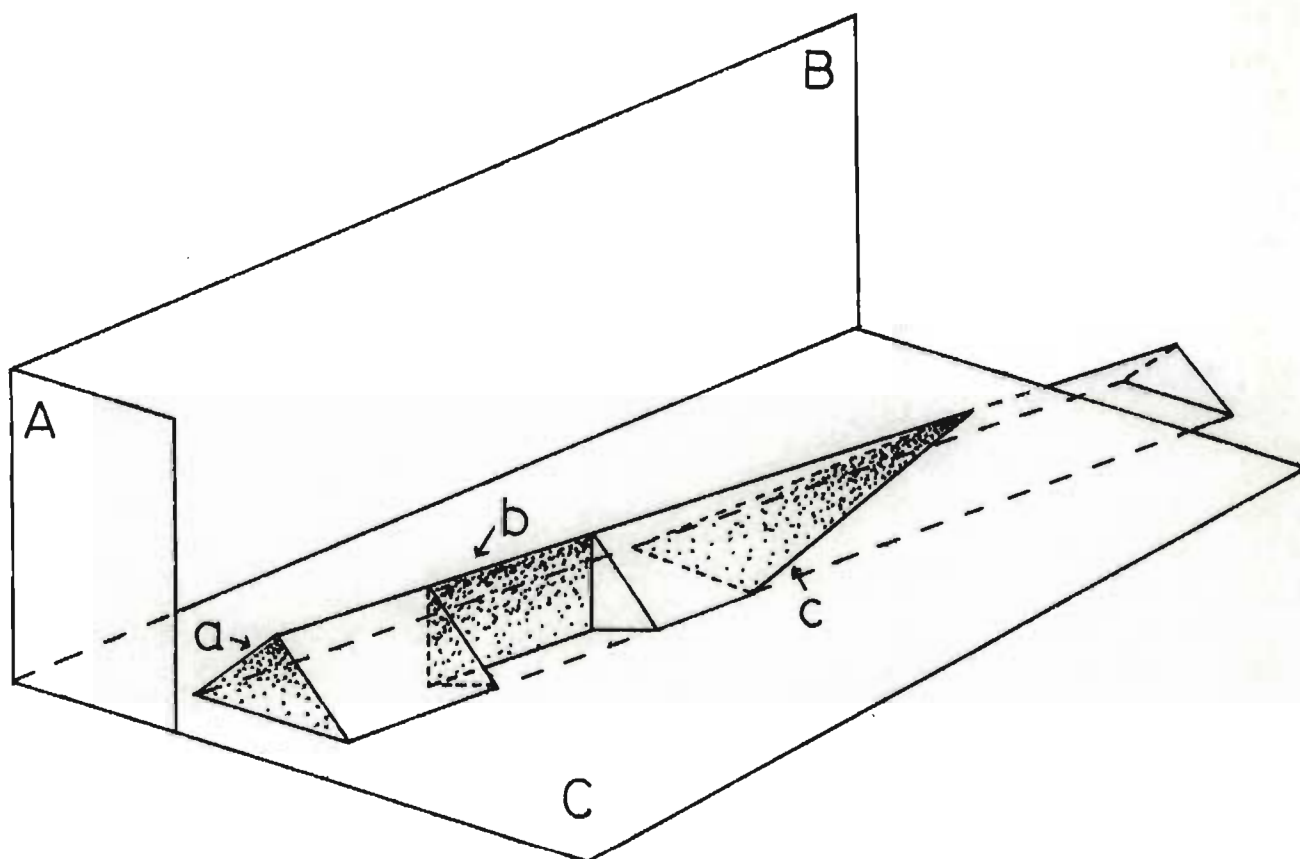
but the density of the damage comprising these rafts is less than the density of the rafts observed at 250°C. The rafts in the material irradiated at 350°C are comprised of rather more dislocations and considerably less black dot damage. The inter-raft areas in the 350°C irradiation also contain a rather low density of damage.

In crystals irradiated at 400°C there is an extremely low density of damage of any kind although occasional groups of dislocations are seen (Figure 7.4). These groups of dislocations in general consist of a few very straight dislocations containing very few jogs or tangles of any kind. Occasionally these dislocation groups appear as if they could be remnants of rafts or rudimentary rafts since some of them have macroscopic shapes similar to those of the rafts seen in the 250°C and 350°C irradiated specimens. There is extremely little damage in the regions between dislocation groups.

It should be pointed out that due to the large size of the defect clusters being studied, that both transmission electron microscopy and etch pitting {111} planes enables one to study only thin sections through these three dimensional objects.

### 7.3 PROPOSED SHAPE OF THE PRISM OF RADIATION DAMAGE

From etch pit studies Jackson *et al.*, (1976) found that the long comet-shaped etch pit groups which they observed and which correspond to the comet-shaped rafts observed in the electron microscope, are in fact sections through three dimensional rafts with a triangular cross section (Figure 7.5). The sections a, b and c through the prism of damage shown in (Figure 7.5) are all observed in etch pit work as well as in electron microscope observations. Examples of these sections are shown in Figures 7.6 and 7.7.

FIG (7.5)Proposed "Comet" Geometry

This figure indicates the geometry for the prism of radiation damage as proposed by Jackson (1976). On taking sections parallel to the planes A, B and C one observes the various raft shapes as a, b and c. The 'comets' observed are sections such as c where it is frequently observed that the damage density is greater at the apex (e.g. Figure 7.19). Similarly the 'fan' shaped raft a is often observed to have a density greatest at the apex (e.g. Figure 7.12). The section b is observed to have one rather straight edge which is dense with damage while the other edge is ragged in appearance and considerably less dense (e.g. Figure 7.13).

Figure 7.6

Typical comet-shaped rafts of damage on etched (111) planes.

Temperature of irradiation =  $350^{\circ}\text{C}$ .

(Micrographs supplied by K. Black and P. Nathanson)

Figure 7.6A

Figure 7.6B

Figure 7.6C

Figure 7.6D

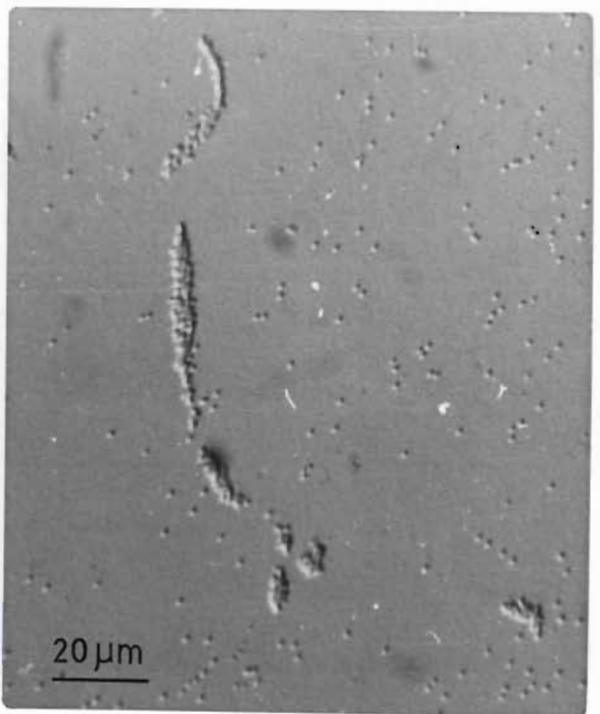
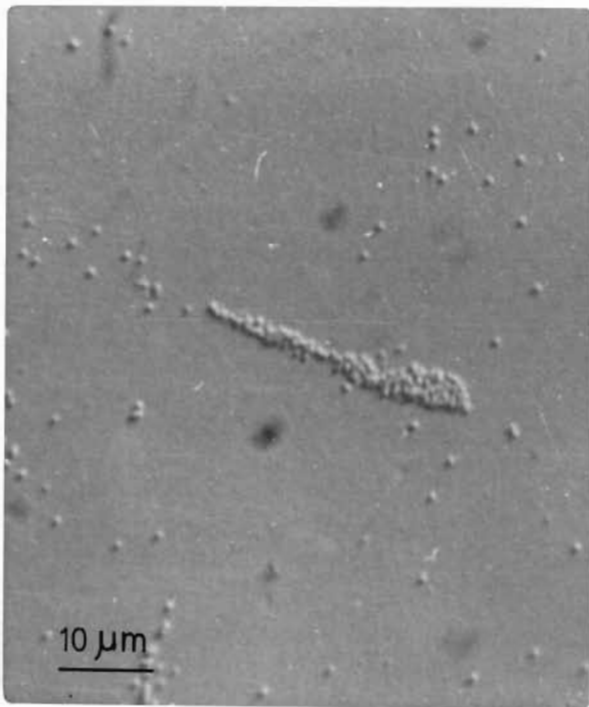
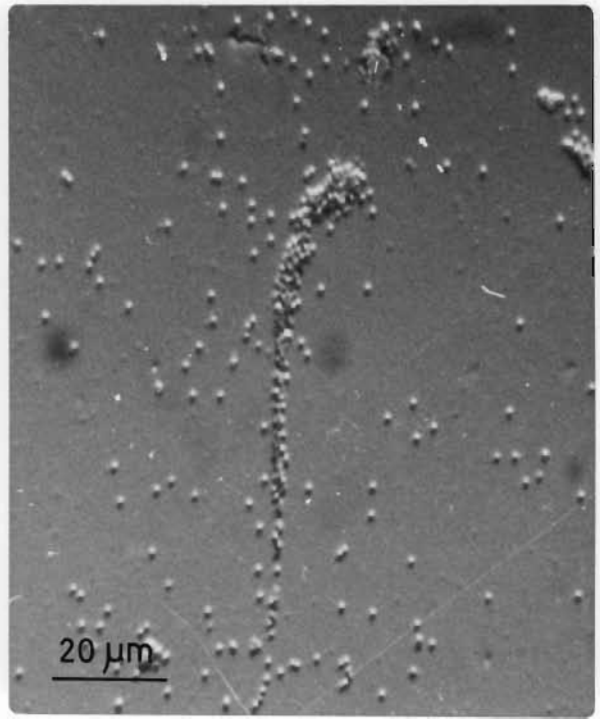
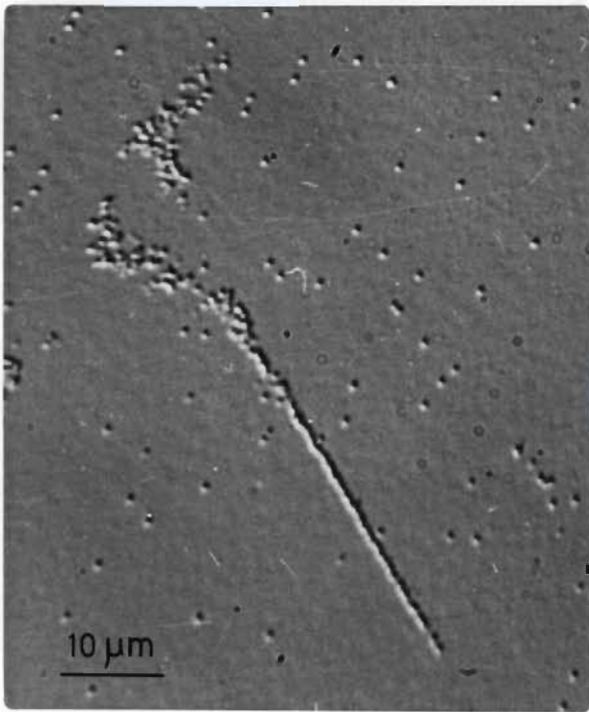


Figure 7.7

Typical rafts of damage on etched (111) planes.

Temperature of irradiation =  $350^{\circ}\text{C}$ .

(Micrographs supplied by K. Black and P. Nathanson)

Figure 7.7A

Figure 7.7B

Figure 7.7C

Figure 7.7D

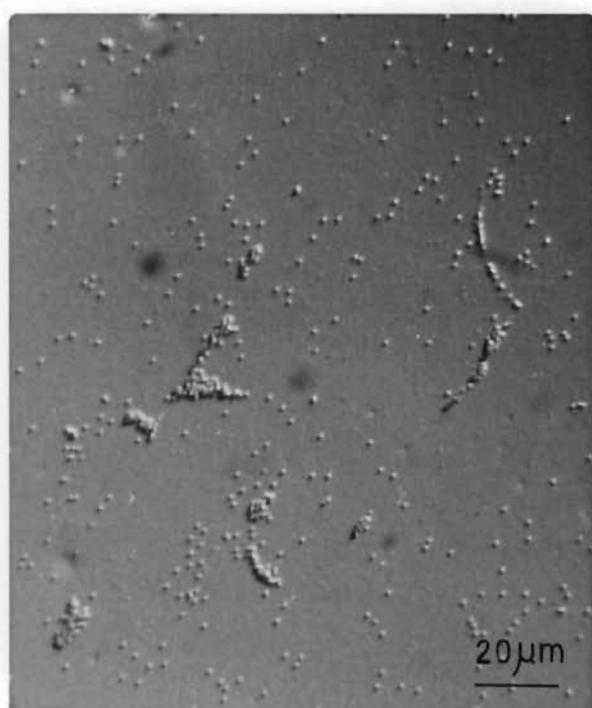
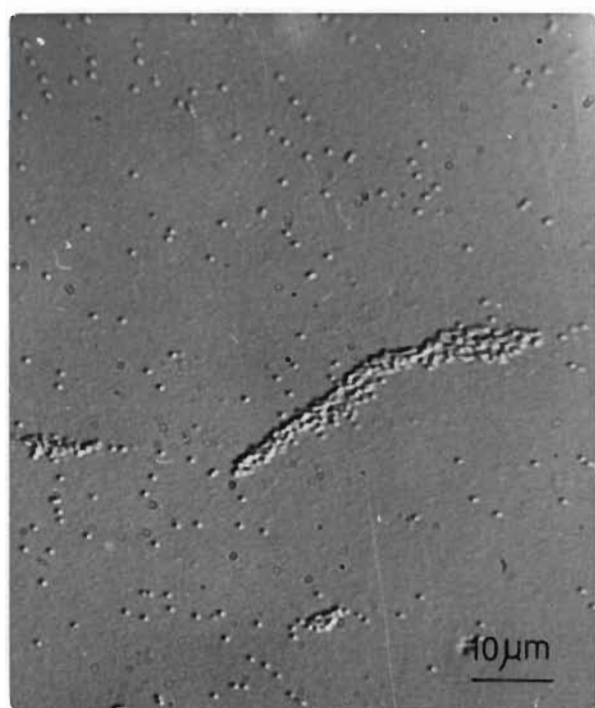
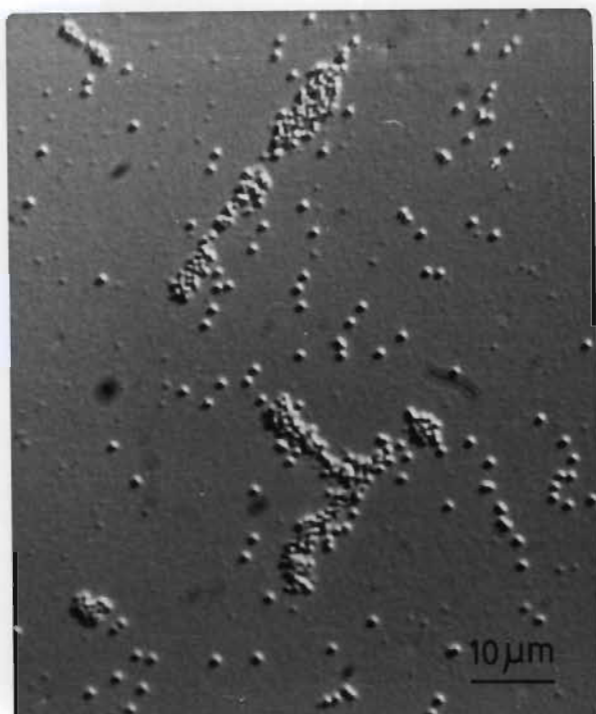
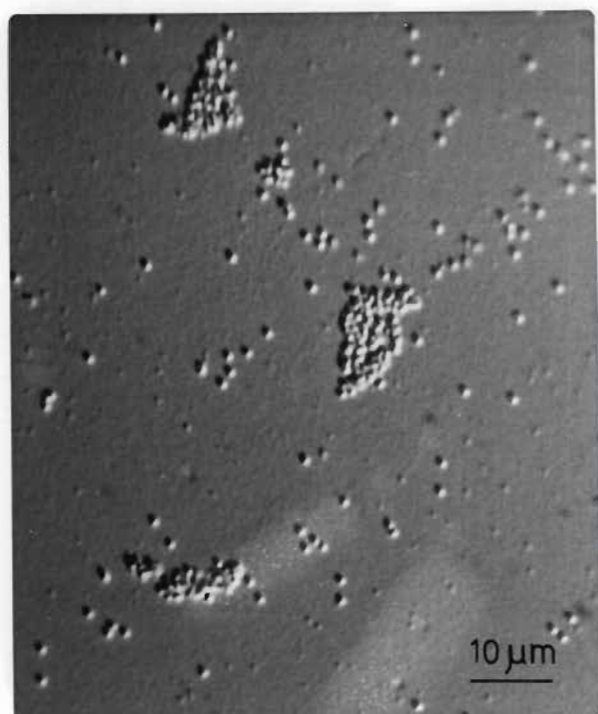
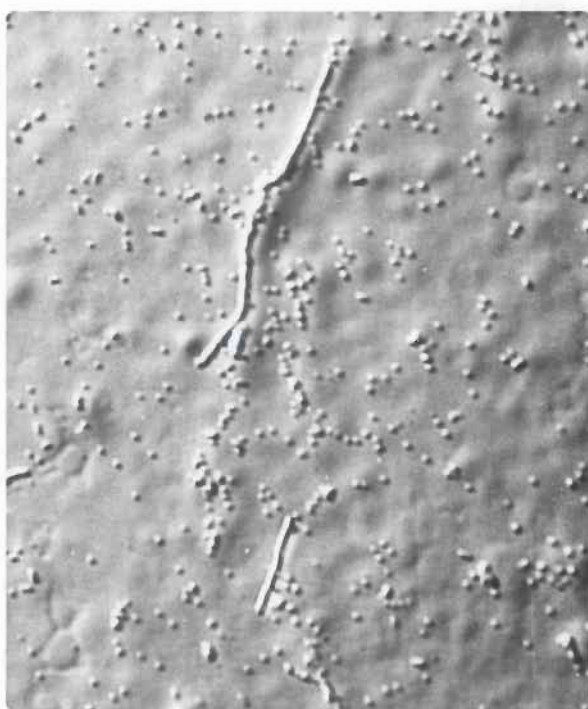
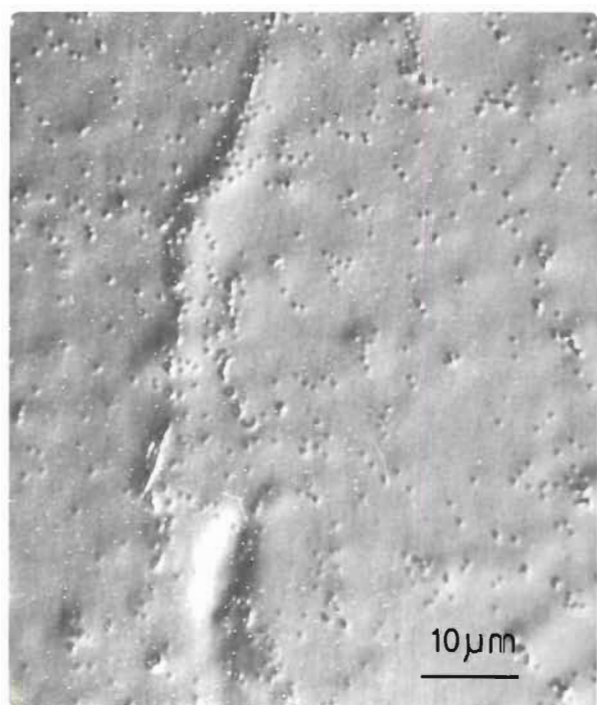
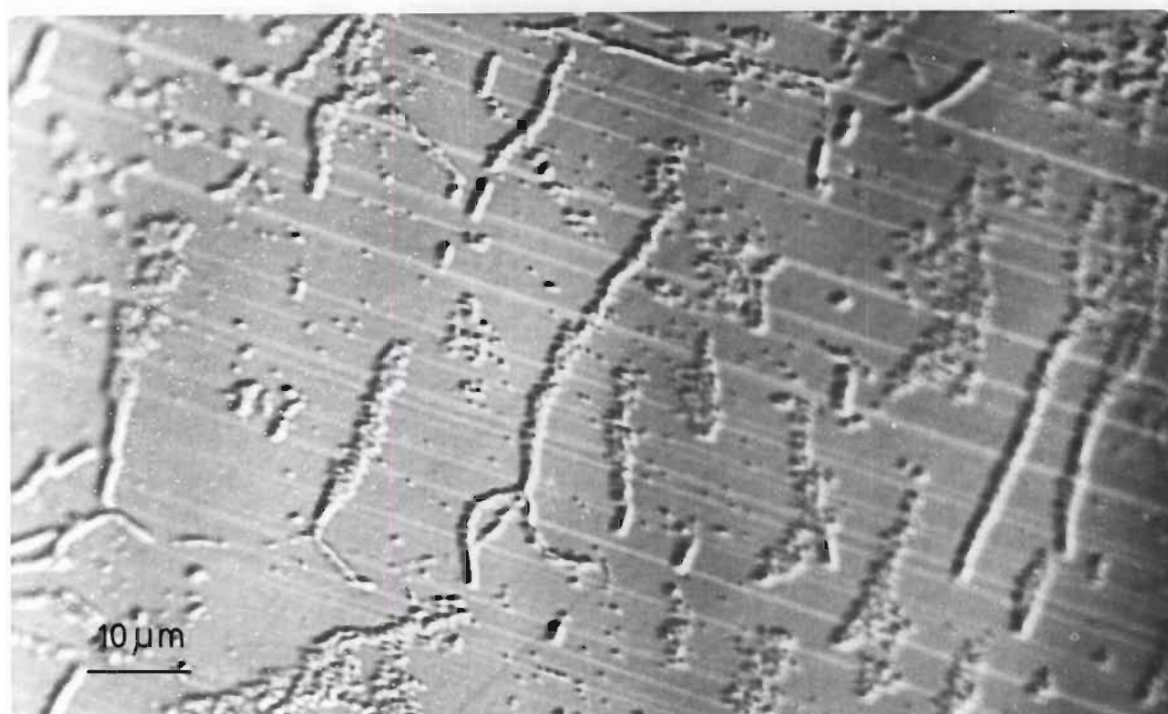


Figure 7.9

An etched (111) plane showing the alignment of a number of comet-shaped rafts. The slip traces are in  $\{110\}$  directions and thus the comets are lying in  $\{211\}$  directions. Irradiation temperature =  $200^{\circ}\text{C}$ . (Micrograph supplied by Dr. P.J. Jackson).

Figure 7.8

A comet-shaped raft before and after electropolishing away a layer of metal about  $1\text{ }\mu\text{m}$  thick and then re-etching. The raft can be seen to become more diffuse (from right to left) indicating a shape such as that in Figure 7.5. Irradiation temperature =  $250^{\circ}\text{C}$ . (Micrographs supplied by K.E. Black).



Jackson *et al.*, (1976) polished and etched the  $\{111\}$  planes of irradiated copper specimens to reveal the comet-shaped rafts after which a thin layer of copper, just sufficient to remove the etch pits, was electropolished away and the specimen was then re-etched (Figure 7.8). Doing this repeatedly on a single specimen they were able to show that the 'comets' have an essentially triangular cross section which can be equated to the fan-shaped rafts observed in etch pit and electron microscope observations.

However there is considerable variation in the sizes, shapes and densities of the rafts observed but etch pit studies have clearly indicated that there seems little doubt that all rafts observed are three dimensional in nature. Due to the large dimensions of the rafts and the extremely thin sections of specimens used in electron microscopy ( $\sim 2000 \text{ \AA}$ ) all rafts examined in the electron microscope, other than extremely small ones, were in fact only thin sections of the complete raft. The fact that the rafts extended over the whole thickness of the electron microscope foils was checked by means of stereo microscopy.

#### 7.4 ALIGNMENT OF COMET-SHAPED RAFTS

It was noticed by Jackson *et al.*, (1976) that the directions of many of the comet-shaped rafts are aligned with each other - this can be seen in Figure 7.9. The slip traces which are evident on the  $\{111\}$  surface of Figure 7.9 are parallel to  $\{110\}$  directions and thus it is evident that many of the comets lie along  $\{211\}$  directions in the crystal.

This alignment of comet-shaped rafts along  $\{211\}$  directions is also observed in many of the electron micrographs (see Section 7.5). In addition on examining many of the other shapes of raft it is noted

that many of the asymmetrical rafts have projections which are parallel to  $(211)$  directions.

## 7.5 DETAILS OF THE GENERAL DAMAGE MORPHOLOGY

### 7.5.1 Specimens irradiated at 250°C

Large dense rafts of radiation damage are observed in specimens irradiated at 250°C. The macroscopic shapes of these rafts vary considerably from long linear comet-shapes (Figures 7.10, 7.11) to 'fan', 'edge' and elliptical shapes (Figures 7.12, 7.13, 7.14, 7.15, 7.16). Rafts of irregular shape (e.g. Figures 7.17, 7.18) are also present but these irregular shapes are usually confined to small rafts.

The sizes of the various rafts observed also vary considerably. The largest are the long comet-shaped rafts which can reach 100  $\mu\text{m}$  in length - Figure 7.19 is an example which is 36  $\mu\text{m}$  in length. These comet-shaped rafts are very rarely more than 1  $\mu\text{m}$  in width.

The smallest rafts seen are usually approximately circular or elliptical in shape having diameters of the order of 0,5  $\mu\text{m}$  to 1  $\mu\text{m}$  (e.g. Figure 7.20). There are many intermediate sized rafts of varying shapes having dimensions of about 3 or 4  $\mu\text{m}$  in diameter or in length depending on their shape (e.g. Figures 7.11, 7.15) and this size of raft is the most common size observed.

The damage comprising the rafts consists of three components:

1. Dislocation line segments.
2. Resolvable dislocation loops.
3. Black dot damage which is assumed to be unresolvable loops (Section 8.5).

Figure 7.10

Comet-type raft

Irradiation temperature = 250°C

Zone axis =  $\langle 111 \rangle$   $\vec{g} = \langle 22\bar{4} \rangle$

The shape of this raft can be compared to that in  
Figure 7.6B

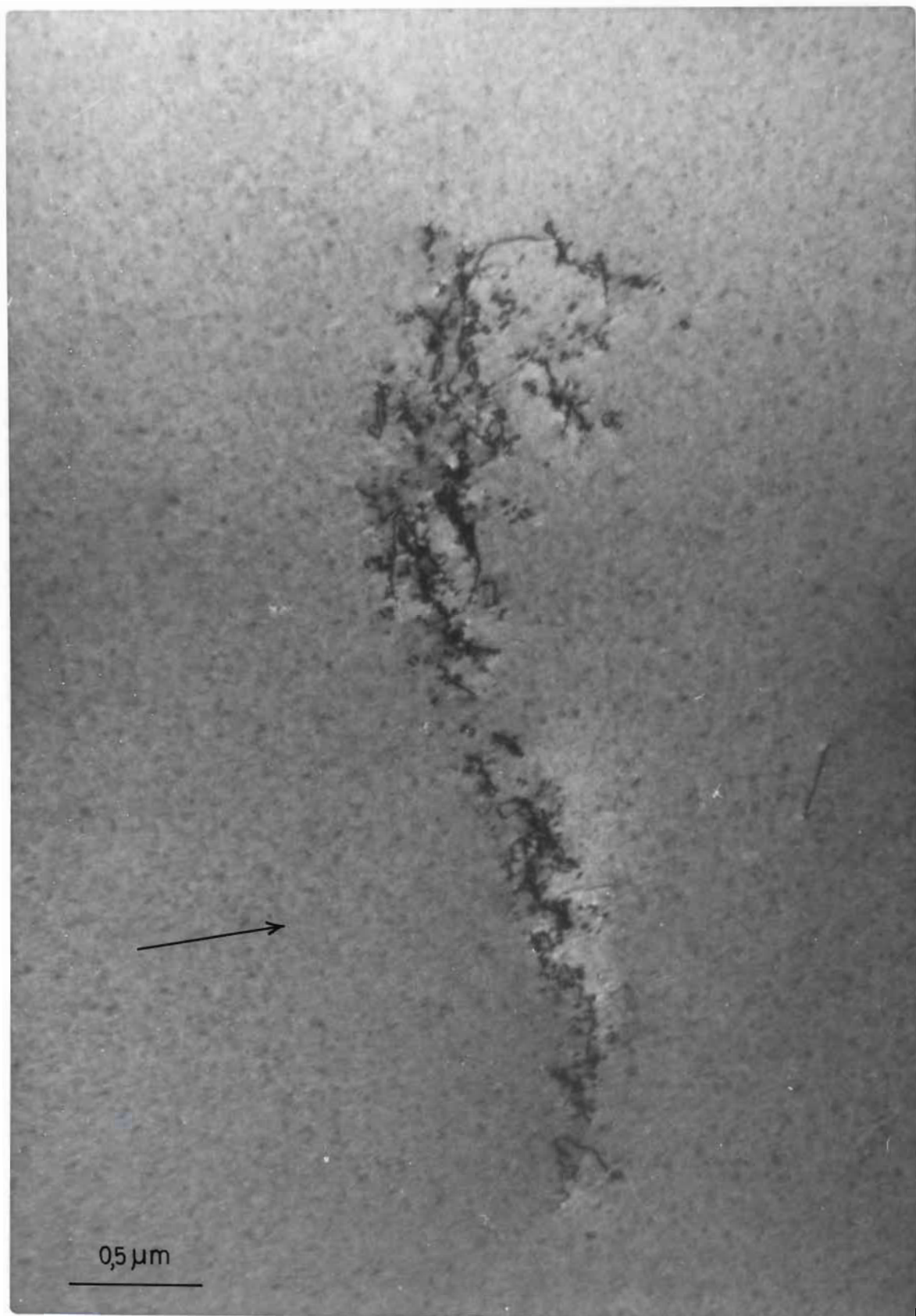


Figure 7.11

Typical comet-shaped rafts of damage. Irradiation temperature = 250°C.

A.

The shape of this raft may be compared to that in Figure 7.6C. Zone axis =  $\langle 111 \rangle$   $\vec{g} = \langle \bar{2}\bar{2}4 \rangle$

B.

The shape of this raft may be compared to that in Figure 7.6D. Zone axis =  $\langle 111 \rangle$   $\vec{g} = \langle \bar{2}\bar{2}4 \rangle$

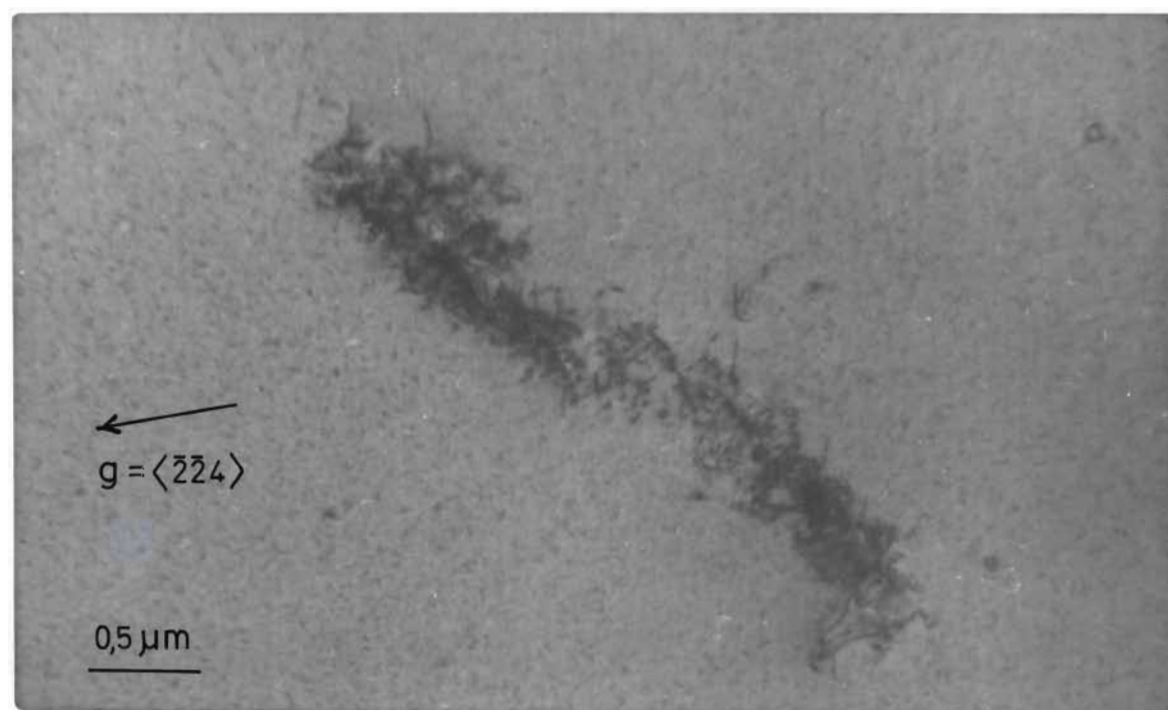
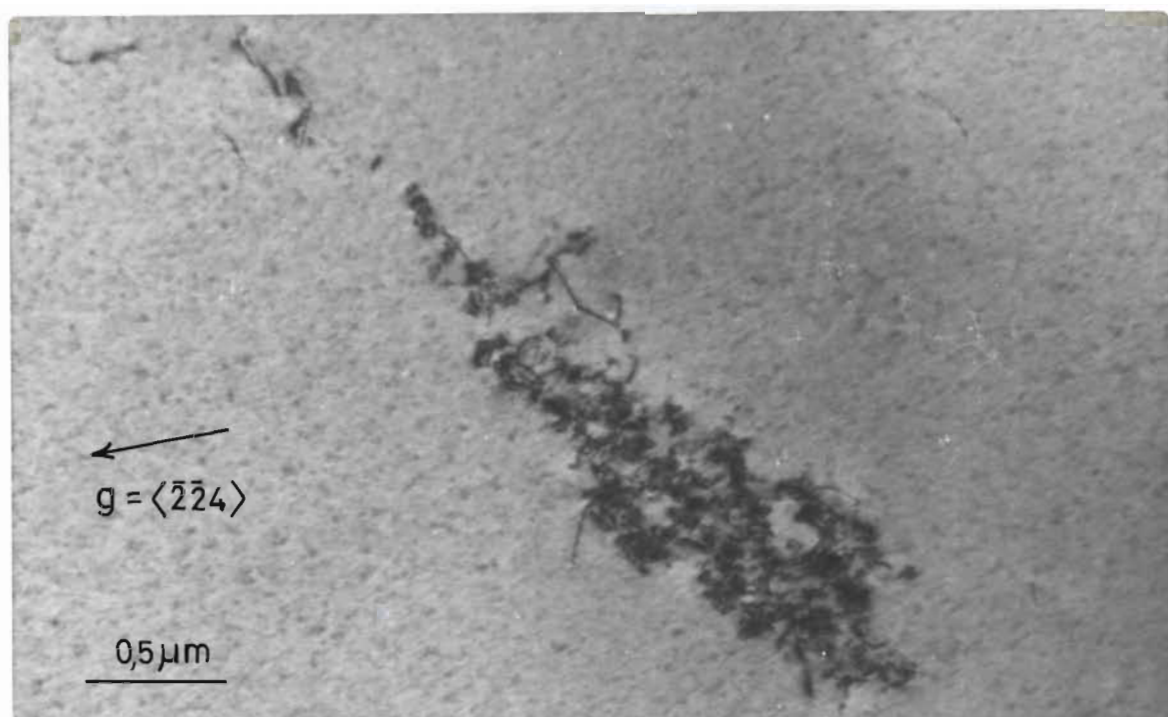


Figure 7.12

Typical fan-shaped raft of damage. Irradiation temperature = 250°C.

The shape of this raft may be compared to that in Figure 7.7D. Zone axis =  $\langle 111 \rangle$   $\vec{g} = \langle \bar{2}20 \rangle$

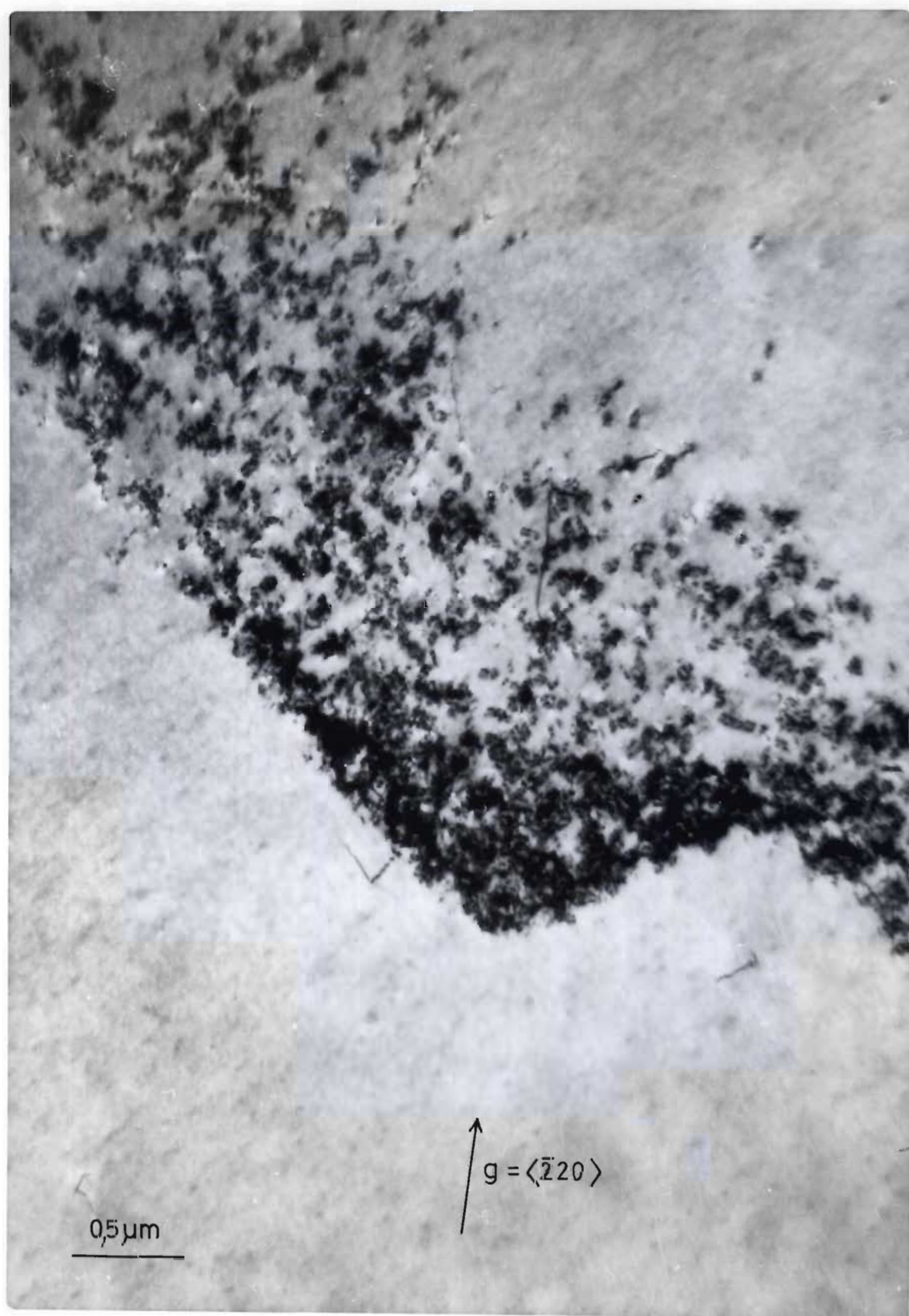


Figure 7.13

Typical edge-shaped raft of damage. Irradiation temperature = 250°C.

The shape of this raft may be compared to that in Figure 7.7C.

Zone axis =  $\langle 111 \rangle$   $\vec{g} = \langle 20\bar{2} \rangle$



Figure 7.14

Typical edge-shaped raft of damage.

Irradiation temperature = 250°C.

Zone axis =  $\langle 111 \rangle$   $\vec{g} = \langle 02\bar{2} \rangle$



Figure 7.15

Typical elliptical shaped rafts of damage.

Irradiation temperature = 250°C.

A.

Zone axis =  $\langle 211 \rangle$   $\vec{g} = \langle \bar{1}11 \rangle$

B.

Zone axis =  $\langle 211 \rangle$   $\vec{g} = \langle \bar{1}11 \rangle$

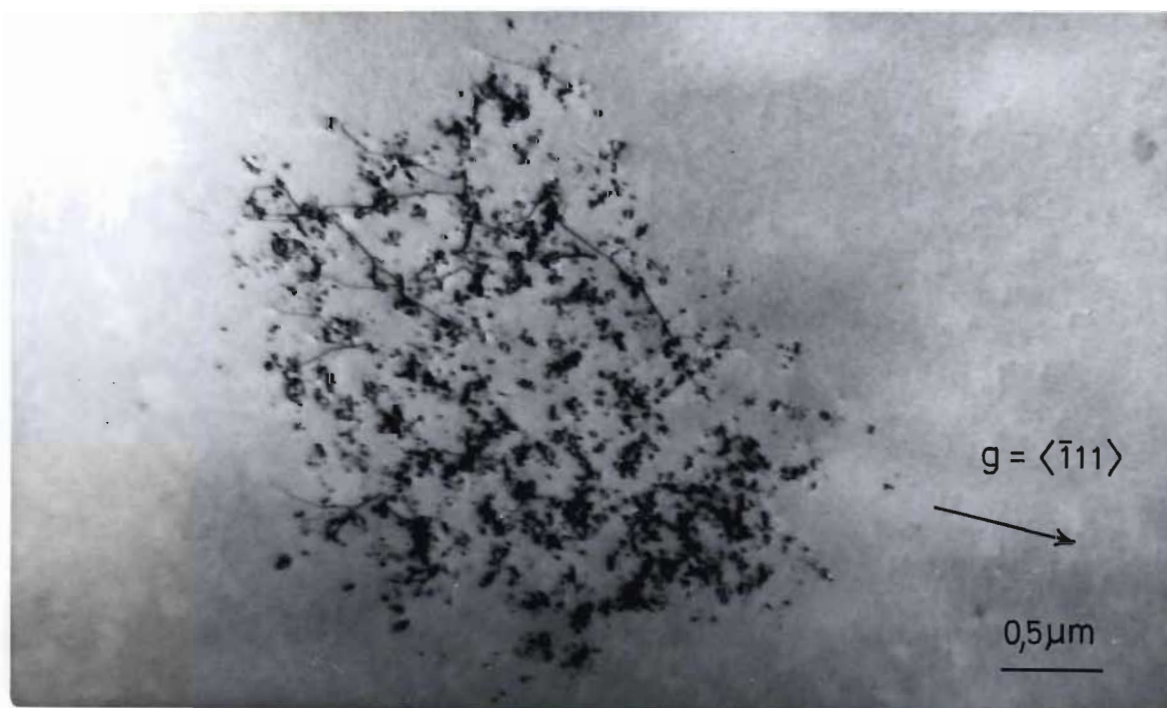
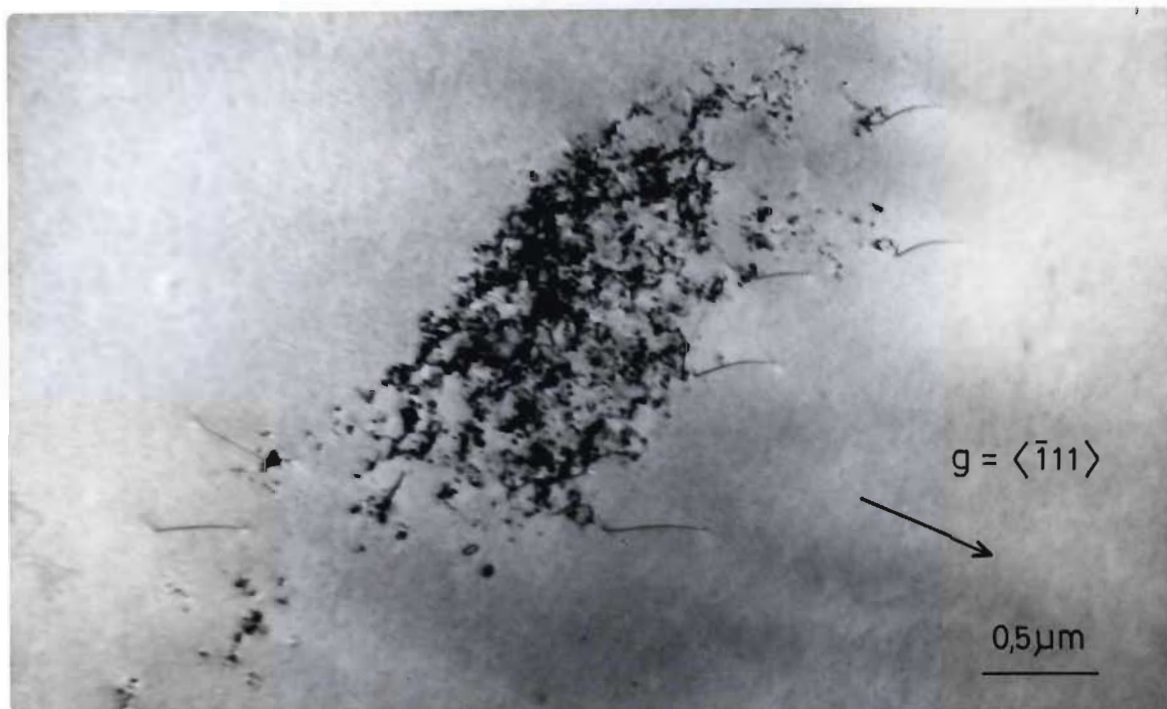
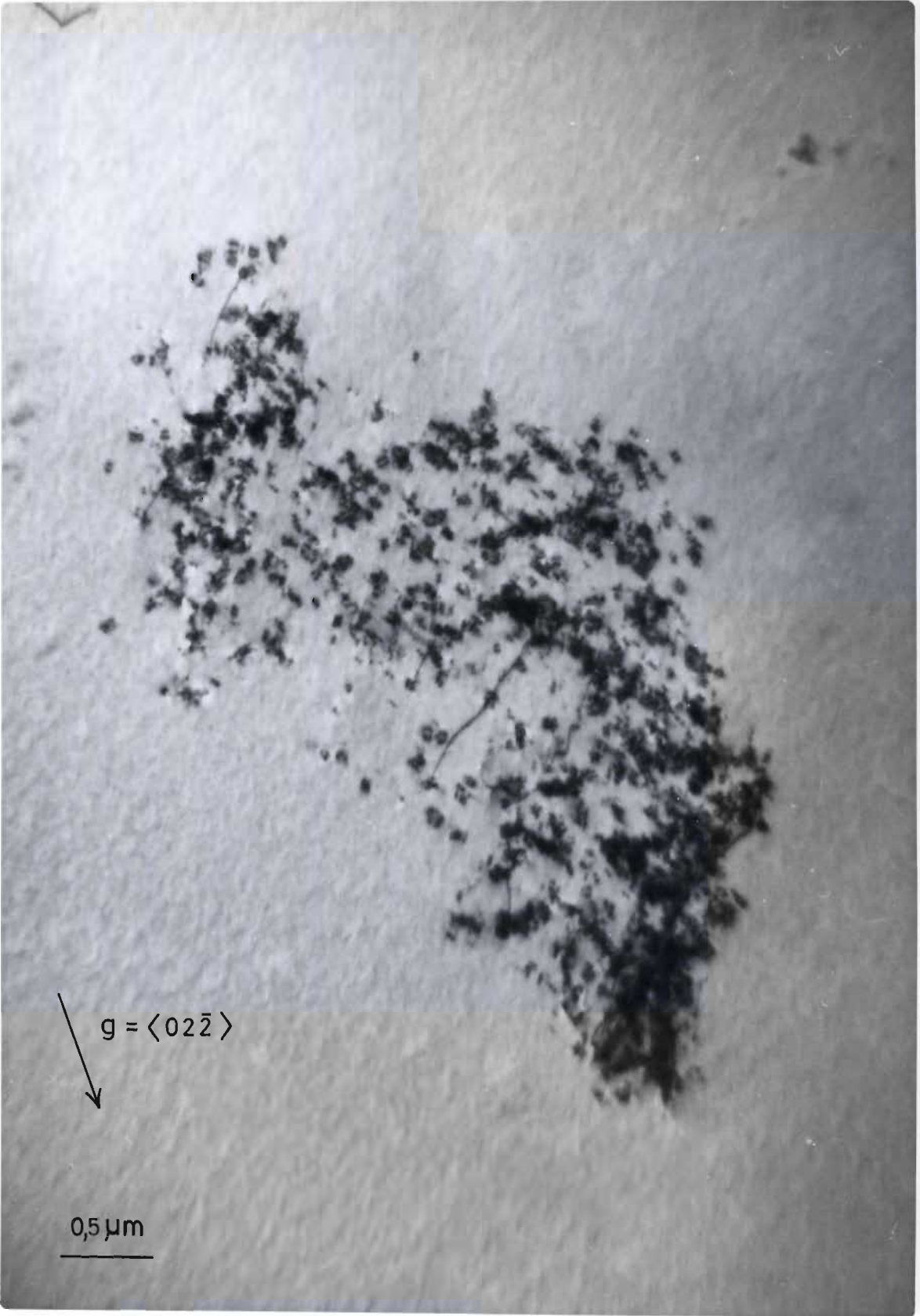


Figure 7.16

Typical elliptical-type raft of damage. Irradiation  
temperature = 250°C, Zone axis =  $\langle 111 \rangle$ ,  $\vec{g} = \langle 02\bar{2} \rangle$



$g = \langle 02\bar{2} \rangle$

0,5  $\mu\text{m}$

Figure 7.17

Typical irregular-shaped rafts of damage.

Irradiation temperature = 250°C.

A.

Zone axis =  $\langle 111 \rangle$ ,  $\vec{g} = \langle \bar{2}02 \rangle$

B.

Zone axis =  $\langle 111 \rangle$ ,  $\vec{g} = \langle 2\bar{2}0 \rangle$

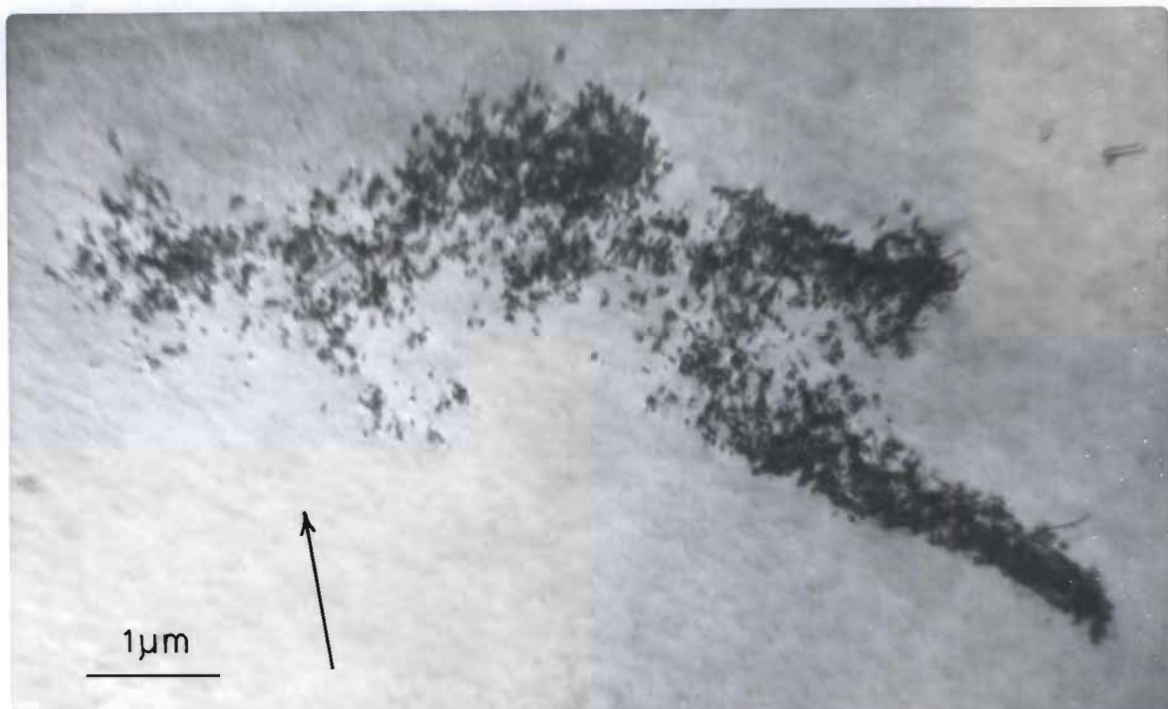


Figure 7.18

Typical irregular-shaped rafts of damage.

Irradiation temperature = 250°C.

A.

Zone axis =  $\langle 111 \rangle$ ,  $\vec{g} = \langle 02\bar{2} \rangle$

B.

Zone axis =  $\langle 211 \rangle$ ,  $\vec{g} = \langle 1\bar{3}1 \rangle$

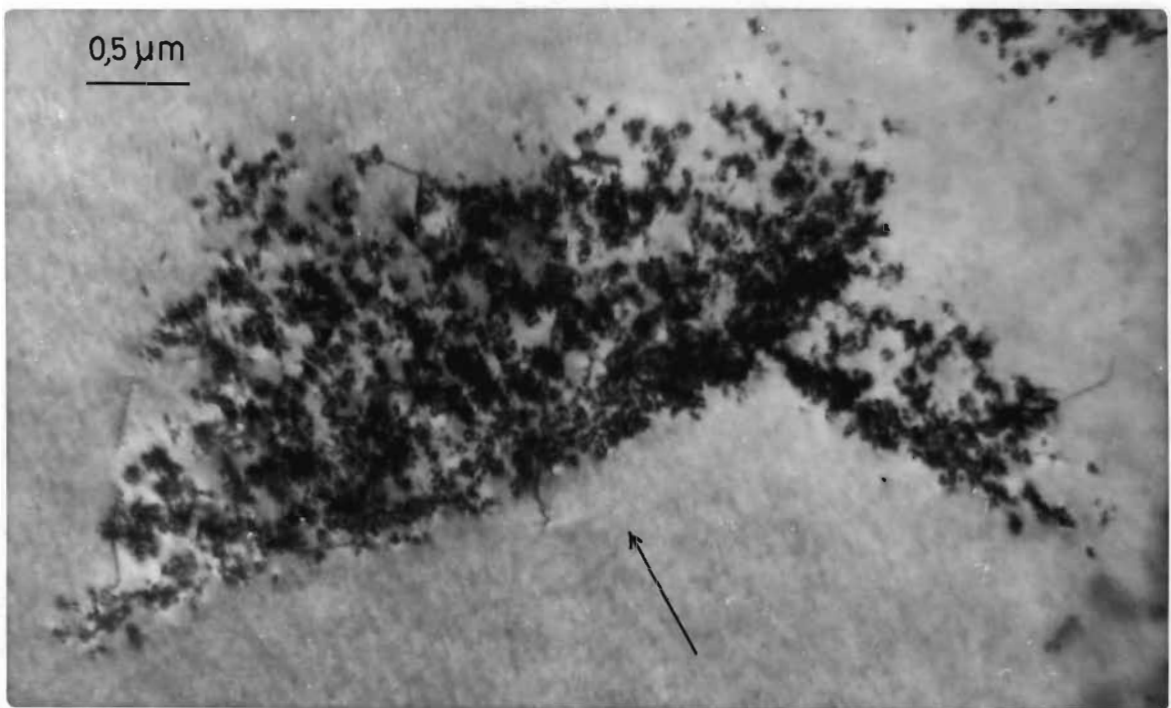
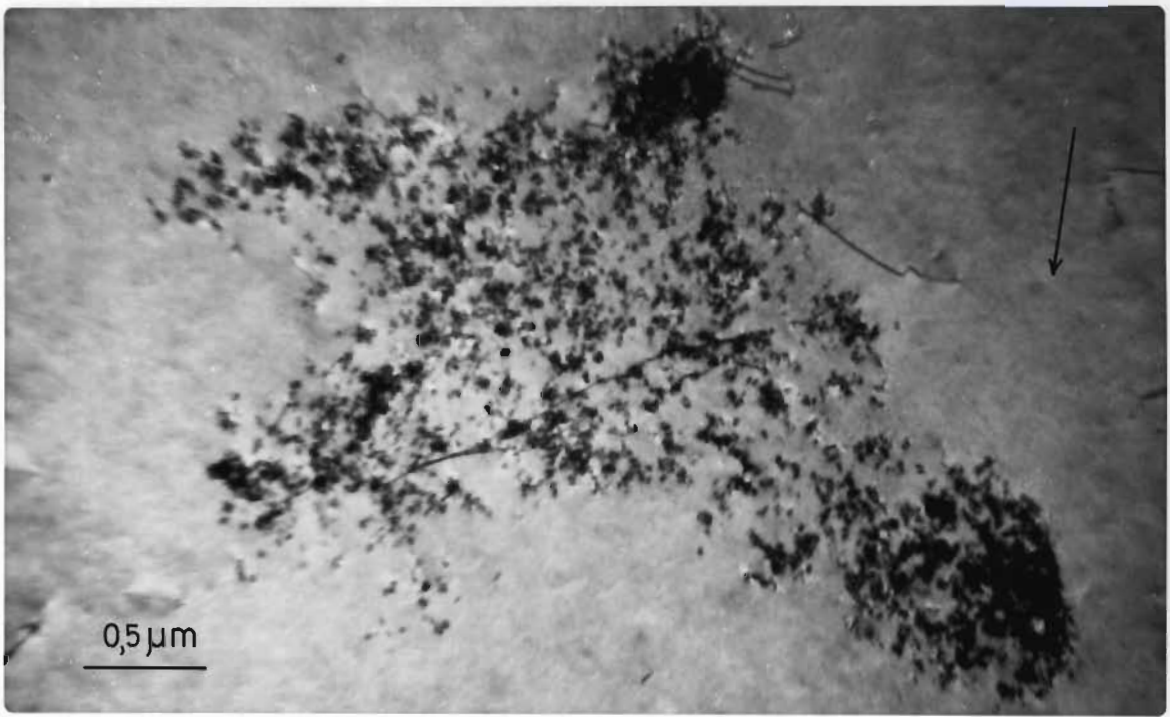


Figure 7.19

Large comet-shaped raft of damage.

The shape of this raft may be compared to that in Figure 7.6A.

Irradiation temperature = 250°C.

Total length = 36  $\mu\text{m}$ .

Zone axis =  $\langle 111 \rangle$   $\vec{g} = \langle 02\bar{2} \rangle$

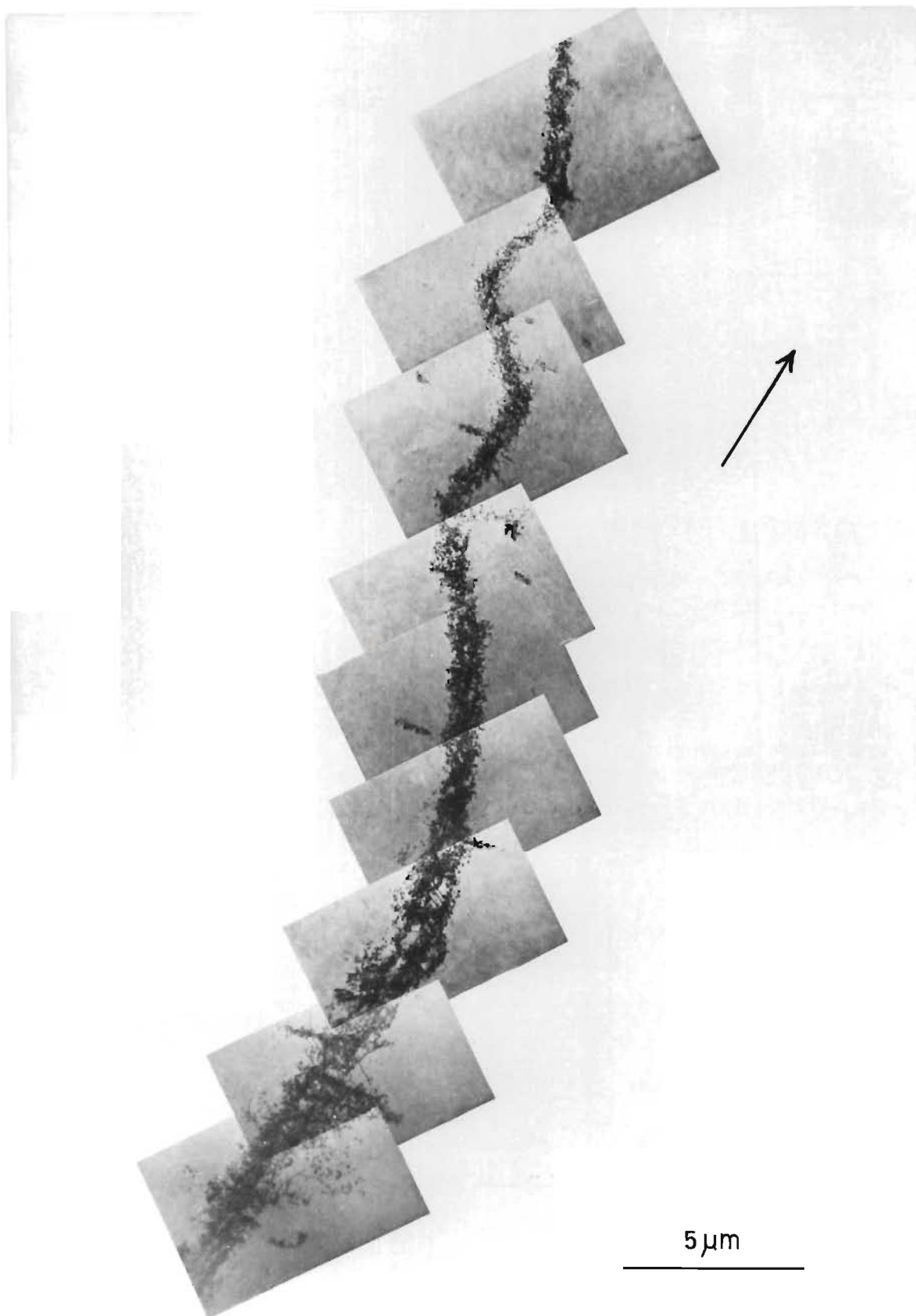


Figure 7.20

Examples of smallest rafts of damage seen.

Irradiation temperature = 250°C.

A.

Diameter  $\sim 0,5 \mu\text{m}$

Zone axis =  $\langle 111 \rangle$   $\vec{g} = \langle 02\bar{2} \rangle$

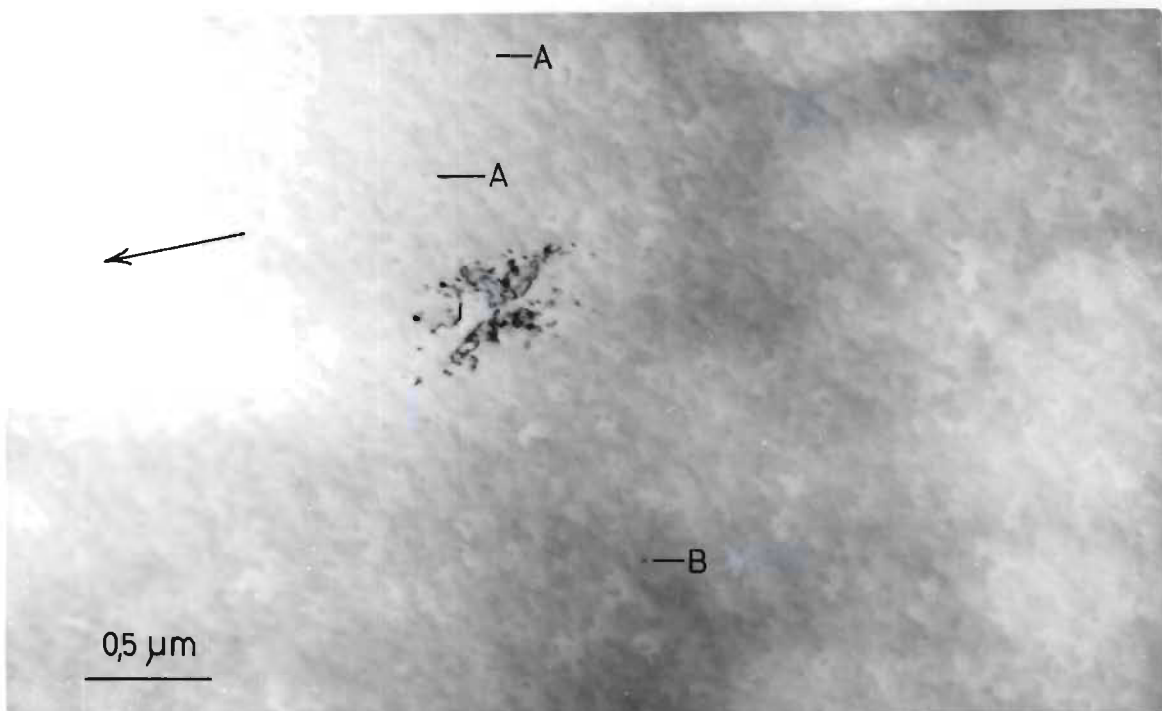
Two black dot defects are marked A.

A small loop ( $\sim 170 \text{ \AA}$ ) is marked B.

B.

Diameter  $\sim 1 \mu\text{m}$

Zone axis =  $\langle 211 \rangle$   $\vec{g} = \langle \bar{1}11 \rangle$



In general the rafts in this temperature range are dense as in Figures 7.12, 7.19 etc. and contain relatively few dislocation line segments and larger resolvable dislocation loops. However a small number of rafts exhibit more line segments and larger loops than the average (e.g. Figure 7.21). Also the rafts are usually very densely packed with damage (e.g. Figure 7.19) but again not all rafts obeyed this general rule. A triangular shaped raft is shown in Figure 7.22 which is rather loosely packed and Figure 7.23 shows rafts of rather irregular shapes which are very loosely packed with damage.

It is also generally observed that the rafts in these specimens have rather well defined boundaries with little damage projecting from them (e.g. Figure 7.19). Again however, there are exceptions to this general rule and Figure 7.22 shows small rafts with diffuse boundaries. Sometimes larger rafts (e.g. Figure 7.21) were seen which had diffuse boundaries which are out of character and which are penetrated in many places by dislocations.

Another marked feature of the radiation damage morphology in this temperature range is the extremely low density of damage in the large areas between rafts (Figure 7.20). In these areas one finds a very small amount of black dot damage and occasional dislocations. In Figure 7.20 a few black dots can be observed in the area surrounding the raft (some are marked "A") and one defect, marked "B", is just resolvable as a loop. An examination of these inter-raft areas was made, and by utilizing the weak-beam technique which is very sensitive to weak lattice strains (Figure 8.9) and high magnifications (Figure 8.8), it was shown that there is no extra resolvable component of background damage revealed by these techniques which is not discernable in normal

Bright Field micrographs (e.g. Figure 7.16).

As described in Section 7.4 the etch pit technique revealed that there is often correlation in the crystallographic directions in which the large rafts lie. This feature is also observed in the electron microscopy examinations and in addition electron microscopy revealed that many smaller rafts also exhibited this tendency. Furthermore rafts of shapes other than 'comets' sometimes have projections or asymmetrical shapes which are also often observed to align themselves parallel. The series of diagrams in Figure 7.24 are the outlines, drawn to scale, of the shapes of various rafts taken from a set of micrographs from a single specimen. The degree of correlation in crystallographic direction of the various features of the rafts can be seen. Many of the rafts are observed to align themselves along  $(211)$  directions in the crystal.

#### 7.5.2 Specimens irradiated at 300°C

Large rafts of damage are not observed in specimens irradiated at a temperature of 300°C. The damage consists rather of a large collection of tangled dislocations, resolvable dislocation loops, dislocation line segments, and black dot damage, which extends throughout the entire specimen area as shown in Figure 7.25A. Many of the dislocations form small tangles but there are in addition a number of isolated dislocations which are not associated with tangles and which are found in the spaces between the small tangles.

The largest tangles of dislocations which are seen clustered together in what can be described as one group, are approximately 4  $\mu\text{m}$  in dimension and have no particular macroscopic shape (Figure 7.25B). The smallest tangles of dislocations which are found are between 0,5

and 1  $\mu\text{m}$  in dimension (Figure 7.26) and again these tangles exhibit no marked macroscopic shape. The most common size of dislocation tangle is between 1 and 2  $\mu\text{m}$  in extent. The macroscopic shapes of these tangles vary considerably and no particular correlation of macroscopic shape is observed. The occurrence of dislocation tangles in the specimens is essentially homogeneous over a large area and the spacing between neighbouring dislocation tangles in general varies between 10 and 20  $\mu\text{m}$ . Examples of typical tangles seen are shown in Figures 7.27, 7.28.

The background to the dislocation tangles consists of an essentially homogeneous distribution of black dot damage and dislocations. Both the dislocations in tangles, and those in the inter-tangle areas, are heavily jogged and in addition there is considerable evidence that the motion of dislocations has been impeded by the pinning of the dislocations (e.g. at A Figure 7.26B). Large resolvable dislocation loops are not often seen but on the other hand are not as rare as they are in the damage of the specimens irradiated at the other temperatures studied. The largest resolvable loops seen are in general less than 1000  $\text{\AA}$  in diameter and any loops greater than 1000  $\text{\AA}$  which are noted are in general not circular but are of distorted shape and are jogged.

### 7.5.3 Specimens irradiated at 350°C

Large rafts of damage are observed in specimens irradiated at 350°C. They are similar to those observed after an irradiation at 250°C. Rafts in this temperature range also vary in shape from the long linear comet shapes to fan and elliptical shapes as well as irregular shapes (Figures 7.29, 7.30, 7.31). The sizes of rafts also vary greatly, with the largest rafts being comet shapes which can be as long as 100  $\mu\text{m}$

in length (Figure 7.29). Again these 'comets' are narrow and are approximately  $1\text{ }\mu\text{m}$  thick. The majority of the rafts observed however are about  $5\text{ }\mu\text{m}$  in size and generally tend to be approximately elliptical or fan-shaped.

The rafts observed in material irradiated at  $350^{\circ}\text{C}$  consist of the same three components of damage as those observed after an irradiation at  $250^{\circ}\text{C}$ , i.e. dislocation line segments, resolvable dislocation loops and black dot damage (Figure 7.31). However the relative proportions of the components of the damage structure of the rafts at  $350^{\circ}\text{C}$  are very different to those of rafts observed at  $250^{\circ}\text{C}$ . This is the most striking difference between the damage observed at  $350^{\circ}\text{C}$  and that observed at  $250^{\circ}\text{C}$ . The rafts at  $350^{\circ}\text{C}$  are composed primarily of dislocation line segments and contain extremely little black dot damage (Figures 7.29, 7.30). Also the damage is much more homogeneously distributed over the area of the raft than is the case at  $250^{\circ}\text{C}$ .

The boundaries of rafts in this temperature range are less sharply defined than at  $250^{\circ}\text{C}$  and are rather diffuse. There are frequently dislocations projecting from the rafts (e.g. Figure 7.29) or black dot damage distributed around the periphery of the rafts (e.g. Figure 7.31). Because the boundaries are diffuse it is difficult to decide on the minimum size of raft present. The smaller rafts are just loose groupings of the three damage components (e.g. Figure 7.32) and cannot really be distinguished from the occasional dislocations and black dot damage found in the inter-raft spaces (Figure 7.33). In addition a number of dipole dislocations are found (Figure 7.23A and Section 8.6).

The rafts at  $350^{\circ}\text{C}$  are also three dimensional as indicated by etch pitting and stereo electron microscopy.

Figure 7.21

Rafts of damage containing a large number of dislocation line segments. Irradiation temperature = 250°C.

A.

Zone axis =  $\langle 211 \rangle$      $\vec{g} = \langle \bar{1}11 \rangle$

B.

Zone axis =  $\langle 211 \rangle$      $\vec{g} = \langle 0\bar{2}2 \rangle$

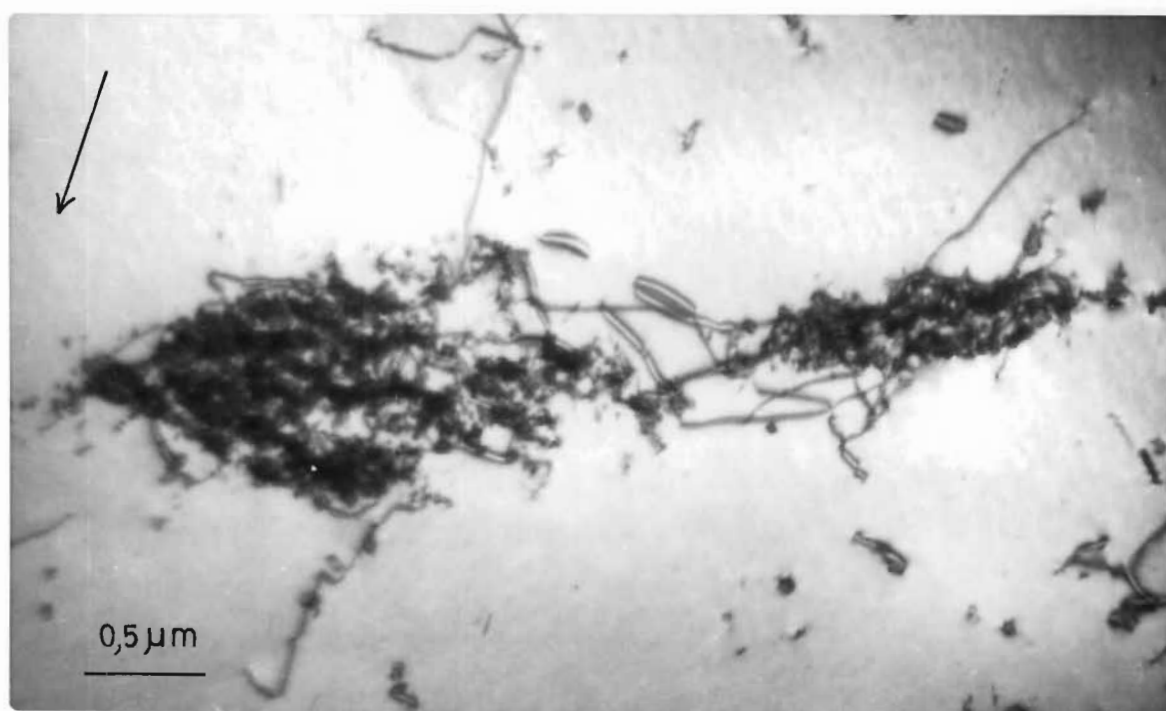
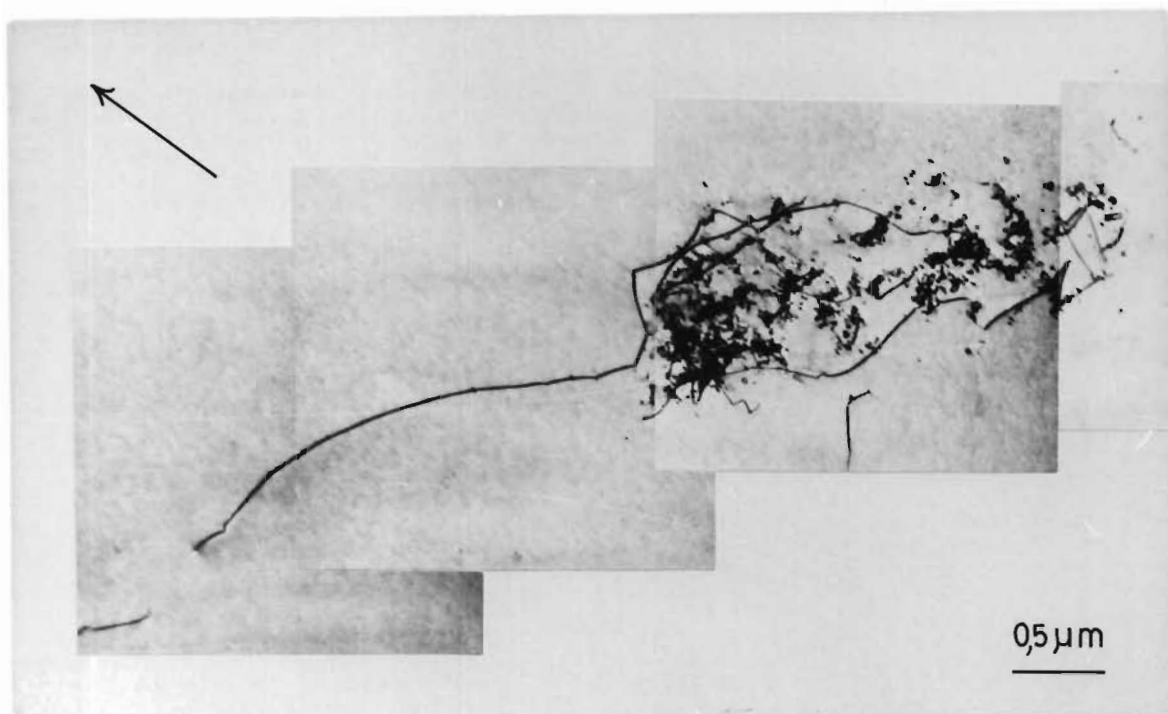


Figure 7.22

Loosely packed rafts of damage with diffuse boundaries. Irradiation temperature = 250°C.

A.

This raft is approximately triangular in shape.

Zone axis =  $\langle 211 \rangle$   $\vec{g} = \langle 02\bar{2} \rangle$

B.

Zone axis =  $\langle 111 \rangle$   $\vec{g} = \langle 02\bar{2} \rangle$

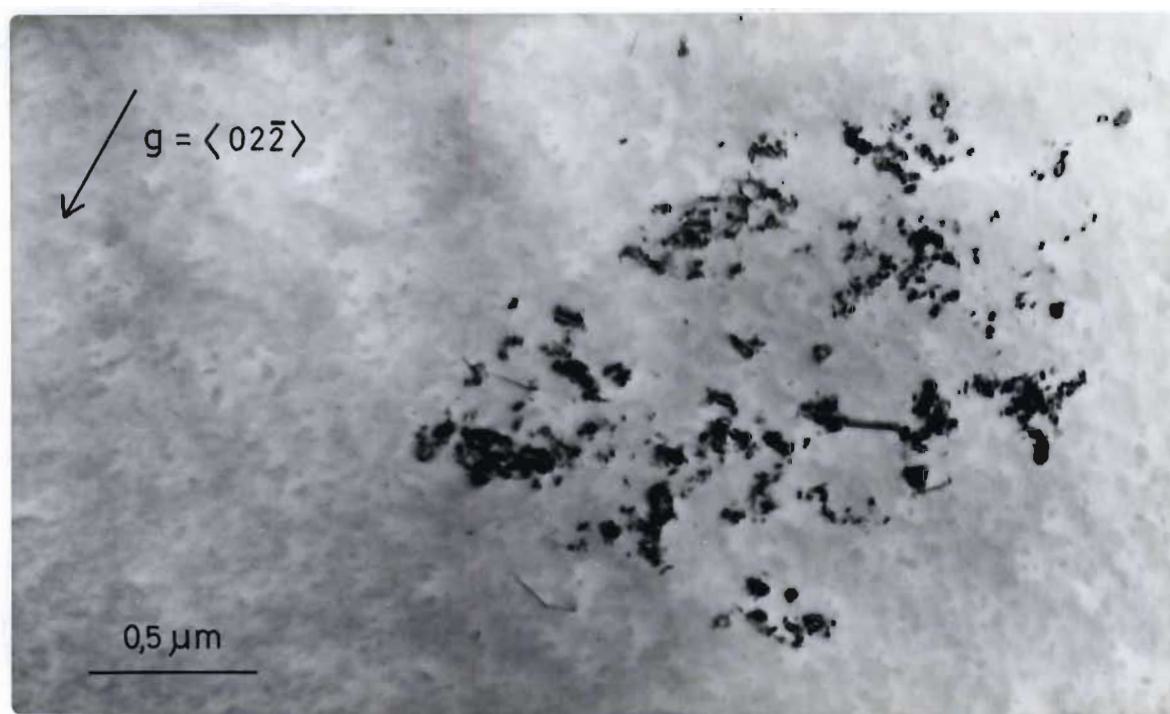


Figure 7.23

Loosely packed rafts of damage with diffuse boundaries. Irradiation temperature = 250°C.

A.

Zone axis =  $\langle 211 \rangle$   $\vec{g} = \langle \bar{1}11 \rangle$

B.

A few dipole dislocations can be seen in this raft (Section 8.6).

Zone axis =  $\langle 111 \rangle$   $\vec{g} = \langle \bar{2}02 \rangle$

Note

The small white spots that appear in these photographic prints are the result of incorrect photographic glazing and are not defects in the specimen.

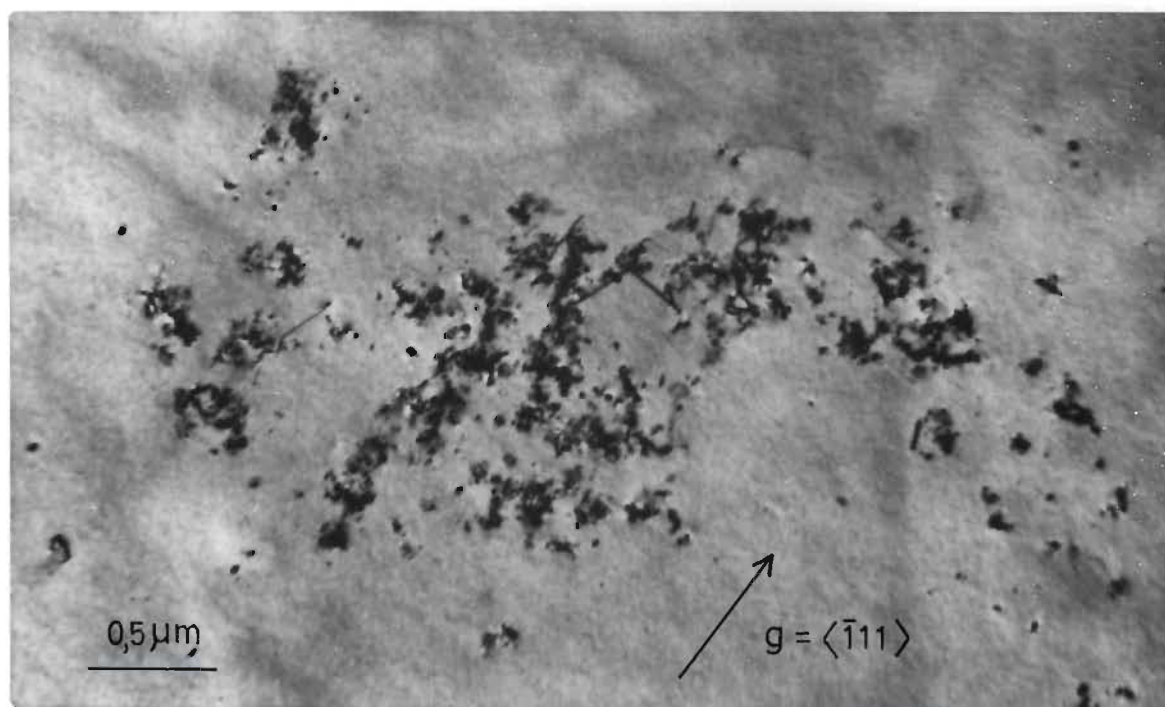
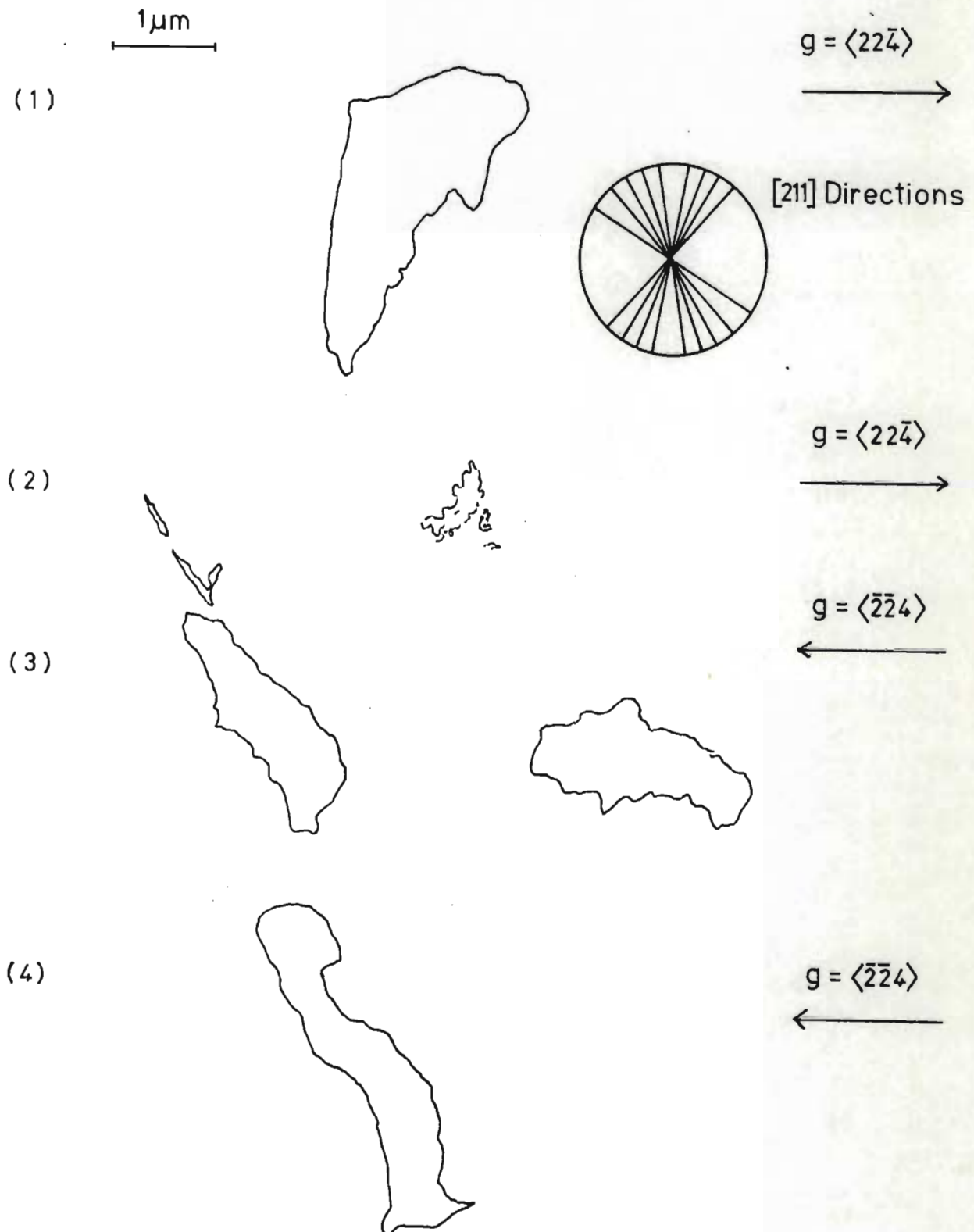
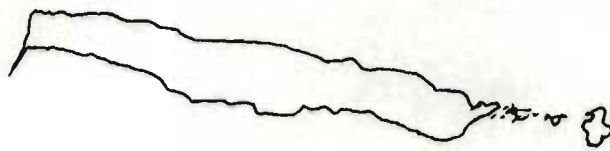


FIG (7.24)

The shape of various rafts drawn to scale and orientated correctly with respect to one another. Irradiation temperature =  $250^{\circ}\text{C}$ . Zone axis of all micrographs =  $\langle 111 \rangle$



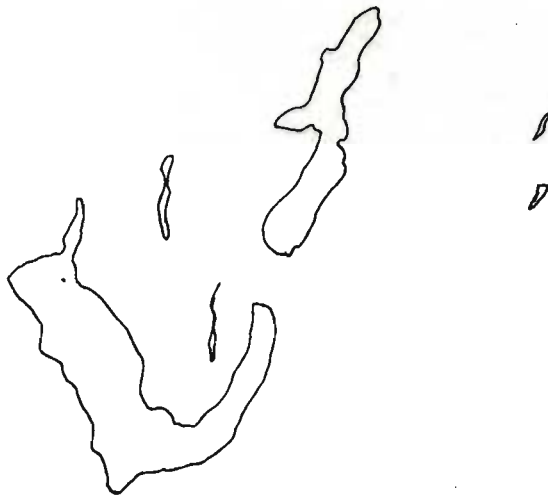
(5)



$$g = \langle 22\bar{4} \rangle$$



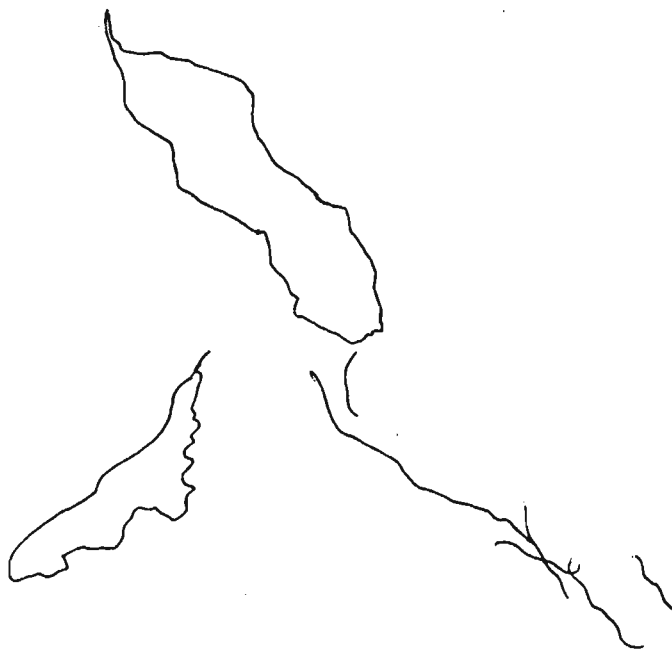
(6)



$$g = \langle 22\bar{4} \rangle$$



(7)



$$g = \langle 22\bar{4} \rangle$$



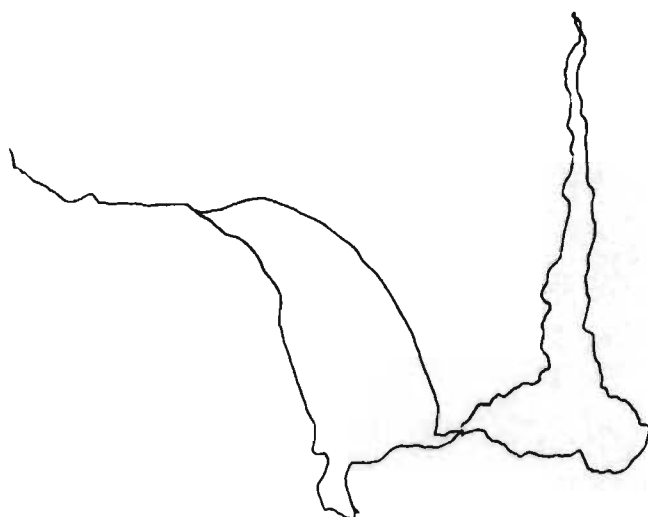
(8)



$$g = \langle 22\bar{4} \rangle$$



(9)



$$g = \langle 22\bar{4} \rangle$$



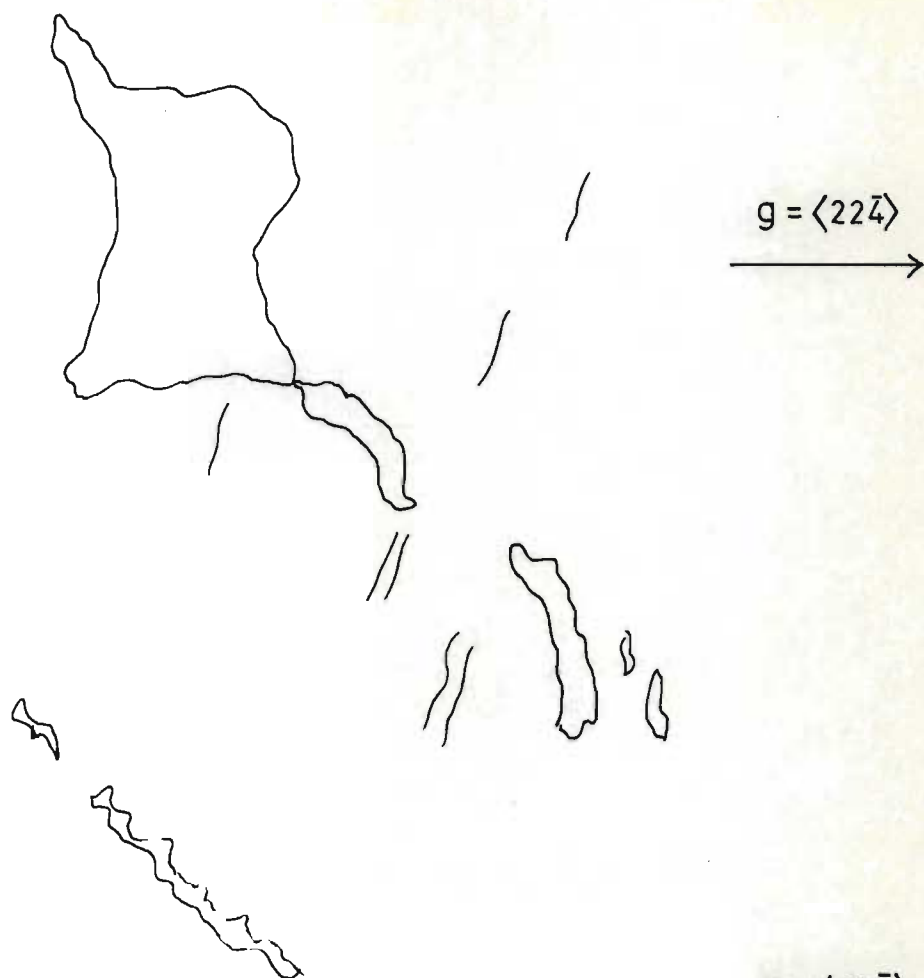
(10)



$$g = \langle 22\bar{4} \rangle$$



(11)



(12)



(13)



Figure 7.25

A.

Typical area of a specimen irradiation at  
300°C.

Zone axis =  $\langle 211 \rangle$   $\vec{g} = \langle 1\bar{1}\bar{1} \rangle$

B.

Typical largest dislocation tangle found  
in a specimen irradiated at 300°C.

Zone axis =  $\langle 211 \rangle$   $\vec{g} = \langle 1\bar{1}\bar{1} \rangle$

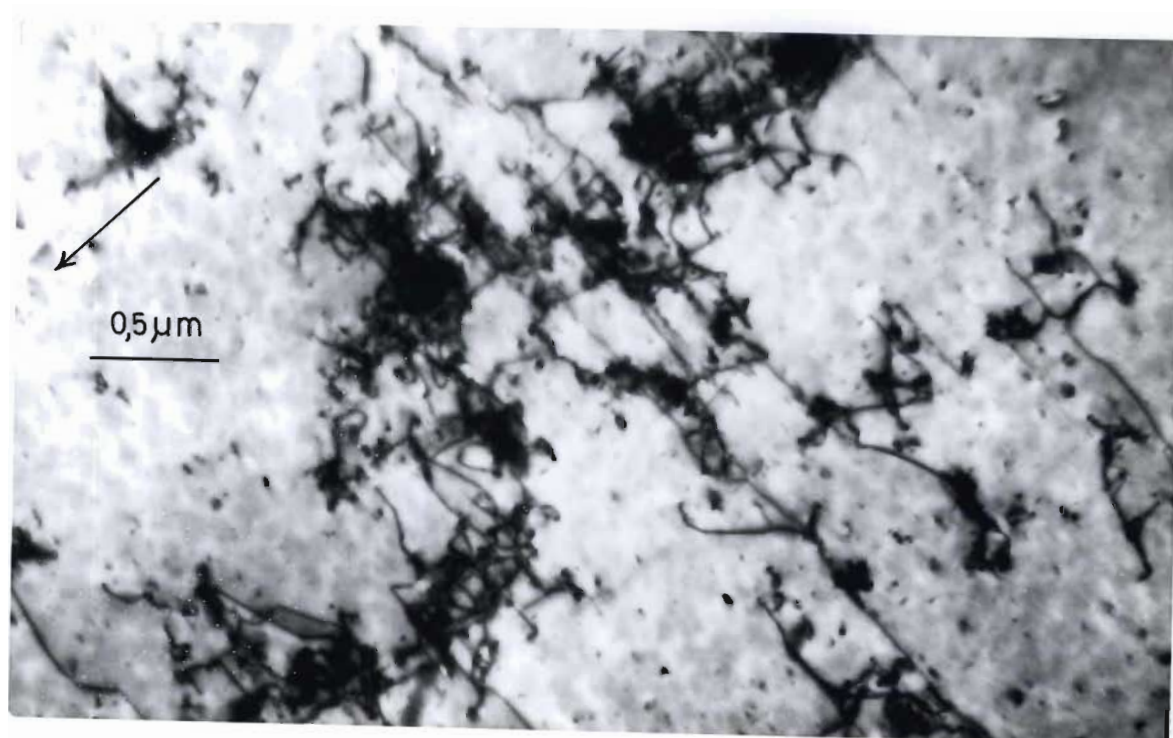
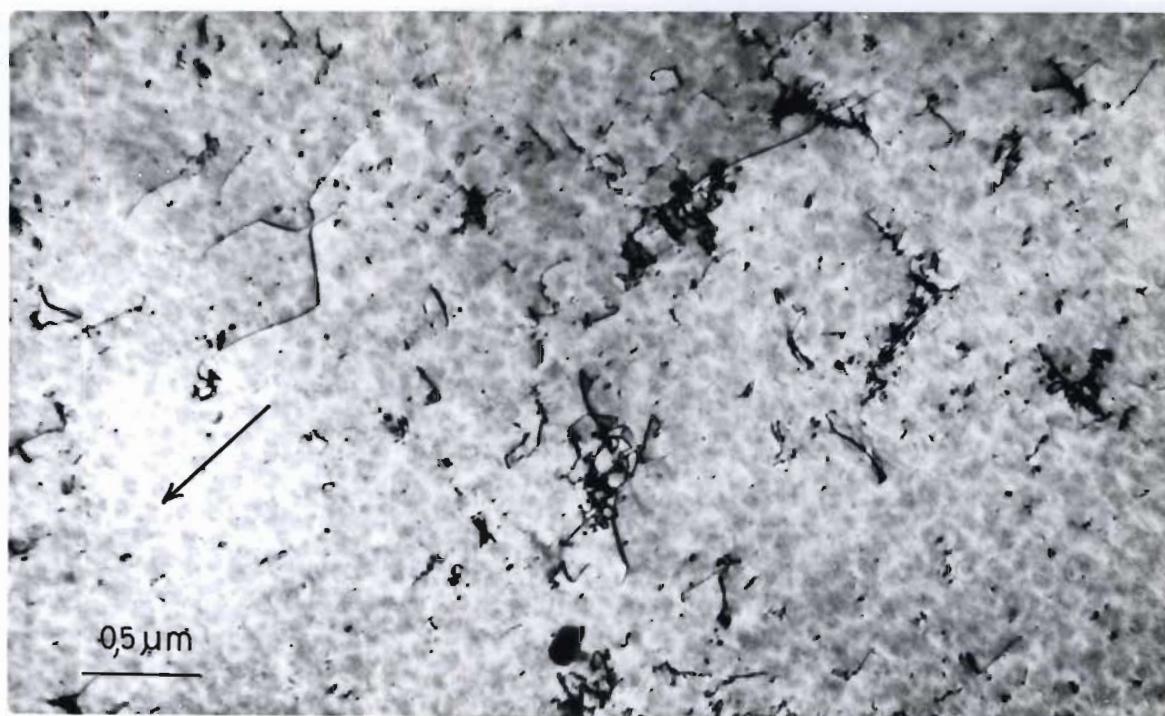


Figure 7.26

Typical smallest dislocation tangles found after  
an irradiation at 300°C.

A.

Zone axis =  $\langle 211 \rangle$     $\vec{g} = \langle 1\bar{1}\bar{1} \rangle$

B.

Zone axis =  $\langle 211 \rangle$     $\vec{g} = \langle 1\bar{1}\bar{1} \rangle$

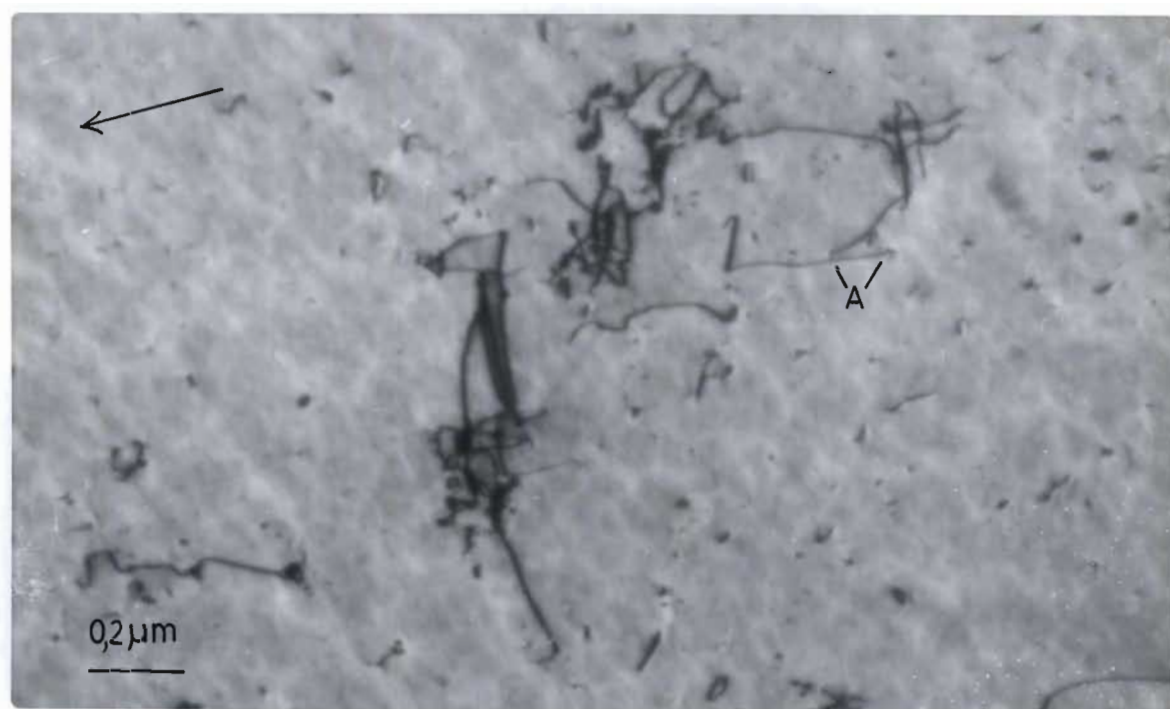


Figure 7.27

Typical dislocation tangles seen after an irradiation  
at 300°C.

A.

Zone axis =  $\langle 211 \rangle$   $\vec{g} = \langle 1\bar{1}\bar{1} \rangle$

B.

Zone axis =  $\langle 211 \rangle$   $\vec{g} = \langle 1\bar{1}\bar{1} \rangle$

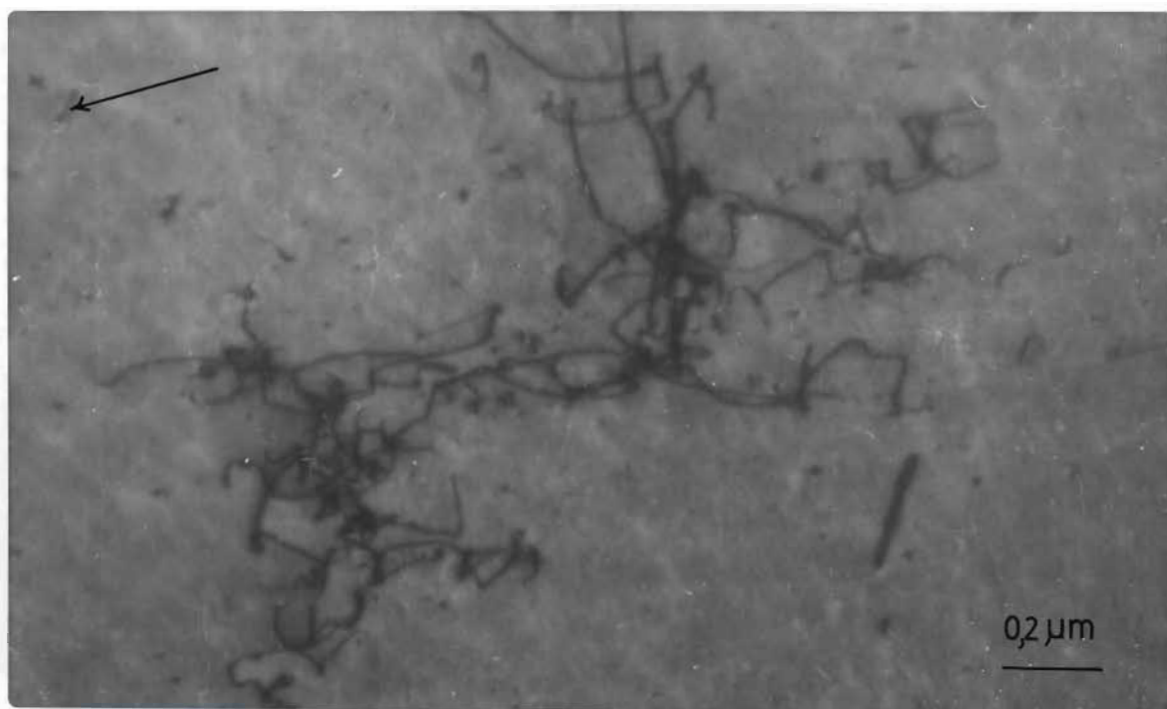
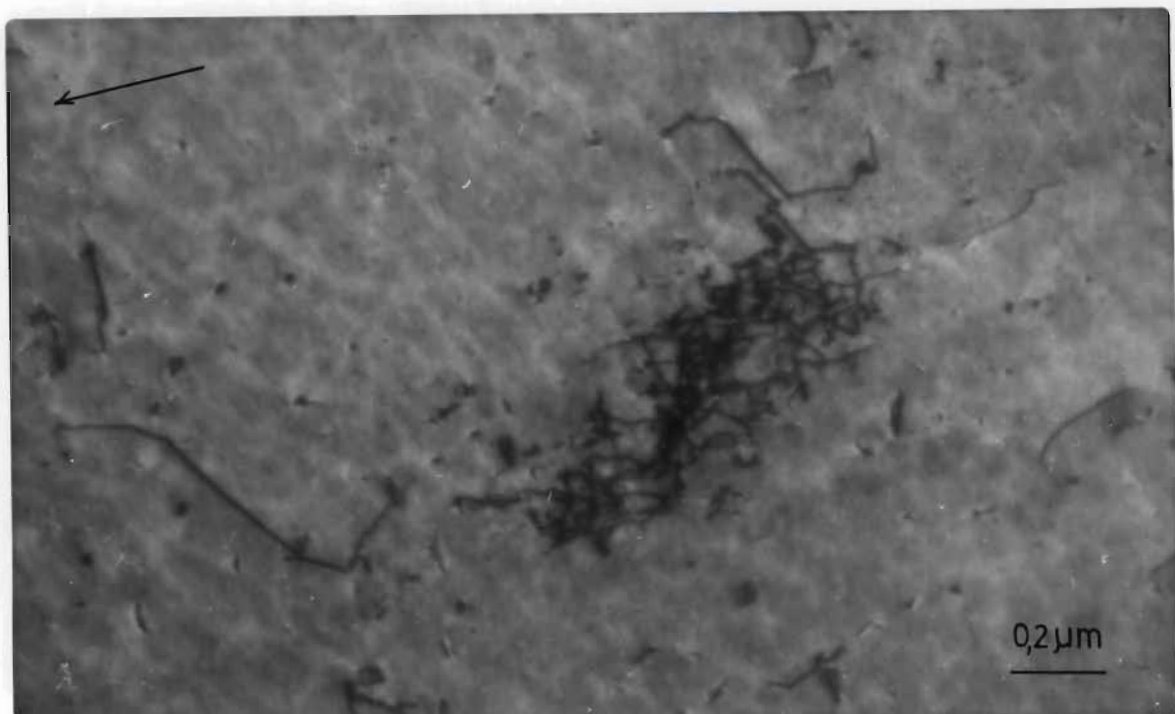


Figure 7.28

Typical dislocation tangles seen after an irradiation  
at 300°C.

A.

Zone axis =  $\langle 211 \rangle$     $\vec{g} = \langle \bar{1}11 \rangle$

B.

Zone axis =  $\langle 211 \rangle$     $\vec{g} = \langle 02\bar{2} \rangle$

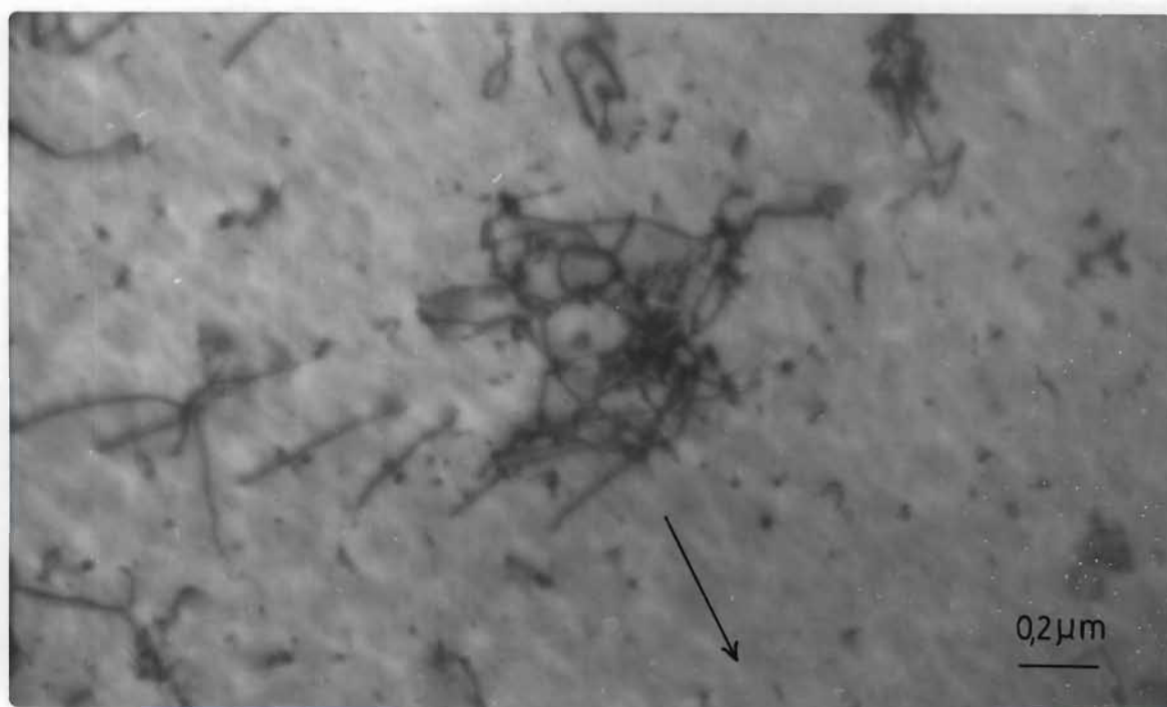
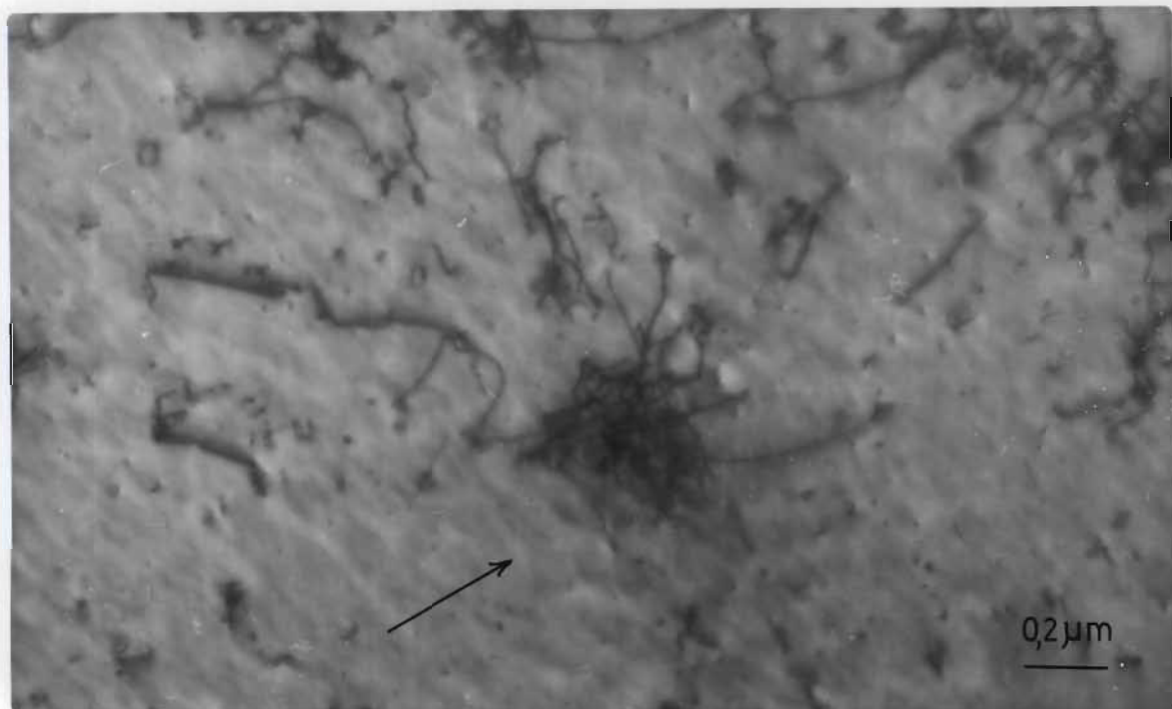


Figure 7.29

Large raft observed after an irradiation at 350°C.

This raft is 104  $\mu\text{m}$  in length.

Zone axis =  $\langle 111 \rangle$   $\vec{g} = \langle 0\bar{2}2 \rangle$

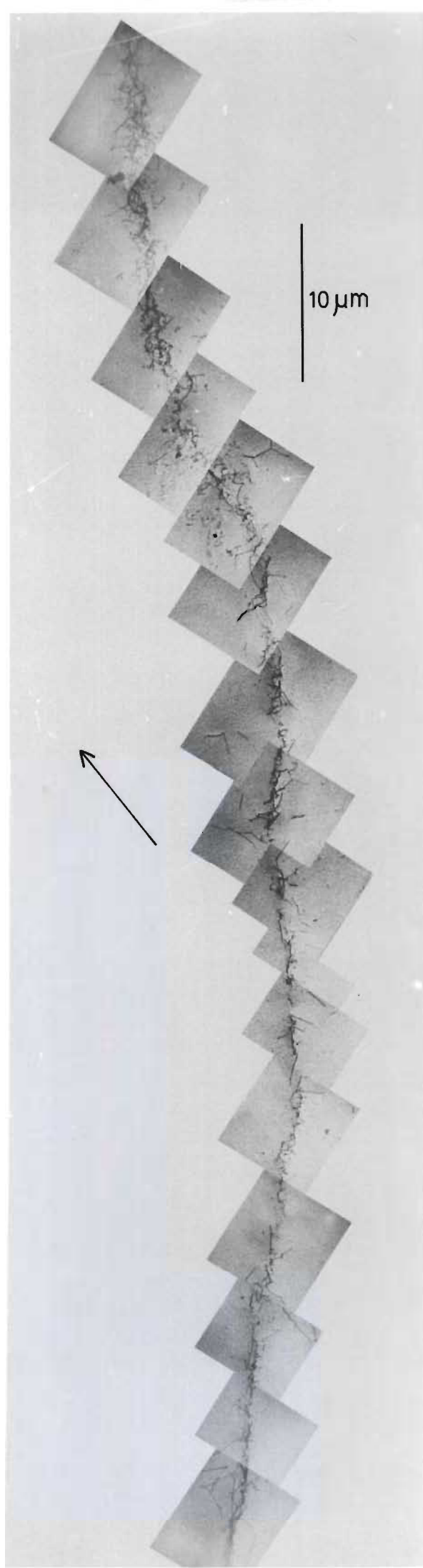


Figure 7.30

Fan-shaped raft.

Irradiation temperature = 350°C

Zone axis =  $\langle 211 \rangle$   $\vec{g} = \langle 1\bar{1}\bar{1} \rangle$

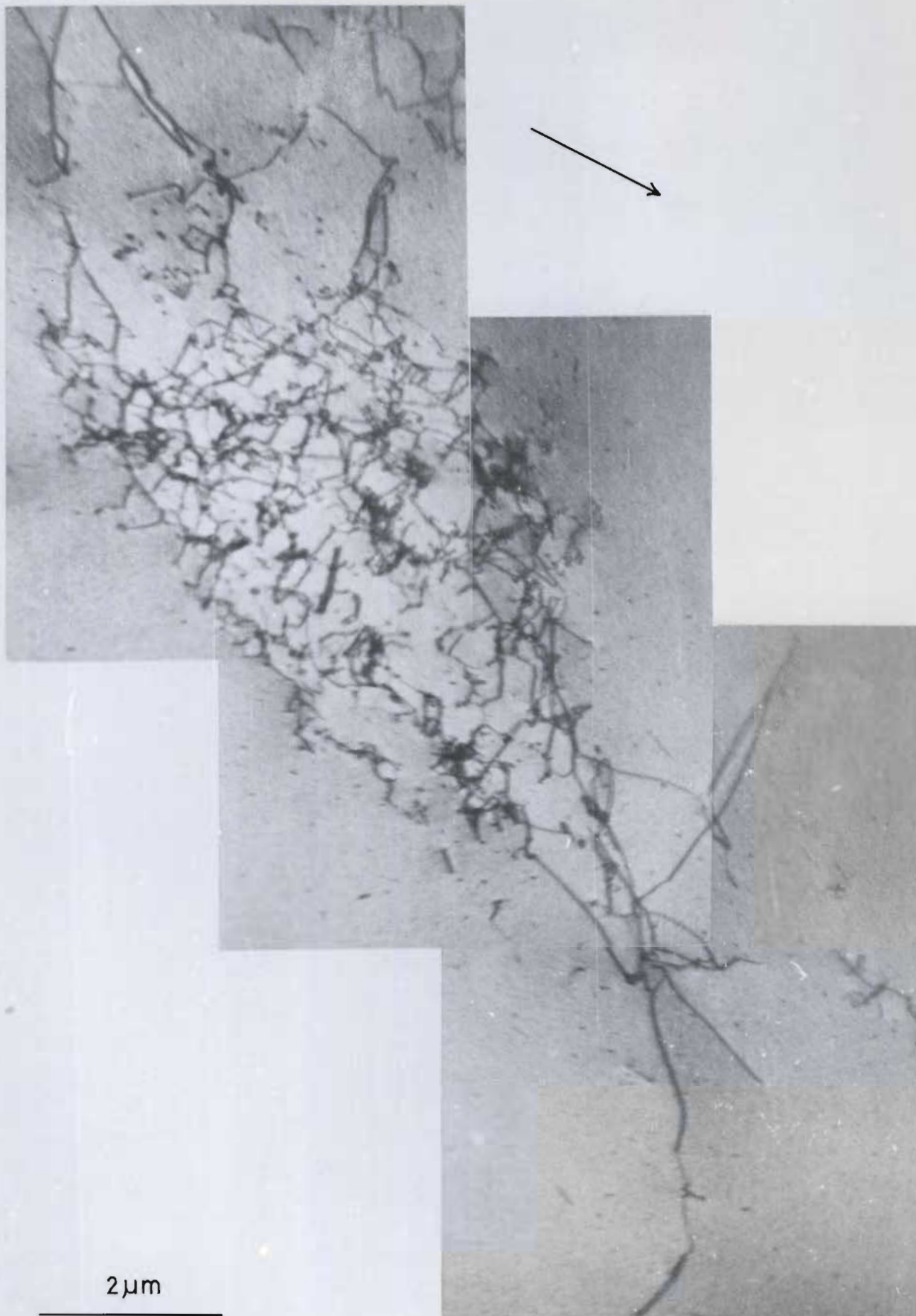


Figure 7.31

Irregular shaped raft. Irradiation temperature  
= 350°C. Zone axis =  $\langle 111 \rangle$   $\vec{g} = \langle 2\bar{2}0 \rangle$



Figure 7.32

Examples of small loose rafts after an irradiation  
at 350°C.

A.

Zone axis =  $\langle 111 \rangle$     $\vec{g} = \langle 0\bar{2}2 \rangle$

B.

Zone axis =  $\langle 111 \rangle$     $\vec{g} = \langle 0\bar{2}2 \rangle$



Figure 7.33

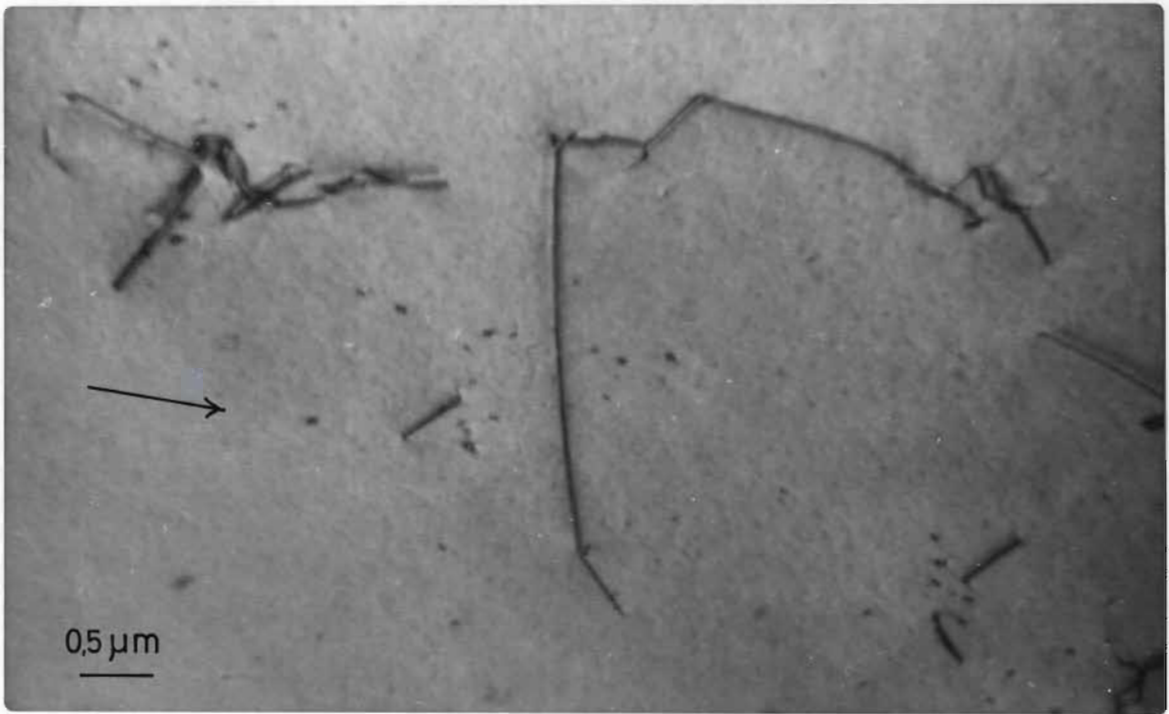
Examples of dislocations and black dot damage found in the inter-raft spaces after an irradiation at 350°C. Pinning of the dislocations is evident.

A.

Zone axis =  $\langle 111 \rangle$   $\vec{g} = \langle 0\bar{2}2 \rangle$

B.

Zone axis =  $\langle 211 \rangle$   $\vec{g} = \langle \bar{1}11 \rangle$



In the 350°C temperature range there is, as at 250°C, an extremely low density of inter-raft or background damage. Occasional dislocations which have a maximum length of about 1,5 µm and which are usually rather smooth andunjogged, although often pinned, are seen in addition to a small amount of black dot damage which is sparsely and inhomogeneously scattered around in the inter-raft regions.

Rafts are observed also to align themselves along {211} directions in this temperature range.

#### 7.5.4 Specimens irradiated at 400°C

No large rafts of damage are observed in specimens irradiated at 400°C. The most marked feature of these specimens is the extremely low density of damage of any kind. Groups of rather straight and generally unjogged dislocations (e.g. Figures 7.34A, 7.36A) are the most common feature seen in these specimens. These groups of dislocations are widely spaced and in general single dislocations do not appear in isolation. There is very little tangling of the dislocations forming a group, but there is evidence of the pinning of the dislocations by other damage present (e.g. Figure 7.34B).

The damage observed in material irradiated at 400°C does not always conform to the general pattern of small dislocation groupings; and as is the case at irradiation temperatures of 250°C and 350°C, there are deviations from the general damage appearance. In some cases one observes considerably more tangled dislocation groupings which contain a large incidence of small pieces of dislocation line segment and black dot damage in the immediate area of the dislocation cluster. An example of the most dense dislocation clusters observed is shown in Figure 7.34B.

The largest dislocation groupings seen are about 20  $\mu\text{m}$  in length (e.g. Figure 7.35) and these larger dislocation groupings are not found to consist of a more dense cluster of damage than that indicated by Figure 7.35. Damage as dense as that in the dislocation cluster in Figure 7.34B, which is about 6  $\mu\text{m}$  square, was not seen in larger groupings of damage.

The large dislocation groups such as Figure 7.35 all exhibit a long linear appearance as if they could be reminiscent of comet-type rafts. These long linear groups are less than about 4  $\mu\text{m}$  in width which is wider than the comet-shaped rafts of approximately 1  $\mu\text{m}$  in width which are observed in material irradiated at 250°C and 350°C.

Smaller dislocation groupings also sometimes tend to exhibit the fundamental macroscopic shapes as observed in the large rafts of damage present in the 250°C and 350°C irradiations. A linear type group of dislocations is shown in Figure 7.36A while in Figure 7.36B a fan type group is seen. Both these configurations are observed quite frequently.

The smallest groupings of dislocations observed are about 4  $\mu\text{m}$  in extent (e.g. Figures 7.34A and 7.36) and the most common size of group is 4 or 5  $\mu\text{m}$ .

Occasional isolated dislocations are found (e.g. Figure 7.37) and these dislocations are in general short and unjogged. A small amount of black dot damage is found in the background areas. Occasionally more dense accumulations of damage consisting of small pieces of dislocation line, black dots and resolvable loops are observed (Figure 7.38B). These higher densities of damage however exist over very small areas - usually less than 10  $\mu\text{m}$  square. A number of the comet-shaped rafts are found to be aligned along  $\{211\}$  directions.

Figure 7.34

A.

Typical dislocation group observed after an  
irradiation at 400°C.

Zone axis =  $\langle \bar{2}33 \rangle$   $\vec{g} = \langle 311 \rangle$

B.

An example of the densest damage clusters  
observed after an irradiation at 400°C.  
There is evidence of the pinning of the  
dislocations by the other damage present  
in this damage cluster.

Zone axis =  $\langle 211 \rangle$   $\vec{g} = \langle \bar{1}11 \rangle$



Figure 7.35

Example of the largest dislocation groups seen  
after an irradiation at 400°C.

This group is 16  $\mu\text{m}$  in length.

The dislocation loop at the top of the picture  
is 5600 Å in diameter and is interstitial in  
character.

The mottled background is an effect due to a  
rough specimen surface.

Zone axis =  $\langle 110 \rangle$      $\vec{g} = \langle 1\bar{1}\bar{1} \rangle$

1  $\mu$ m

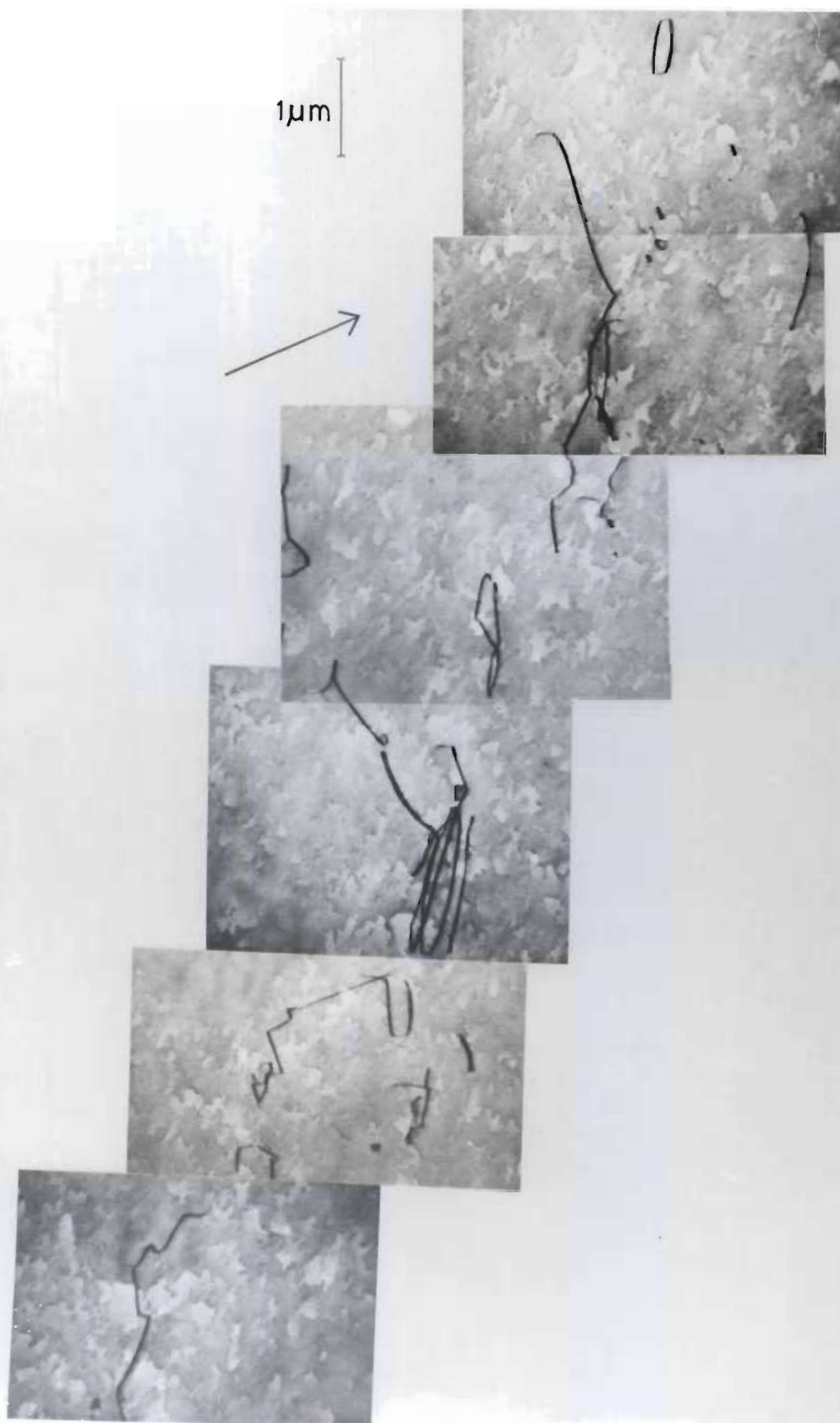


Figure 7.36

Typical dislocation structures after an  
irradiation at a temperature of 400°C.

A.

Linear-type group of dislocations

Zone axis =  $\langle \bar{2}33 \rangle$ ,  $\vec{g} = \langle 0\bar{2}2 \rangle$

B.

Fan-type group of dislocations

Zone axis =  $\langle 211 \rangle$ ,  $\vec{g} = \langle 1\bar{1}\bar{1} \rangle$

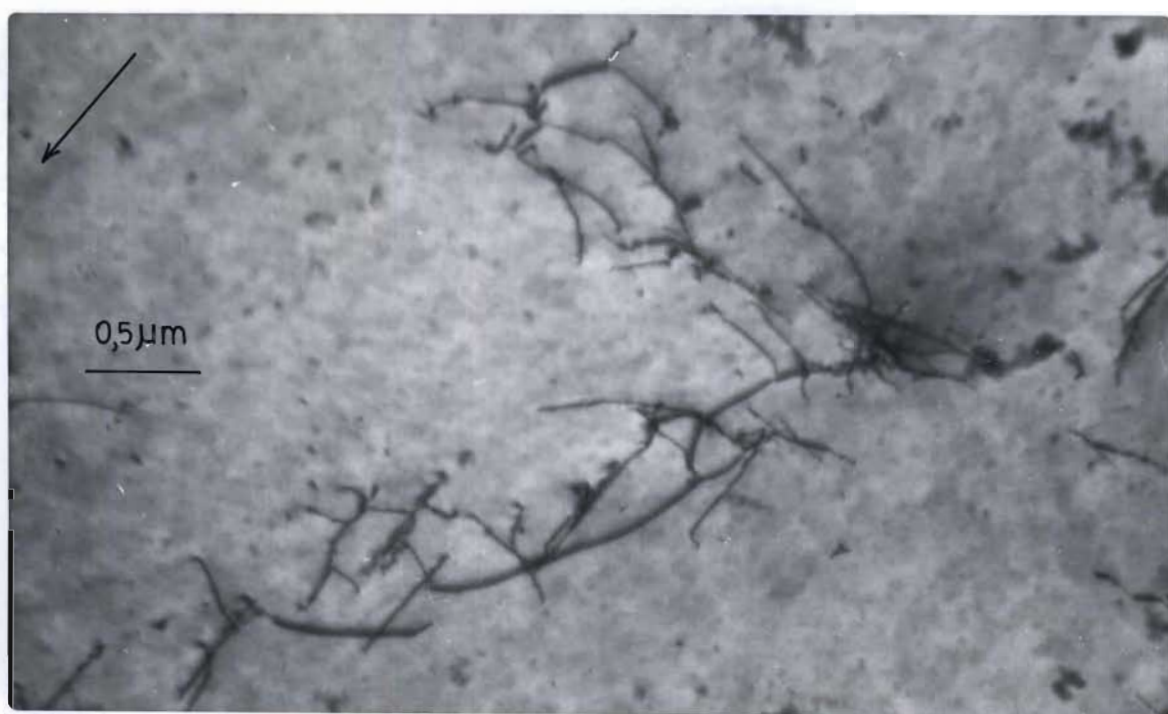
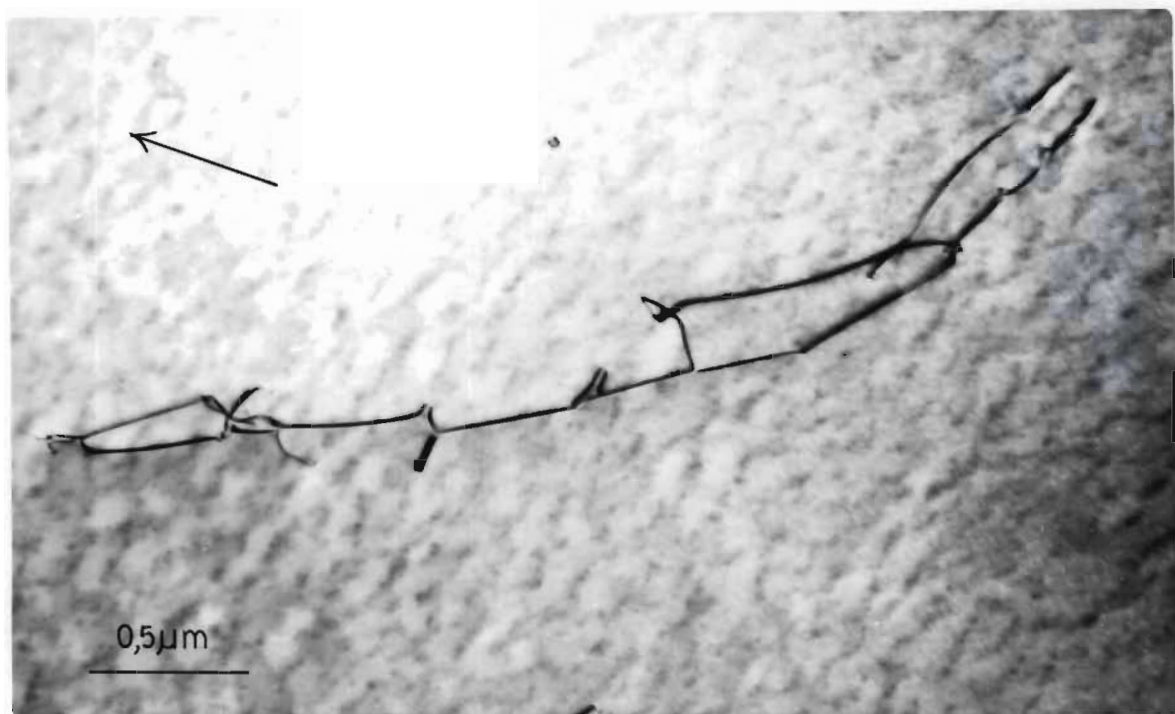


Figure 7.37  
Isolated dislocations  
Irradiation Temperature = 400°C

A.

Zone axis =  $\langle \bar{2}33 \rangle$ ,  $\vec{g} = \langle 311 \rangle$

B.

Zone axis =  $\langle \bar{2}33 \rangle$ ,  $\vec{g} = \langle 311 \rangle$

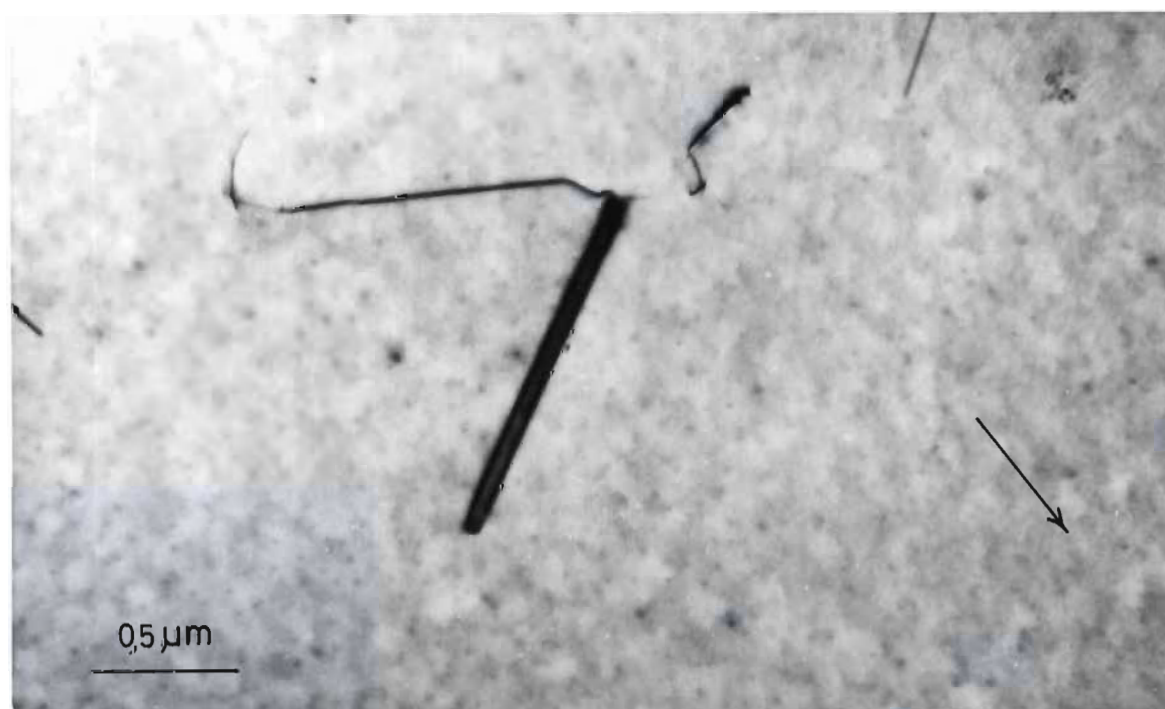
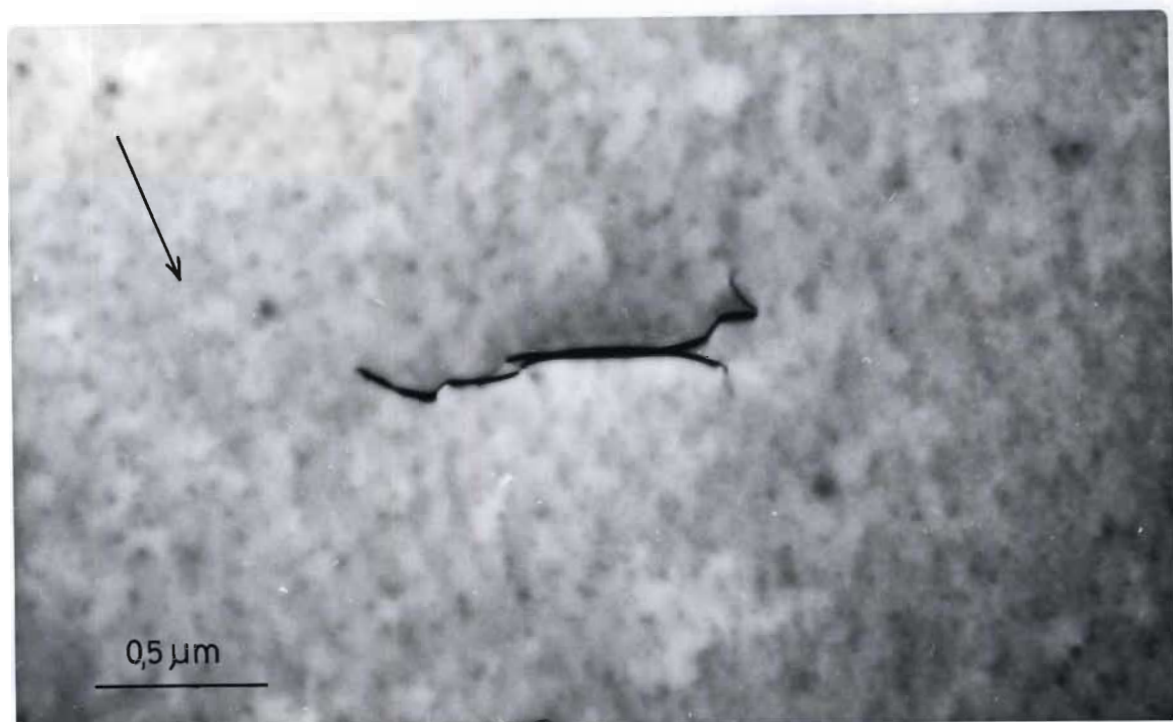


Figure 7.38

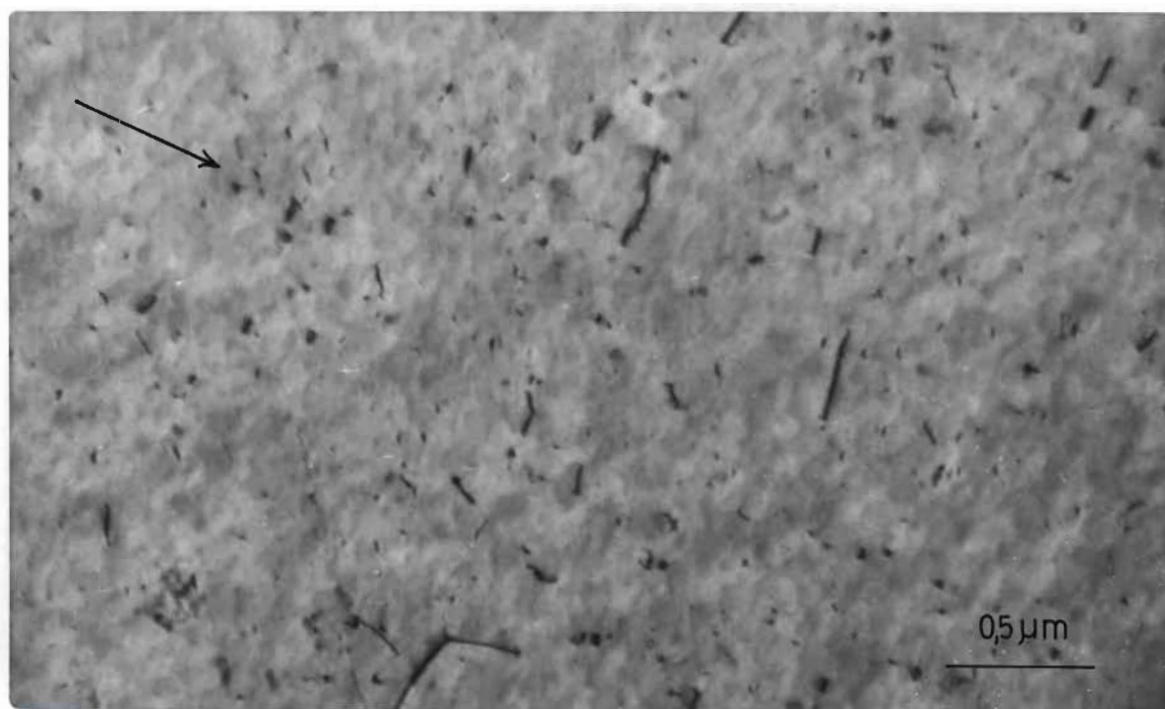
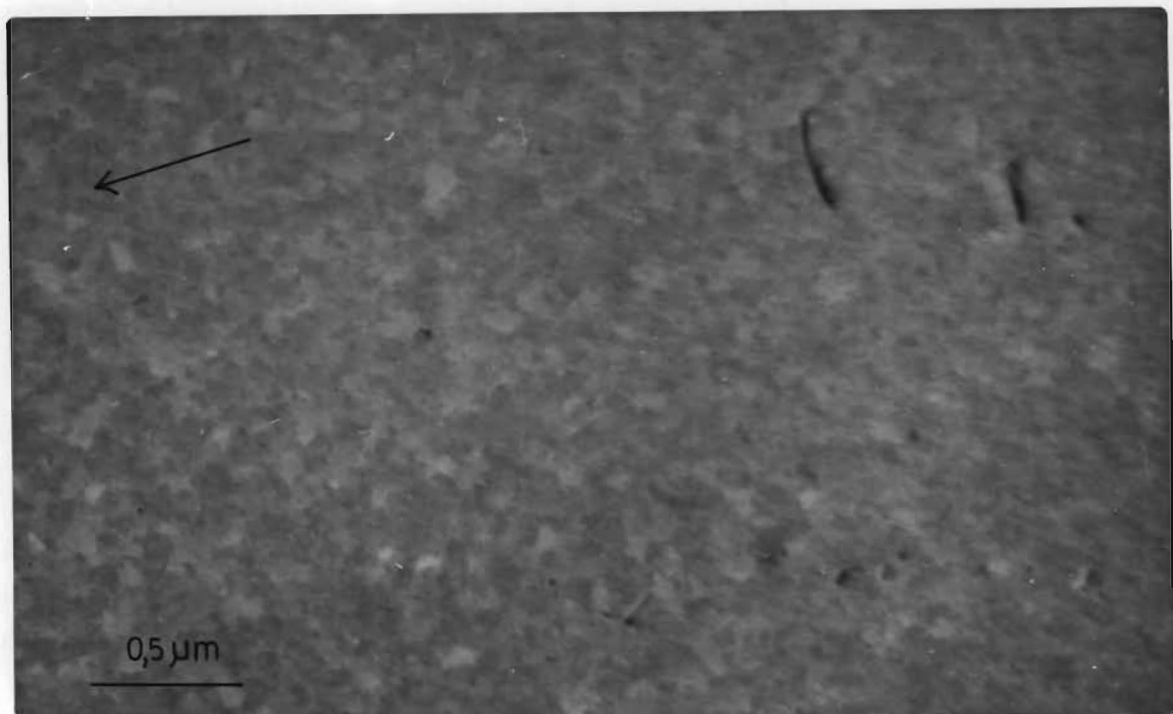
A.

Typical background area showing low damage density.

Irradiation temperature =  $400^{\circ}\text{C}$ . Zone  
axis =  $\langle 111 \rangle$ ,  $\vec{g} = \langle 02\bar{2} \rangle$

B.

Background area showing the occasional high density of background damage. Irradiation temperature =  $400^{\circ}\text{C}$ , Zone axis =  $\langle 211 \rangle$ ,  
 $\vec{g} = \langle \bar{1}11 \rangle$



On comparing the damage morphology of the etch pit photographs and electron micrographs in the previous sections of this chapter, it is quite easy to correlate the various large shapes observed in the etch pit photographs from the 250°C and 350°C irradiations with the large rafts observed in the electron micrographs of the same specimens.\* The comet-shaped defect in the etch pit photograph, Figure 7.6B, can be compared to the comet-shaped raft of Figure 7.10 and in addition fan-shaped rafts such as those in Figure 7.7A can be compared to etch pit features such as those in Figures 7.12 and 7.30. It must be remembered that in comparing the etch pit photographs with electron micrographs, that the dimensions of the rafts are often different although large rafts comparable in size to those observed by etch pitting are often seen in electron microscopy (e.g. Figures 7.19 and 7.29).

On comparing the etch pit photographs and electron micrographs for the irradiation temperatures of 300°C and 400°C one finds that similarities are not so obvious. The etch pit photographs for these specimens exhibit no large scale clustering of damage and in fact merely show an almost homogeneous distribution of individual etch pits. This fact is however not in conflict with the damage morphology observed in electron microscopy.

In the case of the irradiation at 300°C it has been shown in Section 7.5.2 that most of the dislocation tangles observed in these specimens, by means of electron microscopy, are in the order of 1  $\mu\text{m}$  in size. The etch pitting technique will in general produce only one large etch pit for a defect or defect cluster of the order of 1  $\mu\text{m}$  and thus each of the dislocation tangles observed in the electron microscope will appear as a single etch pit in an etched specimen. In addition, the

---

\*Jackson P.J., Black K.E., Nathanson P.D.K., and Spalding D.R., Phil Mag 35 509 (77).

dislocation tangles and other damage observed by means of electron microscopy in the specimens irradiated at 300°C are almost homogeneously distributed throughout the specimen in agreement with the etch pit results.

Similarly in the case of specimens irradiated at 400°C loose dislocation groupings occur throughout the specimen. These dislocation groups are also in general small enough to produce only one or two etch pits in an etched specimen, and even the occasional large dislocation groups observed in this temperature range (e.g. Figure 7.35) will not produce a raft-like shape on etching. This is due to the fact that these large groups of dislocations are so loosely grouped that individual dislocations comprising the group intersecting the etched (111) plane will give rise to individual etch pits. Thus a large dislocation group such as the one in Figure 7.35 will give rise to a few etch pits in a row and will not produce a raft-like structure as observed in the specimens irradiated at 250°C and 350°C.

In Table 7.2 data obtained from the etch pit work carried out by Black (1976) is shown. The pre-irradiation dislocation densities of the various specimens were similar (Table 7.2) and thus comparisons can be made between the post-irradiation defect morphologies. The post-irradiation dislocation densities recorded in Table 7.2 for the specimens irradiated at 250°C and 350°C were obtained by carrying out an etch pit count and ignoring the large rafts, and thus these figures essentially represent the inter-raft or background dislocation density.\* Any small rafts of the order of 1 or 2  $\mu\text{m}$  in size would produce only a single etch pit and thus would be counted as a single defect.

The figures in Table 7.2 for specimens irradiated at temperatures of 300°C and 400°C and designated 'Post Irradiation Defect Density' are

\*See the calculation on p 150 for the case of the 300 °C irradiation.

TABLE 7.2

DATA OBTAINED FROM ETCH PITTING {111} PLANES. (Results of Black 1976)

	250°C	250°C	300°C	350°C	400°C
Pre-irradiation dislocation density (cm <sup>-2</sup> )	2,4 × 10 <sup>6</sup>	Not measured	7,1 × 10 <sup>6</sup>	9,7 × 10 <sup>6</sup>	11,4 × 10 <sup>6</sup>
Neutron dose (f.n. cm <sup>-2</sup> )	1,24 × 10 <sup>17</sup>	2,47 × 10 <sup>17</sup>	2,92 × 10 <sup>17</sup>	2,79 × 10 <sup>17</sup>	2,59 × 10 <sup>17</sup>
Post-irradiation dislocation density (cm <sup>-2</sup> ) (inter-raft)	4,4 × 10 <sup>6</sup>	Not measured		3,7 × 10 <sup>6</sup>	
Post-irradiation defect density (pits per cm <sup>3</sup> ) (all etch pits counted as a single defect)			5,6 × 10 <sup>6</sup>		9,5 × 10 <sup>6</sup>
Raft area ratio	10%	Not measured		1,4%	
Average distance between rafts	20 μm	Not measured		35 μm	
Number of rafts per cm <sup>2</sup>	1,8 × 10 <sup>5</sup>	Not measured		1,9 × 10 <sup>5</sup>	

figures obtained by Black (1976) from a count of etch pits. Since dislocation tangles or groups of the order of  $1\text{ }\mu\text{m}$  will produce only one etch pit these figures do not represent a dislocation density but rather the total number of dislocations and dislocation tangles or groups present in these specimens.

The 'Raft Area Ratio' in Table 7.2 is the ratio of the total area of the rafts to the total area of etched surface examined for the cases of those specimens which exhibit rafts. Thus in the case of the  $250^{\circ}\text{C}$  irradiation when an etched surface is examined 10% of the area will be covered by rafts. This Raft Area Ratio is taken to be an approximate index of the total percentage of the specimen consisting of raft damage.

On examining the graph produced by Larson and Young (1972) (Figure 3.5) which is produced by making use of the technique of anomalous Bormann transmission of X-rays to show, as a function of irradiation temperature, the total amount of damage present in neutron irradiated copper specimens, one finds that the total amount of damage which these workers measured has values as shown in Table 7.3. In the entry in Table 7.3 headed  $^{250}/350$  the author has shown the ratio of amount of damage observed by Larson and Young at  $250^{\circ}\text{C}$  to the amount that they observed at  $350^{\circ}\text{C}$  for the three X-ray wavelengths used by these researchers. The value of the Raft Area Ratio at  $250^{\circ}\text{C}$  to the Raft Area Ratio at  $350^{\circ}\text{C}$  as obtained from the results of Black (1976) is also shown. This figure of 7,14 is close to the figure of 5,83 obtained from Larson and Young's results for  $\text{Cu K}_{\alpha}$  X-radiation (wavelength  $1,54\text{ }\text{\AA}$ ). For  $\text{Ag K}_{\alpha}$  X-radiation (wavelength  $0,56\text{ }\text{\AA}$ ) the correlation is not so good and the ratio obtained from Larson and Young's results is an order of magnitude less than the ratio obtained from the etch pit data.

TABLE 7.3  
X-RAY DATA FROM LARSON AND YOUNG (1972)  
(for irradiated copper)

X-rays are most absorbed by defects whose strain fields have dimensions of the order of the wavelength of the incident X-rays.

Therefore larger wavelengths will not be so sensitive to small strain fields as will shorter wavelengths.

In the work of Larson and Young (1972) they found that at an irradiation temperature of  $250^{\circ}\text{C}$  that Cu radiation was more heavily absorbed than was Ag radiation. This fits in with the current work since at this temperature a large number of small dislocation loops are present in the rafts and therefore one would expect there to be a considerable strain associated with the defect regions. Therefore the larger X-ray wavelength would be heavily absorbed.

After an irradiation at  $350^{\circ}\text{C}$  Larson and Young found that the Ag radiation was more heavily absorbed than the Cu radiation. In the current work it was found that the density of the rafts was considerably lower at this temperature and therefore one would not expect the larger wavelength to be so heavily absorbed as the shorter wavelength which will be sensitive to the relatively small strain fields associated with dislocation line segments as against dislocation loops.

Thus one would expect the larger wavelength Cu radiation to be a better index of the overall raft size than the Ag radiation which would be a better index of a smaller number of low strain field defects. Therefore it is reasonable to expect that data obtained from etch pitting (which indicates macroscopic shapes) is more likely to correspond to the larger X-ray wavelength data. This is seen to be the case.

However it must be pointed out that the electron micrographs of Larson and Young do not show the large scale rafts which are observed in the current work, although they do show agglomerates of damage 1 to 2  $\mu\text{m}$  in size. In addition, the irradiation parameters of Larson and Young are slightly different to those of the current work - their total fast neutron doses ( $E > 0,6 \text{ MeV}$ ) differed by amounts ranging over an order of magnitude but were all normalized to  $1 \times 10^{18} \text{ f.n. cm}^{-2}$  while in the current work all neutrons of energies greater than 0,1 MeV were included and the total doses were approximately  $3 \times 10^{17} \text{ f.n. cm}^{-2}$  (Table 7.1).

As far as the  $400^{\circ}\text{C}$  irradiation is concerned very little damage is found to exist after the irradiation, which correlates well with the results of Larson and Young. In the case of the  $300^{\circ}\text{C}$  irradiation a large amount of damage is found in the specimens, which also correlates with their results.

Thus it appears that the total volume of damage present as a function of irradiation temperature as measured by Larson and Young by means of anomalous X-ray transmission methods is reasonably well correlated quantitatively by the electron microscopy and etch pit techniques as described in this work.

CHAPTER EIGHTTHE ANALYSIS OF THE COMPONENTS OF THE DAMAGE

- 8.1 Introduction
- 8.2 The association of damage with dislocations
- 8.3 Rafts of damage contain all possible Burgers vectors
- 8.4 The character of large loops
- 8.5 Small loops
- 8.6 Dislocation dipoles
- 8.7 Different doses for irradiations at 250°C

## 8.1 INTRODUCTION

In this chapter individual features of the radiation damage morphology are discussed and analysed quantitatively. (Note: All electron microscope foils examined had foil normals parallel to  $\langle 111 \rangle$  directions).

## 8.2 THE ASSOCIATION OF DAMAGE WITH DISLOCATIONS

There is considerable evidence to indicate that the radiation damage morphology which is observed in the copper specimens irradiated at high temperatures is often the result of the clustering of radiation damage in the immediate vicinity of dislocations. It is believed that as the point defects are generated by the bombarding neutrons they precipitate on or near grown-in dislocations in the crystal lattice which then glide and climb into the large damage features which are observed. Thus each raft of damage is the result of radiation damage precipitating on or near one or more grown-in dislocations.

In the etch pit photographs many of the etched features observed correspond directly to well known dislocation shapes e.g. Figure 8.1A . Also it can be seen from Figure 8.1B that the etched  $\{111\}$  surface in this case shows a distinct network which is a characteristic of dislocations. The network bears a resemblance in both scale and shape to the decorated dislocation networks seen by Hedges and Mitchell (1953) in silver bromide. In F.C.C. crystals such networks are expected to lie on  $\{111\}$  planes, as did this network Nabarro (1967) p 244.

## 8.3 RAFTS OF DAMAGE CONTAIN ALL POSSIBLE BURGERS VECTORS

If the large rafts are the result of the glide and climb

Figure 8.1

(Micrographs supplied by K.E. Black)

A.

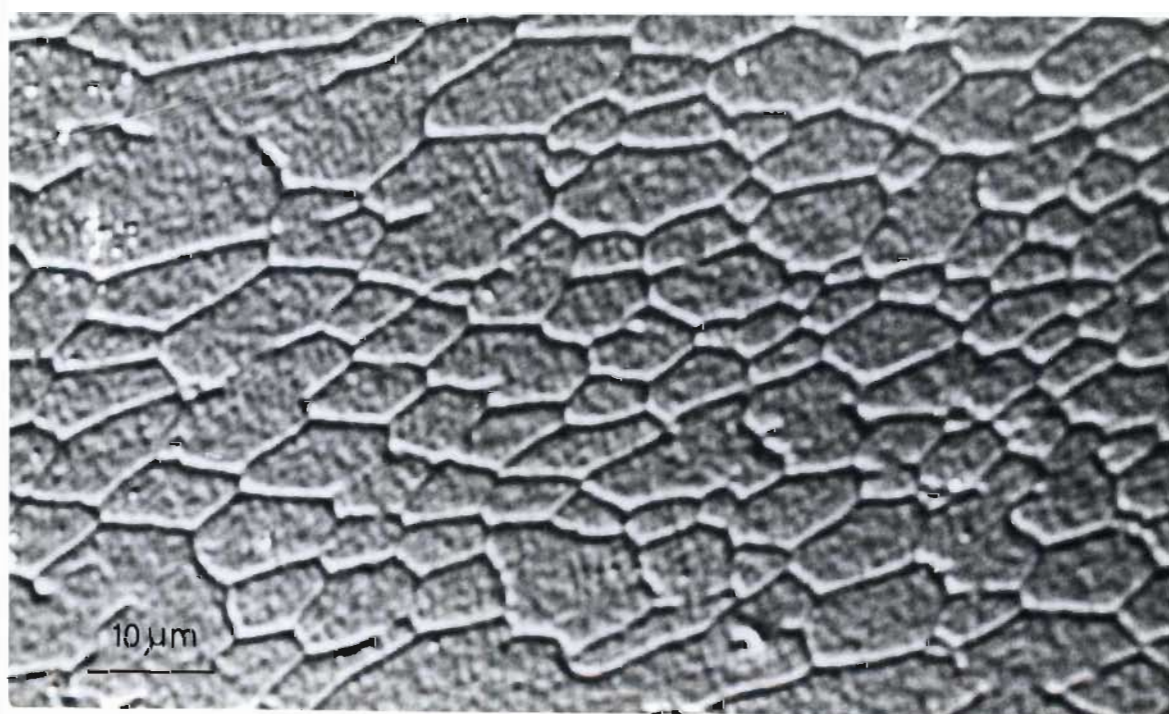
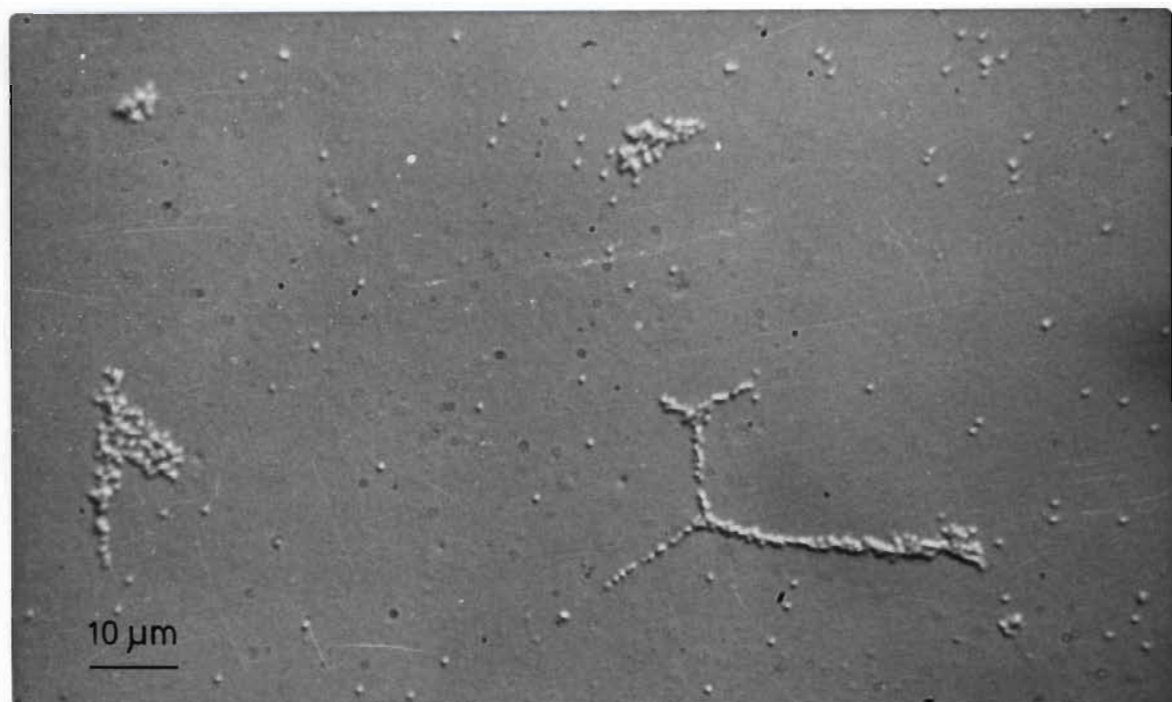
An etched (111) plane showing an etched raft similar in shape to a typical dislocation shape.

Temperature of irradiation =  $350^{\circ}\text{C}$ .

B.

An etched (111) plane showing a raft network which is typical of dislocation networks.

Temperature of irradiation =  $250^{\circ}\text{C}$ .



of dislocations as a result of point defects precipitating on or near them, the possibility arises that an entire raft could be the result of point defects migrating to a single grown-in dislocation. As interstitial atoms precipitated\* on this dislocation it would climb, and since all parts of the dislocation would not climb at the same rate this could result in many dislocation loops being formed from this single dislocation as it tangled itself up during glide and climb.

If this process alone occurred then the entire raft so formed would have the same Burgers vector.

If this were the case then it would be possible to find a reflecting  $\vec{g}$  such that the phase factor  $\vec{g} \cdot \vec{b} = 0$  for the particular Burgers vector common to a particular raft and hence the raft would be out of contrast.

To test this, micrographs with a wide range of  $\vec{g}$  values were taken of rafts. No reflections  $\vec{g}$  were found for which a raft lost diffraction contrast for all its constituent defects simultaneously (Figure 9.2 is a typical example showing a series of micrographs taken with the beam directions close to the three  $\{211\}$  zone axes using all possible  $\{220\}$  reflections and  $\{111\}$  reflections) at these orientations. It can be seen that  $\vec{g} \cdot \vec{b}$  is not equal to zero for an entire cluster in any of these orientations. However specific defects are out of contrast in some of the reflections used implying that the damage comprising rafts and dislocation tangles and groups does not have only a single Burgers vector.

This result indicates that the process of loop formation as a result of the glide and climb of a dislocation is not the only damage formation mechanism in operation in the production of the damage observed, and that dislocation loops with all possible Burgers vectors are nucleated near a grown-in dislocation or raft, or migrate in the form of loops to the raft.

#### 8.4 THE CHARACTER OF LARGE LOOPS

The vacancy or interstitial character of the larger loops observed ( $\sim 200 \text{ \AA}$ ) was determined by the method (Section 4.4) of determining the inclination of the loops and then, with fixed sign of  $\vec{S}$ , noting for which  $\vec{g}$  vectors they exhibit 'inside' and 'outside'

contrast. Examples of 'inside' and 'outside' contrast for large loops are shown in Figure 8.3.

In general very few large resolvable loops are seen in any of the specimens. The larger loops which are observed can be divided into two categories:

1. Those loops which are in inter-raft areas far away from any raft.
2. Those loops which are in or near a large raft or tangle of damage.

In specimens irradiated at 250°C no loops from category 1. were found. Loops from category 2. were only seen near small rafts containing many line segments (Figure 8.4A) and very few of these loops were found to be greater than about 300 Å in size. These loops are vacancy in character.

Since large loops in this temperature range are only found in or near rafts containing an above average number of dislocation line segments, and since these loops are found to be vacancy, they are most probably formed by the climb mechanism of Risbet and Levy (Section 2.3.3).

In specimens irradiated at 300°C no large rafts of damage are observed and there are no damage free inter-raft areas, and thus category 1. does not apply. In this temperature range both vacancy and interstitial loops are seen (Figure 8.4B) and the very large loops ( $> \sim 1000$  Å) are usually vacancy while the interstitial loops are of lesser size. The vacancy loops are again probably the result of the Risbet and Levy climb mechanism since any vacancy loops nucleated are

Figure 8.2

A raft which has been tilted into the three  $(211)$  positions

Figure 8.2A

Zone axis =  $\langle 111 \rangle$      $\vec{g} = \langle 20\bar{2} \rangle$

Figure 8.2B

$\vec{g} = \langle \bar{1}11 \rangle$

Zone axis =  $\langle 211 \rangle$

Figure 8.2C

$\vec{g} = \langle 02\bar{2} \rangle$

Figure 8.2D

$\vec{g} = \langle 11\bar{1} \rangle$

Zone axis =  $\langle 112 \rangle$

Figure 8.2E

$\vec{g} = \langle 2\bar{2}0 \rangle$

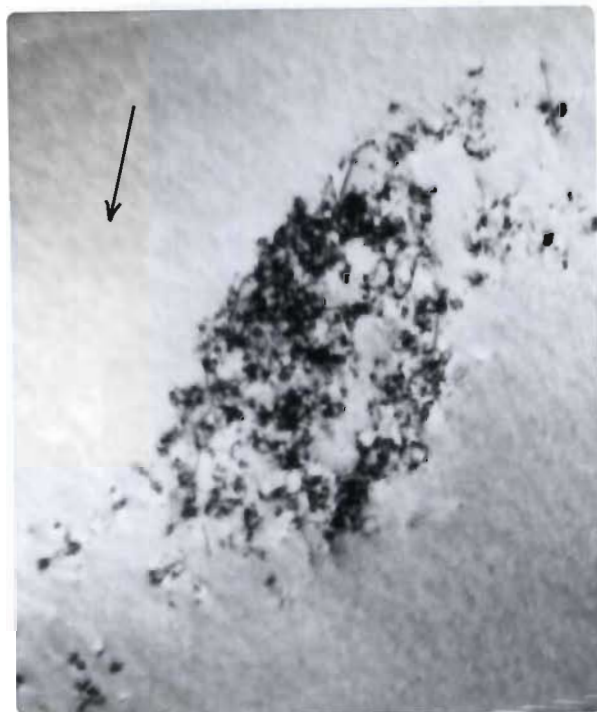
Figure 8.2F

$\vec{g} = \langle 1\bar{1}1 \rangle$

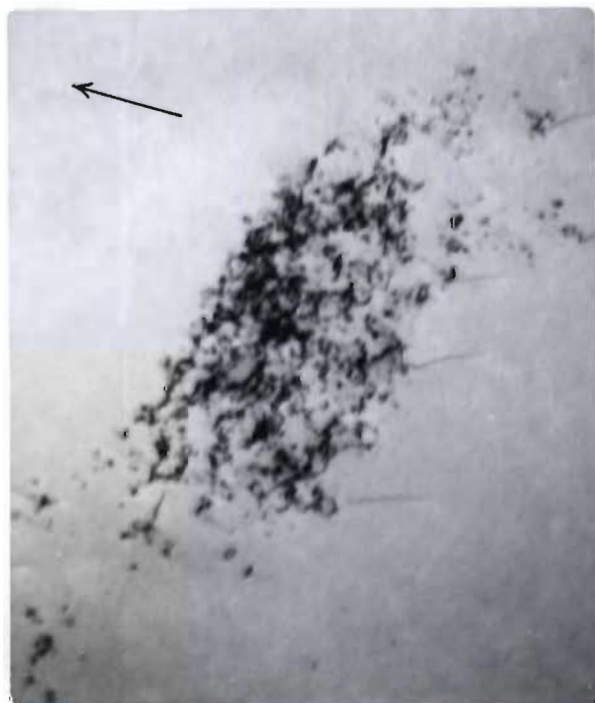
Zone axis =  $\langle 121 \rangle$

Figure 8.2G

$\vec{g} = \langle \bar{2}02 \rangle$



0,5  $\mu$ m



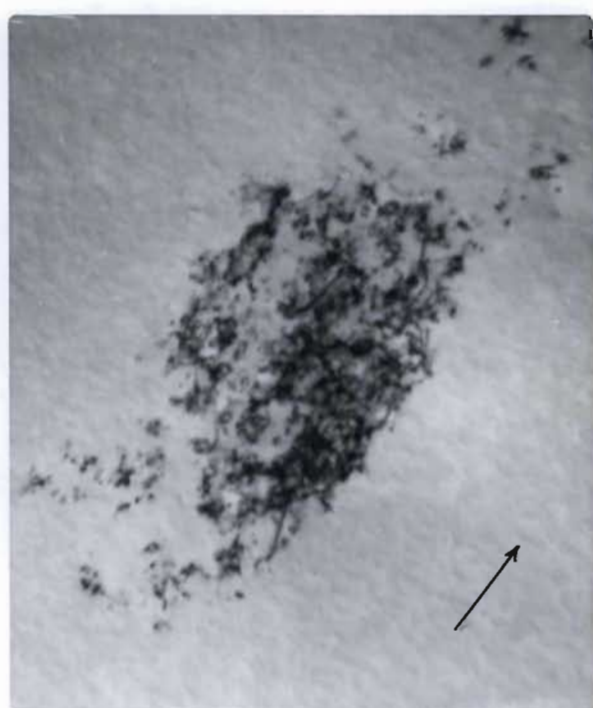
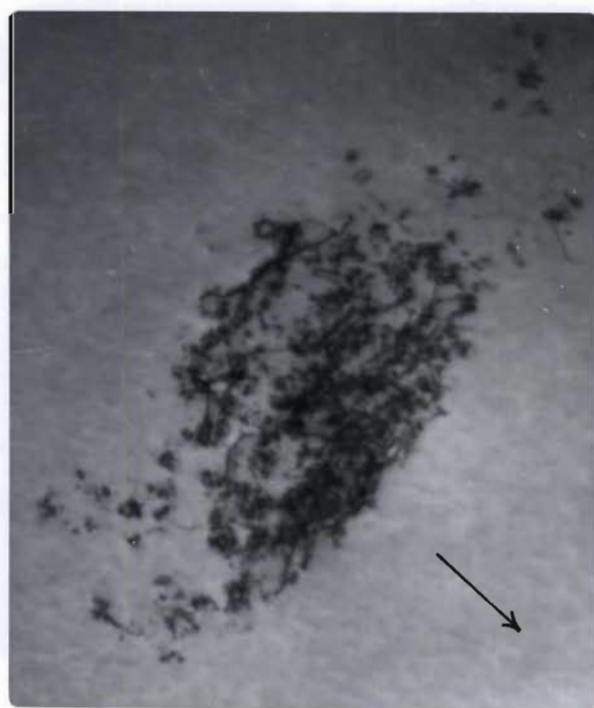
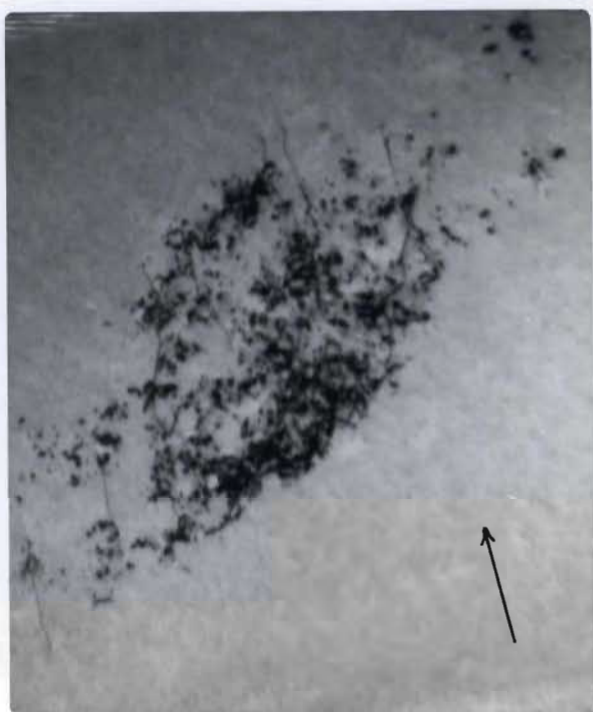
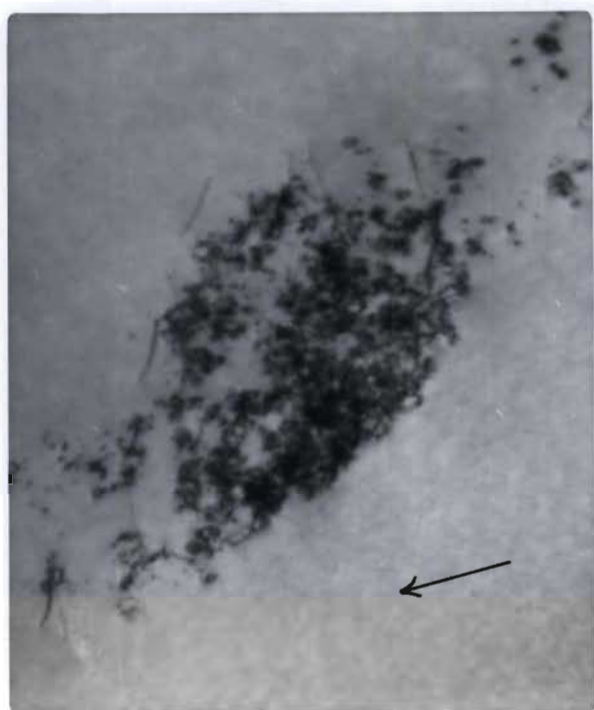


Figure 8.3

Example of inside outside contrast in a dislocation loop.

This loop is interstitial in character. Zone axis =  $\langle 211 \rangle$

Figure 8.3A

$$g = \langle 0\bar{2}2 \rangle$$

Figure 8.3B

$$g = \langle 02\bar{2} \rangle$$

Figure 8.4

Figure 8.4A

Irradiation temperature =  $250^{\circ}\text{C}$

The large loops are vacancy in character. Zone axis =  $\langle 111 \rangle$

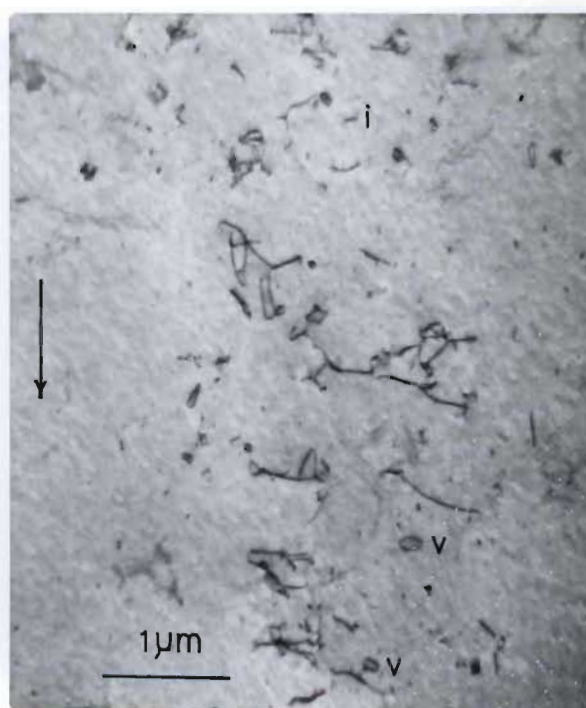
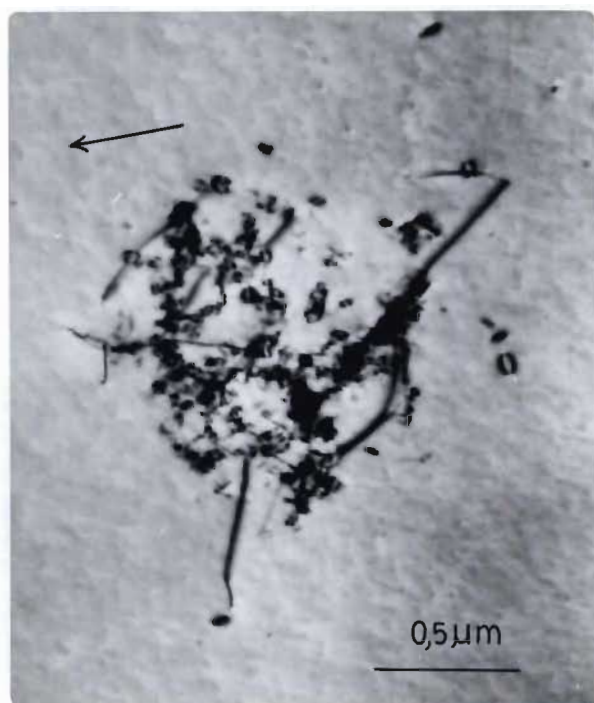
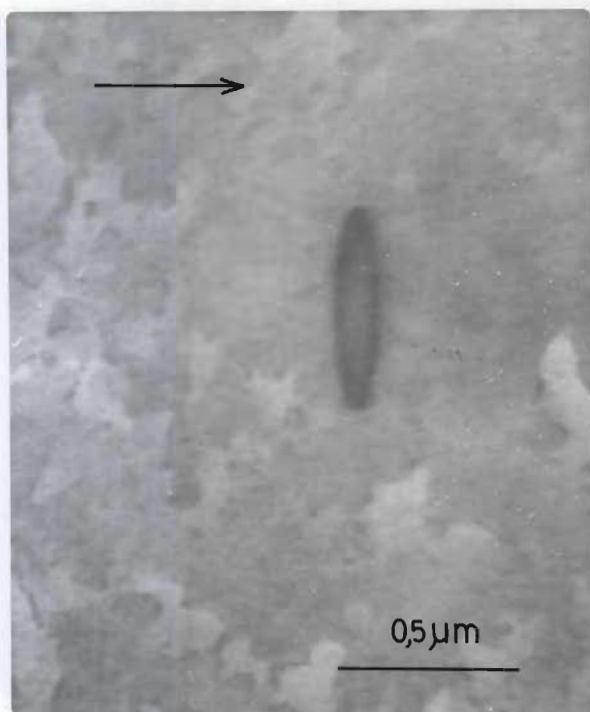
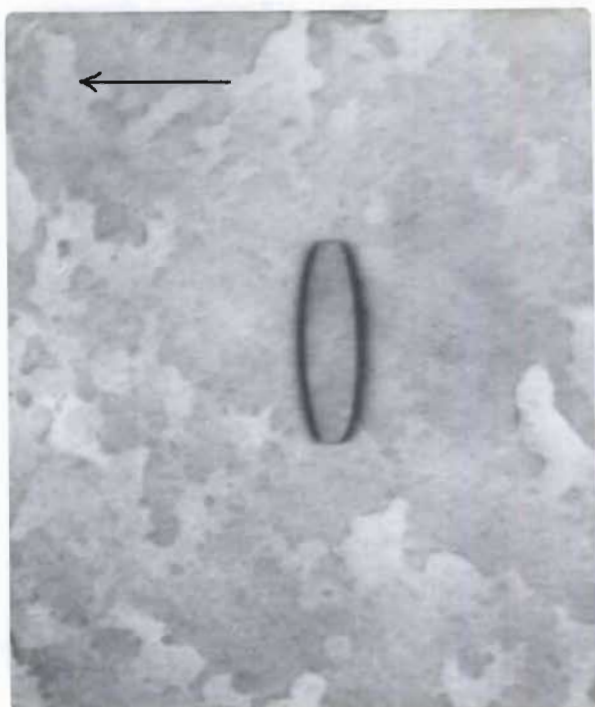
$$\vec{g} = \langle 02\bar{2} \rangle$$

Figure 8.4B

Irradiation temperature =  $300^{\circ}\text{C}$

The loops marked "V" are vacancy in character. Zone axis =  $\langle 111 \rangle$

$$\vec{g} = \langle 2\bar{2}0 \rangle$$



expected to shrink during irradiation (Section 2.3.2).

Those loops which fall into category 1. in the case of an irradiation at  $350^{\circ}\text{C}$  are found to be interstitial in character. Again though, large loops are not common in these specimens. Few loops are found corresponding to category 2. (Figures 7.30, 7.31) and here both vacancy and interstitial loops are found, and from the small numbers that it is possible to count it appears that there are more interstitial loops than vacancy loops.

In specimens irradiated at  $400^{\circ}\text{C}$  no vacancy loops were found at all. Some of the loops which are found are very large, such as the one next to the dislocation group in Figure 7.35 (Diameter =  $5600 \text{ \AA}$ ) and which is interstitial in character.

The approximate largest sizes of circular or elliptical loops (i.e. unjogged and untangled loops) seen in each temperature range are given in Table 8.1.

## 8.5 SMALL LOOPS

All of the specimens examined contain small dislocation loops ( $< 300 \text{ \AA}$ ). The numbers of these loops differ considerably from one irradiation temperature to another.

These black dots are assumed to be small Frank loops since when imaging under dynamical two beam conditions ( $W \sim 1$ ) strong black-white contrast results, and the operating  $\vec{g}$  vector is not always parallel to the  $\vec{l}$  vector of the black-white lobes (Figure 8.5A). This indicates that the black dot defects are not spherically symmetrical and are therefore small dislocation loops. Carrying out this test on the black dots observed at all irradiation temperatures showed that in each

TABLE 8.1  
LARGE LOOPS

Irradiation temperature	Category (1) Loops in inter-raft areas	Category (2) Loops in or near rafts or tangles or groups of dislocations
250°C	No loops	Vacancy
300°C	Does not apply	Vacancy and interstitial (larger loops are vacancy)
350°C	Interstitial	Interstitial and vacancy (Majority of interstitial loops)
400°C	Interstitial	Interstitial

Maximum size of loops observed

250°C	750 Å
300°C	2000 Å
350°C	1000 Å
400°C	6000 Å

Figure 8.5

A.

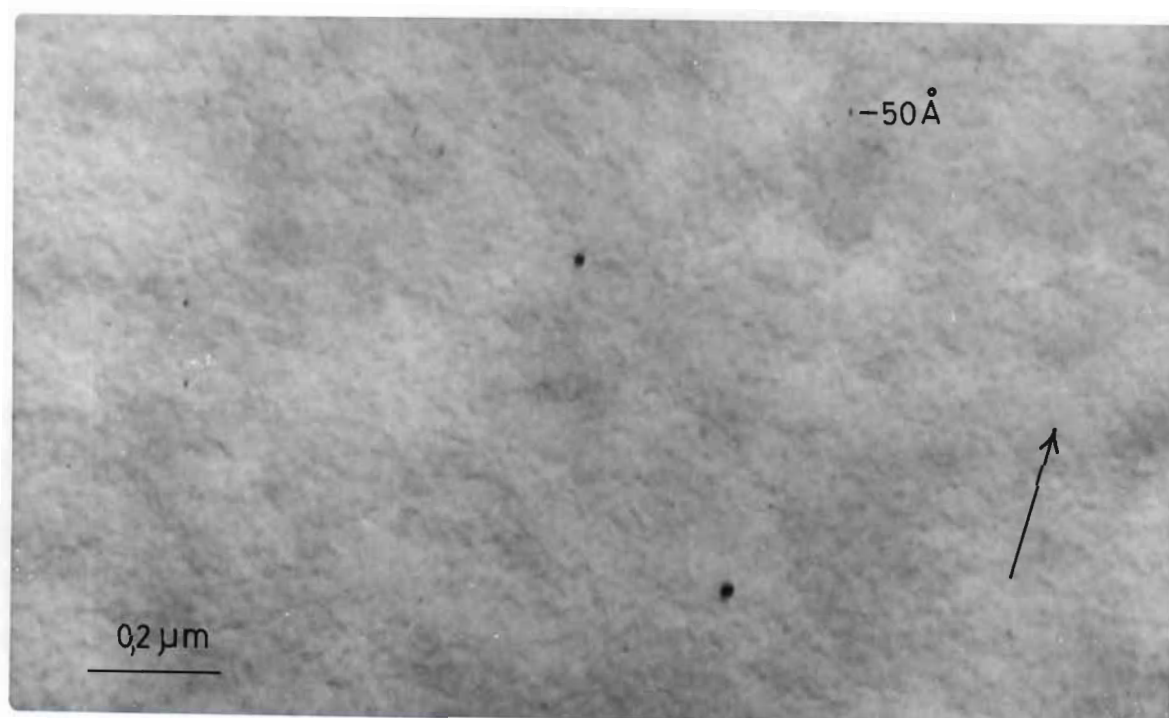
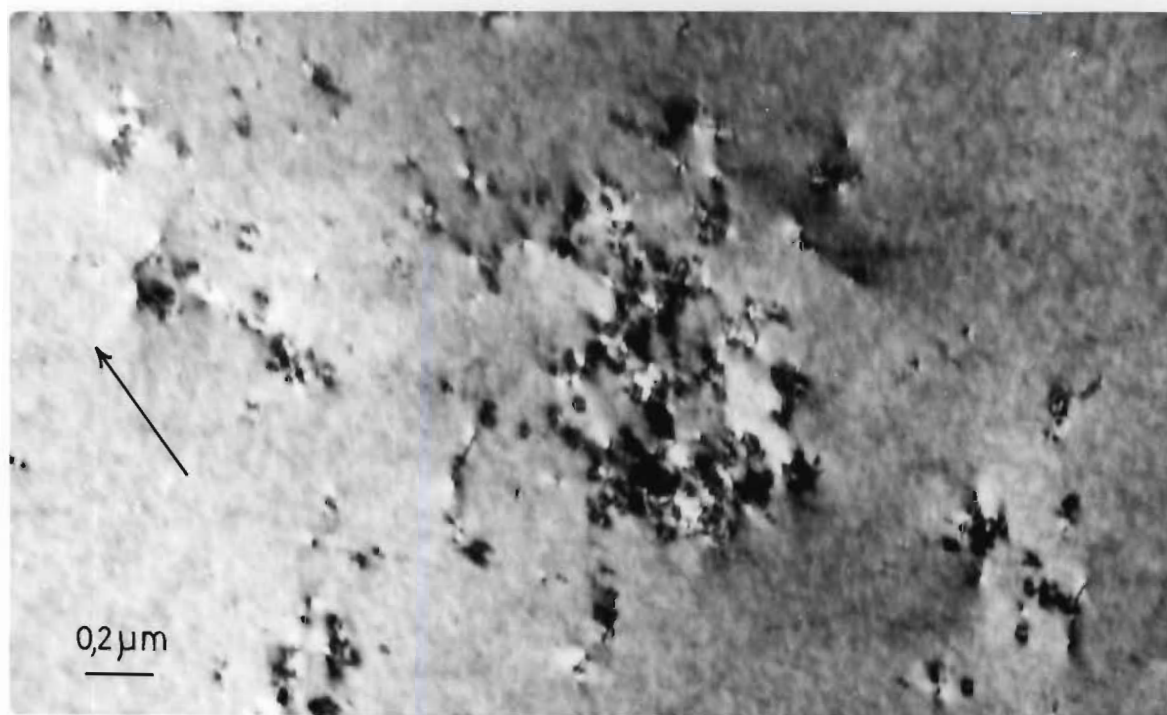
Raft formed after an irradiation at 250°C.  
Micrograph taken under  $S = 0$  conditions showing  
the black dots exhibiting black-white lobes.

Zone axis =  $\langle 111 \rangle$      $\vec{g} = \langle \bar{2}02 \rangle$

B.

Inter-raft area after an irradiation at 250°C  
showing the low density of black-dot damage.  
A few loops of  $\sim 50 \text{ \AA}$  in diameter can be seen.

Zone axis =  $\langle 211 \rangle$      $\vec{g} = \langle \bar{1}11 \rangle$



case the black dots are dislocation loops. Also a number of small loops are just large enough to be resolvable as dislocation loops (e.g. Figure 7.15B).

In specimens irradiated at  $250^{\circ}\text{C}$  a large number of small loops are observed but the vast majority of these loops are found in the rafts and are so densely packed that most of them are not resolvable as individuals (e.g. Figures 7.12, 7.17, 7.19). In those rafts which are not densely packed (e.g. Figures 7.22, 7.23) a number of independent black dots are found. A small number of small loops are found in the inter-raft spaces (Figure 8.5B).

In material irradiated at  $300^{\circ}\text{C}$  small loops are found over the entire area of the specimen. In many cases it can be seen that dislocations have been pinned by the black dot defects (e.g. Figures 7.24, 7.25, 7.27).

In the specimens irradiated at  $350^{\circ}\text{C}$  small loops are found in the rafts (e.g. Figures 7.30, 7.31) and to a lesser extent in the inter-raft spaces. There are relatively few small loops within the rafts themselves compared to the numbers observed at  $250^{\circ}\text{C}$ , and a further contrast is that they are essentially evenly distributed over the area of the raft (Figures 7.30, 7.31). Those small loops associated with loose rafts or small groups of dislocations (e.g. Figures 7.32, 7.33) are again found to be scattered around the immediate area and their distribution is essentially homogeneous. Many dislocations (e.g. Figure 7.33) are also found to be pinned by the black dot damage.

In general there are extremely few black dots found in the specimens irradiated at  $400^{\circ}\text{C}$  and the area of the specimen appears virtually damage free (e.g. Figures 7.36A, 7.37, 7.38A). On rare occasions

quite a large number of small loops are found associated with a dislocation group (e.g. Figure 7.38B) but this local density of defects is extremely high and is not a general feature of specimens irradiated at this temperature.

A loop size spectrum was determined for all temperatures of irradiation (Figure 8.6) and it was found that in all cases most loops have diameters in the order of 200 Å and that there are relatively few loops with diameters much smaller or much larger than this size. These size spectra were produced from micrographs in which the small loops were sufficiently spread out so as to make it possible to count them without error. In the case of the 250°C irradiation it was not possible to count the small loops in the very dense rafts.\* It should be noted that the results of Scheidler *et al.*, (1966) for irradiations at ambient temperatures (Figures 3.2, 3.3) are very different to the present results.

In view of this difference an investigation was made to find out if there might not be a large density of very small loops ( $< 100$  Å) which were not readily visible. This was done by studying high magnification micrographs (Figure 8.7) and by using the weak beam technique (Figure 8.8) to look for small loops. Using the weak beam technique does not reveal a picture which differs significantly from the one observed under normal bright field conditions i.e. no large density of small loops was detected.

Number densities of loops were not calculated for the temperatures of 250°C, 350°C and 400°C since the inhomogeneity of the distribution of small loops in these specimens would make such calculations meaningless. Only in the case of the 300°C irradiation are the small loops sufficiently homogeneously distributed to make such a calculation meaningful. The number density of loops in this temperature range was found to be

---

\*See the calculation on p 150 for the case of the 300 °C irradiation.

Loop Size Spectra

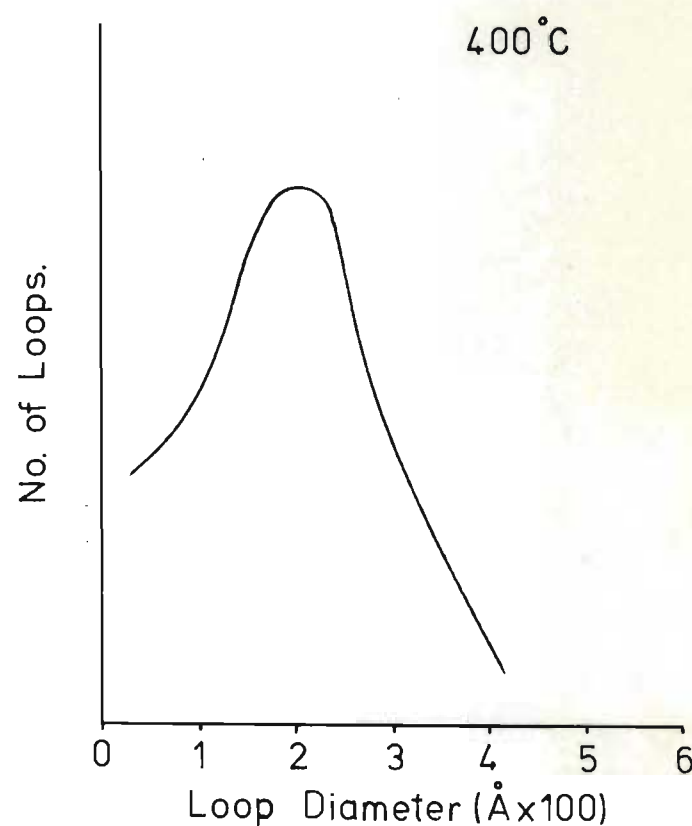
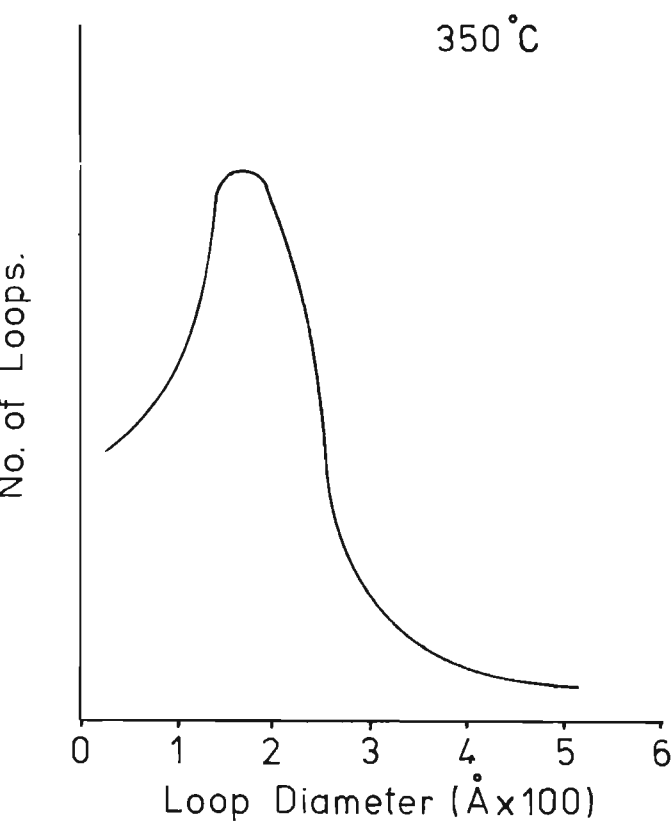
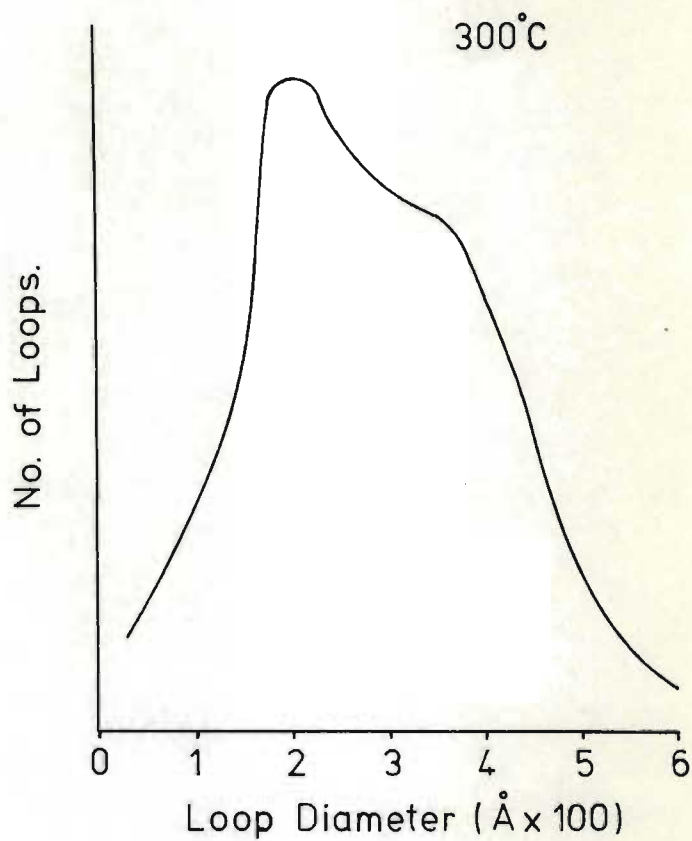
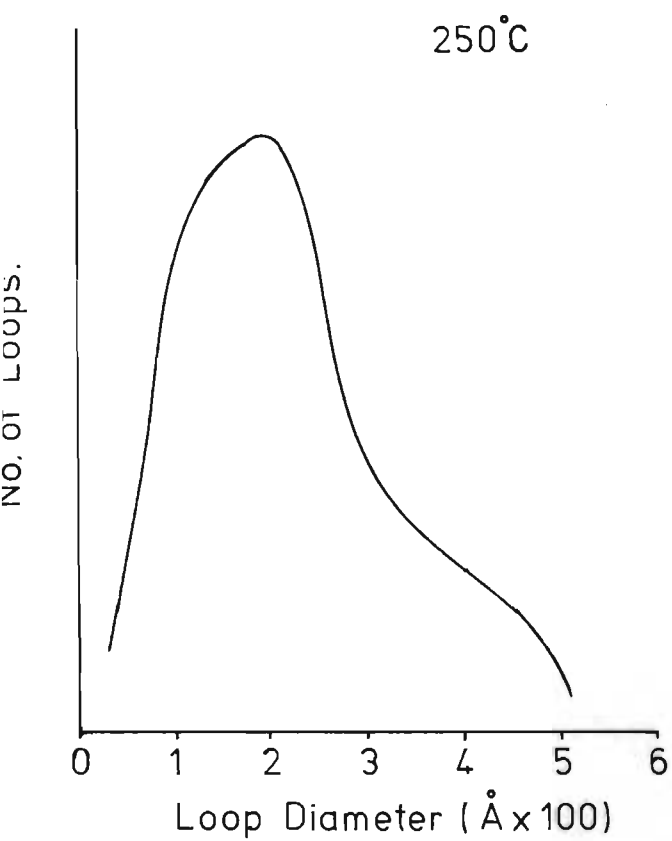


Figure 8.7

High magnification micrograph of part of a  
raft.

Irradiation temperature = 250°C.

Zone axis =  $\langle 211 \rangle$   $\vec{g} = \langle \bar{1}11 \rangle$



Figure 8.8.

Weak beam micrograph of part of a raft.

Irradiation temperature = 250°C.

Zone axis =  $\langle 111 \rangle$   $\vec{g} = \langle 2\bar{2}0 \rangle$



$$1,7 \times 10^{14} \text{ cm}^{-3}.$$

The contribution of these loops to the total dislocation density can be calculated from

$$\rho_D^L = N_L 2 \pi \bar{r}_L$$

where  $N_L$  = number density of small loops

$\bar{r}_L$  = mean radius of small loops.

Taking 250 Å as the mean loop diameter at 300°C (Figure 8.6) we get  $1,3 \times 10^{11} \text{ cm}^{-2}$  as their contribution to the total dislocation density.

The contribution of the dislocation tangles was estimated to be in the order of  $10^9 \text{ cm}^{-2}$ . This is a difficult estimation to perform accurately due to the difficulty in measuring the total line length of the tangles, but  $10^9 \text{ cm}^{-2}$  is a reliable lower limit - the true dislocation density of the tangles is estimated to be less than  $10^{10} \text{ cm}^{-2}$ . \*

## 8.6 DISLOCATION DIPOLES

In the inter-raft areas in both the specimens irradiated at 250°C and at 350°C a small number of isolated dislocations are observed. It was noted that a large number of these dislocations, and also a number of those dislocations closely associated with rafts in the 350°C irradiation, exhibit double images. It was found that a large number of these dislocations are dislocation dipoles.

In Figure 8.9 the difference between a dislocation pair and a

\*Note that the situation existing for the other temperature ranges is discussed on pp 136 and 148.

dislocation dipole is illustrated - the dislocation pair both have the same Burgers vector while the two members of a dipole have opposite Burgers vectors. Dislocation pairs have spacings between 20 and 1000 Å and Bell *et al.*, (1964) have reported that the image consists of two single dislocation images for spacings  $> \sim 200$  Å.

Dislocation dipoles, which are held in position by their own elastic interaction, produce an image similar to that for two closely spaced dislocations when the image spacing is  $> \sim 300$  Å. However a difference between dipoles and dislocation pairs (Bell *et al.*, (1964), Forwood and Humble (1970)) is that the spacing of dislocation dipole images changes on reversing the sign of  $\vec{g}$ , or of  $\vec{S}$ , while the spacing of dislocation pairs does not.

In addition these workers report that the contrast exhibited by a closely spaced, steeply inclined dislocation pair is very different to the contrast of a closely spaced, steeply inclined dipole which exhibits a characteristic centre of inversion (Figures 8.9, 8.10).

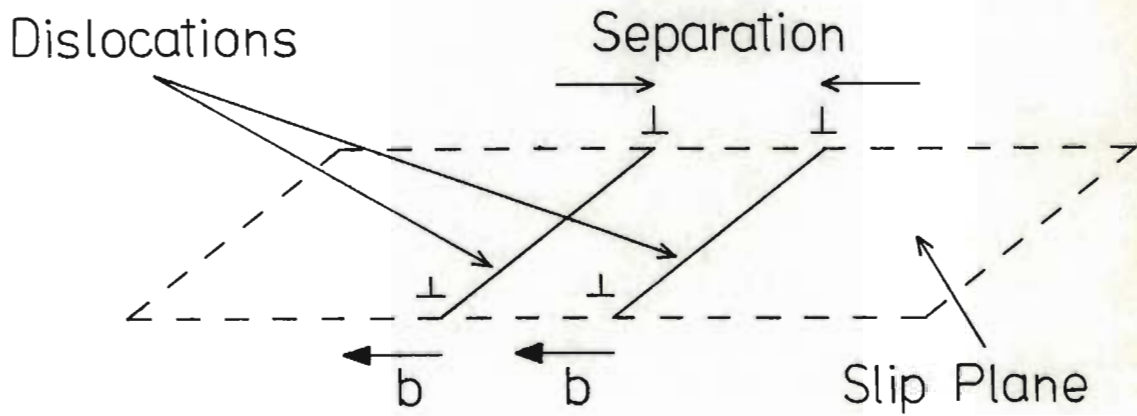
An inter-raft dipole in a specimen irradiated at 250°C is shown in Figure 8.10 while dipoles associated with a small raft can be seen in Figure 7.23A.

#### 8.7 DIFFERENT DOSES FOR IRRADIATIONS AT 250°C

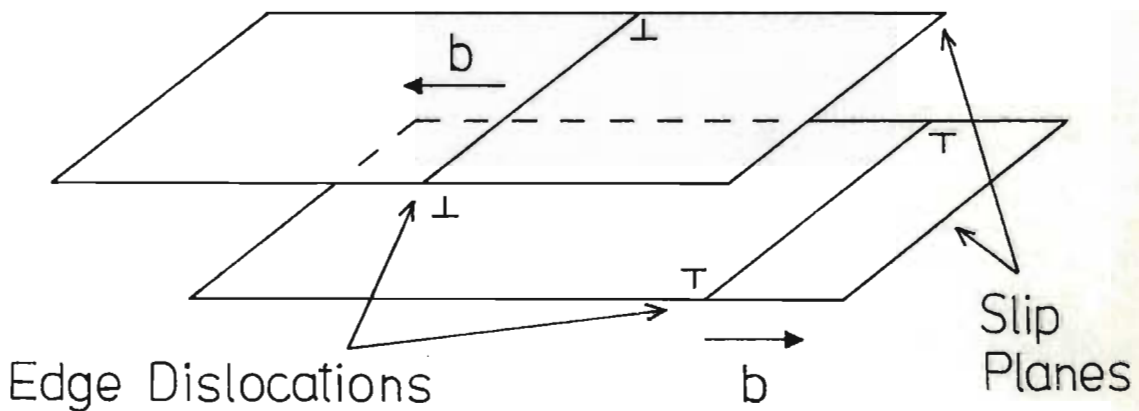
Two different sets of crystals were irradiated at a temperature of 250°C to different doses - the one being twice the other -  $1,24 \times 10^{17}$  f.n. cm<sup>-2</sup> and  $2,47 \times 10^{17}$  f.n. cm<sup>-2</sup>.

There appeared to be no difference in the constitution of the rafts, and also no difference in the raft size distribution was noted.

Difference Between Dislocation Pairs and Dipoles



(A) Dislocation Pair



(B) Dislocation Dipole



(C) Schematic Contrast

Figure 8.10

A dipole dislocation found in an inter-raft area after  
an irradiation at 250°C.

A

Centre of inversion

Zone axis =  $\langle 211 \rangle$

$\vec{g} = \langle 0\bar{2}2 \rangle$

B

Centre of inversion

Zone axis =  $\langle 211 \rangle$

$\vec{g} = \langle 02\bar{2} \rangle$

C

Change in dipole spacing

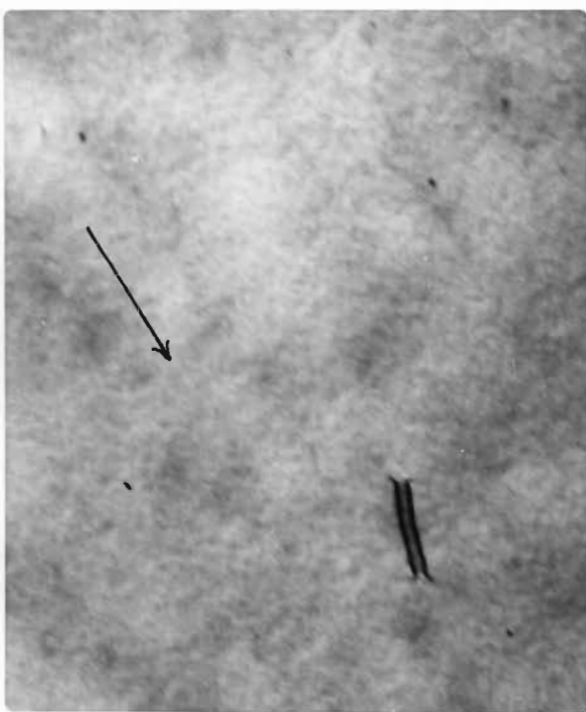
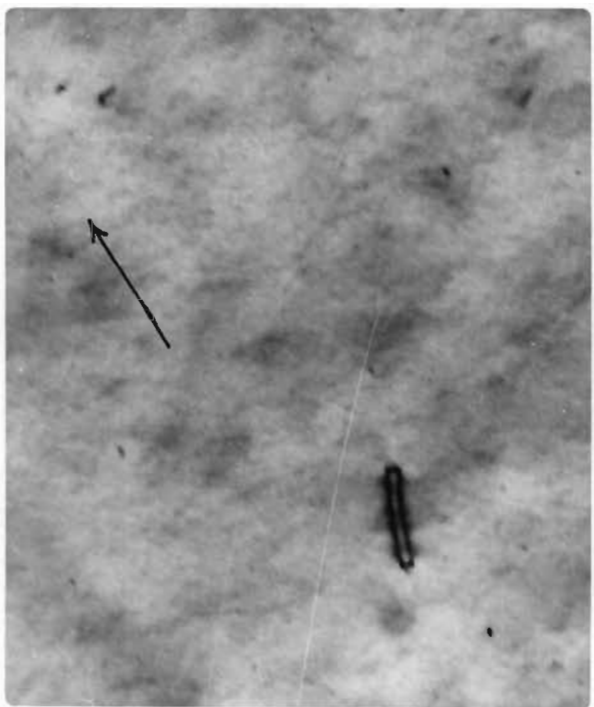
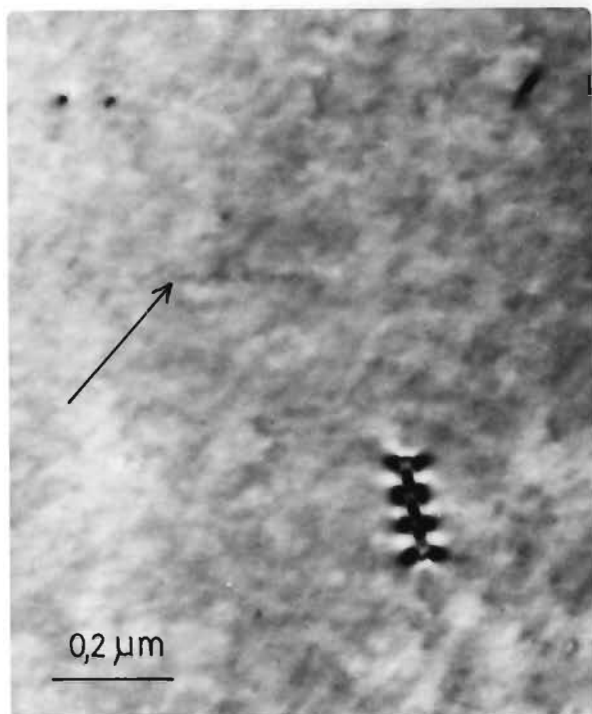
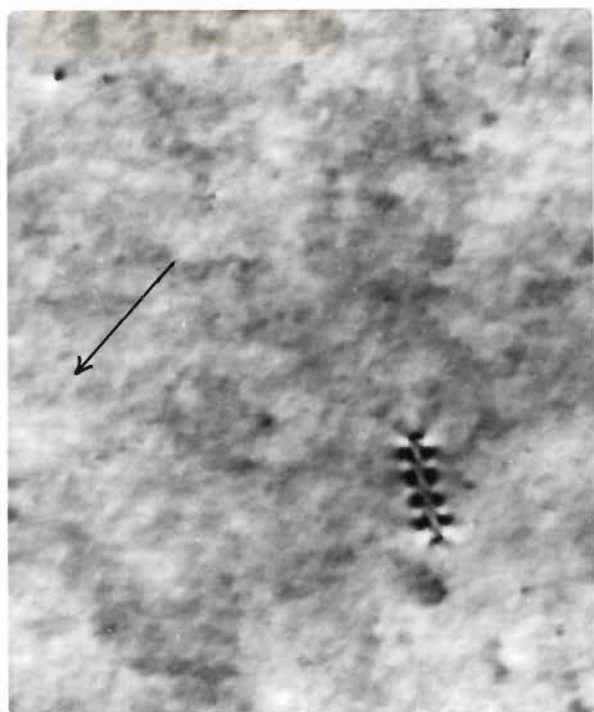
Zone axis =  $\langle 211 \rangle$

$\vec{g} = \langle \bar{1}11 \rangle$

D

Zone axis =  $\langle 211 \rangle$

$\vec{g} = \langle 1\bar{1}\bar{1} \rangle$



No etch pit comparison has been carried out on these specimens but from electron microscope investigations the impression was gained that there are slightly more rafts at the higher dose. Other than this no other difference between the damage morphologies at the two different doses was noted.

CHAPTER NINEDISCUSSION

- 9.1 Introduction
- 9.2 Migration of damage
- 9.3 Discussion of possible mechanism of raft formation
- 9.4 Relation of the proposed formation mechanism to the observed damage morphology

## 9.1 INTRODUCTION

In most radiation damage studies carried out to date the damage has been found to occur homogeneously over the body of the specimen. In the current work large rafts of damage are found inhomogeneously distributed over the specimen. In addition the inter-raft areas are found to contain very little damage. Thus, since the incident fast neutrons are striking the crystal lattice homogeneously and producing collision cascades homogeneously it is clear that a large amount of damage is migrating to particular points and forming rafts, and leaving behind denuded regions. Let us therefore consider the details of this migration. The first point to consider is whether the damage migrates to its final sites as individual point defects or whether it precipitates as loops before migrating.

## 9.2 MIGRATION OF THE DAMAGE

Historically two mechanisms involving defect migration have been suggested to account for dislocation loop growth during a thermal anneal, and which can be considered in the case of the growth of rafts during irradiation at elevated temperatures. These are:

1. Climb by point defect limited diffusion (e.g. Friedel (1964)).
2. Aggregation and coalescence by glide and self-climb (e.g. Johnson (1960)).

The first process can occur by the diffusion of either vacancies or interstitial atoms through the crystal lattice to the loops. Due to the much larger mobility of interstitials in the temperature range under consideration [See (9.1) and Page 158] the migration of interstitials is considered here. Large numbers of vacancy loops are not observed and therefore the large supersaturation of vacancies which must remain must be dispersed over the body of the crystal in the form of individual vacancies or very small vacancy clusters.

Following Meakin and Greenfield (1965) we consider the progress of an interstitial as a random walk in which, on average, each site is visited once. If an interstitial has a jump frequency of  $\nu_i \text{ Sec}^{-1}$  and the equilibrium concentration of free vacancies during irradiation is  $C$  then the mean lifetime of a defect will be of the order of  $\frac{1}{2} (C \nu_i)^{-1}$ , since an interstitial must make about  $C^{-1}$  jumps before annihilation and  $\nu_i^{-1}$  is the time taken for an interstitial to jump. The interstitial has a higher mobility than the vacancy and therefore the lifetime of either is controlled by  $\nu_i$ .

We can now use a simple model which treats point defect motion like that of a gas to which kinetic theory applies to evaluate the mean diffusion distance of each defect, before annihilation by recombination is likely. The mean diffusion distance in three dimensions, of a defect of diffusion coefficient  $D$ , after a time  $t$  is:

$$\bar{x} = \sqrt{6 D t}$$

For our purposes a sufficiently accurate value of  $D$  is  $\frac{1}{6} \nu a^2$  (Meakin and Greenfield (1965)) where  $\nu$  is the defect jump rate and  $a$  is the lattice parameter. The values of  $\bar{x}$  are then

$$\bar{x}_i \sim 0,2 a C^{-\frac{1}{2}} \text{ for interstitials}$$

and

$$\bar{x}_v \sim 0,2 a \left( \frac{\nu}{\nu_i} \right)^{\frac{1}{2}} C^{-\frac{1}{2}} \text{ for vacancies} \quad (9.1)$$

This can intuitively be seen to be correct since if there is a concentration  $C$  of vacancies, an interstitial must make about  $C^{-1}$  jumps

before annihilation, and the root mean square diffusion distance would then be of the order of a  $c^{-1/2}$ .

From (9.1) it can be seen that since  $v_v \ll v_i$  that  $\bar{x}_v$  for vacancies is very small in comparison to  $\bar{x}_i$  for interstitials.

The vacancy concentration during irradiation at any temperature cannot be less than the thermal equilibrium concentration at that temperature, and thus if we consider the thermal equilibrium concentration we can calculate an upper limit for the diffusion distance of interstitials.

From Simmons and Balluffi (1960), we have that the thermal equilibrium vacancy concentration at temperature T is:

$$C_V = \exp\left(\frac{S_V^f}{k}\right) \cdot \exp\left(\frac{-E_V^f}{kT}\right) \quad (9.2)$$

where  $S_V^f$  is the vacancy formation entropy.

$E_V^f$  is the vacancy formation energy.

k is the Boltzman's constant ( $0,86 \times 10^{-4}$  eV.  $^{\circ}\text{C}^{-1}$ )

The value of  $S_V^f/k$  for copper has been calculated to be  $\sim 1,5$  (Huntington, Shirn and Wajda (1955), Damask and Dienes (1971)) and from Table (2.1)  $E_V^f$  is 1,27 eV. Thus from (9.2) and (9.1) for different temperatures we get for interstitials:

$\bar{x}_i$  at 523 $^{\circ}\text{K}$  (250 $^{\circ}\text{C}$ ) is 46  $\mu\text{m}$

and

$\bar{x}_i$  at 673 $^{\circ}\text{K}$  (400 $^{\circ}\text{C}$ ) is 0,63  $\mu\text{m}$

Meakin and Greenfield (1965) calculate  $\bar{x}_i \sim 3 \mu\text{m}$  for an irradiation at  $500^\circ\text{K}$  with a neutron flux of  $10^{12} \text{ f.n. cm}^{-2} \text{ s}^{-1}$ . ( $\bar{x}_V \sim 3 \times 10^{-4} \mu\text{m}$  for vacancies under these conditions). For these calculations Meakin and Greenfield used vacancy concentrations during irradiation as calculated by Wechsler (1963).

Thus we have shown that during an irradiation at  $250^\circ\text{C}$  interstitials can migrate considerably further than vacancies.

Before considering this in any more detail we turn to consider the second mechanism on page 155. The analysis of Eyre and Maher (1971) seems to rule this mechanism out. The driving force in this mechanism is the elastic interaction between adjacent loops (Foreman and Eshelby (1962)).

In the case of two loops of radii  $r_0$  and  $r_1$  having identical Burgers vectors and separated by  $R$  (Figure 9.1) Foreman and Eshelby (1962) show that the forces exerted by one loop on the other in the glide and climb directions,  $F_g$  and  $F_c$  respectively are:

$$F_g = \frac{-B \pi r_0^2 r_1^2 f(\theta)}{R^4} \quad (9.3)$$

$$F_c = \frac{B \pi r_0^2 r_1^2 g(\theta)}{R^4} \quad (9.4)$$

where

$$B = \frac{\mu b^2}{4(1-\nu)}$$

$\mu$  is the shear modulus

$\nu$  is Poisson's ratio

$b$  is the Burgers vector

and 
$$f(\theta) = 3 \cos \theta (3 - 30 \cos^2 \theta + 35 \cos^4 \theta)$$

$$g(\theta) = 3 \sin \theta (1 + 10 \cos^2 \theta - 35 \cos^4 \theta)$$

Considering the question of loop glide Eyre and Maher (1971) show from (9.3) that it is possible to define a critical interloop distance  $R_{crit}^g$  below which the force  $F_g$  exceeds that required for one of the loops to glide:

$$R_{crit}^g = - \left[ \frac{B r_0^2 f(\theta)}{\sigma_g} \right]^{1/4} \quad (9.5)$$

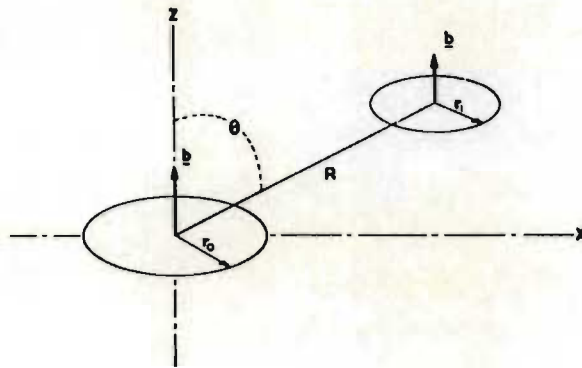


Figure 9.1

From Eyre and Maher (1971)

Schematic diagram defining position of loop having a radius  $r_1$  with respect to loop at the origin having a radius  $r_0$ , in terms of coordinates  $z$ ,  $x$ ,  $R$  and  $\theta$ .

where  $\delta_g$  is the resolved normal stress for glide of loop  $r_1$ . (for  $r_0 > r_1$ ).

These workers also derive an expression (9.6) for the separation at which loops will coalesce by means of self-climb.

$$R_{crit}^C = \left[ \frac{5 B r_0^2 t a^5 v_0 \exp \left( \frac{-Q_L}{kT} \right) g(\theta)}{2 r_1 kT} \right]^{1/5} \quad (9.6)$$

Considering the question of loop glide Syre and Mahari (1971)

show from (9.2) that it is possible to define a critical interloop distance  $R_c$  below which the force  $F$  exceeds that required for one of the loops to glide:

$$R_c = \left[ \frac{b^2 \times 10^8}{4 \times F} \right]^{1/2} \quad (9.3)$$

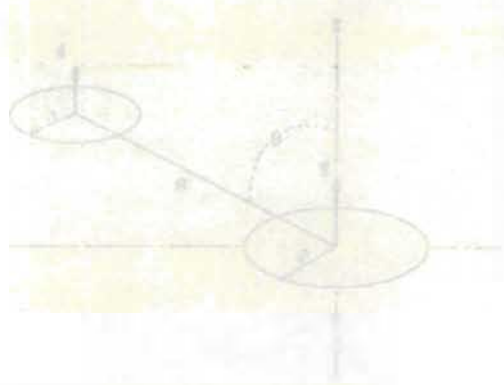


Figure 9.1  
Syre and Mahari (1971)

Schematic diagram defining position of loop having a distance  $R$  with respect to loop at the origin having a

\* A number of vacancies present in the lattice will not condense into vacancy loops and these vacancies would then be homogeneously distributed over the volume of the crystal. These vacancies could exist as independent vacancies, divacancies, trivacancies, etc. or larger 3-dimensional groups which have not collapsed to form loops. These small groups of vacancies would not be resolved by the electron microscope and thus quite a large number could be present in the lattice and remain undetected. It is probable that the number of vacancies in this situation would very soon reach an equilibrium since the large number of free interstitials present in the lattice would ensure that many of these vacancies would be annihilated. **P.T.O.**

where  $t$  is the time in seconds  
 $a$  is the lattice parameter  
 $\nu_0$  is the jump frequency ( $\sim 10^{13} \text{ s}^{-1}$ )  
 $Q_L$  is the activation energy for pipe diffusion.

Evaluating these equations using  $\mu = 7,3 \times 10^{10} \text{ N.m}^{-2}$ ,  
 $\vec{b} = 2,55 \times 10^{-8} \text{ cm}$ ,  $\nu = 0,33$ ,  $Q_L = 0,3 \text{ eV}$  and a time of 50 hours we see that the critical distances necessary for coalescence by the mechanisms of glide and self-climb are small - of the order of  $R_{\text{crit}}^g \sim 3170 \text{ \AA}$  and  $R_{\text{crit}}^c \sim 61600 \text{ \AA}$  for  $r_0 = 500 \text{ \AA}$  and  $r_1 = 50 \text{ \AA}$  at a temperature of  $T = 523^\circ\text{K}$ .

A distance  $r_0$  for the case of a large raft would be very difficult to calculate due to the fact that the net strain field would be a complicated sum of the various components of the raft. Nevertheless it can be seen from the work of Eyre and Maher that even in the case of a large raft these mechanisms will contribute very little to the general clustering of all the damage observed in the large rafts.

We return therefore, in the next section, to consider the climb of loops by interstitial diffusion.

### 9.3 DISCUSSION OF POSSIBLE MECHANISM OF RAFT FORMATION

Due to the fact that the current irradiations were carried out at high temperatures (and not cryogenic temperatures) the vacancies in the depleted zone formed by an incident neutron would condense into a vacancy cluster<sup>\*</sup> which, if it is big enough, will collapse to form a small vacancy loop (Section 2.3.1). This process will occur homogeneously over the body of the specimen. The free interstitials so formed are readily mobile at the temperatures under consideration, and will very rapidly migrate to the small vacancy loops, and since vacancies are not as mobile as the interstitials the vacancy loops will not grow but will shrink. Eyre and Maher (1971) show that the shrinkage rate of vacancy loops with  $r < 30 \text{ \AA}$

By far the majority of interstitials in the inter-raft areas would recombine with vacancies. Of those that remain it would be expected that the homogeneous nucleation of some small interstitial clusters would occur. A theory, frequently referred to as the BKM theory, has been developed to predict the loop density and mean radius expected after a given irradiation. [Brown, Kelly and Mayer Phil Mag 19 721 (1969)].

This model is based on chemical reaction rate theory and assumes that no clusters are formed directly from the damage process. The clustering is assumed to be taking place at a temperature where interstitials are mobile but vacancies are unable to migrate. A di-interstitial is considered to be a stable and stationary nucleus for a cluster.

According to the theory, the saturation number of interstitial loops per unit volume  $n_L^\infty$  is given by:

$$n_L^\infty = 2,5 \left[ \frac{G(1 + \frac{1}{2}v\Omega n_b t_0)}{v\Omega} \right]^{\frac{1}{2}}$$

In the presence of an impurity, nucleation can take place when an interstitial combines with another interstitial, already attached to the impurity atom. The BKM theory treats this type of nucleation by using a reduced speed for the interstitials.

For a pure material we get:

$$n_L^\infty = 2,5 \left[ \frac{G}{v\Omega} \right]^{\frac{1}{2}}$$

since  $n_b$  is the number per unit volume of impurity atoms present.

$G$  is a defect generation rate

$v$  is the interstitial velocity

and  $\Omega$  is a cross section.

these quantities are calculated for the case under consideration as described in Brown et al (1969). The BKM theory gives the mean defect radius as:

$$\bar{r} = 0,63 a t^{\frac{1}{3}} \left[ \frac{Gv\Omega}{1 + \frac{1}{2}v\Omega n_b t_0} \right]^{\frac{1}{6}}$$

where  $a$  is the distance between interstitial sites and  $t$  is the irradiation time. P.T.O.

is very size dependent and that the smaller loops disappear very rapidly.

This is the situation envisaged in dislocation free areas, and accounts for the lack of visible damage between rafts.

However, those interstitials which, by chance, are created near a grown-in dislocation will experience a force (due to the dislocation strain field) attracting them towards the dislocation. Interstitials are attracted by the dislocation more strongly than are vacancies (Section 2.3.2) thus causing it to climb, and so increasing the dislocation line length. The climbing dislocation therefore becomes a more efficient sink for the arriving interstitials.

We will now briefly consider the situation existing in a solid which is not being irradiated but which is at the temperature under consideration. As we have already seen, the energy of a point defect in the lattice is lower near a dislocation than elsewhere and so migration towards dislocations will occur. In general the interaction energy falls off as  $\frac{A}{r}$  where  $r$  is the distance to the dislocation and  $A$  is a constant (Nabarro (1967)).

As the migration proceeds with time to the equilibrium situation, the concentration at the dislocation increases until a Maxwellian atmosphere results. If the concentration remote from the dislocation is  $C_0$  then equilibrium is reached when:

$$C(r) = C_0 e^{-\frac{E(r)}{kT}} \quad (9.7)$$

where, as we have seen, the general form of  $E$  is:

$$E(r) = -\frac{A}{r} \quad (9.8)$$

\*Bullough and Newman, Rep Prog Phys 33 101 (1970).

For the irradiation under consideration at a temperature of 250 °C these quantities were found to be:

$$n_L^\infty = 1,08 \times 10^{13} \text{ cm}^{-3}$$

$$\bar{r} = 92,9 \text{ \AA}$$

Thus these figures indicate that very large interstitial loops would not be expected to form, and that in fact a larger density of smaller loops is expected. However any clusters that do nucleate do not appear to grow to loops which are large enough to be detectable in the electron microscope, since none have been observed.

† Electron irradiation of copper in the temperature range under consideration results in a defect distribution as predicted by the BKM theory, whereas the neutron irradiation experiments do not.

The essential difference is that displacement damage caused by electron irradiation in the HVEM produces point defects homogeneously throughout the crystal and no spike formation takes place in the damage process, as is the case in neutron irradiation.

Hossain and Brown (1974) state in reference to HVEM irradiation of Ni-Si alloys,: "The BKM theory appears to be capable of explaining the experimental data, except at the highest temperatures, where the Arrhenius curves show a sudden large increase in slope. This cannot result from vacancies becoming mobile, because calculations using the BKM model indicate that vacancy mobility cannot significantly affect the interstitial loop density."

Thus it would appear that the explanation for the observed difference in electron irradiation results and neutron irradiation results may lie in the spike phenomenon in the case of neutron irradiation.

Hossain M.K., and Brown L.M. p 360 in High Voltage Electron Microscopy. ed. Swan, Humphreys and Goringe, Academic Press 1974.

From an initial condition of  $C = C_0$  everywhere, the interstitials migrate to the dislocation where precipitation may occur. If all the interstitials arriving are absorbed we have a perfect sink, but if the interstitials can only be absorbed at a finite rate we have a rate-limited sink. Bullough and Newman (1970) show that the case of the perfect sink is represented by Figure 9.2A in which the Maxwellian atmosphere is never formed and the concentration falls off monotonically as the dislocation is approached. In the case of a rate-limited sink Bullough and Newman show that Figure 9.2B is the situation which exists in which the concentration builds up to a maximum near the dislocation.

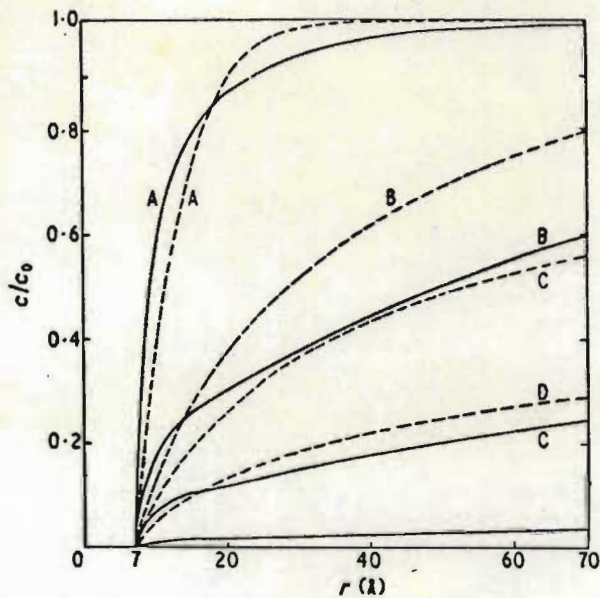
† We now return to consider our crystal which is being irradiated and therefore contains an infinite supply of point defects. Since point defects are being created continuously a Maxwellian-type atmosphere will not occur from random walk diffusion after some period of time, and also the concentration of point defects is large in comparison to the thermal equilibrium concentration.

The first possible mechanism of raft formation therefore, is one in which a dislocation starts to climb by absorbing the interstitials immediately around it. More interstitials then diffuse towards the depleted area in the vicinity of the climbing dislocation and then precipitate onto it in large numbers, thereby producing considerably more climb. The original dislocation would then tangle itself up into a complicated shape and would also throw off a number of small loops during climb, and a raft of damage would therefore result. The entire raft so formed would have the same Burgers vector since all components of the raft resulted from the climb of a single dislocation.

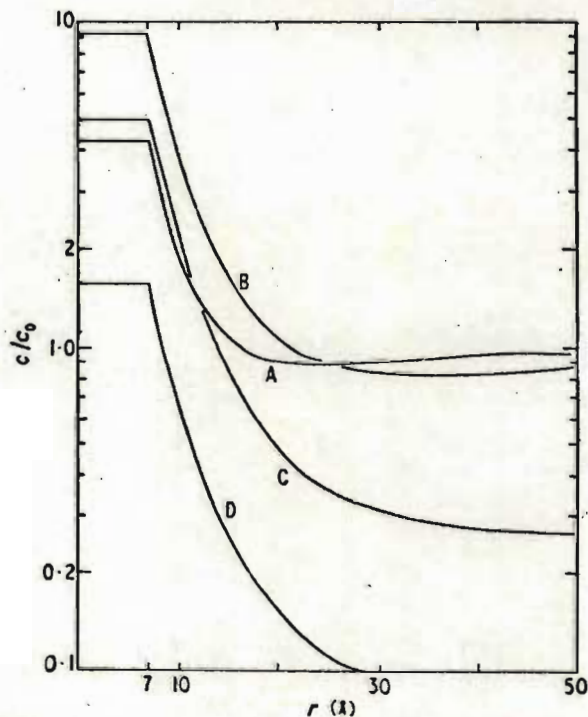
It has been shown (Section 8.3) that rafts contain all possible Burgers vectors and therefore this mechanism is not entirely correct.

Interstitial concentration distributions near a dislocation.

{From Bullough and Newman (1970)}



- A. Concentration distributions at various reduced times  $m = Dt/r_c^2$  ( $r_c = 7 \text{ Å}$ ) with no rate limitation at the dislocation core. The full curves are when the interaction potential is zero: curve A,  $m = 1$ ; curve B,  $m = 100$ ; curve C,  $m = 400$ ; curve D,  $m = 1000$ . The dislocation density is  $10^{11} \text{ cm}^{-2}$ .



- B. Concentration distributions at various reduced times  $m = Dt/r_c^2$  ( $r_c = 7 \text{ Å}$ ) with a constant rate limitation at the dislocation core of  $\alpha^2 = 0.1$ : curve A,  $m = 2$ ; curve B,  $m = 10$ ; curve C,  $m = 500$ ; curve D,  $m = 1000$ . The dislocation density is  $10^{11} \text{ cm}^{-2}$ . ( $\alpha^2 = 2 r_c^2 K_p / DZ$  where  $K_p$  is the transfer velocity and  $Z$  is the average separation of the precipitate particles). Initially at  $m = 0$ ,  $c/c_0 = 1$ .

Rafts contain a number of small loops which are assumed to be interstitial and which must have been nucleated in the immediate vicinity of the raft since they cannot have migrated large distances to join the raft (Section 9.2). This implies a large concentration of interstitials in the immediate vicinity of the raft. Thus diffusion alone cannot account for the observed rafts since if diffusion alone was responsible then the interstitial concentration would be least in the immediate vicinity of a raft and greatest in inter-raft areas, and therefore interstitial precipitation would not occur near rafts.

The second possible mechanism of raft formation must therefore involve diffusion in a non-random walk process in which the attraction between the interstitials and the dislocations plays a part.

The interstitials will fall into the influence of the strain field of a dislocation when they are some distance from the dislocation. Interstitials and dislocations interact in various ways, and Bullough and Newman (1970) have evaluated the various contributions to the overall attraction and have shown that the most important long-range interaction arises from the Cottrell (1953) size effect, in which the interstitial is regarded as a centre of dilation. The detailed mathematical treatment of Heald (1975) and Heald and Speight (1975) shows that interstitials feel the influence of a dislocation's strain field when they are at a characteristic distance  $L$  away from a dislocation where

$$L = \frac{(1 + \nu) \mu \Delta V b}{3(1 - \nu) k T \pi} \quad (9.9)$$

where

$\nu$  is Poisson's ratio

$\mu$  is the shear modulus

$b$  is the Burgers vector

and  $\Delta V$  is the volume change due to the interstitial.

For copper at the temperatures under consideration  $L$  varies from about  $100 \text{ \AA}$  to a few hundred  $\text{\AA}$ . Levy (1974) shows that in aluminium, voids form preferentially in an area of the order of  $1 \text{ }\mu\text{m}$  from a dislocation and thus the influence of the dislocation-interstitial interaction extends over a range of this order.

Heald (1975) and Heald and Speight (1975) point out that although the magnitude of the dislocation preference for interstitials is still uncertain the bias arises because point defects do not randomly diffuse to a dislocation but are subjected to a force  $E(r, \theta)$  arising from the dislocation - point defect interaction. These workers therefore give the flux of either species to a dislocation as

$$J = D \text{ grad } C + \frac{DC}{kT} \text{ grad } E(r, \theta) \quad (9.10)$$

where  $C$  is the concentration  
 $D$  is the diffusion coefficient  
 $r, \theta$  are the polar coordinates of the point defect with respect to the dislocation.

The first term in (9.10) is the normal random walk diffusion while the second term gives rise to the dislocation bias since it is different for vacancies and interstitials. These researchers show that for an edge dislocation in an elastically isotropic crystal that

$$E(r, \theta) = \frac{(1 + \nu)}{3(1 - \nu)} \cdot \frac{\mu \Delta V \cdot b \sin \theta}{\pi r} \quad (9.11)$$

where  $\nu$  is Poisson's ratio  
 $\mu$  is the shear modulus  
 $b$  is the Burgers vector  
 and the volume change  $\Delta V$  is related to the gradient of the inter-atomic potential  $\phi(r)$  at the displaced atomic positions in

accordance with

$$\Delta V = - \frac{1}{3K} \sum_S S_j \frac{\partial \phi}{\partial x_j} \Big|_{s+u} \quad (9.12)$$

where  $S$  are the lattice sites and  
 $u$  their displacements  
 and  $K$  is the bulk modulus.

In steady state conditions the divergence of the flux of point defects to a dislocation is zero and thus Heald and Speight show that (9.10) becomes

$$\nabla^2 C + \frac{1}{kT} \text{grad } C \cdot \text{grad } E(r, \theta) = 0 \quad (9.13)$$

since  $E(r, \theta)$  is harmonic.

Heald and Speight consider that the concentration of defects must equal the thermal equilibrium level at the dislocation core ( $r = r_0$ ) and so one of the boundary conditions to (9.4) is that at  $r = r_0$

$$C = C^{\text{th}} \cdot \exp - E(r_0, \theta) / kT \quad (9.14)$$

where  $C^{\text{th}}$  is the thermal equilibrium concentration far from a dislocation.

At distances far from a dislocation  $E(r, \theta) \rightarrow 0$  and Heald and Speight assume that midway between dislocations (at  $r = R$ ) the concentration is some average value  $C^0$ . Then at  $r = R$ ,

$$C = C^0 \quad (9.15)$$

These boundary conditions do not include any production of point defects within the volume of material surrounding the dislocation, but instead there is a steady flow of defects into the region from an unlimited source.

The solution to (9.13) subject to boundary conditions (9.14) and (9.15) has been given by Margvelashvili and Saralidze (1973) as

$$C(r, \theta) = C^{th} \exp \left[ \frac{-E(r, \theta)}{kT} \right] + (C^0 - C^{th}) \exp \left[ \frac{-E(r, \theta)}{2kT} \right] \psi(r, \theta) \quad (9.16)$$

$$\text{where } \psi(r, \theta) = \frac{K_0(L/2r) \cdot I_0(L/2r_0) - I_0(L/2r) \cdot K_0(L/2r_0)}{K_0(L/2R) \cdot I_0(L/2r_0) - I_0(L/2R) \cdot K_0(L/2r_0)} \quad (9.17)$$

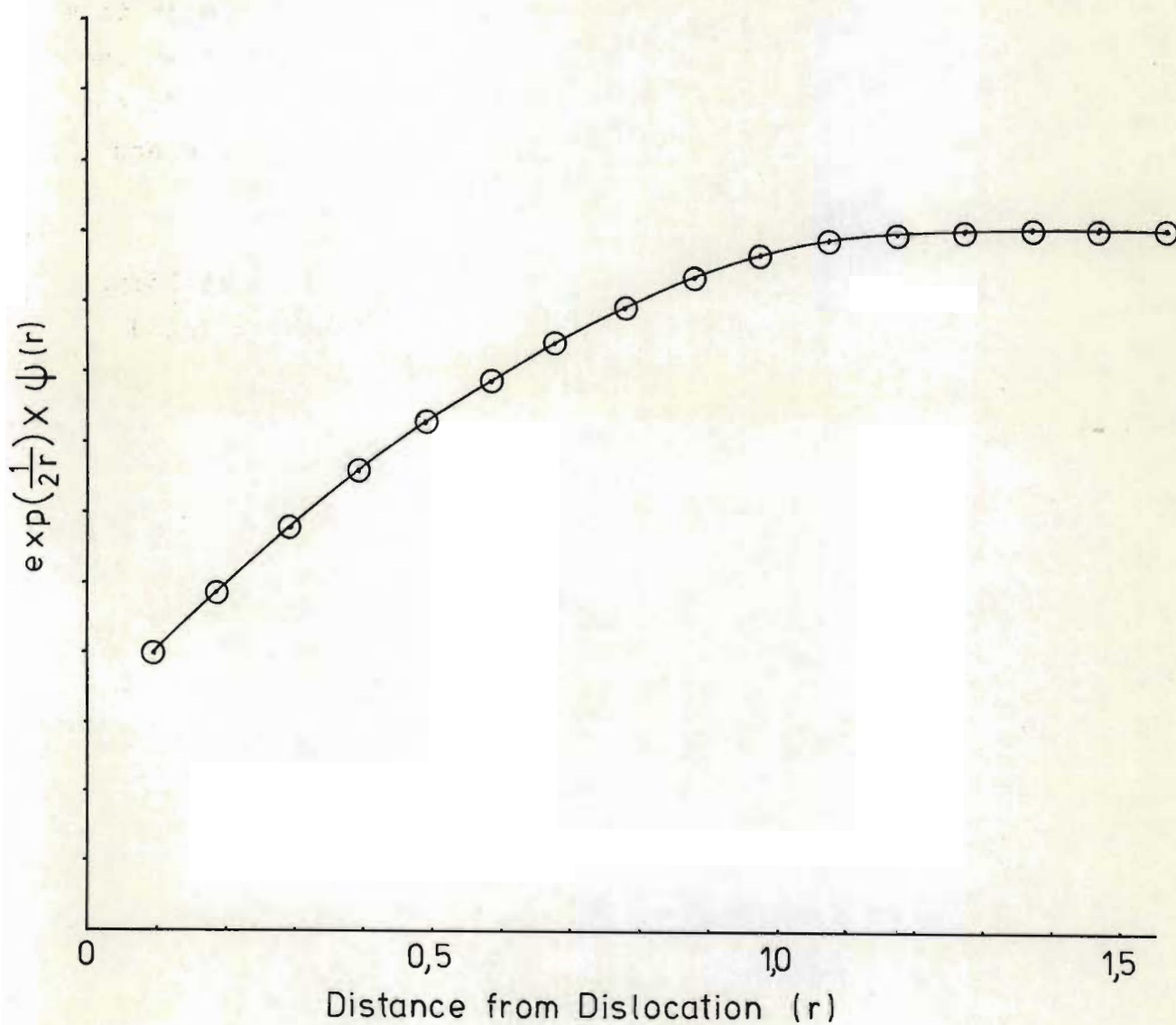
in which  $K_0(Z)$  and  $I_0(Z)$  are the modified Bessel functions of zero order and  $L$  is the characteristic range of the interaction potential (9.9).

On examining the expression for the interstitial concentration distribution (9.16) the first term is due to the normal random walk diffusion and the second term is due to the irradiation. On plotting this second term one finds that the concentration decreases monotonically as one approaches the dislocation (Figure 9.3). Therefore one would not expect interstitial loops to nucleate near the dislocation. The boundary condition (9.14) implies that the dislocation is a perfect sink for excess point defects, which is not usually the case (Nabarro (1967) Chapter 6). In addition the present experimental results show quite clearly that there is precipitation of point defects in rafts, particularly at a temperature of 250°C. Therefore, since there is precipitation, the situation which exists must be like Figure 9.2B and not like Figure 9.2A, i.e. the climbing dislocations constituting rafts are rate limited sinks and not infinite sinks.

FIG (9.3)

Graph of  $\exp\left(\frac{1}{2r}\right) \psi(r)$  vs distance from the dislocation

This graph shows the trend of the interstitial concentration as determined by the second term in equation (9.16). This term is the contribution due to irradiation.



$r$  is in units of  $L$  (equation (9.9))

A further consideration is that the dislocation must not be considered to be static but moving. Thus if a dislocation has a high concentration of interstitials in the cylinder around it as a result of non-random walk diffusion, and it then suddenly climbs in one particular direction, then a local high concentration of interstitials will be left at the position just vacated by the dislocation. These interstitials would then tend to coalesce and interstitial loops would be nucleated.

In Section 9.2 it was shown that it is not possible for dislocation loops to migrate large distances to join a raft, but the glide and climb equations (9.5) and (9.6) show that those loops which are very close to the raft will be drawn into it and so a more tightly tangled cluster of damage will result. It therefore appears that a raft, once formed, will tend to compact itself.

The high purity copper specimens were all irradiated under a helium atmosphere, and were free from oxide when placed into the H.T.R. before irradiation. Therefore it is extremely unlikely that any impurities were responsible for the raft formation mechanism.

#### 9.4 RELATION OF THE PROPOSED FORMATION MECHANISM TO THE OBSERVED DAMAGE MORPHOLOGY

The damage morphology observed in both the specimens irradiated at 250°C and 350°C is similar. The main difference observed is that the rafts at 250°C contain more black dot damage while those at 350°C contain more dislocation line segments (e.g. Figures 7.19 and 7.29). This is possibly due to the mean free path of an interstitial before annihilation by a vacancy being larger at the lower temperature and thus the catchment volume of a raft is greater at the lower temperature. Also the dislocation climb rate would be higher at the higher temperature enabling interstitials to be rapidly absorbed by climbing dislocations,

and so increasing the dislocation line length while inhibiting the formation of many small interstitial loops. Thus it appears that the precipitation of interstitials is predominant at  $250^{\circ}\text{C}$  while at  $350^{\circ}\text{C}$  there is considerably more climb and less precipitation taking place.

At an irradiation temperature of  $400^{\circ}\text{C}$  where the mean free path of an interstitial before annihilation is small, and where the dislocation climb rate is high, groups of rather smooth dislocations are seen (Figure 7.36). Due to the low damage density and the untangled nature of the dislocation groups it appears that relatively few interstitials migrated to dislocations during an irradiation at  $400^{\circ}\text{C}$ .

After an irradiation at  $300^{\circ}\text{C}$  no rafts are evident, but a large amount of damage is present. The X-ray measurements of Larson and Young (1972) also indicate a large amount of damage present at this temperature (Figure 3.5). It is possible that if the combination of the various parameters at this temperature (e.g. climb rate, diffusion rate, etc.) are such that damage accumulates at a very rapid rate, then damage may form so rapidly that a large number of smaller dislocation tangles rather than a smaller number of large rafts form. The very different damage morphology observed at this temperature may however be due to some other additional factor and not temperature alone, and therefore more irradiations must be carried out in this temperature range to check if the damage morphology remains unchanged.

Rafts of damage are often observed to align themselves along  $\{211\}$  directions. In a completely unstrained crystal any dislocations present would not be expected to have a preferred orientation. However if a crystal was subjected to some stress resulting in a strain, such as would be expected to occur during crystal growth i.e. as a result of the thermal contraction of crystals on cooling in the crystal mould, then dislocations would be expected to multiply preferentially on one slip

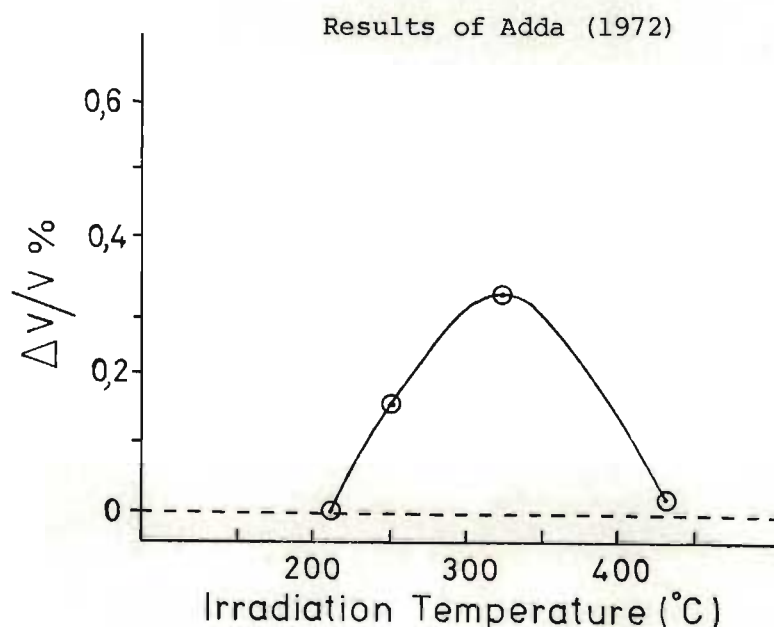
system. As is well known (Fourie (1964)) such a situation would result in a number of edge dislocations lying along a single  $\langle 211 \rangle$  direction in the lattice. Therefore if rafts originate from grown-in dislocations they would sometimes be expected to exhibit a preferential alignment along  $\{211\}$  directions.

A single edge dislocation climbing in a crystal would climb along its 'extra plane of atoms' and thus would move in a specific direction. Thus if a raft of damage formed on and around an edge dislocation it might be possible that the triangular prism shape of the raft (Figure 7.12) might result from the entire raft tending to climb in the preferential direction of the original dislocation.

The process of damage precipitation in the neighbourhood of dislocations might be relevant to the phenomenon of radiation induced swelling. Adda (1972) shows the amount of swelling as a function of irradiation temperature for copper (Figure 9.4) and this graph is similar to that of Larson and Young (1972) (Figure 3.5) which correlates with the present results. Also Bloom (1972) shows a micrograph of dislocation

Figure 9.4

The amount of swelling as a function of  
irradiation temperature for copper



loops clustered about grown-in dislocations in annealed 304 stainless steel irradiated at 370°C to a dose of  $2 \times 10^{21}$  neutrons  $\text{cm}^{-2}$ . The micrograph of Bloom (1972) is similar in appearance to that of Scheidler *et al.*, (1966) for copper irradiated at ambient temperatures.

CHAPTER TENFUTURE WORK

## 10.1      Summary of future work

## 10.1

SUMMARY OF FUTURE WORK

A number of points have arisen from the present work which are considered worthy of further investigation.

1. A number of extra irradiations need to be carried out, particularly over two temperature ranges viz. the range  $150^{\circ}\text{C}$  to  $250^{\circ}\text{C}$  and the range in the region of  $300^{\circ}\text{C}$ . In the first range it is important to determine at which point the onset of marked clustering of radiation damage into rafts occurs. The damage observed in the present work did not cluster into rafts after an irradiation at  $300^{\circ}\text{C}$  and thus investigation of this temperature range is of importance.
2. With electron microscopy and etch pit techniques it is not possible to determine the total amount of damage present in specimens irradiated at high temperatures. However there now exists, at the Atomic Energy Board in Pretoria, a Low Angle Neutron Scattering Facility which is ideally suited to determining, from the bulk specimens, the total amount of damage accumulated in the rafts (Mayer (1976)). With this facility the total damage generated both as a function of neutron dose and of irradiation temperature can be determined. These results can then be correlated with the damage morphology observed in electron microscopy.
3. The pre-irradiation dislocation densities of the crystals used in this work were not very low (Table 7.1) and crystals of low dislocation density should be grown and irradiated. Since it is believed that long range point defect migration to dislocations is responsible for raft growth, it is important to carry out experiments with low dislocation density crystals to see if the damage morphology changes in character

as a function of dislocation density.

A crystal growing system to produce low dislocation density crystals is currently being assembled in Pietermaritzburg.

4. A number of experiments need to be carried out using neutron doses much lower and much higher than those used in the current work. The low dose experiments should enable one to determine the onset of the clustering of damage into rafts and also the mechanism by which rafts start to form. Experiments using high doses will provide information on the damage morphology as rafts become very large and/or very dense.
5. The annealing of the high temperature damage in situ in the electron microscope using a heating stage should also provide interesting results, especially in connection with any rearrangement of the macroscopic shapes of rafts which might occur.
6. Mechanical properties analyses, using the tensile testing apparatus of Nathanson (1975), should be carried out on specimens from all of the irradiations carried out.
7. No rafts similar to those examined in this work have yet been found in metals other than copper. Thus it is of interest to irradiate other metals to see if similar rafts of damage can be formed. It is also of interest to irradiate certain copper alloys (e.g. Cu Al) to see how the damage morphology is altered by the addition of different amounts of a different atom species.

REFERENCES

- |  |       |  |
|--|-------|--|
| Adda, Y.   | 1972  | 'Radiation - induced voids in metals'.<br>ed. J.W. Corbett and L.C. Ianniello, p.31. |
| Ashby, M.F. and<br>Brown, L.M.                           | 1963a | Phil. Mag., <u>8</u> , 1083.   |
| Ashby, M.F. and<br>Brown, L.M.                           | 1963b | Phil. Mag., <u>8</u> , 1649.   |
| Aspeling, J.   | 1976  | Private communication.   |
| Barnes, R.S. and<br>Mazey, D.J.                          | 1960  | Phil. Mag., <u>5</u> , 1247.   |
| Beeler, J.R.   | 1966  | Phys. Rev., <u>150</u> , 470.  |
| Bell, W., Roser, W.R.<br>and Thomas, G.                  | 1964  | Acta. Met., <u>12</u> , 1247.  |
| Bell, W.L. and<br>Thomas G.                              | 1966  | Phil. Mag., <u>13</u> , 395.   |
| Bentley, J.  | 1974  | Ph.D. Thesis, University of Birmingham.  |
| Bentley, J.,<br>Eyre, B.L. and<br>Loretto, M.H.          | 1974  | Proc. 8th Int. Conf. on Electron<br>Microscopy, Canberra, Vol. 1, p.612.             |
| Black, K.  | 1976  | M.Sc. Thesis, University of Natal.   |
| Bloom, E.E.  | 1972  | 'Radiation - induced voids in metals'.<br>ed. J.W. Corbett and L.C. Ianniello, p.1.  |
| Bourassa, R.R. and<br>Lengler, B.                        | 1976  | Journal of Phys. F., <u>6</u> , 1405.  |
| Bourret, A. and<br>Dautreppe, D.                         | 1967  | Phys. Stat. Sol., <u>19</u> , 251.   |
| Brimall, J.L.,<br>Kulcinski, G.L. and<br>Kissinger, H.E. | 1971  | Rad. Eff., <u>9</u> , 273.   |
| Brinkman, J.A.   | 1954  | J. Appl. Phys., <u>25</u> , 961.   |

- |  |       |   |
|--|-------|---|
| Brinkman, J.A.,<br>Dixon , C.E. and<br>Meechan, C.J. | 1954  | Acta. Met., <u>2</u> , 38.  |
| Brown, L.M.  | 1964  | Proc. Sym. Electron Microscopy,<br>ed. B.U.F.F.A.P., Rome.                          |
| Bullough, R.,<br>Eyre, B.L. and<br>Krishan, K.       | 1975  | To be published.  |
| Bullough, R.,<br>Newman, R.C.                        | 1970  | Rep. Prog. Phys., <u>33</u> , 101.  |
| Chik, K.P.   | 1966  | Phys. Stat. Sol., <u>16</u> , 685.  |
| Corbett, J.W.,<br>Smith, R.B. and<br>Walker, R.M.    | 1959a | Phys. Rev., <u>114</u> , 1452.  |
| Corbett, J.W.,<br>Smith, R.B. and<br>Walker, R.M.    | 1959b | Phys. Rev., <u>114</u> , 1460.  |
| Cotterell, A.H.                                      | 1953  | 'Dislocation and plastic flow in crystals'. Oxford.                                 |
| Crump III, J.C.                                      | 1968  | Bull. Am. Phys. Soc., <u>13</u> , 462.  |
| Damask, A.C. and<br>Dienes, G.J.                     | 1971  | 'Point defects in metals'.<br>pub. Gordon and Breach, p.195.                        |
| Diepers, H.  | 1967a | Phys. Stat. Sol., <u>24</u> , 235.  |
| Diepers, H.  | 1967b | Phys. Stat. Sol., <u>24</u> , 623.  |
| Diepers, H. and<br>Diehl, J.                         | 1966  | Phys. Stat. Sol., <u>16</u> , K109.   |
| Doran, D.G.  | 1970  | Rad. Eff., <u>2</u> , 249.  |
| Edington, J.W.                                       | 1975  | 'Practical electron microscopy in materials<br>science', Vol. 3, MacMillan, London. |
| Edmondson, B. and<br>Williamson, G.K.                | 1964  | Phil. Mag., 9, 277.   |
| English, C.A.,<br>Eyre, B.L. and<br>Summers, J.      |       | To be published.  |

- |   |      |  |
|---|------|--|
| English, C.A.,<br>Eyre, B.L. and<br>Wadley, H.                      | 1975 | To be published.   |
| Essman, U. and<br>Wilkins, M.                                       | 1964 | Phys. Stat. Sol., <u>4</u> , K53.  |
| Evans, J.H.   | 1973 | Rad. Eff., <u>17</u> , 69.   |
| Eyre, B.L.  | 1972 | 'Defects in refractory metals'.<br>Proc. Int. Discussion meeting, Mol., Sept. 1971.<br>S.C.K./C.E.N., Mol., Belgium, eds. de Batist,<br>R., Nihoul, J. and Stals, L. |
| Eyre, B.L. and<br>English, C.A.                                     | 1974 | Consultant symposium 'The physics of<br>irradiation produced voids'.<br>Harwell, A.E.R.E., R7934, p.239.   |
| Eyre, B.L. and<br>Maher, D.M.                                       | 1971 | Phil. Mag., <u>24</u> , 767.   |
| Eyre, B.L.,<br>Maher, D.M. and<br>Bartlett, A.F.                    | 1971 | Phil. Mag., <u>23</u> , 439.   |
| Foreman, A.J.E.   | 1974 | Rad. Eff., <u>21</u> , 81.   |
| Foreman, A.J.E. and<br>Eshelby, J.D.                                | 1962 | A.E.R.E. Rep., 4170.   |
| Forwood, C.T. and<br>Humble, P.                                     | 1970 | Aust. J. Phys., <u>23</u> , 697.   |
| Fourie, J.T.  | 1964 | Phil. Mag., <u>10</u> , 1027.  |
| Frank, F.C.   | 1957 | Disc. Faraday Soc., <u>23</u> , 122.   |
| Frank, W. and<br>Seeger, A.   | 1975 | Rad. Eff., <u>25</u> , 17.   |
| Friedel, J.   | 1964 | 'Dislocations'. Pergamon Press, London.  |
| Gibson, J.B.,<br>Goland, A.W.,<br>Milgram, M. and<br>Vineyard, G.H. | 1960 | Phys. Rev., <u>120</u> , 1229.   |
| Glowinski, L.,<br>Fiche, C., Lott, M.                               | 1973 | J. Nucl. Mat., <u>47</u> , 295.  |

- |   |      |  |
|---|------|--|
| Goringe, M.J.   | 1971 | 'Electron microscopy in materials science'.<br>ed. U. Valdre, Academic Press, New York, p.462. |
| Greenfield, I.G. and<br>Wilsdorf, H.G.F.  | 1960 | Naturwissenschaften, <u>47</u> , 395.  |
| Greenfield, I.G. and<br>Wilsdorf, H.G.F.  | 1961 | J. Appl. Phys., <u>32</u> , 827.   |
| Groves, G.W. and<br>Kelly, A.   | 1961 | Phil. Mag., <u>6</u> , 1527.   |
| Groves, G.W. and<br>Kelly, A.   | 1962 | Phil. Mag., <u>7</u> , 892.  |
| Haussermann, F.   | 1972 | Phil. Mag., <u>25</u> , 537.   |
| Hazzledine, P.  | 1963 | Institute of Physics Conf. on<br>Elec. Mic., Cambridge.  |
| Heald, P.T.   | 1975 | Phil. Mag., <u>31</u> , 551.   |
| Heald, P.T. and<br>Speight, M.V.  | 1974 | Phil. Mag., <u>30</u> , 869.   |
| Heald, P.T. and<br>Speight, M.V.  | 1975 | Acta. Met., <u>23</u> , 1389.  |
| Hedges, J.M. and<br>Mitchell, J.W.  | 1953 | Phil. Mag., <u>44</u> , 223.   |
| Hesketh, R.V. and<br>Rickards, G.K.   | 1966 | Proc. Roy. Soc., <u>A289</u> , 353.  |
| Hevesy, G. and<br>Obrutsheva, A.  | 1925 | Nature, <u>115</u> , 674.  |
| Hirsch, P.B.  | 1962 | Phil. Mag., <u>7</u> , 67.   |
| Hirsch, P.B., Howie,<br>A., Nicholson, R.B.,<br>Pashley, D.W. and<br>Whelan, M.J. | 1965 | 'Electron microscopy of thin crystals'.<br>Butterworths.                                       |
| Hirsch, P.B.,<br>Howie, A. and<br>Whelan, M.J.                                    | 1960 | Phil. Trans. Roy. Soc. (London), <u>A252</u> , 499.  |
| Howie, A.   | 1963 | Proc. Roy. Soc., <u>A271</u> , 268.  |

- |   |      |   |
|---|------|---|
| Howie, A.   | 1970 | 'Modern diffraction and imaging techniques in material science'. eds. S. Amelinckx, R. Gevers, G. Remaut and J. van Landuyt. North-Holland, Amsterdam, p.295. |
| Howie, A. and Whelan, M.J.                              | 1961 | Proc. Roy. Soc., <u>A263</u> , 217.   |
| Howie, A. and Whelan, M.J.                              | 1962 | Proc. Roy. Soc., <u>A267</u> , 206.   |
| Hulett, L.D., Baldwin, T.O., Crump J.C. and Young, F.W. | 1968 | J. Appl. Phys., <u>39</u> , 3945.   |
| Huntington, H.B., Shirn, G.A. and Wajda, E.S.           | 1955 | Phys. Rev., <u>99</u> , 1085.   |
| Iphorski, M. and Brown, L.M.                            | 1970 | Phil. Mag., <u>22</u> , 931.  |
| Isebeck, K.   | 1972 | Rad. Eff., <u>14</u> , 143.   |
| Jackson, P.J.   | 1968 | Unpublished work.   |
| Jackson, P.J.   | 1976 | To be published in Phil. Mag.   |
| Jackson, P.J., Kemm, K.R. and Spalding, D.R.            | 1974 | Proc. 8th Int. Conf. on Electron Microscope, Canberra, <u>1</u> , 626.  |
| Jenkins, M.   | 1974 | Phil. Mag, <u>29</u> , 813.   |
| Johnson, C.A.   | 1960 | Phil. Mag., <u>5</u> , 1255.  |
| Kelly, P.M. and Blake, R.G.                             | 1973 | Phil. Mag., <u>28</u> , 415.  |
| Kemm, K.R.  | 1973 | M.Sc. Thesis, University of Natal.  |
| Kemm, K.R. and Spalding, D.R.                           | 1974 | Proc. 8th Int. Conf. on Electron Microscopy, Canberra, <u>1</u> , 628.  |
| Kikuchi, S.   | 1928 | Proc. Imp. Acad., Japan, <u>4</u> , 271.  |
| Kinchin, G.H. and Pease, R.S.                           | 1955 | Rep. Prof. Phys., <u>18</u> , 1.  |

- Labbe, M., Poirier, J.P. 1973 J. Nucl. Mat., 46, 86.
- Larson, B.C. and Young, F.W. 1972 Albany Conf. 710601 - 'Radiation induced voids in metals', p.672.
- Levy, V. 1974 Sym. The Physics of Irr. Produced voids, p.50.
- Lothe, J. 1960 J. Appl. Phys., 31, 1086.
- Love, G. 1964 Acta. Met., 12, 731.
- Love, G. and Shewman, P.G. 1963 Acta. Met., 11, 899.
- Maher, D.M. and Eyre, B.L. 1971 Phil. Mag., 23, 409.
- Makin, M.J. and Manthorpe, S.A. 1963 Phil. Mag., 8, 1725.
- Makin, M.J., Whapham, A.D. and Minter F.J. 1960 Proc. 1st Europ. Reg. Conf. on Electron Microscopy, Delft, 1, 423.
- Makin, M.J., Whapham, A.D. and Minter F.J. 1961 Phil. Mag., 6, 465.
- Makin, M.J., Whapham, A.D. and Minter, F.J. 1962 Phil. Mag., 7, 285.
- Margvelashvili, I.G. and Saralidze, Z.K. 1973 Fiz Tverd. Telu., 15, 2665.
- Matano, C. 1934 Jap. J. Phys., 9, 41.
- Mayer, R.M. 1976 Private communication.
- Mazey, D.J. and Barnes, R.S. 1968 Phil. Mag., 17, 387.
- Mazey, D.J., Barnes, R.S. and Howie, A. 1962 Phil. Mag., 7, 1861.
- McIntyre, K.G. 1967 Phil. Mag., 15, 205.
- McIntyre, K.G. and Brown, L.M. 1966a J. Phys. Radium, 27, C3-178.
- McIntyre, K.G. and Brown, L.M. 1966b 'Symposium on the nature of small defect clusters', Harwell A.E.R.E Rep., R5269, p.351.

- |  |       |  |
|--|-------|--|
| Meakin, J.D. and<br>Greenfield, I.G.                                     | 1965  | Phil. Mag., <u>11</u> , 277.   |
| Mitchell, J.W.,<br>Chevrier, J.C.,<br>Hockey, B.J. and<br>Monaghan, J.P. | 1967  | Canadian J. of Phys., <u>45</u> , 453.   |
| Mott, N.F.   | 1951  | Proc. Phys. Soc. (London), <u>B64</u> , 729.   |
| Muncie, J.W.,<br>English, C.A. and<br>Eyre, B.L.                         |       | Unpublished work.  |
| Nabarro, F.R.N.  | 1967  | 'Theory of crystal dislocations' (Oxford).   |
| Nathanson, P.  | 1975  | M.Sc. Thesis, University of Natal.   |
| Nelson, R.S.<br>Etherington, E.W. and<br>Smith, M.F.                     | 1971  | U.K.A.E.A. report TRG 2152D.   |
| Norris, D.I.R.   | 1967  | 'Interaction of radiation with solids'.<br>New York Plenum Press, p.525.   |
| Norris, D.I.R.   | 1969  | Phil. Mag., <u>19</u> , 527.   |
| Norris, D.I.R.   | 1971  | Phil. Mag., <u>23</u> , 135.   |
| Norris, D.I.R.   | 1972a | Rad. Eff., <u>14</u> , 1.  |
| Norris, D.I.R.   | 1972b | Rad. Eff., <u>15</u> , 1.  |
| Packan, N.H.   | 1971  | J. Nucl. Mat., <u>40</u> , 1.  |
| Pashley, D.W. and<br>Presland, A.E.B.                                    | 1961  | Phil. Mag., <u>6</u> , 1003.   |
| Risbet, A.   | 1974  | Thèse de Doctorat, Orsay - C.E.A. report<br>to be published.   |
| Risbet, A. and<br>Levy, V.   | 1975  | Phil. Mag., <u>31</u> , 975.   |
| Robinson, M.T. and<br>Oen, O.S.  | 1963  | Referred to as a private communication by<br>Piercy, G.R., Brown, F. and Davies, J.A.,<br>(1964), Can. J. Phys., <u>42</u> , 1116. |

- Robinson, M.T. 1971 'Radiation induced voids in metals'. eds. J.W. Corbett and L.C. Fanniello, Albany, N.Y., U.S.A., A.E.C. Symposium Series, (conf.-710601).
- Rühle, M. 1967a Phys. Stat. Sol., 19, 263.
- Rühle, M. 1967b Phys. Stat. Sol., 19, 279.
- Rühle, M. 1968 Phys. Stat. Sol., 26, 661.
- Rühle, M., Häussermann, F., Huber, P., and Wilkens, M. 1968 4th European Reg. Conf. on Electron Microscopy, Rome, 1, 377.
- Rühle, M., Häussermann, F. and Rapp, M. 1970 Phys. Stat. Sol., 39, 621.
- Rühle, M. and Wilkens, M. 1967 Phil. Mag., 15, 205.
- Rühle, M., Wilkens, M. and Essmann, U. 1965 Phys. Stat. Sol., 11, 819.
- Scheidler, G.P., Makin, M.J., Minter, F.J. and Schilling, W.F. 1966 Symposium on the nature of small defect clusters, Harwell, A.E.R.E. Rep., R5269, p.405.
- Schilling, W., Burger, G., Isebeck, K. and Wenzl, H. 1970 'Vacancies and interstitials in metals'. ed. A. Seeger *et al.*, p.255.
- Seeger, A. 1955a Z. Naturforschg, 10a, 251.
- Seeger, A. 1955b 'Handbuch der Physik'. ed. S. Flügge (Springer, Berlin/Göttingen, Heidelberg), VII/1, 383.
- Seeger, A. 1955c 'Defects in crystalline solids', p.311.
- Seidman, D.N. and Balluffi, R.W. 1967 'Lattice defects and their interactions'. ed. R.R. Hasiguti, Pub. Gordon and Bred.
- Seitz, F. and Koehler, J. 1965 J. Solid State Phys., 2, 305.

- |                                      |       |  |
|--------------------------------------|-------|--|
| Shimomura, Y.                        | 1969  | Phil. Mag., <u>19</u> , 773.   |
| Silcox, J. and<br>Hirsch, P.B.       | 1959a | Phil. Mag., <u>4</u> , 72.   |
| Silcox, J. and<br>Hirsch, P.B.       | 1959b | Phil. Mag., <u>4</u> , 1356.   |
| Silsbee, R.H.                        | 1957  | J. App. Phys., <u>28</u> , 1246.   |
| Simmons, R.O. and<br>Balluffi, R.W.  | 1960  | Phys. Rev., <u>119</u> , 600.  |
| Takagi, S.                           | 1962  | Acta. Crystallogr., <u>15</u> , 1311.  |
| Thompson, M.W.                       | 1969  | 'Defects and radiation damage in metals'.<br>Cambridge Univ. Press.  |
| Thompson, R.M. and<br>Balluffi, R.W. | 1962a | J. Appl. Phys., <u>33</u> , 803.   |
| Thomson, R.M. and<br>Balluffi, R.W.  | 1962b | J. Appl. Phys., <u>33</u> , 817.   |
| Turnbull, D. and<br>Hoffman, R.E.    | 1954  | Acta. Met., <u>2</u> , 419.  |
| Urban, K. and<br>Seeger, A.          | 1974  | Phil. Mag., <u>30</u> , 1395.  |
| Walker, R.M.                         | 1962  | 'Radiation damage in solids'.<br>ed. Billington, Academic Press.   |
| Wechsler, M.S.                       | 1963  | A.S.T.M., S.T.P., No. 34, p.86.  |
| Weertman, J.                         | 1955  | J. Appl. Phys., <u>26</u> , 1213.  |
| Weertman, J.                         | 1957  | J. Appl. Phys., <u>28</u> , 362.   |
| Wilkins, M.                          | 1964  | Phys. Stat. Sol., <u>6</u> , 939.  |
| Wilkins, M.                          | 1966  | Phys. Stat. Sol., <u>13</u> , 529.   |
| Wilkins, M.                          | 1970a | 'Vacancies and interstitials in metals'.<br>ed. A. Seeger <i>et al.</i> , p.485.                               |
| Wilkins, M.                          | 1970b | 'Modern diffraction and imaging techniques<br>in material science'. ed. S. Amelinckx <i>et al.</i> ,<br>p.233. |
| Wilson, M.M.                         | 1971  | Phil. Mag., <u>24</u> , 1023.  |
| Wolfenden, A.                        | 1972  | Rad. Eff., <u>15</u> , 255.  |